Application of a modern scanning electron microscope for materials characterization

Zur Erlangung des akademischen Grades eines
Doktors der Naturwissenschaften
von der KIT-Fakultät für Physik
des Karlsruher Instituts für Technologie (KIT)

genehmigte
DISSERTATION
von

M.Eng. Cheng Sun
aus
Shandong (China)

Tag der mündlichen Prüfung: 18. Oct. 2019

Referentin: Prof. Dr. D. Gerthsen

Korreferent: Prof. Dr. E. Spiecker

angefertigt am
Laboratorium für Elektronenmikroskopie (LEM)
Karlsruher Institut für Technologie (KIT)

CONTENTS

LIST OF ACRONYMS

A549	One type of lung cells
AE	Auger electron
Al_2O_3	Aluminum oxide
Au	Gold
aC	Amorphous carbon
BCP	Block copolymer
BF	Bright-field
BSE	Backscattered electrons
CBS	Concentric backscattered detector
CeO_2	Cerium dioxide
CeTE	Computation of electron transport equation
CCD	Charge-coupled device
CNT	Carbon nanotube
C-S-H	Calcium silicate hydrates
DF	Annular dark-field
EBSD	Electron backscatter diffraction
ECCI	Electron channeling contrast imaging
ECP	Electron channeling pattern
EDXS	Energy dispersive X-ray spectroscopy
EFTEM	Energy-filtered TEM
ETD	Everhart-Thornley detector
FEG	Field emission gun
Fe_2O_3	Ferric oxide
FIB	Focused-ion-beam

HAADF	High-angle annular dark-field
HRTEM	High-resolution TEM
ICD	In-column detector
ICE	Ion conversion and electron detector
KIT-6	One type of mesoporous silica
LLTO	$Li_{3x}La_{2/3-x}TiO_3$
Low-keV STEM	Low-energy STEM
MC	Monte-Carlo
MD	Mirror detector
Ni	Nickel
$NiIr_4$	Nickel iridium
NP	Nanoparticle
OsO_4	Osmium tetroxide
PS-b-PI	Polystyrene-b-polyisoprene
Pt	Platinum
SE	Secondary electron
SEM	Scanning electron microscope
SiO_2	Silicon oxide
$SrTiO_3$	Strontium titanate
$SrTi_{1-x}Fe_xO_{3-\delta}$	Strontium titanate doped with Fe
STEM	Scanning transmission electron microscopy
TE	Forward scattered electrons/Transmitted electrons
t-EBSD	Transmission electron backscatter diffraction/transmission Kikuchi diffraction
TED	Transmission electron diffraction

TEM   Transmission electron microscope

TiO_2 Titanium dioxide

TKB   Transmission Kikuchi band

TKD   Transmission Kikuchi diffraction

TLD   Through-the-lens Detector

WD   Working distance

ZB   Zero-order beam

ZnO   Zinc oxide

x

LIST OF SYMBOLS

A	Atomic weight
a_H	Bohr radius
α	Objective aperture-limited semi-angle
$\vec{b}$	Burgers vector
$\vec{b}_e$	The edge Burgers vector part in a mixed dislocation
$\vec{b}_s$	The screw Burgers vector part in a mixed dislocation
α'	One tilt direction for the double-tilt sample holder
β	Gun brightness
β'	Second tilt direction for the double-tilt sample holder
C_c	Lens chromatic aberration coefficient
C_s	Lens spherical aberration coefficient
d	Lattice parameter
d_0	Geometric beam diameter
d_A	Beam diameter related to astigmatism
d_c	Beam diameter related to C_c
d_d	Beam diameter related to diffraction error
d_p	Final/overall beam diameter
d_s	Beam diameter related to C_s
$d\sigma_{el}/d\Omega$	Elastic differential cross-section
$d\sigma_{inel}/d\Omega$	Inelastic differential cross-section
δ	SE yield
E	Primary electron energy
E_c	Ionization energy
F_s	Structure factor

G	Lattice amplitude
$\vec{g}$	Diffraction vector
h	Planck's constant
η	BSE coefficient
Ψ	A plane wave function
Ψ_0	Wave amplitude
Ψ_s	Scattered wave function
I_0	Bright field intensity for a two-beam condition
I_{BF}	BF image intensity by simulation
$I_{Black\text{-}BF}$	Black-level intensity for BF detector
$I_{Black\text{-}HAADF}$	Black-level intensity for HAADF detector
I_{DF1}	DF1 image intensity by simulation
I_{DF2}	DF2 image intensity by simulation
$I_{EXP\text{-}BF}$	BF image intensity by experiment
$I_{EXP\text{-}HAADF}$	HAADF image intensity by experiment
I_g	Dark field intensity for a two-beam condition
I_{HAADF}	HAADF image intensity by simulation
$I_{NOR\text{-}BF}$	Normalized experimental BF image intensity
$I_{NOR\text{-}HAADF}$	Normalized experimental HAADF image intensity
I_P	Electron probe current
$I_{White\text{-}BF}$	White-level intensity for BF detector
$I_{White\text{-}HAADF}$	White-level intensity for HAADF detector
J	Mean ionization potential
$\vec{k}$	Wave vector for scattered wave
$\vec{k}_0$	Wave vector for incident wave

λ	Electron wavelength
p	Momentum of an electron
θ	Scattering angle
θ_B	Bragg angle
R	Electron range in interaction volume
R_x	X-ray escape depth
R_b	Parameter related to a_H and Z
r	Objective aperture radius
$\vec{r}_i$	The position of atom i
ρ	Material density
$\vec{s}$	Excitation error
$\vec{s}_g$	Excitation error for a two-beam condition
s_z	z component for excitation error
σ	Total electron yield
t	Sample thickness
$\vec{u}$	Line direction of a dislocation
Z	Atomic number
$\bar{Z}$	Average atomic number
ζ	Detector correction
ξ_g	Extinction distance
$\xi_{g,eff}$	Effective extinction distance
Δf_A	Distance between different focus points
ΔE	Energy aberration in incident electron beam

1 INTRODUCTION

In the early 1930s, Ruska and Knoll were the first to design and introduce the transmission electron microscope while Von Ardenne invented the scanning electron microscope [1, 2]. Since then electron microscopy has tremendously grown in importance and became an indispensable tool in many fields of science ranging from solid state physics, materials science, chemistry, geoscience to life sciences. Increasing requirements for analyzing electron-beam sensitive and soft materials have led to a steadily growing interest in low-energy electron microscopy in the past few years. Investigation at low primary electron energies substantially reduces knock-on damage in the sample and enhances contrast of low-density/low-atomic-number materials due to the increase of inelastic and elastic electron scattering cross-sections [3-9]. As a first approach to low-energy electron microscopy, transmission electron microscopes (TEMs), typically operated at electron energies of 80 keV and above, were aligned to be used at considerably lower electron energies. The need for low-energy electron microscopy is underlined by considerable efforts to improve the resolution of transmission electron microscopes at low electron energies with the development of high-end electron optical components such as aberration correctors and monochromators [4, 10-13].

Another approach to low-energy electron microscopy is scanning electron microscopy which up to now has been mainly used for surface topography imaging of bulk samples at electron energies of 30 keV and below. The capabilities of scanning electron microscopes (SEMs) are considerably enhanced by the implementation of a scanning transmission electron microscopy (STEM) detector for bright-field (BF), annular dark-field (DF) and high-angle annular dark-field (HAADF) STEM imaging of electron-transparent specimens. Although STEM detectors are already available in scanning electron microscopes for many years, low-energy STEM (low-keV STEM) in SEM has not been extensively exploited up to now and only few methodological studies were published [14-20]. A few dedicated investigations have appeared in the past few years where low-keV STEM in a scanning electron microscope was applied to study organic materials (organic solar cells and biological cells) which significantly profit from higher contrast at low electron energies [21-23]. The marginal interest in low-keV STEM in scanning electron microscopes can be partly attributed to the fact that resolution has been limited to about 1 nm. Nevertheless, the benefits of the technique have been recognized

which led to the improvement of BF-STEM resolution clearly into the sub-nanometer range where lattice fringes with a distance of 0.34 nm and below were resolved [24-26]. In addition to the improvement of resolution, additional capabilities are necessary to develop STEM in a SEM into a complete characterization technique for electron-transparent specimens. Decisive is the capability of recording on-axis transmission electron diffraction (TED) patterns, which has to be clearly distinguished from the established technique of transmission electron backscatter diffraction (off-axis t-EBSD) where the charge-coupled device (CCD)-camera below the specimen is inclined at a large angle with respect to the optic axis [27]. On-axis TED patterns are indispensable for the orientation of crystalline specimens in well-defined directions with respect to the incident electron beam for defect analysis or high-resolution STEM. Besides, the on-axis CCD-camera can also be applied for the acquisition of transmission Kikuchi patterns to form on-axis t-EBSD maps for the quantification of grain orientation and sizes especially for polycrystalline materials. On-axis CCD-cameras were installed only recently in scanning electron microscopes and first published results demonstrate that well-focused TED patterns are observed although a projection lens system is missing [28, 29]. Another essential ingredient for STEM in a SEM is the availability of a double-tilt specimen holder in order to orient electron-transparent specimens to well-defined diffraction conditions [65].

With the implementation of an on-axis CCD-camera and a double-tilt holder, the application range of low-keV STEM in SEM can be as wide as STEM in TEM offering great potential for material characterization, which is far beyond its traditional application for surface topography imaging of bulk samples. Regarding the lack of research on low-keV STEM in SEM, the motivation of this thesis is to explore various functions, especially low-keV STEM, in a modern SEM to study electron-transparent specimens for a variety of materials. It turned out that SEM and STEM imaging can be used in a correlative way providing complementary and comprehensive information of the same specimen region that cannot be obtained by traditional (S)TEM alone. In particular, defect analyses were successfully performed in a scanning electron microscope, which were not possible in the past.

This thesis is organized in the following way. In chapter 2, the fundamentals of SEM and STEM are described with explanations of the full set of detectors in modern SEMs.

Chapter 3 focuses on the SEM and TEM instruments used in this work for the experiments as well as preparation methods to obtain suitable electron-transparent samples. In chapter 4, correlative SEM/low-keV STEM (simplified as correlative SEM/STEM in the thesis) imaging studies on different material classes comprising magnetic materials, radiation-sensitive materials, micro/nanostructured materials and crystallized solid-state materials are presented and advantages and limits are discussed. Defect characterization by low-keV STEM in a SEM instrument is presented in chapter 5. Systematic analyses of dislocation Burgers vectors and displacement vectors of stacking faults are demonstrated with indium nitride (InN) and gallium nitride (GaN) samples.

2 FUNDAMENTALS

Within this chapter all methods used in this thesis are introduced. In the first part, the setup of a scanning electron microscope is presented and an overview of the individual components is given. The following subparts will dive deeper into individual microscope components starting with the electron gun. Afterwards the electron optical systems and their inherent aberrations are described. The most common detectors in SEMs are explained in subchapter 3. Subchapter 4 lists the limiting factors in a SEM. In subchapter 5, a short introduction on focused-ion-beam (FIB) systems is given which were used for sample preparation. The second part gives a short overview of transmission electron microscopes and emphasizes their difference with repsect to SEM instruments. The third part deals with the interactions between electrons and matter within the sample of interest. Interactions of electrons with solids generate various useful signals that can be detected by suitable detectors. Theoretical approaches presented in this chapter are mainly based on the presentation in Reimer's textbook [30].

2.1 The scanning electron microscope

In the past decades, scanning electron microscopy was widely used for imaging and analyzing bulk samples and recently also for electron-transparent samples. A basic scheme of a SEM instrument is shown in Fig. 2.1. A beam of electrons is generated by an electron gun and focused on the sample surface by an appropriate lens system. The focused electron beam interacts with the bulk sample producing secondary or backscattered electrons and characteristic X-rays. These signals can be captured with suitable detectors and converted into a digital intensity value. By scanning over the sample surface with the focused electron probe and simultaneously recording the signal intensity at each point, an image is generated. The image magnification can be controlled by changing the size of the scanned region on the sample. In the following, more details will be outlined starting with electron beam generation and ending with the introduction of focused-ion-beam.
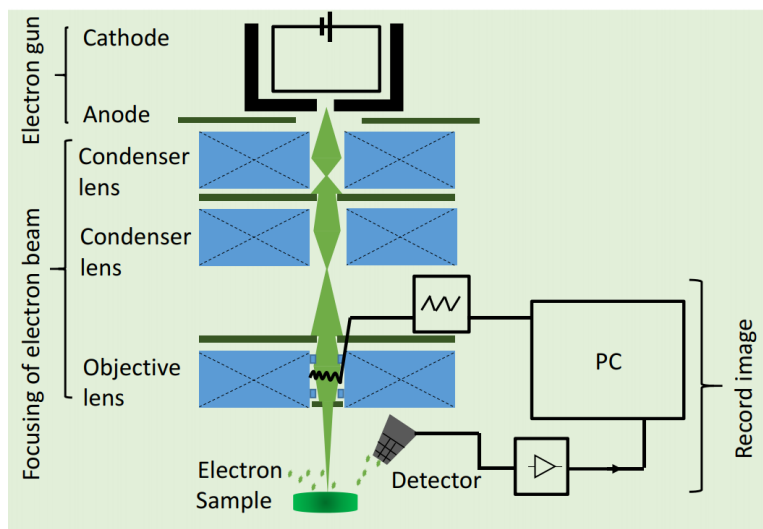
Figure 2.1. Simplified scheme of the components of a scanning electron microscope.

2.1.1 Electron gun

An electron gun is responsible for the generation of the electron beam. In the past, thermionic cathodes with filaments composed of tungsten or lanthanum hexaboride were used for the generation of electrons. Thermionic emitters require the filament to be heated to high temperatures until electrons can overcome the corresponding work function of the cathode tip and escape into vacuum. The negative biased Wehnelt cup near the cathode is used to control the emission current. Afterwards electrons are accelerated towards the anode. Nowadays field emission guns (FEGs) are widely used in electron microscopes. FEGs provide higher brightness, lower energy spread and a smaller virtual source (below 1 nm) compared to thermionic sources [24]. The working principle of FEGs relies on field-enhanced thermionic emission (Schottky FEG) where a strong electric field reduces the barrier for electrons to leave the cathode tip or "cold" field-emission (cold FEG) where the cathode temperature is strongly reduced. The electric field to lower the barrier and extract the electrons is generated by an anode placed closed to the cathode tip. Extracted electrons are accelerated by a second anode to their final energy ranging from 0.1 keV to 30 keV. Even though the electron gun is essential for electron beam generation, the final electron-beam diameter is limited by the electron optical system, i.e., lens aberrations that are explained in the following.

2.1.2 Electron optics

The electron optical system in a SEM consists of a series of lenses. In general, one can distinguish between two types of lenses, magnetic and electrostatic, which focus the electrons by rotational symmetric magnetic or electrostatic fields. Contrary to lenses used in optical microscopes, the focus length can be easily adjusted by changing the field strength. In electron microscopy, magnetic lenses are commonly preferred over electrostatic lenses since magnetic lenses have a higher optical quality and do not require high−voltage insulation [31]. In SEM instruments the electron optical system consisting of condenser and objective lenses is responsible for demagnifying the electron beam generated by the FEG. However, the optical quality of these lenses is in general quite poor due to strong lens aberrations limiting the smallest achievable focus point. The fundamental lens aberrations are exemplified in the following by assuming a parallel beam of electrons passing through a single lens.

Spherical aberration
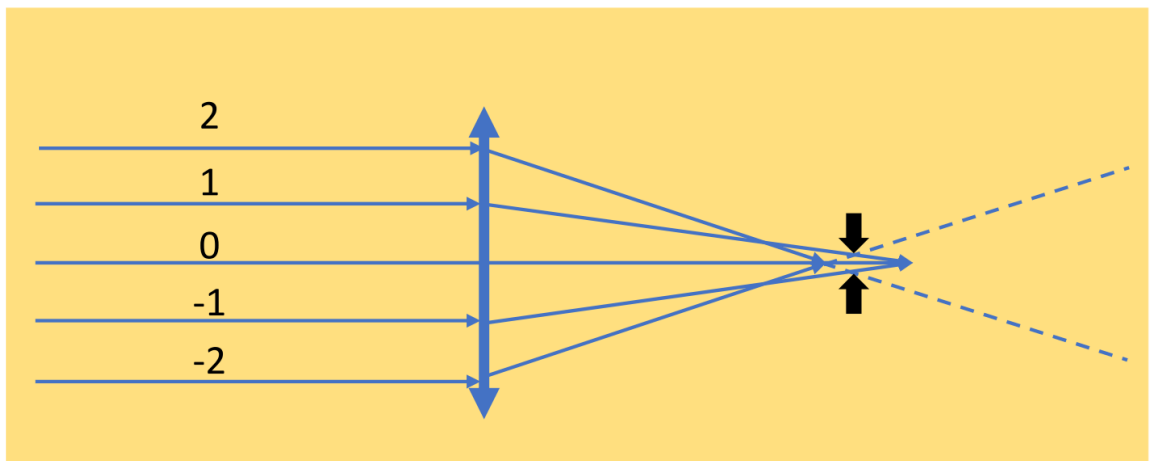
Figure 2.2. Scheme of spherical aberration of an electron lens.

The scheme in Fig. 2.2 pictures the effect of spherical aberration. Electrons far from the optical axis (rays ±2) are diffracted more strongly towards the optical axis by the magnetic field of the lens leading to different focus points. The smallest beam diameter (d_s) can be achieved at the point of least confusion as marked by two black arrows in Fig. 2.2. The beam diameter at the point of least confusion can be approximated by Eq. (1) [30].

$$d_s = 0.5 C_s \, \alpha^3 \qquad (1)$$

Here, the objective aperture-limited convergence half-angle is denoted by α while C_s is the spherical aberration coefficient of the lens. The parameter C_s scales with the focal length of the lens making short focal length desirable [30]. In SEM instruments, small focal length can be achieved by moving the sample closer to the pole piece of the objective lens. The distance between sample and pole piece is usually referred to as working distance ranging between ~1 mm to several 10 mm.

Chromatic aberration
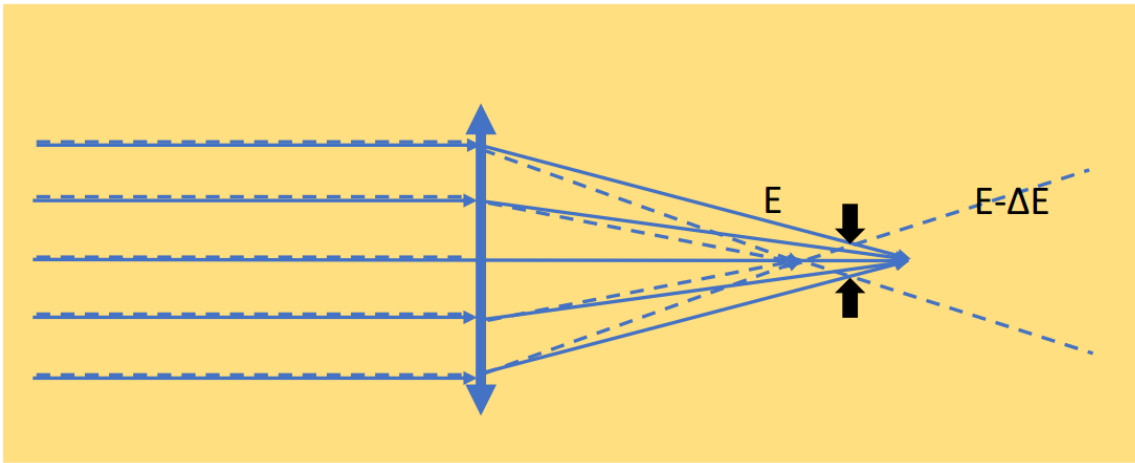
Figure 2.3. Scheme of chromatic aberration of an electron lens.

The deflection of electrons depends on their kinetic energy. Faster electrons are weakly deflected whereas slow electrons are strongly deflected leading to different focus lengths. This is demonstrated in Fig. 2.3 where rays of slow electrons with a kinetic energy of (E-ΔE) are depicted by dashed lines. The energy spread of electrons strongly depends on the type of electron source but also on the electronic stability of acceleration voltage and lens currents. In case of Schottky FEGs which are implemented in the scanning electron microscopes used within this work, the energy spread ΔE is in the range of 0.4 to 0.7 eV with the application of a monochromator [32]. The resulting beam diameter (d_c) due to chromatic aberration can be described as

$$d_c = C_c \frac{\Delta E}{E} \alpha \qquad (2)$$

with E being the electron energy and C_c the chromatic aberration coefficient [30]. Chromatic aberration is especially pronounced for low electron energies as often encountered in SEM where energies are typically between 0.1 and 30 keV.

Astigmatism

Astigmatism is caused by imperfections in the symmetry of the employed magnetic lenses and charging [30]. The asymmetry of the focusing field leads to different focal points for electrons coming from sagittal (plane ABC in Fig. 2.4) or meridional (plane CDF in Fig. 2.4) planes. The diameter related to astigmatism (d_A) can be described as

$$d_A = \Delta f_A \alpha \qquad (3)$$

The distance between the focal point marked by F and the point marked by two black arrows in Fig. 2.4 is Δf_A. Since astigmatism is caused by field asymmetries, it can be easily compensated by introducing an adjustable quadrupole field that can reduce distortions caused by the electron optical system. This leads to the so-called stigmator adjustment function in SEMs.
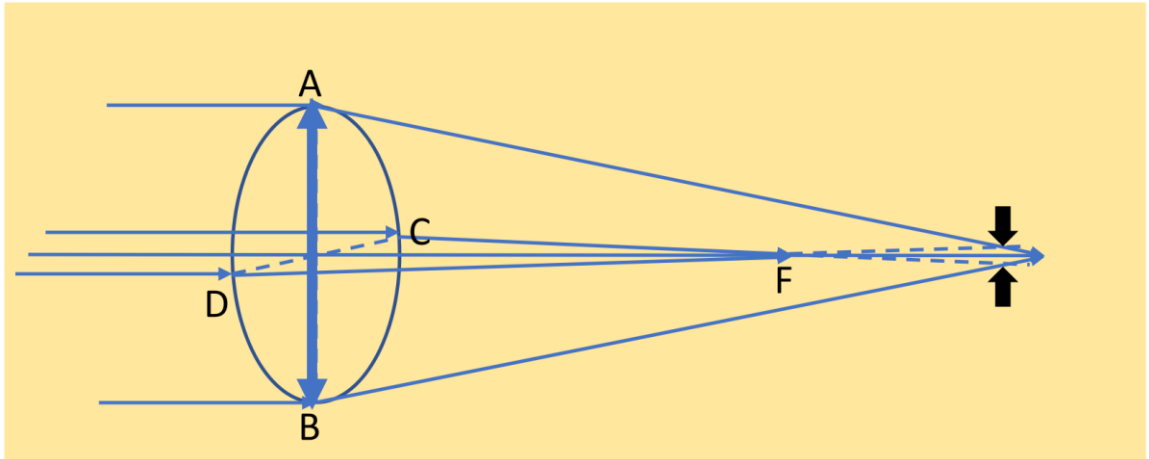
Figure 2.4. Scheme of astigmatism of an electron lens.

Diffraction error

Due to the wave-nature of electrons, an ideal point-like focus cannot be achieved as the propagating electron wave is diffracted by apertures of finite size. Therefore, even a "perfect" optical system is limited in resolution. Electron waves passing through circular apertures as employed in SEM instruments produce a rotational symmetric interference pattern called Airy disc, which is indicated in Fig. 2.5. The full width of the half first maximum d_d can be described by Eq. (4),

$$d_d = 0.6\lambda/\alpha \qquad (4)$$

where λ is the wavelength of the electrons.
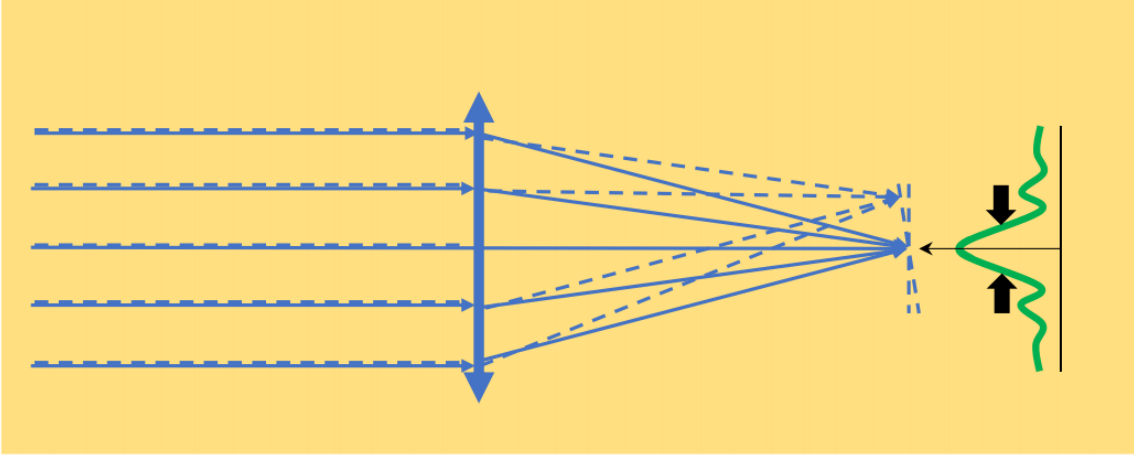
Figure 2.5. Scheme of diffraction error of an electron lens.

Electron-beam diameter

By assuming a Gaussian error distribution for the errors disk due to lens aberrations and diffraction, the diameter of the electron beam d_p [30] is given by

$$d_p^2 = d_0^2 + d_d^2 + d_s^2 + d_c^2 \qquad (5)$$

Here, d_0 represents the geometric beam diameter that can be expressed by

$$d_0 = \left(\frac{4I_p}{\pi^2 \beta}\right)^{1/2} \alpha^{-1} \qquad (6)$$

with I_p being the electron probe current and β the gun brightness. The combination of Eqs. (1-6) gives the full expression for the overall beam diameter d_P.

$$d_p^2 = \left[\left(\frac{4I_p}{\pi^2 \beta}\right) + (0.6\lambda)^2\right] \alpha^{-2} + \frac{1}{4}C_s^2 \alpha^6 + (C_c \frac{\Delta E}{E})^2 \alpha^2 \qquad (7)$$

Based on Eq. (7), the effects of different parameters in a SEM on different error disk diameters were exemplarily simulated in the following. For the simulations, an ideal β value on the upper end is chosen ($5 \times 10^{13} \frac{A}{m^2 \cdot sr}$) [33, 34] while an optimized value of 1 mm is used for both C_s and C_c aberration coefficients.

Effect of working distance on beam diameter
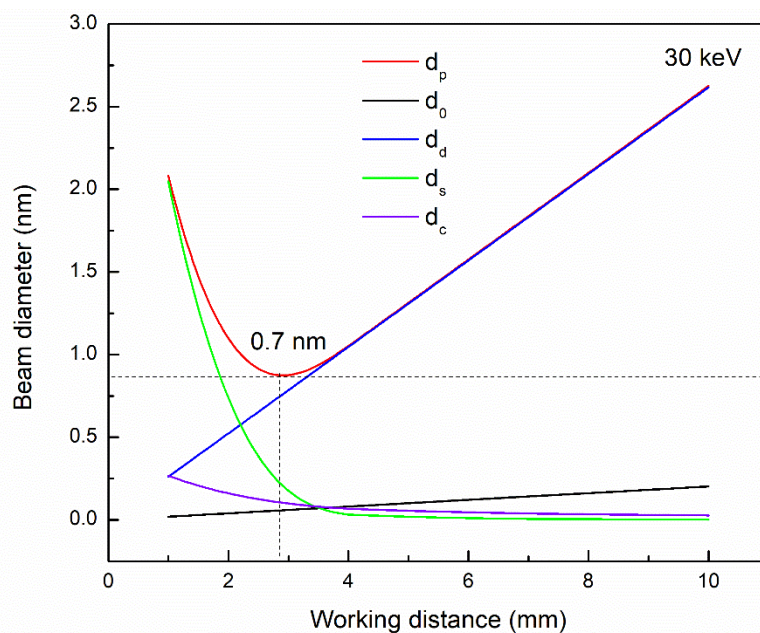
Figure 2.6. Simulated effect of working distance on the beam diameter ($E = 30$ keV, $I_p = 13$ pA, $\Delta E = 0.5$ eV, objective aperture diameter 32 μm). The red line indicates the overall beam diameter d_p. d_0, d_d, d_c and d_s show contributions of different aberrations and effects (see legend).
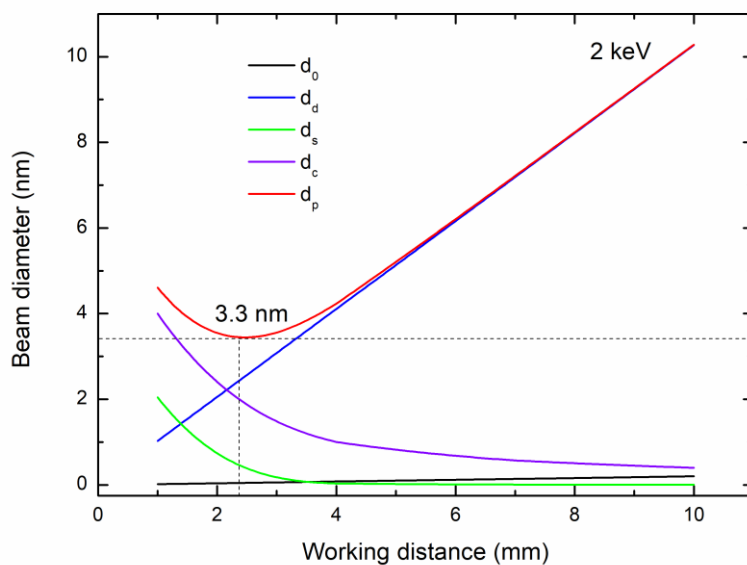
Figure 2.7. Simulated effect of working distance on the beam diameter ($E = 2$ keV, $I_p = 13$ pA, $\Delta E = 0.5$ eV, objective aperture diameter 32 μm). The red line indicates the

overall beam diameter d_p. d_0, d_d, d_c and d_s show contributions of different aberrations and effects (see legend).

The objective aperture is the closest aperture to the specimen in a SEM and typically determines the convergence half-angle α of the electron beam. As shown in Eq. (8), α is defined by the radius of the objective aperture r and the working distance WD.

$$tan\,\alpha = \frac{r}{WD} \quad , \quad WD = \frac{r}{tan\,\alpha} \qquad (8)$$

As WD is the typical parameter set in the microscope settings, simulations are given as a function of WD instead of convergence semi-angle. The aperture size was assumed to be r = 16 µm. Simulations of the beam diameter as a function of WD are displayed in Fig. 2.6 and Fig. 2.7 for 30 keV and 2 keV respectively.

With decreasing WD and therefore increasing convergence semi-angle, the overall beam diameter d_p (red line) for 30 keV in Fig. 2.6 reaches its minimum of 0.7 nm for a WD around 3 mm. For smaller WD, d_p is limited by the spherical aberration disk d_s (green line) while d_c (purple line), d_d (blue line) and d_0 (black line) are considerably smaller. Contrarily, at large WDs, d_p is mainly limited by the diffraction error disk d_d. The curves in Fig. 2.7, simulated for 2 keV show similar trends for large WDs as those in Fig. 2.6. However, the smallest probe size d_p is 3.3 nm which is considerably higher compared to the smallest probe size at 30 keV (0.7 nm). The larger minimal beam diameter is mainly caused by a considerable higher diffraction error d_d (blue line) and the steep rise of the chromatic aberration with increasing convergence semi-angle.

In order to further decrease beam size, contributions of limiting components must be reduced. As the diffraction error is a property that cannot be avoided, smaller WDs or larger aperture sizes and therefore, larger convergence semi-angle are desirable to keep the contribution of d_d to the final beam diameter d_p low. In this case it becomes obvious that the smallest beam diameter is limited by the spherical aberration for higher electron energies like 30 keV whereas at 2 keV the contribution of chromatic aberration is considerably higher. Nowadays, both C_s and C_c can be corrected in transmission electron microscopes using commercially available corrector systems [35, 36]. However, until now they are rarely seen in scanning electron microscopes. Only Haider and Zach have developed a C_s- and C_c-corrected microscope at the beginning of the 1990ties [37]. As the electron energy in SEM can be low, the chromatic aberration is dominant under these

conditions. One approach to limit the contribution by chromatic aberration is by reducing the energy spread of the electron source. As seen in Eq. (2) d_c scales linearly with the energy spread ΔE, which can be reduced by either using better electron guns or additional energy filters like monochromators.

Effect of electron energy on beam diameter
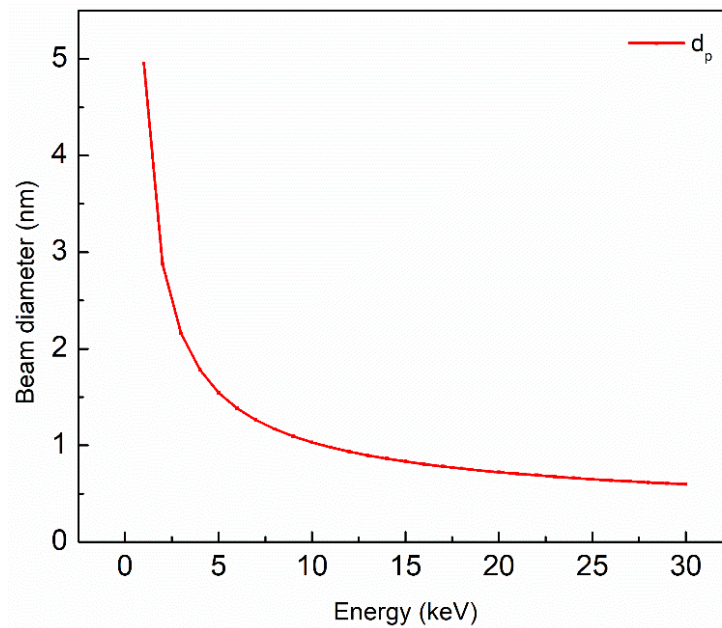
Figure 2.8. Simulated effect of the primary electron energy on the beam diameter (WD = 2 mm, I_p = 13 pA, ΔE = 0.5 eV, α = 8 mrad). The red line indicates the overall beam diameter d_p.

The effect of electron energy on the resulting beam diameter was simulated for electron energies ranging from 0.5 to 30 keV, which is a typical range for SEM instruments. The same parameters except WD and electron energies were used as in the previous section. The beam convergence semi-angle was set to 8 mrad where the beam diameter under the given condition is lowest. As shown in Fig. 2.8, it is obvious that the beam diameter (red line) decreases with increasing beam energy. Hence, uncorrected SEM instruments tend to have the smallest probe size at the highest electron energy.

Effect of beam current on beam diameter

In Fig. 2.9, the impact of beam current I_p on the beam diameter d_p is displayed for 30 keV (black curve) and 2 keV (red curve). When changing the beam current from 1 pA to 1 nA, only a moderate increase of the beam diameter of about 16.4 % (0.098 nm) is observed

for 30 keV and 0.7 % (0.02 nm) for 2 keV. It emphasizes that the effect of increasing beam current from 1 pA to 1 nA on the beam diameter in a SEM is small especially for low energies.
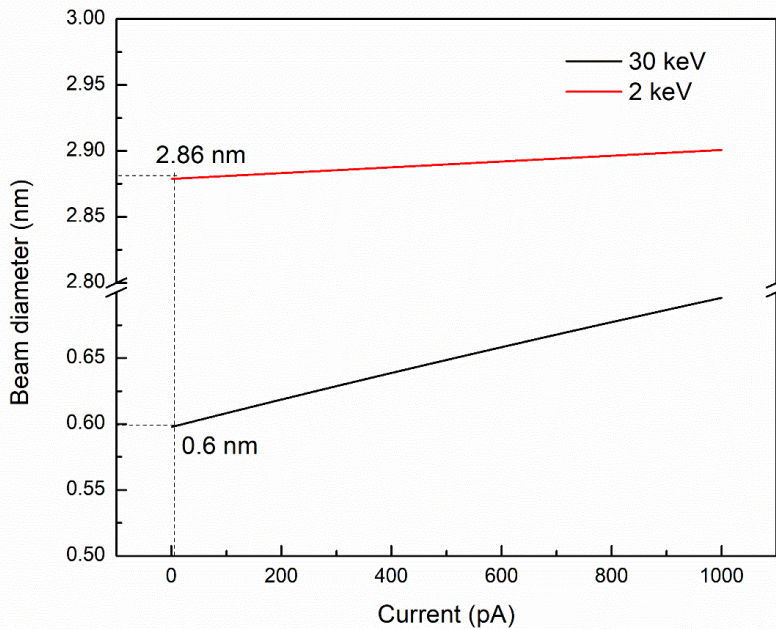
Figure 2.9. Simulated effect of the beam current on the overall beam diameter d_p (WD = 2 mm, $\Delta E = 0.5$ eV, $\alpha = 8$ mrad).

2.1.3 Signal detection in SEM

The interaction of the primary electron beam with the sample leads to the generation of various useful signals that can be detected by customized detectors. Fig. 2.10 displays all types of signals generated for either bulk (Fig. 2.10 (a)) or electron-transparent (Fig. 2.10 (b)) specimens. For bulk samples signal detection occurs above the sample surface as no electrons or X-rays are able to penetrate completely through the sample. The type of generated signals include secondary electron (SE), backscattered electron (BSE) and X-rays. For thin specimens, in addition to previously mentioned signals, transmitted electrons can be detected. Depending on the scattering angle of the transmitted electrons additional information compared to conventional SE and BSE detection can be obtained. In the following the most important detectors found in modern SEMs are introduced.

SE and BSE detection

For SE detection in SEM, the detectors are usually designed with a scintillator and photomultiplier. With the combination of a suction tube, the SEs can be attracted by the positive voltage applied on a grid at the entrance of the detector. SEs attracted by the grid will move to the scintillator and are converted into photons. Resulting photons are detected by a photomultiplier tube and converted to a digital intensity value that is processed by the computer system. Usually SE detectors are either positioned in the SEM chamber or within the electron column. The design of the standard SE detector (Everhart-Thornley detector, ETD) also allows operation in BSE mode by applying a negative voltage on the grid. Hence, only electrons with sufficient kinetic energy can pass the grid and are therefore detected. However, BSE collection efficiency is rather low because the collection angle of this type of detector is quite small.

BSE detectors with high collection efficiency are mainly solid-state detectors that typically consist of a reversed-biased p-n junction diode. When BSEs reach the diode, electron-hole pairs are generated. If the electron-hole pair reaches the depletion region of the p-n junction, the charges are separated leading to a small electric current. This current is amplified and digitalized to generate a BSE image. In the past, BSE detectors in SEM were typically located directly below the objective pole piece. However, nowadays there are also BSE detectors situated inside the electron column.

SEs and BSEs generated by the sample can be scattered by microscope components and therefore produce additional SEs or BSEs that are not related to the investigated samples. In Fig. 2.10 all types of SE and BSE signals are sketched. Depending on detector position some of these background signals are more pronounced which will be discussed in the following.

Detectors in the electron column (in-the-lens) can have a high collection efficiency in detecting SE1 or BSE1 electrons shown in Fig. 2.10 while the detectors in the SEM chamber will collect all types of SE and BSE electrons except SE4. Since SE1 and BSE1 signals are primarily excited from the sample inspection area, which is exactly under the electron beam, their possibility of reaching the in-the-lens detectors are high. SE2s and BSE2s are emitted from the regions further away which can be detected by the detectors in the chamber. The SE3 signal is generated due to the collisions between BSE2 or SE2 with the objective pole piece, while very few SE4s are generated due to the collision

between SE1 or BSE1 and the inner wall of the electron column. Thus the SE4s inside the lens are not acquired by chamber detectors. Fig. 2.10 (a) displays the SE/BSE signals generated from bulk samples while for thin TEM samples, more SE5s (Fig. 2.10 (b)) appear resulting from further scattering of forward scattered electrons/transmitted electrons (TEs) by detectors under the sample.

Apart from the electron-beam diameter, the resolution of a SEM image is determined by the localization of the initial electron generation step. Since SE2-5 and BSE2 signals in Fig. 2.10 carry larger sample volume information compared to SE1 and BSE1, respectively, the delocalization of SEs and BSEs results in the limitation of the spatial resolution of the image. Therefore, the images obtained by detectors in the electron column usually have higher resolution than those acquired with detectors in the chamber. Another advantage of in-the-lens detectors is the capability of using them in combination with an immersion lens. Here, the magnetic field extends into the sample area to reach higher beam convergence angles resulting in lower contributions of C_s and C_c. Nowadays, imaging with SEs can potentially reach resolutions, which can compete with conventional TEM. An electron beam diameter of 0.1-0.15 nm for SE imaging was already achieved in a C_s-corrected STEM/SEM instrument at 200 keV showing atomic resolution [38, 39].

TE detection

When the electron beam scans over a TEM specimen, forward scattered electrons (TEs) propagate through the thin sample as showed in Fig. 2.10 (b). An annular semiconductor detector is placed below the sample to detect electrons scattered in a certain angle. This technique is referred to as scanning transmission electron microscopy (STEM). STEM detectors are typically solid-state semiconductor detectors similar to the one discussed for BSE detection. With a superior coherent cold FEG, lattice fringes (0.157 nm) can be visualized with STEM in SEM [40]. However, some of the modern SEM instruments are also equipped with a charge-coupled device (CCD) camera. Since the CCD-camera is located directly below the specimen, this type of cameras is referred to as on-axis CCD-camera. They can be used to capture on-axis transmission electron diffraction patterns (TED) like in a transmission electron microscope. The camera includes a fluorescent screen that is inserted directly under the thin sample. Transmitted electrons are converted into light and then recorded with a conventional CCD-camera.
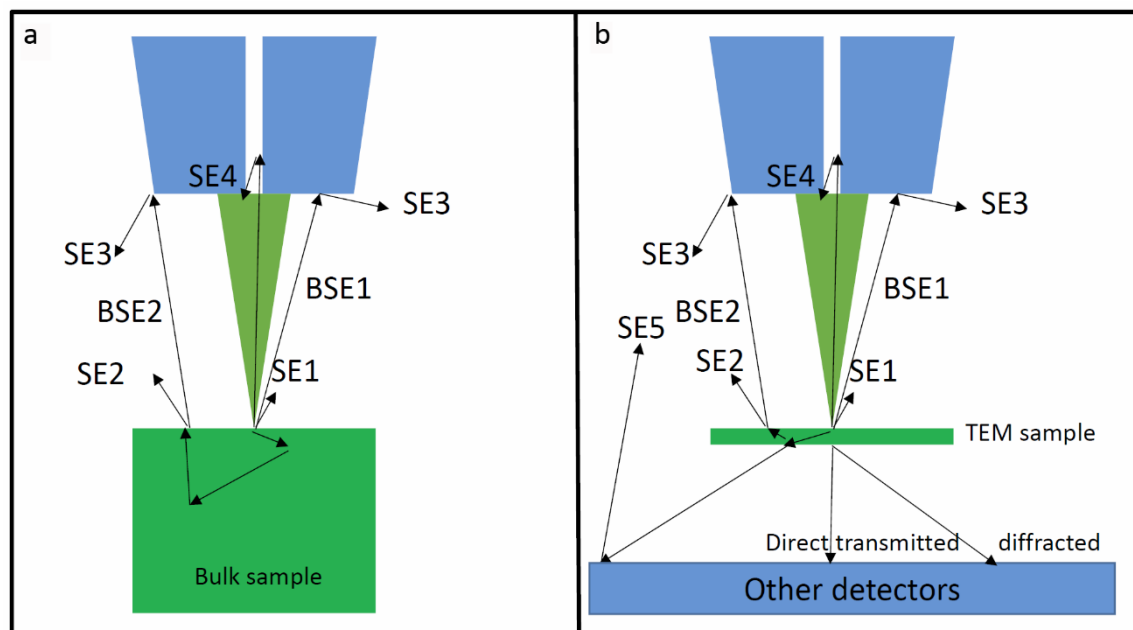
Figure 2.10. Different SE and BSE signals from the interaction volume of a (a) bulk sample and (b) thin TEM sample [41].

X-ray detection by EDXS

The energy-dispersive X-ray spectroscopy (EDXS) detector is commonly applied for the detection of X-rays. X-ray detectors are semiconductor based. According to Moseley's Law [30], there is a specific relation between the energy of the X-ray and the atomic number. By the analysis of the X-ray energy and intensity, qualitative and quantitative elemental information can be obtained from the specimen.

2.1.4 Limiting factors in SEM

In electron microscopes, the spatial resolution represents the smallest distance between two independent objects, which are still distinguishable in the microscope image. Apart from the electron-beam diameter, there are other factors that will limit resolution. In most cases, the interaction volume limits the lateral resolution. This can be counteracted by using thin electron transparent samples (10-100 nm). For very thin samples the interaction volume will be cut and the information depth is not limiting anymore.

Another practical limiting factor, especially for low electron energies, is the building up of contamination during image acquisition due to poor vacuum and a priori specimen contamination. The contamination leads to additional scattering and decrease of image contrast. Contamination in SEM is a result of the reaction between electron beam and

organic adsorbents because of poor vacuum or insufficient sample cleaning. The electron beam leads to cracking of adsorbed hydrocarbon or water molecules on the sample surface [42]. Especially hydrocarbon molecules can be decomposed and reformed as a carbonaceous contamination layer on the sample [43]. As hydrocarbon molecules are highly mobile on the sample surface, additional molecules from surrounding specimen areas can move towards the electron beam leading to increasing contamination with time. However, even for improved vacuum systems, hydrocarbon molecules in the chamber cannot be avoided completely [30] because hydrocarbon molecules also originate from sealing grease. Additionally, the process of focused-ion-beam (FIB) sample preparation, especially beam-induced deposition in SEMs also introduces hydrocarbon contaminations [44].

Various methods were applied for removing the hydrocarbon molecules in SEMs [45]. The first principle is that the SEM samples should be prepared in a clean environment. By applying heat on the sample or exposing samples to an ultraviolet or ozone environment [45], the hydrocarbon layer on the sample surface can be removed partly. Freshly cleaned samples should be inserted into the microscope directly without exposing them to contaminated environments. Samples inserted into the chamber can be cleaned by using a build-in plasma cleaning system that is installed in many SEMs. Such a system was used in this work to remove remaining hydrocarbon molecules from both, SEM chamber and sample surface. Hydrocarbon molecules are reduced due to the highly reactive oxygen radicals generated in the plasma cleaning process.

Apart from hydrocarbon contamination, electron beam exposure can affect the sample in other ways by heating, electrostatic charging, atom displacement (knock-on) damage and ionization damage (radiolysis) [46]. Excitation of phonons by primary electrons increases the sample temperature. Materials with low heat conductivity such as organic polymers or materials with low melting temperature could experience thermal degradation from the electron beam. In this case one needs to consider using a sample holder with cooling capabilities.

Electrostatic charging happens very often for electrically insulating materials. The net charges on the sample depend on the total electron yield σ, which is the sum of the backscatter coefficient η and secondary electron yield δ. If $\sigma < 1$, negative charges build up in the sample; if $\sigma > 1$, the sample is positive charged [47]. In SEM, an easy way to

reduce electrostatic charges is the deposition of a conductive layer (e.g. carbon or platinum) on those insulators. Another way is finding suitable imaging conditions to fulfill $\sigma = 1$ and therefore avoids charging completely.

Knock-on damage occurs when a high-energy electron collides with a nucleus of the specimen atoms and the transferred energy is larger than the atom binding energy. The atomic nuclei can be displaced to interstitial sites during this elastic scattering event. Since the primary electron energy in SEM is lower than in TEM, SEM has the advantage of reducing knock-on damage compared to conventional TEM (80–300 keV).

Another sort of beam damage is radiolysis. It is usually pronounced for non-conductors and organic solids since weak chemical bonds can be easily destroyed by the energy transferred from incident electrons by inelastic scattering. It changes the electronic configuration of molecules causing disorder in the material [46].

2.1.5 FIB in SEM

Focused-ion-beam (FIB) systems were developed by Krohn during the research for liquid-metal ion sources [48, 49]. With the commercialization of applying liquid-metal ion source in the field of semiconductor research, FIB systems were also combined with SEM instruments. Combined SEM-FIB systems are usually called DualBeam microscopes. Such systems can be used for deposition of materials from a precursor gas, nanostructure fabrication by sputtering processes and TEM lamella preparation from an predefined region of a bulk sample (cf. Fig. 2.11).

The liquid-metal ion source in FIB systems is usually a gallium (Ga) source. The gallium ions (light green color in Fig. 2.11) in the heated liquid source can be pulled out of the ion-emitter by an electric field and are then focused by an ion-optical column. Elastic collisions between the gallium ions and sample atoms during sputtering and milling process lead to the excavation of specimen atoms (marked by a medium green color) or backscattered Ga ions (cf. Fig. 2.11). Inelastic collisions result in the secondary ions and blue color marked electrons (Fig. 2.11) which can be detected by ion sensitive detectors. The deposition function in FIB can be used for the deposition of different materials, e.g., platinum (Pt) with the aim to reduce sample surface damage from heavy gallium ions in the course of TEM lamella preparation [49]. For Pt deposition used in this thesis, an organic precursor gas (trimethyl platinum $C_9H_{16}Pt$) containing Pt atoms (marked by

orange/dark-green color in Fig. 2.11) is injected close to the sample surface. With the decomposition of the precursor gas under the ion beam, Pt atoms are deposited on the sample surface while the majority of organic compounds (C_XH_Y) are pumped away. In this thesis FIB was mainly used for TEM lamella preparation which will be described in chapter 3.
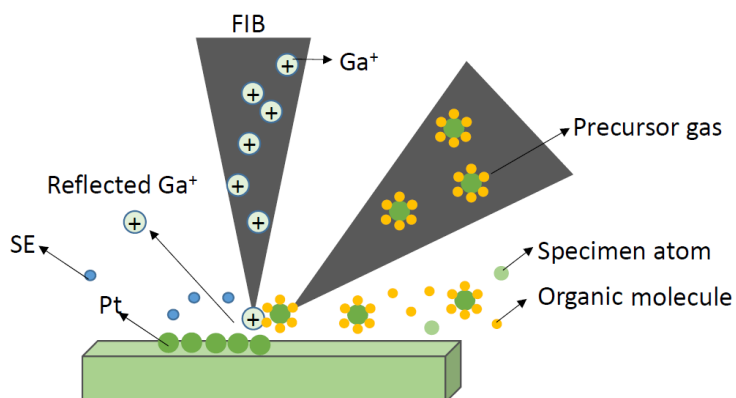
Figure 2.11. FIB milling and deposition procedure.

2.2 The transmission electron microscope

In contrast to SEM, transmission electron microscopes use a defocused beam to illuminate a broad area of the sample and a lens imaging system below the sample to generate a magnified image on an electron sensitive camera. Image formation is parallel instead of sequential as in SEM or STEM. Energy filters in TEMs (EFTEM) are able to filter electrons with specific energy losses. By taking the logarithm of the intensity ratio between unfiltered and zero-loss filtered images, a relative thickness map can be obtained where each pixel contains the information on the local sample thickness in units of the mean free path for plasmon scattering [50]. The thickness map can be generated by the routines implemented in the software Gatan DigitalMicrograph. High-resolution TEM (HRTEM) images were acquired for comparison with lattice fringes recorded with low-keV STEM in SEM. HRTEM, which relies largely on phase-contrast imaging, is often used for obtaining information on crystal orientation under ultra-high magnification [51]. Many TEMs can be also used in STEM mode allowing composition analyses by EDXS from small specimen regions.

2.3 Electron-sample interactions

The illumination of a specimen by a focused electron probe results in numerous electron-sample interactions. Interactions can be distinguished in two types of processes, namely elastic and inelastic electron-atom scattering. The formalisms of these interactions are described in the following.

2.3.1 Elastic scattering

For elastic scattering processes, the total momentum and kinetic energy of the scattering partners are conserved. The classical mechanics model of elastic scattering is shown in Fig. 2.12. Since the positive nucleus will attract the negative electrons, some electrons approaching the atom will be attracted to the nucleus like electrons 1 and 2 in Fig. 2.12. The directions of the parallel electrons are changed by the Coulomb force generated by the nucleus and atomic electrons (screening effect). Therefore, the electrons passing the area dσ in Fig. 2.12 are scattered through a cone of solid angle dΩ with the scattering angle θ. The probability of an electron being elastic scattered from $d\sigma_{el}$ to dΩ can be described by the elastic differential cross-section $d\sigma_{el}/d\Omega$. Among a variety of models for elastic differential cross-sections, the screened Rutherford differential cross-section is commonly used which is given in Eq. (9) [30].

$$\frac{d\sigma_{el}}{d\Omega} = \frac{e^4 Z^2}{4(4\pi\epsilon_0)^2 m^2 v^4} \cdot \frac{1}{[sin^2\left(\frac{\theta}{2}\right) + sin^2\left(\frac{\theta_0}{2}\right)]^2} \ , \ \theta_0 = \frac{\lambda}{2\pi R_b} \qquad (9)$$

The atomic number of the nucleus is denoted by Z. ϵ_0 represents the vacuum permittivity. The parameters e, m, v are the elementary charge, mass and velocity of the electron. λ is the wavelength of the incident electron and the screening radius R_b is given by $a_H Z^{(-1/3)}$ with the Bohr radius a_H [30]. Based on Eq. (9), the elastic differential cross-section $d\sigma_{el}/d\Omega$ is within good approximation proportional to Z^2 and increases with decreasing kinetic electron energy.
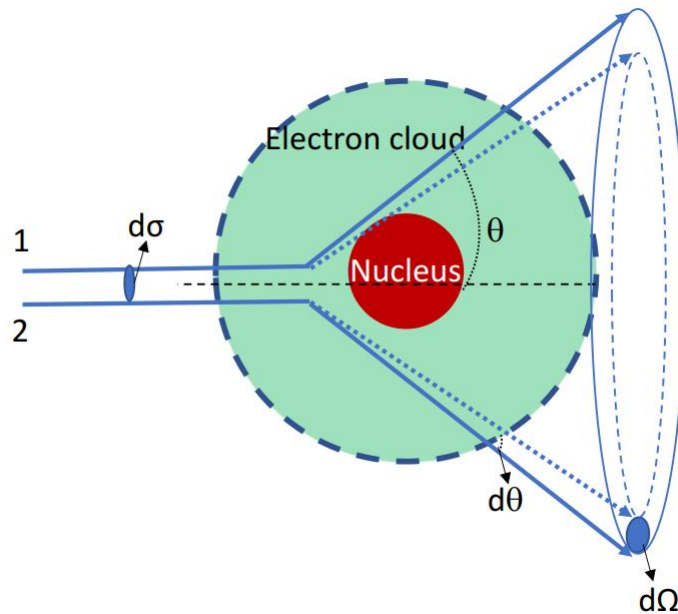
Figure 2.12. Simple model of elastic electron scattering at a nucleus [52].

2.3.2 Inelastic scattering

For inelastic scattering events, the kinetic energy of the interacting particles is not conserved [51]. There are several inelastic electron-electron scattering processes that are explained in the following. As shown in Fig. 2.13, when incident electron 1 interacts with the specimen atom, energy can be transferred to another electron (electron 2 in Fig. 2.13). Depending on the amount of energy transferred, electron 2 can either move to a vacant position at a higher energy level or be released into vacuum. In both cases a vacant position close to the nucleus will be the result (cf. Fig. 2.13). The vacancy can be filled by an electron from a higher energy level (e.g. electron 3). The difference of energy between both energy levels is released by the emission of a X-ray quantum. As the difference between energy levels is dependent on the type of atom, the characteristic energy of the X-ray quantum can be used for chemical composition analysis with EDXS. Instead of releasing a X-ray quantum, the energy difference can also be transferred to an outer shell electron (e.g. electron 4 in Fig. 2.13) which will be released into vacuum. Such an electron 4 is denoted as Auger electron, which is important for Auger electron spectroscopy. In addition, during the electron-electron scattering process, electrons from the conduction or valence bands can be ejected with energies typically ≤ 50 eV leading to the majority of secondary electrons in SEM [51].
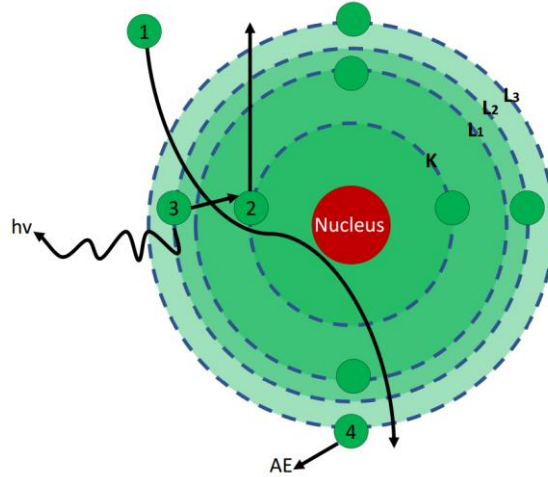
Figure 2.13. Simple model of electron-electron scattering [30].

The electron-electron scattering probability can be described by the inelastic differential cross-section $\frac{d\sigma_{inel}}{d\Omega}$. Studies confirm that inelastic scattering in electron microscopy is mainly with scattering angles smaller than 3° whereas elastic scattering covers all angles (0°~180°) [51].

In order to reduce inelastic differential cross-section $\frac{d\sigma_{inel}}{d\Omega}$, high electron energies are needed according to the inelastic differential scattering cross-section given by Eq. (10) [30].

$$\frac{d\sigma_{inel}}{d\Omega} = \frac{4e^4 Z}{(4\pi\epsilon_0)^2 m^2 v^4} \cdot \frac{1 - \left[1 + \frac{\theta^2 + \theta_E^2}{\theta_0^2}\right]^{-2}}{(\theta^2 + \theta_E^2)^2}, \theta_E = \frac{J}{4E} \qquad (10)$$

J is the mean ionization potential while E is the primary electron energy [30]. Hence, radiolysis can be reduced by using high-energy electrons.

2.3.3 Interaction volume in bulk samples

In SEM, a large number of electron-matter interactions occur for each incident electron generating numerous additional electrons in the process. In Fig. 2.14 [30] a simplified spectrum of the electrons emitted by a bulk sample is depicted. Electrons that are able to leave the sample are by definition separated mainly into two categories. Electrons excited from the sample with an energy of 50 eV or less are called SEs. Electrons with energies above 50 eV are denoted as BSEs. BSEs tend to contain a high fraction of electrons that

are directly backscattered by elastic electron-nucleus interactions [51, 53]. For electron-transparent samples used in (S)TEM, a large fraction of the electrons are forward scattered electrons (TEs) that are discriminated according to their scattering angle.
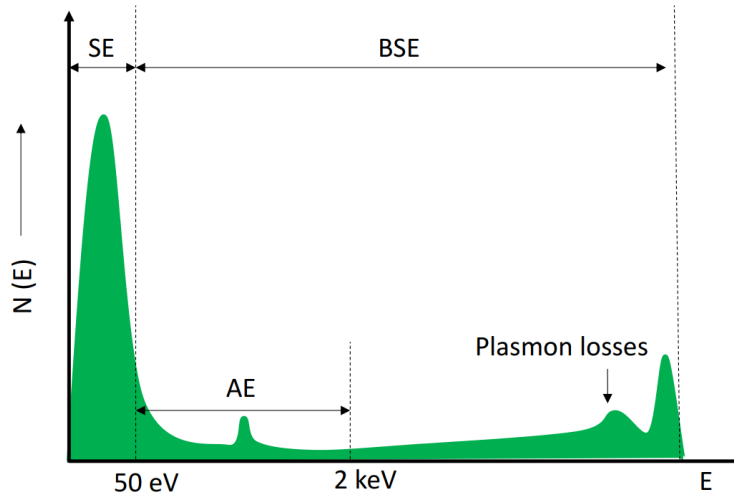
Figure 2.14. Scheme of energy spectrum for electrons emitted from a bulk specimen [30].

In the following, a bulk specimen is assumed. When the incident electron beam interacts with the sample and generates SE, BSE or X-rays signals, the origin of these signals can be attributed to a certain sample volume, the so-called interaction volume. Kanaya [53] deduced Eq. (11) for calculating the size of the interaction volume [30] which was verified to match experiments.

$$R \ [nm] = 27.6 \cdot A \cdot E^{1.67}/(\rho \cdot Z^{0.89}) \qquad (11)$$

A is the atomic weight of the material and ρ is the material density. The electron energy and material together limit the final size of electron range R. For samples in SEM, R is usually in the range of 10 nm - 10 μm [54, 55].

As shown in Fig. 2.15, different signals can be detected from the interaction volume for a bulk sample in SEM. The black line in Fig. 2.15 indicates the surface of the sample. The electrons penetrating deep into sample (the blue region) can lose all the energy and be ultimately absorbed inside the sample. BSEs with high energy are able to leave the specimen from the green region indicated in Fig. 2.15 and can carry information from deep parts of the sample. The exit depth for BSE can be approximated by R/2 from Eq. (11) [30, 53].
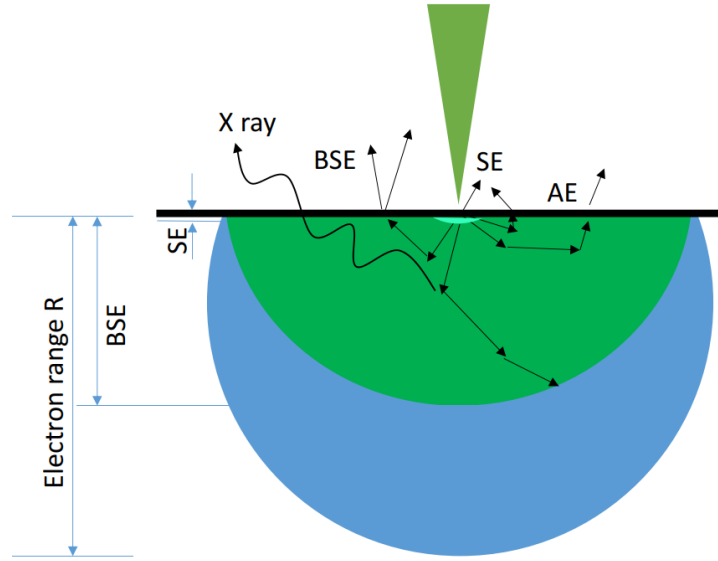
Figure 2.15. Sample-electron interaction volume model with exit volume for BSEs (dark green) and SEs (bright green) [30].

The generation of BSE is described by the BSE coefficient η which gives the number of BSEs per primary electron in Eq. (12) [30].

$$\eta = (1 + cos\,\phi)^{\frac{-9}{\sqrt{Z}}} \qquad (12)$$

η is determined by the atomic number Z and incidence angle ϕ of the primary electrons with respect to the surface normal (normal incidence, $\phi = 0$). Therefore, a BSE image intensity profile could be assigned to atomic number based quantitative analysis of materials [56, 57] considering the Z dependence for η if some pre-knowledge is available of the material system.

SEs are only able to escape from the sample if they are generated close to the sample surface due to their low kinetic energy. A simplified description of SE emission is given by Eq. (13). The SE yield δ gives the number of SEs per primary electron. It strongly depends on the primary electron energy E and the exit depth t_{SE} for SEs. Since the incidence angle of the primary electrons ϕ also influences δ, SEs are mainly used for topography imaging.

$$\delta \propto E^{-1} ln\left(\frac{E}{J}\right)\frac{1}{cos\,\phi}\int_0^\infty exp(-\frac{z}{t_{SE}})\,dz \qquad (13)$$

X-rays are able to escape from the sample even if they are generated far away from the surface (cf. blue region in Fig. 2.15). The escape depth R_x for X-rays is given by Eq. (14) [58].

$$R_x = P(E^{1.68} - E_C^{1.68}) \quad (14)$$

It depends on the primary energy E and the characteristic ionization energy of the material (E_c) with the fit parameter P that is around 10^{-2} for materials with medium average atomic number [58].

2.3.4 Contrast in electron-transparent samples

The TE contrast for electron-transparent samples including diffraction contrast and mass-thickness contrast will be introduced in this subsection. The kinematical theory of electron diffraction is outlined in the following as the simplest approach to understand electron diffraction patterns and TEM contrast which is based on single electron scattering. Using the reciprocity theorem [59], it is known that bright-field (BF) and dark-field (DF)-STEM images show a similar contrast as the corresponding BF/DF-TEM images.

Electrons are described as waves with wavelength λ given by the de Broglie relation Eq. (15),

$$\lambda = \frac{h}{p} \quad (15)$$

where h is Planck's constant and p is the momentum of the electron. The incident beam is described as a plane wave with amplitude Ψ_0 and phase $2\pi\vec{k} \cdot \vec{R}_0$ (Eq. (16)) [51] with wave vector $\vec{k}$ and position vector $\vec{R}_0$.

$$\Psi = \Psi_0 e^{2\pi i \vec{k} \cdot \vec{R}_0} \quad (16)$$

After the incident wave reaches the sample, it will be elastically scattered by the atoms in the sample generating spherical waves emanating from each atom (cf. Fig. 2.16 for the example of two atoms).
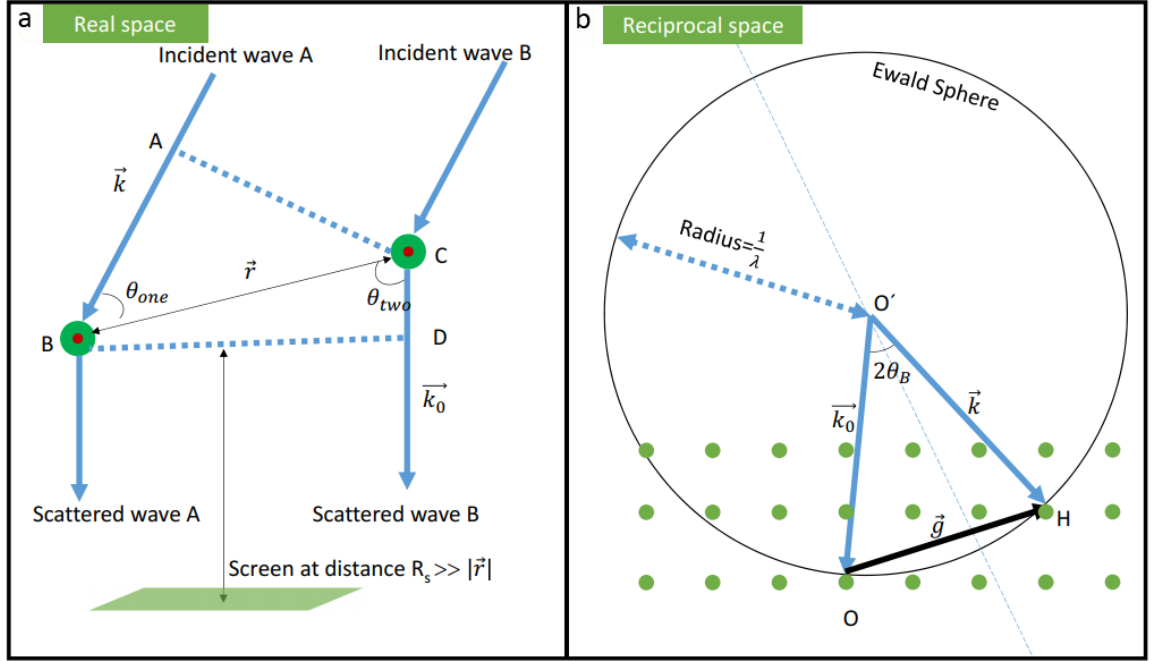
Figure 2.16. (a) Scheme for phase shift between two scattered waves, (b) the Ewald sphere in a reciprocal space [60].

The phase shift between two elastically scattered waves is denoted by $\Delta\varphi$ with $|\vec{k}|=|\vec{k}_0|=\frac{1}{\lambda}$ (wave vectors $\vec{k}$ and $\vec{k}_0$). Therefore, the phase difference for the scattered waves from atoms A and B (cf. Figure 2.16 (a)) can be described by Eq. (17) [30, 60]. Δl is the path difference for the scattered waves. Constructive interference of the two waves will occur if $\vec{r}\cdot(\vec{k}-\vec{k}_0)$ is an integer number.

$$\Delta\varphi = 2\pi\frac{\Delta l}{\lambda} = 2\pi\vec{r}(\vec{k}-\vec{k}_0) \qquad (17)$$

Since the distance from the sample to the screen $|\vec{R_s}|$ is much larger than the distance $|\vec{r}|$ between the (two) atoms, the scattered waves can be regarded as plane waves. The scattered wave Ψ_s at a distance $|\vec{R_s}|$ from arbitrarily positioned M atoms can be described by Eq. (18) [30, 51, 61] along the $\vec{k}$ direction, where

$$\Psi_s = \Psi_0 \frac{exp(2\pi i\vec{k}\cdot\vec{R_s})}{R_s}\sum_{i=1}^{M} f_i(\theta)\,exp(2\pi i[\vec{k}-\vec{k}_0]\vec{r_i}) \qquad (18)$$

is the elastically scattered wave from M atoms with the individual atoms located at $\vec{r_i}$. $f_i(\theta)$ is the atomic form factor of the atom i. $|f_i(\theta)|^2$ is also equal to the elastic differential scattering cross-section $\frac{d\sigma_{el}}{d\Omega}$.

For scattering at crystals, the scattering amplitude is then given by Eq. (19) [61],

$$F(\theta) = \sum_{all\ atoms\ i} f_i(\theta) \exp\left(2\pi i[\vec{k} - \vec{k}_0]\vec{r}_i\right) = \sum_{all\ atoms\ i} f_i(\theta) \exp(2\pi i\vec{g} \cdot \vec{r}_i) \qquad (19)$$

where $\vec{g}$ equals to $(\vec{k} - \vec{k}_0)$ and $\vec{r}_i$ is the atom position. The intensity of the scattered wave on the screen is proportional to $|F(\theta)|^2$.

As shown in Eq. (20), $\vec{r}_i$ equals to the sum of $\vec{r}_{ki}$, the atom positions in unit cell and $\vec{r}_{pi}$, the position of unit cell.

$$\vec{r}_i = \vec{r}_{ki} + \vec{r}_{pi} \qquad (20)$$

Hence, the scattering amplitude can be written with Eqs. (21-23) [61].

$$F(\theta) = \sum_{\substack{all\ atoms \\ in\ unit\ cell}} f_i(\theta) \exp(2\pi i\vec{g} \cdot \vec{r}_{ki}) \sum_{all\ unit\ cells} \exp\left(2\pi i\vec{g} \cdot \vec{r}_{pi}\right) \qquad (21)$$

$$F_S = \sum_{\substack{all\ atoms \\ in\ unit\ cell}} f_i(\theta) \exp(2\pi i\vec{g} \cdot \vec{r}_{ki}) \qquad (22)$$

$$G = \sum_{all\ unit\ cells} \exp(2\pi i\vec{g} \cdot \vec{r}_{pi}) \qquad (23)$$

F_S is the structure factor, which is determined by the atom positions and atom type in the unit cell. The lattice amplitude G depends only on the shape of the crystal [60]. The scattered wave intensity is proportional to $F_S^2 G^2$.

For crystallized materials, if constructive interference happens, this is also called Bragg diffraction condition with fulfilling Bragg's law (Eq. (24)) [62].

$$n\lambda = 2d \sin \theta_B \qquad (24)$$

θ_B is the Bragg angle, n is an integer number and d is the lattice plane distance. The length of the reciprocal lattice vector $\vec{g}$ that belongs to a set of lattice planes with distance d is given by Eq. (25).

$$|\vec{g}| = \frac{1}{d}n \qquad (25)$$

An equivalent description of Bragg diffraction is the so called Laue condition with $\vec{g} = \vec{k} - \vec{k}_0$. A graphical visualization of the Laue condition is the Ewald sphere construction

(Fig. 2.16 (b)) with the radius of the Ewald sphere given $\frac{1}{\lambda}$. Each reciprocal lattice point (green dots in Fig. 2.16 (b)) corresponds to a set of lattice planes in real space. If the Ewald sphere intercepts a reciprocal lattice point such as the one indicated by H in Fig. 2.16 (b) (Laue condition), the Bragg condition for the corresponding lattice planes is fulfilled. It also hints $F_S^2G^2$ is not zero for this diffraction spot. However, Bragg diffraction spots can also appear in the diffraction pattern even though the Laue condition is not perfectly fulfilled. This is due to the fact that electron transparent specimens have a finite thickness regarding the direction of electron propagation leading to extended reciprocal lattice rods instead of reciprocal lattice points. A diffraction pattern is shown in Fig. 2.17 with several Bragg reflections that represent different lattice planes in real space. An exception is the zero-order beam (ZB) in Fig. 2.17, which is formed from the direct transmitted part of the primary electron beam but not from Bragg diffraction. The shape of the reciprocal lattice points depends on the sample geometry in real space which has an effect on the lattice amplitude G.
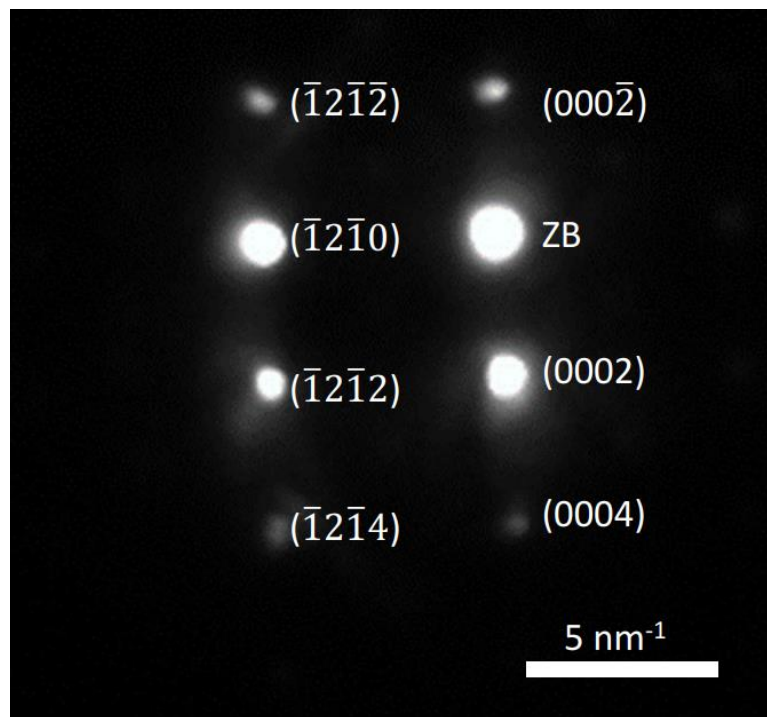
Figure 2.17. 30 keV transmission electron diffraction pattern for GaN in $[10\bar{1}0]$ zone axis.

If a Bragg reflection is not fully excited, then an excitation error $\vec{s}$ exists. G can be further modified to Eq. (26).

$$G = \sum_{all\ unit\ cells} exp\big(2\pi i[\vec{g} + \vec{s}\,]\vec{r}_{pi}\big) \qquad (26)$$

Increasing $|\vec{s}|$ leads to the reduction of G^2. Therefore, different excitation errors for different Bragg reflections in Fig. 2.17 lead to the different intensities of the diffraction spots.

It is convenient to use two-beam excitation conditions in conventional BF and DF images in TEM/STEM where only ZB and one Bragg spot are excited because image interpretation is easier than under multi-beam excitation conditions. Under two-beam conditions, the sum of the ZB intensity I_0 and the intensity of the Bragg spot I_g is normalized to 1. I_g can be described by Eq. (27) where s_z is the z-component (electron propagation direction) of $\vec{s}$. The BF-(TEM/STEM) image is obtained by either a CCD-camera or BF-STEM detector with the illumination mainly from the ZB. In contrast, DF-(TEM/STEM) images are mainly from the Bragg diffracted beam illumination recorded by CCD-camera or annular dark-field (DF-STEM) detector. Hence, the BF image intensity can be described by Eq. (28). Based on Eqs. (27,28), for crystalline samples, the BF/DF diffraction contrast depends on crystal orientation and sample thickness t.

$$I_g = F_S^2 G^2 \propto F_S^2 \frac{sin^2(\pi s_z t)}{(\pi s_z)^2} \qquad (27)$$

$$I_0 = 1 - I_g \qquad (28)$$

The kinematical diffraction theory is only a simplified approximation for qualitatively analyzing diffraction contrast since multiple scattering of electrons in TEM samples have to be taken into account especially for low electron energies. For quantitatively understanding diffraction contrast, the dynamical diffraction theory is needed [61].

For amorphous material, no Bragg diffraction will occur. In this case, mass-thickness contrast is dominant in BF/DF images which means the image contrast depends on material density and thickness of the sample.

Contrast for HAADF-STEM image

Detectors capturing TEs scattered in large angles are denoted as high-angle annular dark-field (HAADF) detectors. Those TEs are usually a result of incoherent elastic scattering. Therefore, diffraction contrast is usually negligible for HAADF-STEM image analysis.

The differential elastic scattering cross-section $\frac{d\sigma_{el}}{d\Omega}$ is approximately proportional to Z^2 as seen in Eq. (9). Hence, HAADF-STEM images are sensitive regarding changes in the average atomic number or local thickness/density of the sample (mass-thickness contrast) [14]. The HAADF-STEM image contrast for low-keV will be further explained with simulations in the following.

Simulation of low-keV HAADF-STEM image intensities

The understanding of STEM contrast is facilitated by STEM-intensity simulations. Monte-Carlo (MC) simulations are routinely used for this purpose which yield angular and energy distributions of electrons leaving the sample. The MC method is a computational algorithm using repeated random sampling to solve problems with numerical results. The number of electrons reaching a STEM detector segment divided by the total number of transmitted electrons is the normalized simulated intensity for the corresponding detector segment. The MC simulations in this work were performed with the NISTMonte package [63]. MC simulations are based on suitable models for differential elastic scattering cross-sections and require the consideration of imaging conditions for STEM such as the collection angle range and the specimen thickness. Energy loss of electrons in MC is described by the continuous slowing down approximation by Joy and Luo [64]. In this thesis, screened Rutherford differential scattering cross-section was chosen for the STEM simulations. We note that MC simulations do not take crystal structures into account. They can only be used for amorphous materials or for crystalline materials at large scattering angles where incoherent electron scattering dominates.

In addition, the CeTE1.4 package [65] was also used for STEM simulations in this thesis which solves the electron transport equation numerically in the analytical formulation of Goudsmit and Saunderson [66]. CeTE1.4 (**C**omputation of **e**lectron **T**ransport **E**quation) is in-house developed by E. Müller and is written in Java (http://openjdk.java.net/ version 1.8.0) [65]. It allows the exact calculation of the angular distribution of multiple-scattered electrons after a given path length by means of expansion in Legendre polynomials. Due to the fast oscillations of Legendre polynomials, the convergence of the expansion series can be slow for short path lengths or higher electron energies. To ensure convergence, CeTE1.4 uses typically 500 expansion terms, a number which can be edited in the source code. The integrals of the Legendre coefficients are calculated by the Gauss-Legendre

quadrature formula [67]. Energy loss of the electrons propagating through the sample is considered by the continuous slowing down approximation [64] for an average path length calculated according to Rose [68]. A correction for the properties of the STEM detector is also implemented in the code, considering threshold energy and efficiency in the charge collection current of the semiconductor detector [30]. CeTE1.4 calculates the angular distribution and energy of electrons scattered in materials of known composition as a function of the thickness and primary electron energy. Numerical solution of the analytical transport equation by CeTE1.4 is faster than MC simulations. This facilitates rapid change of sample properties and instrumentation parameters, but simulations can only be performed for homogenous materials regarding composition and geometry. The threshold energy of the detector used in this thesis is 3 keV.

In order to compare STEM experiments with simulations, the normalization of experimental STEM intensities is necessary according to Eq. (29) [20]. The normalized HAADF-STEM intensity $I_{NOR-HAADF}$ is related to the measured HAADF-STEM intensity $I_{EXP-HAADF}$, the white-level intensity of the detector $I_{white-HAADF}$ with ζ for detector correction considering the fraction of insensitive detector regions and the black-level intensity of the detector ($I_{Black-HAADF}$). The normalization of STEM image intensities from other STEM segments is analogous.

$$I_{NOR-HAADF} = \frac{I_{EXP-HAADF} - I_{Black-HAADF}}{I_{White-HAADF} \cdot \zeta - I_{Black-HAADF}} \qquad (29)$$

Fig. 2.18 was simulated with CeTE 1.4 to show HAADF intensity change for different materials as a function of sample thickness under different beam energies. The red curves in Fig. 2.18 are simulations for copper at 30 kV (red solid line) and 15 kV (red solid line with red suqares) acceleration voltage, respectively.

The 30 keV copper simulation can be used to explain how the HAADF intensity will change with increasing sample thickness. As seen from the red curve, the HAADF intensity increases with increasing specimen thickness up to the maximum because more electrons are scattered in large angles. The HAADF intensity decreases after passing through the maximum since now many electrons are scattered beyond the scattering angle range of the HAADF detector.

When comparing 30 keV and 15 keV simulations for copper, one can notice that the maximum HAADF intensity at 15 keV is shifted to a smaller specimen thickness. This

can be explained by Eq. (9). A lower beam energy leads to a larger differential scattering cross-section. This leads to a shorter elastic mean free path length and higher probability for elastic scattering at 15 keV. This also illustrates the advantage of low-keV STEM for weakly scattering materials compared with STEM in TEM because larger differential cross-sections at low energies will generate a better HAADF-STEM contrast.

In addition, the 30 keV HAADF-STEM intensity for Si and Pd was also simulated (green and black curves). The atomic numbers for Si, Cu and Pd are 14, 29 and 46 respectively. According to the 30 keV simulations, the sample thickness at maximum HAADF intensity shifts to smaller specimen thickness with increasing atomic number.

It is noted that a change of collection angle range for the HAADF-STEM detector will also affect the HAADF intensity.
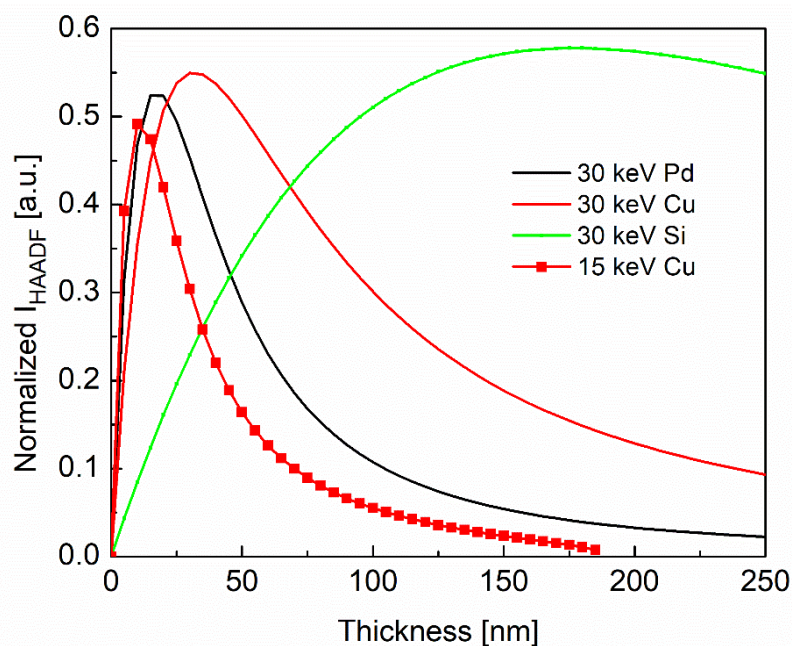
Figure 2.18. Simulated HAADF-STEM intensities of Pd (30 keV), Cu (30/15 keV) and Si (30 keV) as a function of the specimen thickness.

Both mass-thickness contrast and diffraction contrast discussed above are amplitude contrast because it changes the amplitude of the electron wave. However, the phase of the electron wave can also contribute to the contrast of an image. Phase contrast imaging with low-keV BF-STEM is feasible in modern SEM [40]. The interference of at least two beams (e.g. the interference of zero-order and one diffracted beam) on the BF detector can generate high-resolution lattice fringe images. The interference of coherent waves

requires large convergence angles to generate an overlap of ZB and Bragg reflection disks on the BF detector. It can be easily disturbed by inelastically scattered electrons reaching the BF detector with small scattered angles. Therefore, except large convergence angle, a thin sample is also essential for low-keV BF-STEM lattice fringe imaging in order to reduce the inelastic scattering events of low energy electrons.

2.3.5 Electron channeling

When crystalline materials are investigated in SEM, grains with different orientation can be often recognized by SE or BSE imaging. This is because BSE coefficient and SE yield are not only dependent on material and topography but also crystal orientation, which is introduced in the following.

The effect of crystal orientation on BSE and SE emission is referred to as channeling effect. It allows to visualize grains in polycrystalline materials and can be applied for defect characterization. The channeling mechanism is usually explained by Bloch wave theory as shown in Fig. 2.19, assuming the excitation of two Bloch waves [30]. The type 1 Bloch wave in Fig. 2.19 (a) propagates through the specimen with its maximum near the atomic sites. It has a high possibility of being backscattered by the atomic nuclei. In comparison, the type 2 Bloch wave has its maximum in the channels between lattice planes resulting in less attenuation of the wave on its way through the sample. In other words, the scattering of the electrons from the two Bloch waves depends on the angle (θ_1) between incident beam and specimen lattice planes. As shown in Figs. 2.19 (b,c), if θ_1 equals to the Bragg angle θ_B (Eq. (24)) [62], the BSE intensity reaches its minimum since the type 2 dominated Bloch waves can transmit through the specimen easily.

Conversely if θ_1 is 0, most of the Bloch waves are type 1 giving rise to the maximum BSE intensity in Fig. 2.19 (c). Therefore, electron channeling contrast imaging (ECCI) can be realized for polycrystalline samples with a smooth surface considering that different orientation of the grains corresponds to different θ_1 angles.
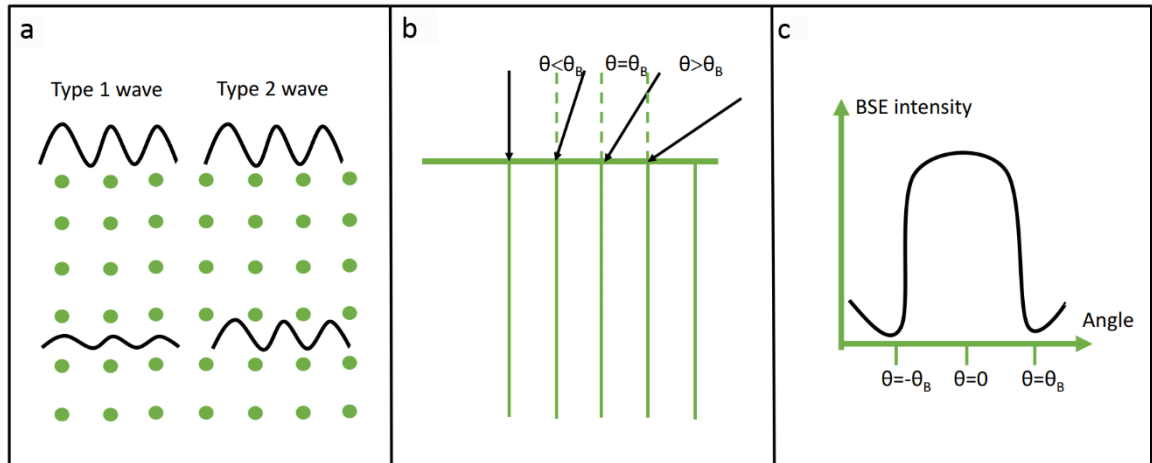
Figure 2.19. (a) Model of channeling with two Bloch waves, (b) comparison of the angle between incident beam and lattice planes with the Bragg angle, (c) the form of channeling band contrast [30].

Except ECCI, electron channeling patterns (ECPs) and electron backscattered diffraction (EBSD) can be obtained with the channeling mechanism [69]. When a beam is rocked through a monocrystalline sample with a large range of incident angles, different channeling bands will be formed in one image (either SE or BSE) which is the ECP. Additionally, the angular distribution of BSEs emitted from a small region of the specimen illuminated by a stationary electron probe can be recorded by a fluorescent screen with the aid of a camera which will generate the backscattered Kikuchi bands. With the indexing of Kikuchi bands, the EBSD patterns [30] containing grain orientation information for the inspected area can be formed with SEM related software.

In addition, inelastically forward scattered electrons can fulfill the Bragg law in a subsequent elastic scattering process. The variety of scattering directions will form two Kossel cones. One transmission Kikuchi band (TKB) can be formed with the intersection of the two Kossel cones with the on-axis CCD-camera [51]. With a scanning electron probe, the TKBs can be applied for assigning the orientations for different sample areas to form a map. Some researchers name the method as on-axis TKD mapping considering the on-axis CCD-camera [70].

In my thesis, the on-axis TKD mapping is named as on-axis transmission-EBSD (t-EBSD) since the difference between on-axis t-EBSD and off-axis t-EBSD which was reported by Keller [27] is only the position of the CCD-camera. The off-axis t-EBSD technique is less sensitive to beam current and beam energy changes and more sensitive

to changes in working distance and detector distance [71] even though it improves the image lateral resolution compared with normal EBSD. Comparatively, on-axis t-EBSD has lower projection distortions and needs a lower electron dose to get similar indexation rates as off-axis t-EBSD. Besides, it is also sensitive to severe plastic deformation materials with high dislocation densities and could reach better depth resolution compared with EBSD and off-axis t-EBSD [70].

3 INSTRUMENTATION AND SAMPLE PREPARATION

In this chapter, the microscopes employed in this work are described. Investigations were exclusively performed on thin electron-transparent samples. Various preparation routes for samples analyzed in chapters 4 and 5 are presented here.

3.1 Instrumentation

The SEM investigations in this thesis were mostly performed on a Helios Nanolab G4 FX SEM (Thermo Fisher). A few results were obtained with a Strata 400S SEM (FEI), Quanta 650 SEM (FEI), Titan[3] 80-300 TEM (FEI), Tecnai Osiris ChemiSTEM (FEI) and CM 200 TEM (Philips).

3.1.1 Strata 400S and Quanta 650
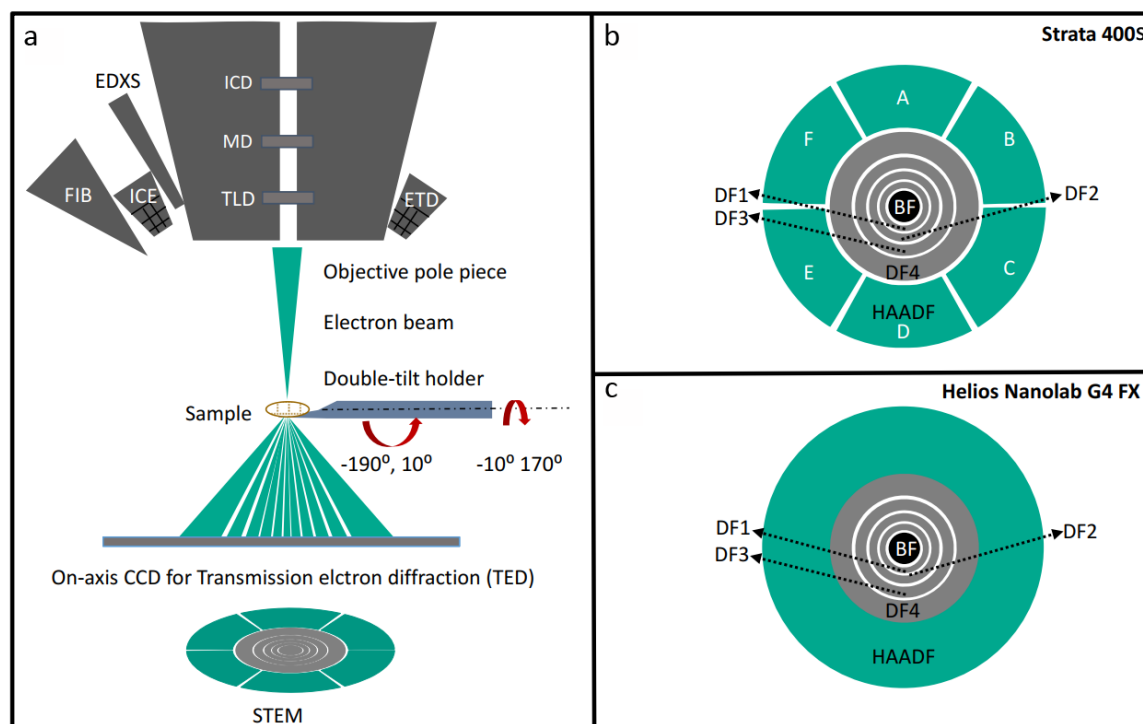
Figure 3.1. (a) Scheme of the Helios Nanolab G4 FX, (b) top view of the STEM detector in Strata 400S, (c) top view of the STEM detector in Helios Nanolab G4 FX.

The Strata 400S (Strata) is a DualBeam FIB/SEM microscope equipped with a Schottky field-emission gun. Within the scope of this thesis, only its through-the-lens detector (TLD, photomultiplier-type detector) and the semiconductor STEM detector were used. SE and BSE imaging with TLD can be influenced by varying the voltage applied on the

grid of the TLD ranging from -245 V to +245 V. For instance, if the grid is set to -245 V, the electrons which have energies smaller than 245 eV will be repelled from the detector. Therefore, only electrons with energies higher than 245 eV can reach the detector, in this case mainly BSEs. A STEM stage with α´ tilt capabilities (named as flip-stage) was used for the measurements of thin TEM samples in the Strata. As shown in Fig. 3.1 (a), the STEM detector in the Strata is located below the sample (18.8 mm below the objective pole piece). The top view of the STEM detector in Strata 400S is displayed in Fig. 3.1 (b). The symmetrically designed STEM detector has one BF, four DF and one HAADF rings. The largest part is the HAADF ring which is subdivided in six segments marked by A-F. The six segments of the HAADF ring can be used separately while the combination of different DF rings is also possible for DF imaging. In the following chapters, DF_1 represents images taken with DF_1 ring while $DF_{1,2,3}$ represents the images taken with DF_1, DF_2 and DF_3 rings simultaneously active. Similarly, $HAADF_{A,B}$ represents images taken with $HAADF_A$ and $HAADF_B$ segments together, while HAADF represents images obtained from the fully activated HAADF detector. Besides, the Strata is equipped with an "XFlash 5010" EDXS detector from Bruker for chemical analysis of samples.

Measurements with a Quanta 650 SEM were also performed. Only the solid-state BSE detector mounted directly below the objective pole piece was used in this instrument for the ECP and ECCI measurements.

3.1.2 Helios Nanolab G4 FX

Helios Nanolab G4 FX (Helios) is another DualBeam microscope which was installed in April 2017. It is equipped with a Schottky field-emission gun and gallium ions source. As shown in Fig. 3.1 (a), two photomultiplier detectors for SE detection, the Everhart-Thornley detector (ETD) in the chamber and the TLD in the electron column were applied in this work. Two solid-state in-lens detectors were used for the BSE detection, the mirror detector (MD) and in-column detector (ICD) with their relative positions displayed in Fig. 3.1 (a). A silicon drift EDXS detector for chemical analysis and a photomultiplier ion conversion electron detector (ICE) for detecting secondary ions are also installed in the Helios chamber (Fig. 3.1 (a)).

In addition, the Helios is equipped with a compustage and a double-tilt specimen holder for the analysis of electron-transparent specimens. The double-tilt holder has large tilt angles for both α´ (-10°~170°) and β´ (-190°~10°) directions. A special designed counter pole piece supporting large beam convergence angles can be inserted for the immersion mode in Helios [72].

A multi-segmented STEM detector was applied for the characterization of electron-transparent samples situated in the double-tilt holder, which was used for obtaining most of the results in this thesis. The STEM detector contains one small inner detector segment for BF-STEM imaging followed by four DF and one HAADF detector rings (Fig. 3.1 (c)). The detection angle range can be varied by changing the working distance, i.e. the distance between specimen and objective lens pole piece. The 40 mm distance between STEM detector and objective pole piece leads to the smaller collection angles for all the STEM detector segments in the Helios compared to the Strata. BF-STEM resolution of Strata 400S is specified as 0.8 nm, while it is substantially improved to 0.34 nm for Helios Nanolab G4 FX.

Besides, an e-Flash^{HR} CCD-camera implemented in a Bruker OPTIMUS^{TM} camera head is installed in Helios for the acquisition of on-axis TED patterns. A projection lens system is not available in Helios but the camera length can be varied by changing the working distance between 1.8 and 4.5 mm.

Images obtained from Helios were taken at electron energies between 1 and 30 keV depending on the specimen, imaging mode and the required resolution.

The FIB with a large range of ion beam energies (0.5 ~30 keV) in Helios was used for the preparation of the electron-transparent samples (e.g. the GaN samples in chapter 5) [65].

3.1.3 Transmission electron microscopes Titan^3 80-300, Tecnai Osiris ChemiSTEM and CM 200

Transmission electron microscopy was also applied in this thesis to complement results from low-energy STEM. A Titan^3 80-300 (Titan) was applied for HRTEM and EFTEM measurements. EDXS measurements were performed with the Tecnai Osiris ChemiSTEM (Osiris) which is equipped with a super-X EDXS system from Bruker comprising four windowless silicon drift detectors. HAADF-STEM imaging and EDXS

maps of ZnO in chapter 4 were recorded with Osiris. The CM 200 was applied to obtain the orientation information for InN in chapter 5. Results obtained by TEM are indicated in the text.

3.2 Sample preparation

In the following, four different sample preparation methods are explained which were applied to obtain electron transparent TEM samples.

3.2.1 Electrochemical thinning

For electron-conducting metal samples an electrochemical thinning procedure can be used to reach electron transparency. The first step involves mechanical grinding and polishing to reduce sample thickness to 100 μm or less. By using an ultrasonic drill, a 3 mm disk is cut out from the sample. With a dimple grinder the center of the disk is pre-thinned. The final preparation step to electron transparency was performed in an etchant electrolyte consisting of 95 % acetic acid and 5 % perchloric acid. As schematically shown in Fig. 3.2 the 3 mm sample disk (green) is mounted between two electrodes (dark blue). The sample is connected to the positive electrode (anode) of a direct current power supply while the negative electrode (cathode) is connected to the negative pole. When the power supply is turned on, sample atoms located at the anode will lose electrons (oxidation). The generated positive charged ions will then move to the cathode due to the electrical field. With this method, the sample continuously loses material. The power is turned off once the inner part of the sample reaches electron transparency. Fig. 3.2 (b) displays a side-view of a crystallized sample before etching. The etching speed for grains with different orientations is different (Fig. 3.2 (c)), since etching usually follows the orientations which need the least energy [73] (c.f. $Fe_{0.90}Si_{0.05}Al_{0.02}C_{0.03}$ steel sample (chapter 4, 4.1)).
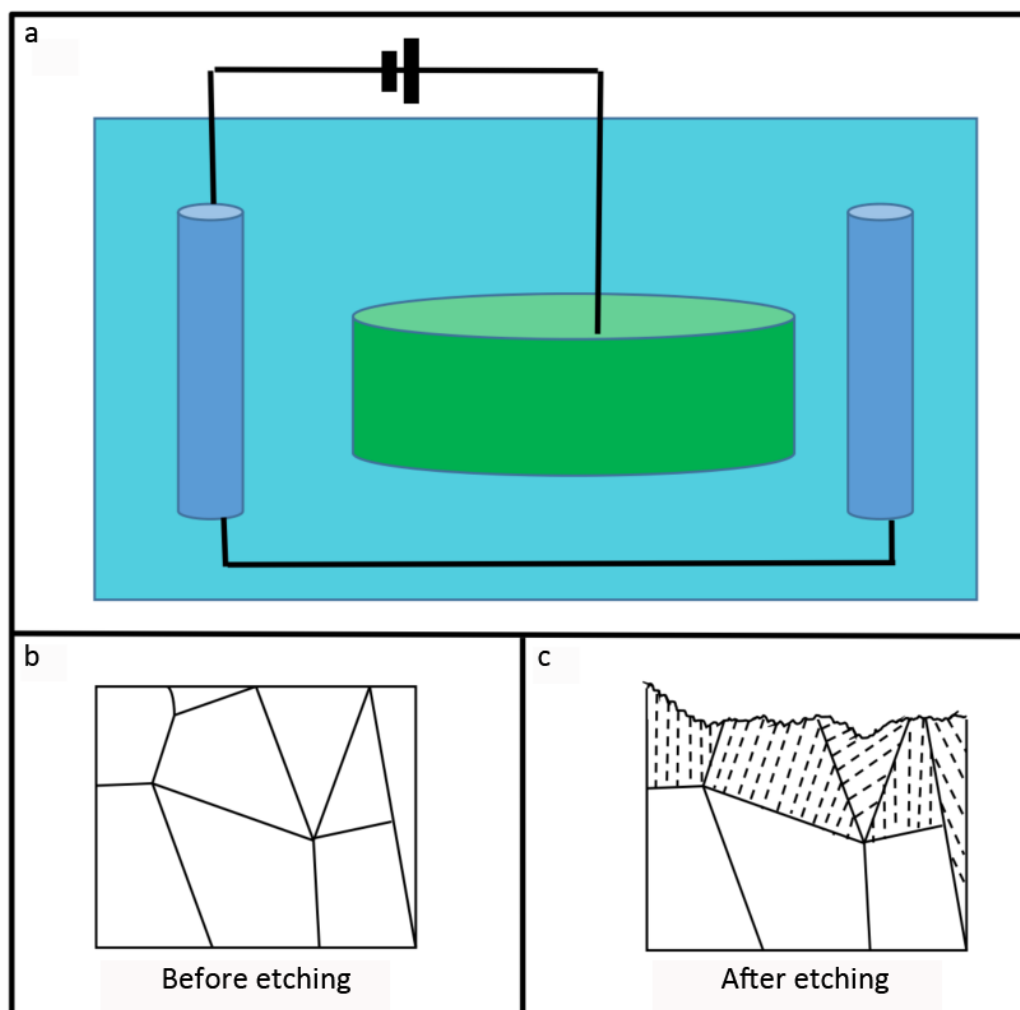
Figure 3.2. (a) Simplified scheme for TEM sample preparation by electrochemical etching. Side view of a crystallized sample (b) before etching and (c) after etching.

3.2.2 Standard mechanical preparation

Standard mechanical TEM sample preparation was used to obtain electron-transparent specimens from $Li_{3x}La_{2/3-x}TiO_3$, $SrTiO_3$ and $SiTi_{1-x}Fe_xO_{3-\delta}$ from chapter 4 and InN from chapter 5. The essential steps of this procedure are displayed in Fig. 3.3. First, mechanical cutting and polishing were used to reduce sample dimensions. The resulting piece (Fig. 3.3 (a)) was embedded into a brass or ceramic tube with an outer diameter of 3 mm according to the procedure described by Klaar and Hsu [74]. The tube is cut into slices of 400 µm thickness (Fig. 3.3 (b)). With mechanical polishing, the thickness is reduced to approximately 70 µm. As displayed by Fig. 3.3 (c), the 70 µm thickness slice is then dimpled on both sides until less than 1 µm thickness in the thinnest center part is reached.

Preparation to electron transparency (around 100 nm) was performed in a precision ion polishing system PIPS (Gatan Inc.) by argon ion milling [65] (Fig. 3.3 (d)). The milling rate can be controlled by the energy of the argon ions. Low argon ion energies towards the end of the milling process are advised to reduce surface damage.
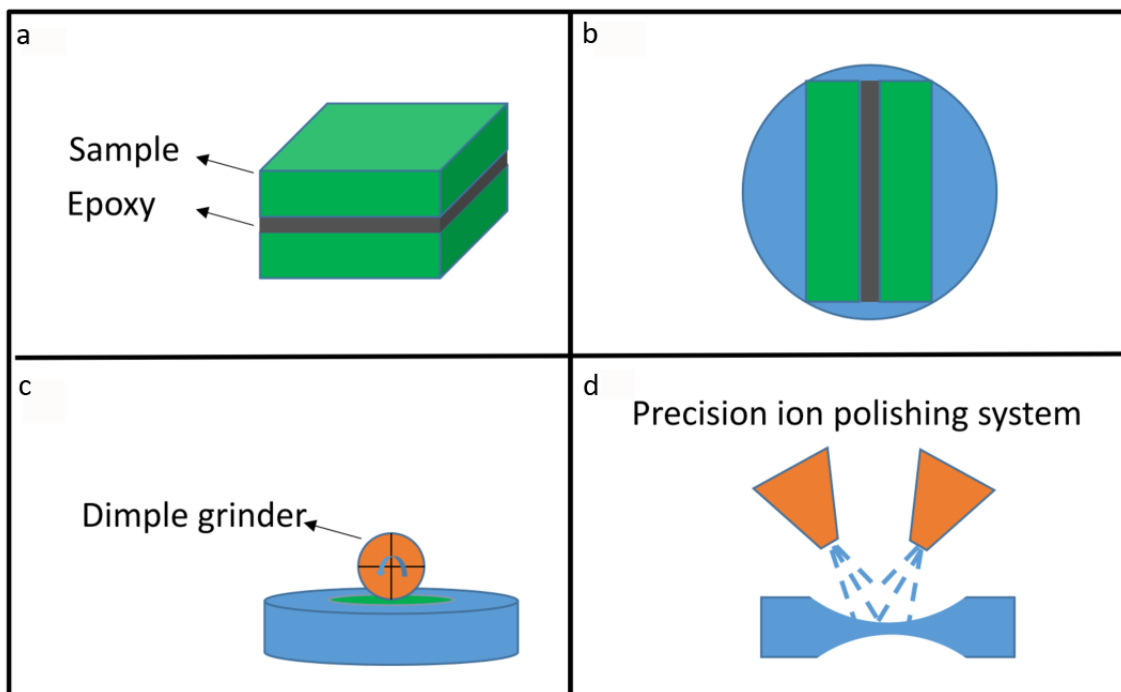
Figure 3.3. A simplified scheme for standard mechanical TEM sample preparation. (a) Side view after preparation of a sandwich structure, (b) top view of a disk from the sample, (c) dimpling procedure, and (d) final argon ion etching to electron transparency.

3.2.3 Deposition on carbon film

Xonotlite, tobermorite, carbon nanotube (CNT) and KIT-6 (silica material) samples from chapter 4 were prepared by a simple procedure. Sample powder was deposited on a commercial TEM copper grid covered by either a holey carbon film or an ultrathin carbon film (<3nm) on carbon lacey support film (Fig. 3.4 (a)). The net structure from the carbon film will support the sample particles (green color in Fig. 3.4 (b)). Other micro- and nano-structured samples in chapter 4 were available in the form of particle/fluid suspensions. By evaporation of the suspension on TEM copper grids (Fig. 3.4 (b)) with amorphous carbon film (Fig. 3.4 (a)), NPs can be investigated in TEM/STEM mode.
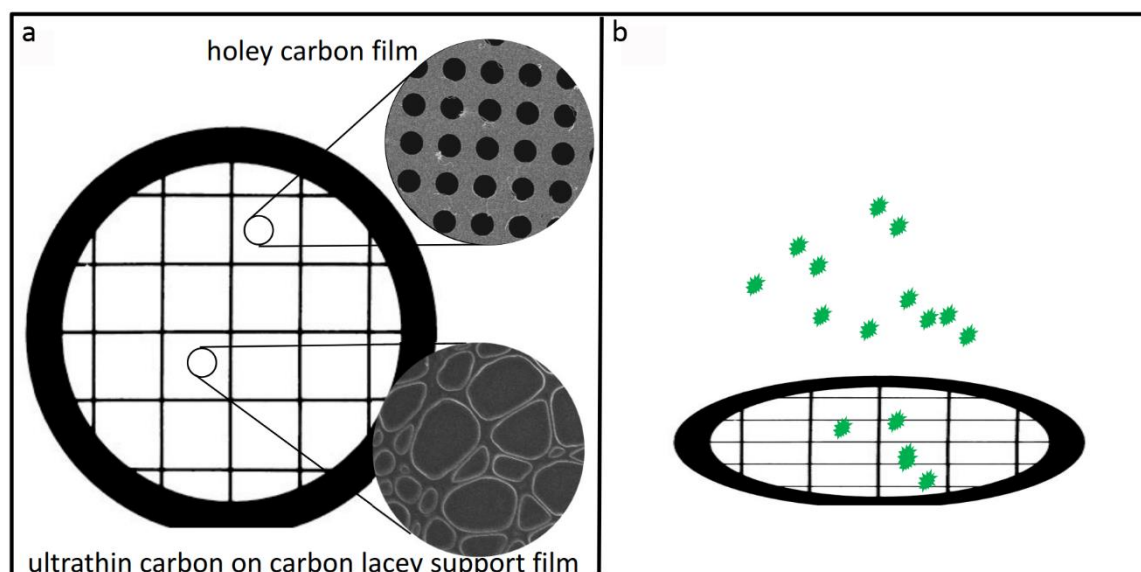
Figure 3.4. Simplified scheme of TEM sample preparation for micro- and nanoparticles (NPs). (a) The top view of a copper grid covered with two types of carbon films. (b) The deposition of NPs.

3.2.4 FIB method
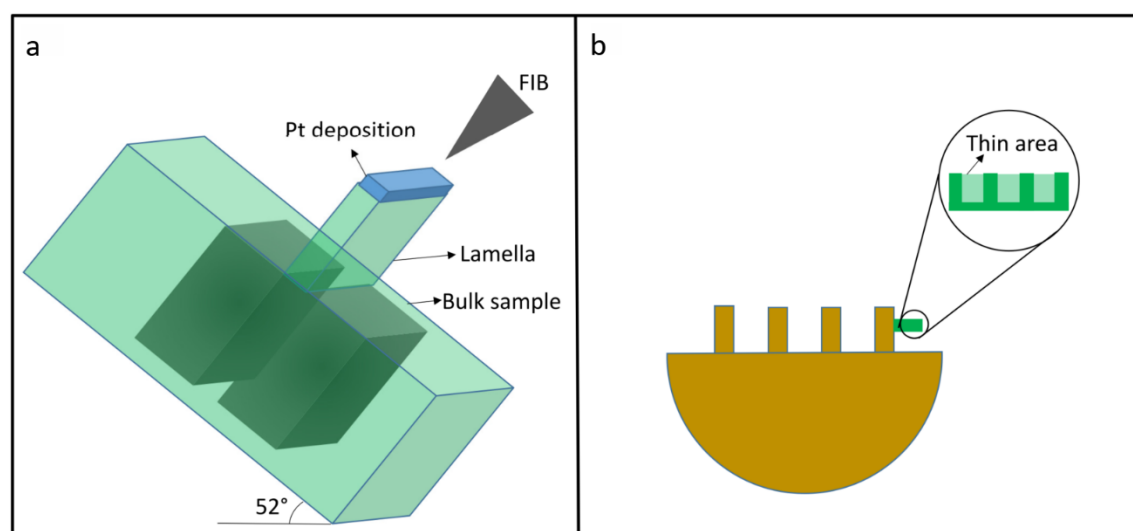
Figure 3.5. Simplified scheme for FIB-based TEM lamella preparation. (a) Lamella cutting from bulk sample and (b) electron-transparent lamella on a support grid after final polishing with low energy gallium ions.

The last method is FIB-based lamella preparation which is already introduced in chapter 2 [75]. The sample milling and thinning steps using FIB in Helios or Strata are shown in Fig. 3.5. The bulk sample is tilted until the sample surface is perpendicular to the ion

beam (typically 52°) as illustrated in Fig. 3.5 (a). A thin layer of platinum (Pt) (marked by blue color in Fig. 3.5 (a)) is deposited on the surface to protect the material underneath. Then two trenches (dark green color in Fig. 3.5 (a)) are milled next to the Pt-protected region using gallium ions. Afterwards the sample is tilted towards the electron beam and a micromanipulator tip is attached to the lamella (Fig. 3.5 (a)) by Pt-deposition. By performing a cut on the sides and bottom of the region between the trenches, the resulting lamella can be lifted out by the micromanipulator and transferred to a copper support grid (Fig. 3.5 (b)). Pt deposition is used to attach the lamella shown in Fig. 3.5 (b) to the side of a copper pin on the FIB lift-out copper grid. The last step involves thinning the lamella by tilting the lamella parallel to the ion beam. Higher ion energies and currents are applied for coarse thinning while lower ion energies and currents are necessary for the final polishing step of the lamella. This reduces amorphization on the sample surface. The most suitable thinning parameters are material dependent [76]. The copper grid in Fig. 3.5 (b) can be directly mounted on the compustage in Helios. Hence, electron transparency can be monitored during the final thinning by BF-STEM imaging. This provides the advantage that the fabrication and investigation of the sample can be performed without unloading the sample from the microscope which is beneficial for air-sensitive samples.

4 CORRELATIVE SEM AND LOW-KEV STEM IMAGING IN A MODERN SCANNING ELECTRON MICROSCOPE

The use of STEM in SEM offers advantages by combining SEM and STEM imaging techniques in a correlative way to gain information on surface topography and the interior of the specimen from the same specimen region. In this chapter, the benefits of correlative SEM and low-keV STEM imaging in modern scanning electron microscopes are exemplified by structure analyses from representative sample classes that are in part challenging to study by conventional TEM. The first part of the chapter will deal with the class of magnetic materials exemplified by magnetic alloy steel. The second part describes the convenience of applying correlative SEM/STEM method on soft-matter materials such as biological cells. For the third part, the enormous information gained from the investigations of various micro- and nanoscale materials by the combination of SEM and low-keV STEM is discussed. In the last part, additional solid-state materials were characterized in order to illustrate some extra benefits in a modern SEM.

4.1 Magnetic materials

The investigation of magnetic materials poses a challenge in conventional TEM as the specimen is situated in the strong magnetic field of the objective lens. This leads to drawbacks like the necessity to frequently realign the microscope due to the strong interaction of the magnetic specimen with the magnetic lens field as soon as sample, apertures or electron-beam are moved. In addition, the strong magnetic field of the objective lens can fracture the specimen with the risk that fragments remain within the microscope causing severe image distortions. The field-free imaging mode in a scanning electron microscope is particularly interesting for a correlative SEM/STEM study of magnetic material as it confines the probe-forming magnetic field of the objective lens within the pole-piece and therefore, avoiding the exposure of the specimen to the magnetic field.

The benefits of correlative SEM/STEM for the study of magnetic materials are illustrated by the investigation of $Fe_{0.90}Si_{0.05}Al_{0.02}C_{0.03}$ steel using the field-free mode in the Strata

400S microscope which does not require any readjustment. Electron transparent samples were obtained by electrochemical thinning as described in chapter 3.

Fig. 4.1 (a) shows an overview SE image of a macroscopic region of the prepared TEM specimen. Representative grain-size data can be obtained despite very large grain sizes because grain boundaries are well visible and SE-channeling leads to different image intensities from different grain orientations. The hole in the center of Fig. 4.1 (a) and the electron-transparent region around the hole show dark contrast and it is clear that representative grain-size measurements would not be possible by (S)TEM considering the comparatively small electron transparent region. A small region near the edge of the hole marked by the ellipse is further magnified and simultaneously imaged by SE and BF-STEM (Figs. 4.1 (b,c)). The contrast changes in the BF image can be well understood with the surface topography information provided by the SE image. Dark regions in the BF image can be correlated with elevated, i.e. thicker specimen regions (cf. rectangles marked region in Figs. 4.1 (b,c)). The bright region (marked by white arrow) close to the edge of the TEM specimen in Fig. 4.1 (b) indicates that it is noticeably bent which also leads to a contrast change marked by the black arrow in the BF image. The capability of defect imaging by Bragg contrast in BF-STEM is demonstrated in Fig. 4.1 (d), where numerous short dislocation segments are visible [65].

Without the topography contrast provided by SE imaging, it is more difficult to evaluate the different contrast mechanisms from STEM imaging. The inhomogeneous contrast from Figs. 4.2 (a,b) illustrates that the contrast for the inspected area is not uniform. This could originate either from thickness variation of the sample or different orientations of the grains or even different phases in the crystallized sample. Nevertheless, the BF contrast for defects such as dislocations (cf. inset in Fig. 4.2 (a)) is still easily observable. It is even possible to extract the type of dislocations and their Burgers vector using SEM instruments equipped with on-axis CCD-cameras and double-tilt holders such as Helios. This will be discussed in chapter 5. Similarly, without SE the interpretation of the contrast in a HAADF image would also become harder. The HAADF image contrast usually reveals the mass-thickness contrast for the material. For Fig. 4.2 (c) the HAADF image of the magnetic steel sample, there are areas such like the ones marked by the white arrow which have darker intensity than the rest. Considering that the HAADF intensity does not

scale monotonically with sample thickness, topography information is necessary to come to right conclusions for the thickness distribution of the sample.
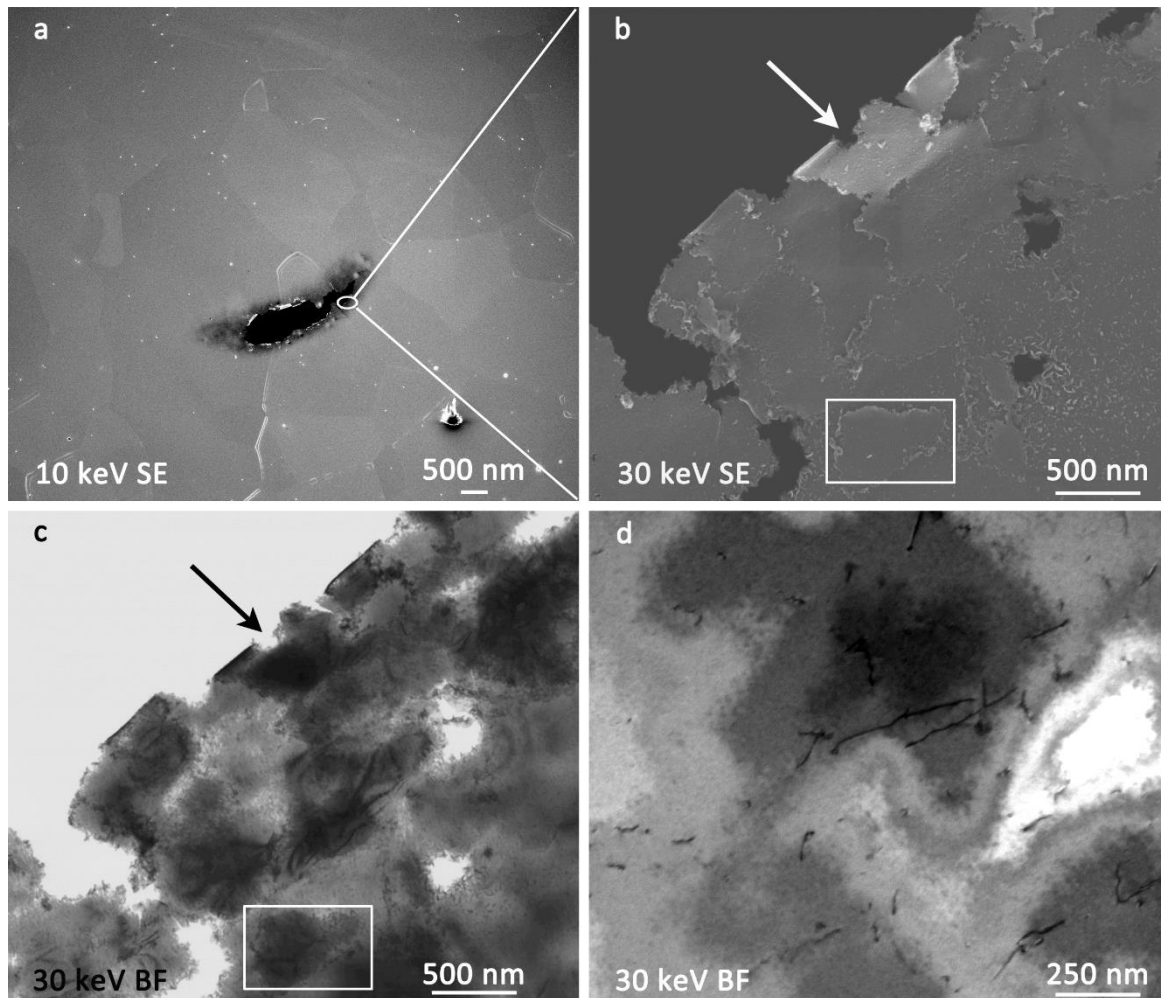
Figure 4.1. Correlative SEM/STEM imaging of magnetic steel. (a) 10 keV SE-TLD overview image, (b) 30 keV SE-TLD image at higher magnification close to the hole edge of the TEM specimen, (c) 30 keV BF-STEM image of the same region as (b) and (d) 30 keV BF-STEM image of dislocations. The bright spots in (a) correspond to contamination particles [65].
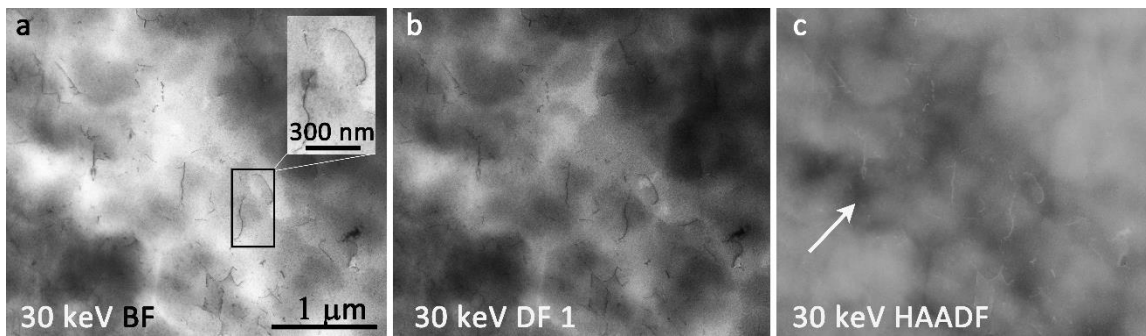
Figure 4.2. Low-keV STEM imaging of magnetic steel. (a) 30 keV BF-STEM image, (b) 30 keV DF_1-STEM image, (c) 30 keV HAADF-STEM image of the same region. DF_1 indicates the image is taken with DF segment 1 activated. Scale bar in (a) applies to (b,c).

Another specimen prepared from the same magnetic steel is presented in Fig. 4.3. A low-magnified SE image allows easy distinction of separate grains even far away from the electron transparent area in the middle of the image (cf. Fig. 4.3 (a)). The magnified region in Fig. 4.3 (b) clearly demonstrates that the contrast is not generated by channeling alone but also by changes of surface roughness between adjacent grains. There are etching induced features on the surface of the grains due to the electrochemical etching procedure. Thus not only channeling contrast but also the sample preparation procedure could assist distinguishing different grains using SE detectors. The same area in Fig. 4.3 (b) was simultaneously measured with HAADF-STEM detector (cf. Fig. 4.3 (c)). Black areas in Fig. 4.3 (c) either do not contain matter (hole in the middle) or are too thick for scattering electrons in the collection-angle range of the HAADF-STEM detector.
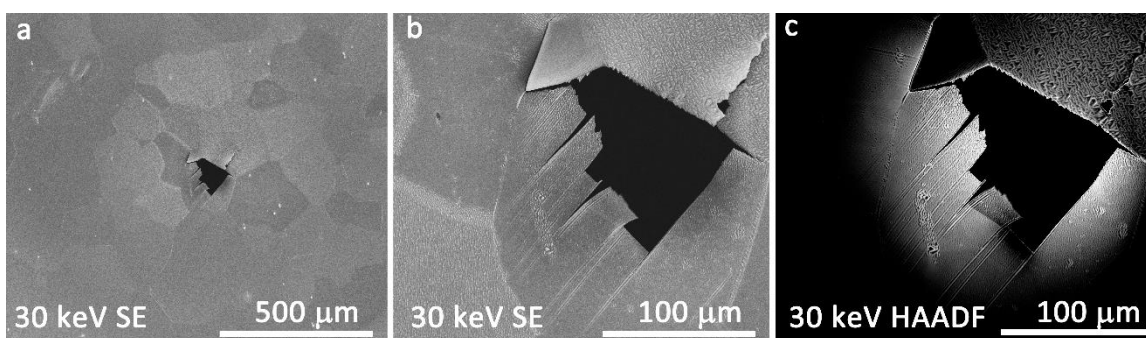
Figure 4.3. SEM/STEM imaging of magnetic steel. (a,b) 30 keV SE-TLD images, (c) 30 keV HAADF-STEM image of the same region as (b).

Even though most of the grains can be distinguished by SE imaging (cf. Fig. 4.1 (a) and Fig. 4.3 (a)), there is always the possibility that adjacent grains share the same grayscale

value leading to significant errors. This can be overcome by acquiring multiple SE images with different sample tilts. Tilting the specimen leads to a change of channeling contrast due to the angle change between the incident beam and crystal lattice [77]. The SE images in Fig. 4.4 demonstrate the tilt angle effect on channeling contrast. The grain boundaries marked by white arrows are easily distinguishable in Fig. 4.4 (a) with an α´ tilt of -5° while the grain boundaries disappear in Fig. 4.4 (b) with an α´ tilt of 5°.
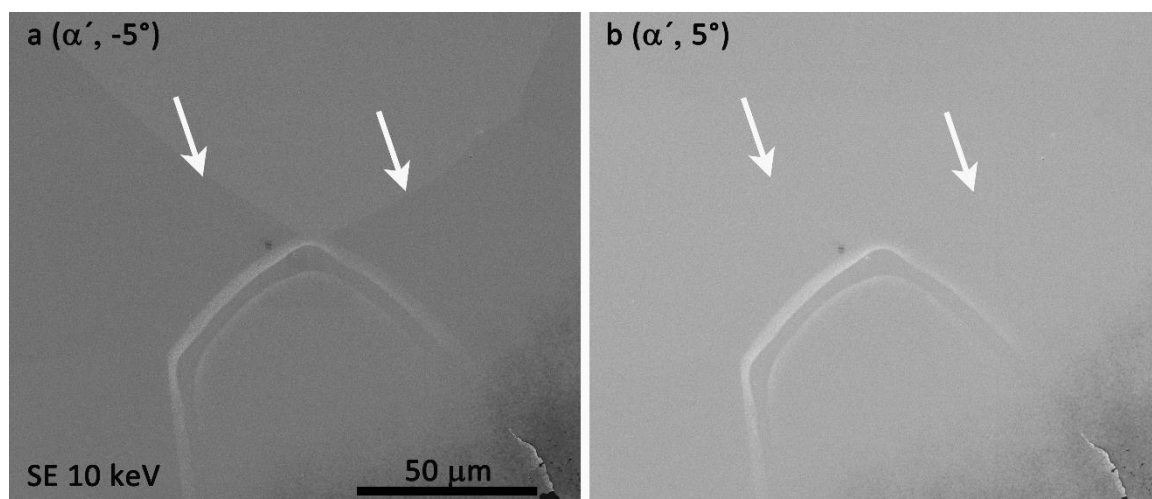
Figure 4.4. SE-TLD imaging of magnetic steel. (a) 10 keV with α´ tilt -5°, (b) 10 keV with α´ tilt 5°. Scale bar in (a) applies to (b).

The study of magnetic steel demonstrates that macroscopic information can be obtained from a prepared TEM specimen by correlative SEM/STEM imaging (here statistically relevant grain-size data) that cannot be obtained by (S)TEM alone. Moreover, defects can be imaged in the low-keV BF-STEM mode as in high-energy (S)TEM. Combining SEM and STEM information also facilities the understanding of STEM contrast changes due to thickness and orientation changes. It emphasizes that the results were obtained in the field-free operation mode during a quick investigation without realignment of the SEM microscope whereas a dedicated TEM study is much more time-consuming due to the need of frequent realignment of the microscope [65].

4.2 Soft-matter materials

The low-keV STEM method is advantageous for the study of soft-matter materials because electron scattering is more pronounced at low electron energies. Therefore, even materials with low atomic number and similar material properties yield pronounced

contrast in low-keV STEM [23]. However, the application of low-keV STEM on soft-matter materials should be cautious since radiolysis is often a severe problem for these materials.

One class of soft-matter materials presented here are biological materials. Recently, studies on toxicological effects of nanoparticles (NPs) on the human cells became interesting. Therefore, it is necessary to analyze the location of NPs in cells and eventually quantify their concentration. Combined SEM/STEM studies are advantageous for this purpose, especially by combining low magnification and high-resolution measurements [78].
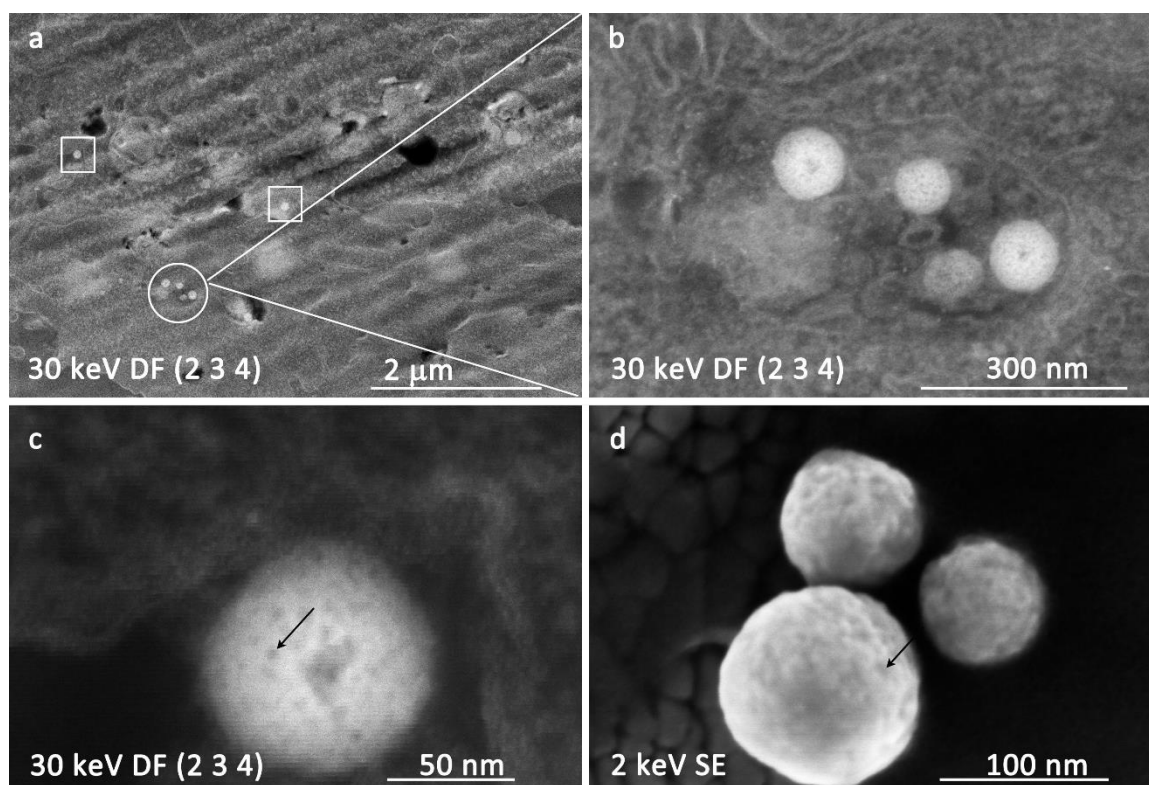
Figure 4.5. STEM/SEM imaging of A549 cell and SiO_2 NPs. (a) 30 keV $DF_{2,3,4}$-STEM image, (b) 30 keV $DF_{2,3,4}$-STEM image of a magnified region from (a). (c) $DF_{2,3,4}$-STEM image from one magnified area in (b), (d) 2 keV SE-TLD image for SiO_2 NPs. $DF_{2,3,4}$ indicates the image is taken with DF segments 2, 3 and 4 activated.

The investigated biological materials are A549 lung cancer cells which are in-vitro incubated with SiO_2 NPs [79]. Osmium tetroxide (OsO_4) was used for the fixation of the cell during thin-section preparation without any further poststaining [80, 81]. Images of a thin section of an A549 cell containing several SiO_2 NPs are presented in Figs. 4.5 (a-

c). The low-magnification DF image of the cell specimen Fig. 4.5 (a) contains several SiO$_2$ NPs marked by squares and circles. The bright straight broadened lines are thickness variations of the thin section which are artifacts from ultramicrotomy. With further magnification of the circle-marked area, mass-thickness contrast in Fig. 4.5 (b) shows membranes with distinct contrast although poststaining was not applied. SiO$_2$ NPs are contained in a vesicle here as opposed to being directly embedded in the cytosol of the cell. By magnifying one of the SiO$_2$ NPs, small dark regions (cf. black arrow in Fig. 4.5 (c)) can be recognized. SEM can be applied to distinguish between surface topography and porosity. The SE SEM image Fig. 4.5 (d) shows surface topography features with the same scale as the dark spots in the STEM image (Fig. 4.5 (c)), indicating that surface topography is mainly responsible for the observed STEM contrast rather than porosity.
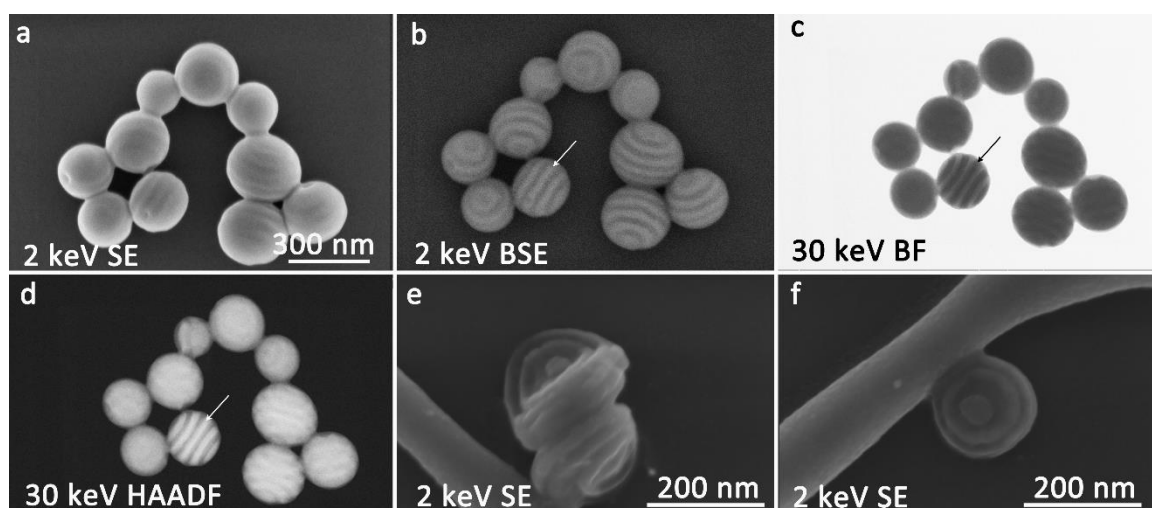
Figure 4.6. Correlative SEM/STEM imaging of polymer NPs. (a) 2 keV SE-TLD image, (b) 2 keV BSE-TLD image, (c) 30 keV BF-STEM image, (d) 30 keV HAADF-STEM image, (e) 2 keV SE-TLD image, (f) 2 keV SE-TLD image. NPs in (a-d) were stained with OsO$_4$ while NPs in (e,f) were unstained. Scale bar in (a) applies to (b-d).
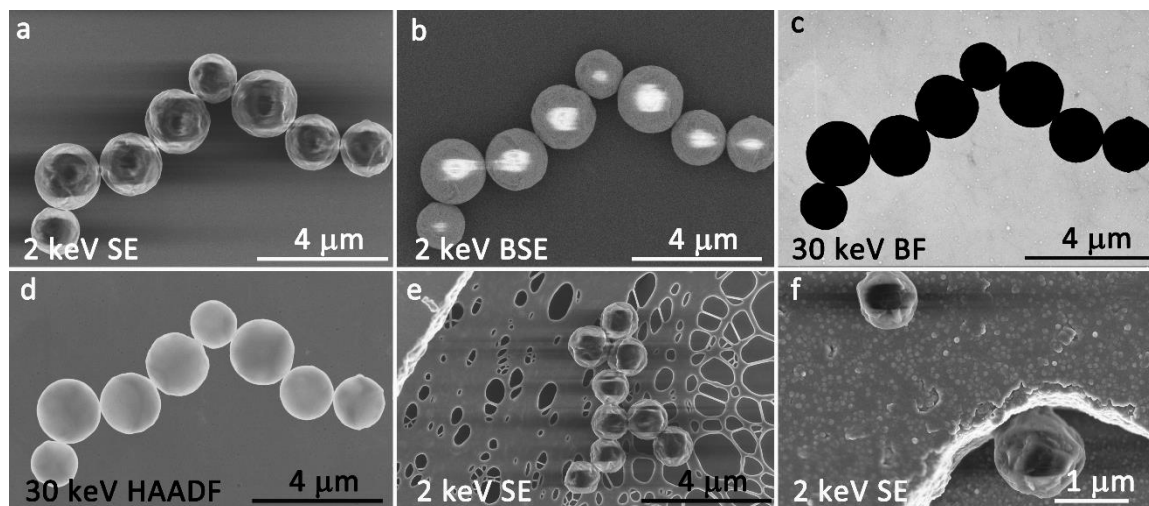
Figure 4.7. Correlative SEM/STEM imaging of polymer particles. (a) 2 keV SE-TLD image, (b) 2 keV BSE-TLD image, (c) 30 keV BF-STEM image, (d) 30 keV HAADF-STEM image, (e) 2 keV SE-TLD image, (f) 2 keV SE-TLD image. Particles in (a-d) were stained with Osmium tetroxide while those in (e,f) were unstained.

The second investigated type of soft-matter material are block copolymer (BCP) particles [82]. Self-assembled BCPs are powerful polymer materials which have great potential to construct controllable nanostructures [82, 83]. Correlative SEM/STEM was used to study the morphologies of different BCP-based particles. It is especially interesting to observe the topography contrast difference between the OsO_4 stained and unstained particles which is not possible with conventional TEM.

The polymer particles shown in Fig. 4.6 and Fig. 4.7 are polystyrene-b-polyisoprene (PS-b-PI) BCP materials. The PS part of the PS-b-PI BCP particles in Fig. 4.6 was fabricated to include halide (PS1) while those in Fig. 4.7 include azide (PS2). Usually the staining procedure will only oxidize the PI part by introducing Os to the layer.

Figs. 4.6 (a-d) display correlative SEM/STEM images of stained PS1-b-PI particles whereas Figs. 4.6 (e,f) show images of unstained particles. The SE image Fig. 4.6 (a) exhibits smooth surfaces for the stained PS1-b-PI particles. In contrast, the SE images Figs. 4.6 (e,f) clearly show fluctuations on the surface of the particles resulting from the stacking of the PS1 (density, 1.05 g/cm^3) and PI (density, 0.913 g/cm^3) layers. Since PS1 and PI have similar densities, many researchers prefer to stain BCP materials in order to improve contrast. The comparison between Fig. 4.6 (a) and Figs. 4.6 (e,f) demonstrates that staining alters the surface roughness of PS1-b-PI particles. Due to the pronounced

topography of unstained particles, PS1 and PI could not be separated by BF and HAADF-STEM imaging. For stained particles PS1 and PI could be distinguished clearly by both BSE (Fig. 4.6 (b)) and STEM (Figs. 4.6 (c,d)) imaging. As indicated by the arrows in Fig. 4.6, the brighter contrast layer should be the Os contained PI layer considering its larger BSE coefficient η (Eq. (12)). Accordingly, the PI layer shows darker contrast in BF-STEM images and brighter contrast in HAADF-STEM images compared with the PS1 layer (Figs. 4.6 (c,d)).

Stained and unstained PS2-b-PI particles were also investigated by correlative SEM/STEM (Fig. 4.7). In BSE and SE images taken at 2 keV there is noticeable charging visible (cf. Figs. 4.7 (a,b,e,f)). The SE images Figs. 4.7 (a,e,f) demonstrate pronounced surface roughness of both the stained and unstained PS2-b-PI particles. However, HAADF-STEM imaging (Fig. 4.7 (d)) only shows weak contrast within the particles. This indicates that using azide does not lead to the formation of well separated stackings of PS and PI layers. Due to the large size of the particles scattering of electrons in high angles is very pronounced leading to negligible BF signal as shown in Fig. 4.7 (c). This demonstrates one of the shortcomings of low-keV STEM imaging.

4.3 Micro- and nano-structured materials

In recent years there are emerging applications especially of nanostructured materials in many reasearch fields [52]. It becomes daily routine to use microscopes for the observation and characterization of those nanostructures to understand their properties and improve synthesis. Low-magnification SEM images provide macroscopic information as sizes or size distributions of NPs in a statistically relevant way. Structural feature of individual NPs can be complemented by low-keV STEM images in combination with SE/BSE SEM imaging. A variety of micro- and nano-scaled materials were studied to demonstrate the capabilities of correlative STEM/SEM imaging. The interpretation of contrast in low-keV STEM images will be supported by image simulations performed by MC simulations and the solution of the electron transport equation (cf. chapter 2).

4.3.1 ZnO NPs

One of the samples from the class of nanoscaled materials is zinc oxide (ZnO) which is interesting for nanoscaled electronic and photonic devices [84]. Depending on synthesis parameters, the morphology of ZnO particles differs quite strongly resulting in a variety of macroscopic properties.
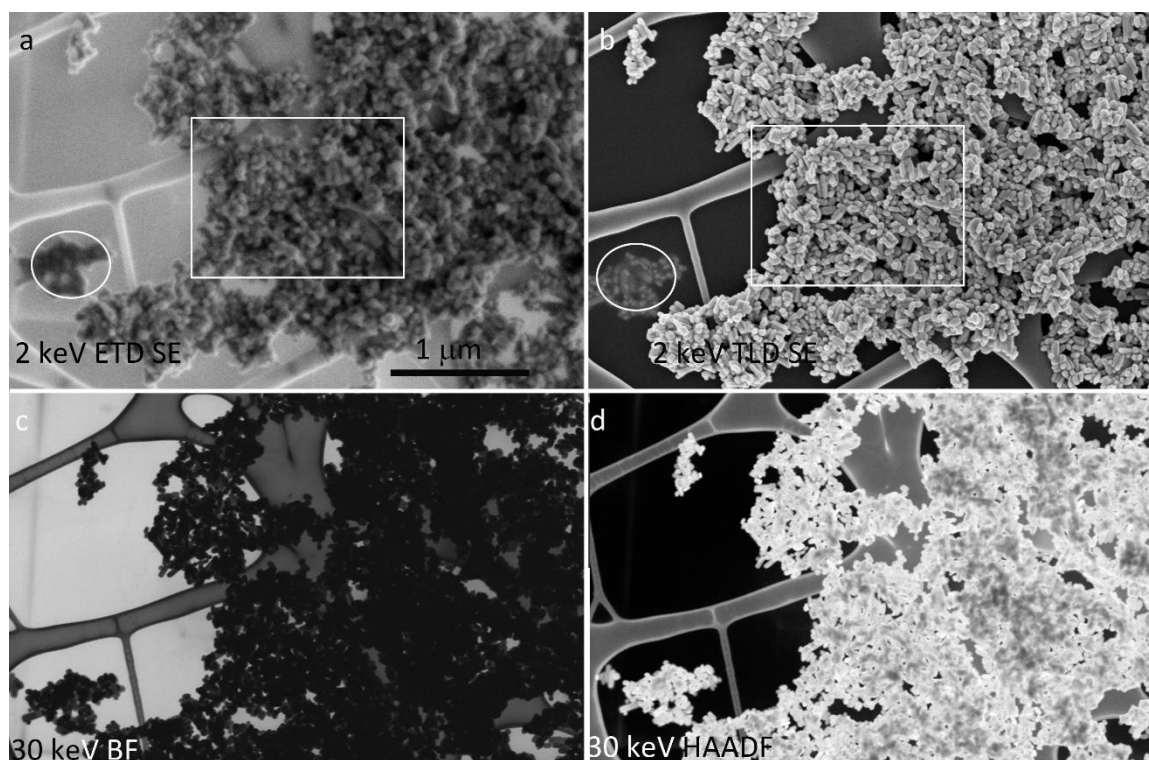
Figure 4.8. Correlative SEM/STEM imaging of the ZnO NPs. (a) 2 keV SE-ETD image, (b) 2 keV SE-TLD image, (c) 30 keV BF-STEM image, (d) 30 keV HAADF-STEM image. Scale bar in (a) applies to (b-d).

The images of ZnO NPs in Figs. 4.8 (a,b) were taken by two different SE detectors in Helios Nanolab G4 FX. Fig. 4.8 (a) is the SE image acquired with the ETD detector while the SE image obtained from the TLD detector is shown in Fig. 4.8 (b). When comparing the area in the rectangles, obviously the image taken by TLD has a better resolution. The TLD is situated within the column and therefore, except for very few SE4 electrons, the acquired SE signal mainly consists of SE1 (chapter 2, Fig. 2.10) which is strongly localized at the electron probe. In addition, the ETD is situated outside of the electron column and detects SE1, SE2 , SE3 and SE5 signals (chapter 2, Fig. 2.10). SE2, especially SE3 and SE5 do not contain information from the focus position of the electron beam on

the sample and therefore, decrease the signal-to-noise ratio for the SE signal leading to a decrease in resolution. Moreover, for the area in the ellipses in Figs. 4.8 (a,b), the ZnO NPs contrast is worse compared with those in the rectangles. The reason is that NPs with worse contrast are located on the opposite side of the carbon film. Another phenomenon is the contrast inversion for ZnO NPs and carbon film in Figs. 4.8 (a,b). The bright contrast for ZnO NPs compared with the dark carbon film in Fig. 4.8 (b) matches the atomic-number dependence of SE imaging described by P.F. Schmidt [47]. Since the ETD is located within the chamber (cf. chapter 3, Fig. 3.1), it is able to acquire the SE5 signal (chapter 2, Fig. 2.10). The lower contrast of ZnO NPs compared to carbon by ETD imaging can be explained by a higher SE5 signal that is generated at regions only containing the thin carbon film. Since the thin carbon layer is electron transparent, electrons can easily penetrate the carbon film and generate SE5 electrons. Besides, the BF and HAADF-STEM images in Figs. 4.8 (c,d) display the same contrast for ZnO NPs from the top and bottom sides of the carbon film. Since STEM images produce a projected image, ZnO NPs below and above the carbon film are imaged alike.
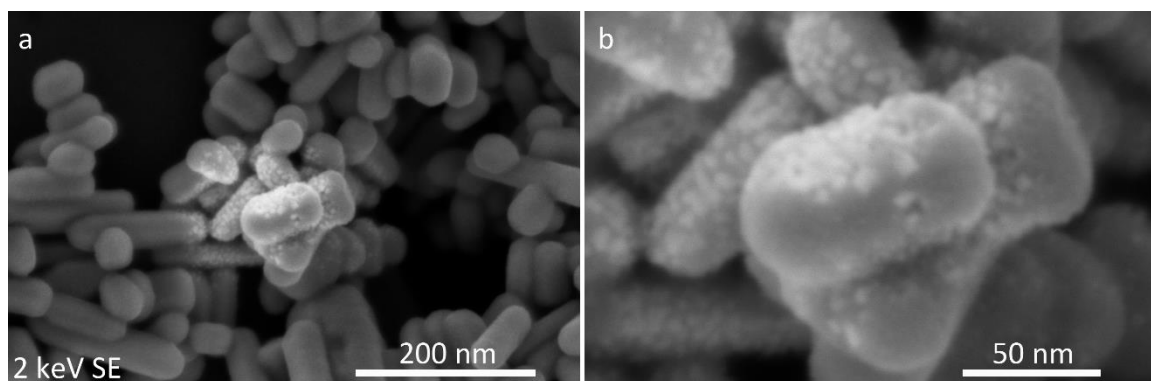
Figure 4.9. (a,b) 2 keV SE-TLD images of the ZnO NPs taken at different magnifications.

Radiation damage on ZnO NPs caused by electron-beam illumination is displayed in the SE images in Fig. 4.9. The center of Fig. 4.9 (a) was used for focusing. Since the electron-beam illumination in this area was extended compared to the surrounding region in Fig. 4.9 (a), more damage was introduced at the center of the SE image. Fig. 4.9 (b) is a high-magnification image of the damaged area from Fig. 4.9 (a) which shows the generation of small pits covering the surface of the ZnO NPs. It illustrates that caution is necessary when interpreting SE images as the surface might be already altered due to beam damage.
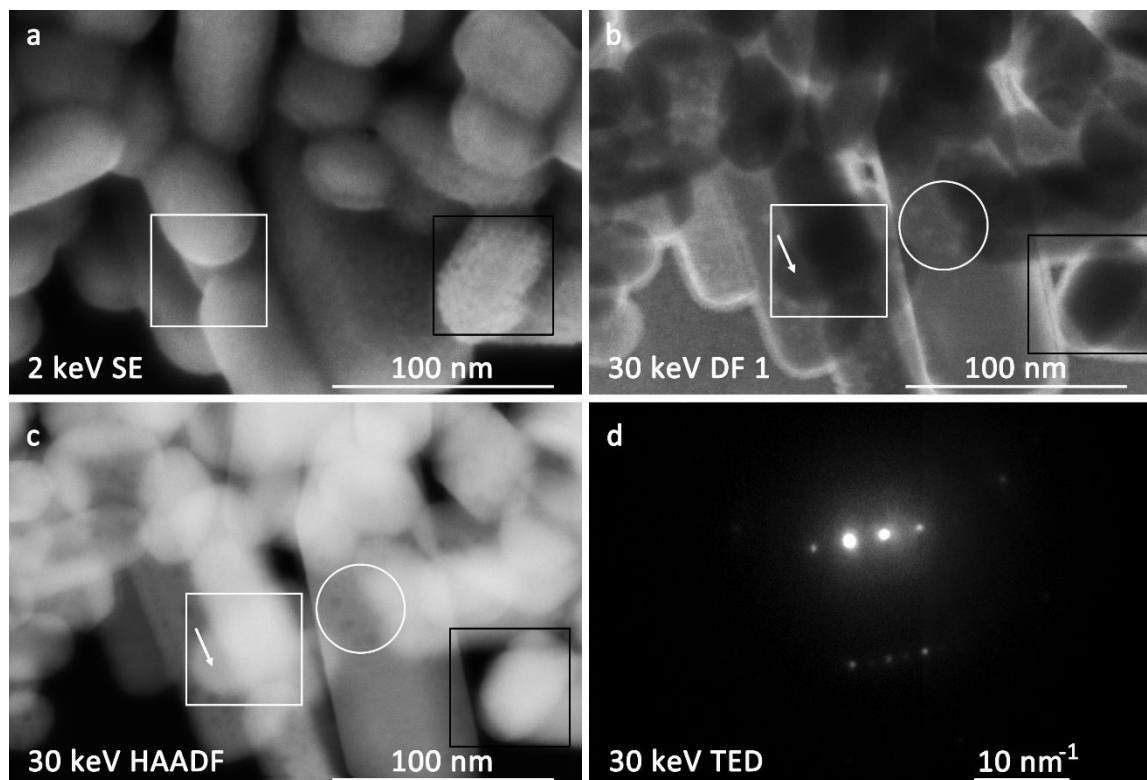
Figure 4.10. Correlative SEM/STEM imaging of the ZnO NPs. (a) 2 keV SE-TLD image, (b) 30 keV DF$_1$-STEM image, (c) 30 keV HAADF-STEM image, (d) 30 keV TED pattern [65].

Fig. 4.10 presents high-magnification STEM and SEM images of ZnO NPs and a TED pattern of a single ZnO NP. The SE image Fig. 4.10 (a) shows the three-dimensional arrangement and surface topography of the NPs. Small surface features on the NP within the black frame became increasingly pronounced after prolonged illumination during image focusing and are less pronounced or missing on the other NPs suggesting that these features are a result of electron-beam radiation. Comparison between the SE image Fig. 4.10 (a) and the STEM images Figs. 4.10 (b,c) reveals further NPs, e.g. marked by white arrows within the white frame, which are located below the NPs that are visible in Fig. 4.10 (a). The size of the ZnO NPs appears to be larger in SE and DF$_1$-STEM images compared to the HAADF-STEM image Fig. 4.10 (c). This observation can be understood by the presence of a shell around the NPs, most likely a contamination layer of amorphous carbon (aC). A NP shell with slightly darker contrast around some NPs can in fact be recognized in the SE image Fig. 4.10 (a) which is, in a very coarse approximation, related to the slight composition sensitivity of SE images where low atomic-number materials

show darker contrast than materials of higher atomic number [85]. The different chemical nature of the shell becomes strikingly visible in the DF-STEM image Fig. 4.10 (b) which is sensitive towards electrons scattered in small angles. Electrons in low-atomic number materials like carbon (atomic number $Z = 6$) are scattered in smaller angles (assuming similar specimen thickness) than electrons in ZnO with average $Z = 19$ which hence appear with dark contrast in Fig. 4.10 (b). On the other hand, only regions consisting of ZnO are visible in the HAADF-STEM image (Fig. 4.10 (c)) because the probability for large-angle electron scattering is negligible for low-atomic-number materials, which also explains the apparent NP-size difference in the images of Fig. 4.10. STEM images also show small round features within NPs in the white circle in Figs. 4.10 (b,c). These contrast features must be related to voids because they do not induce topography contrast in the SE image (Fig. 4.10 (a)). The voids appear bright in DF and dark in the HAADF-STEM images which can be rationalized by simulations of the DF- and HAADF-STEM intensity [65].
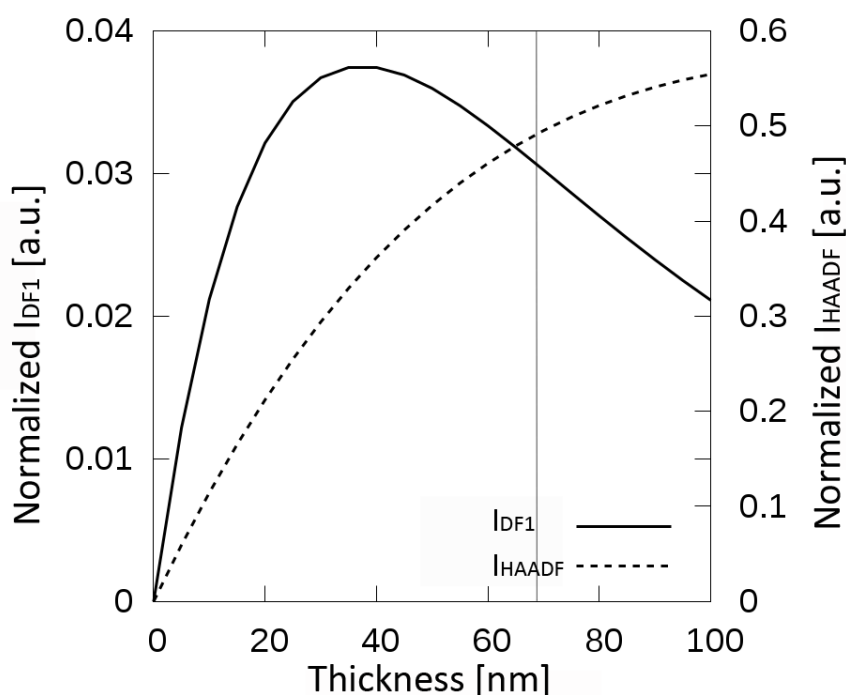
Figure 4.11. Simulated DF_1-STEM and HAADF-STEM intensities of ZnO as a function of the specimen thickness for an electron energy of 30 keV. I_{DF1} and I_{HAADF} are normalized with respect to the intensity of the incident electrons [65].

Fig. 4.11 depicts the simulated I_{HAADF} and I_{DF1} (CeTE 1.4) intensity normalized with the intensity of the incident electrons, as a function of the ZnO thickness at 30 keV. I_{DF1} (detection-angle range 16–23 mrad) and I_{HAADF} (detection-angle range 68–272 mrad) depend strongly on the specimen thickness. Due to the small scattering angle range, I_{DF1} (solid line in Figure 4.11) is in general smaller than I_{HAADF}. The maximum of I_{DF1} corresponds to the thickness at which the largest number of electrons are collected by the DF segment 1. At larger thicknesses, the electrons are scattered preferentially into larger angles leading to a decrease of I_{DF1}. The same behavior is observed for I_{HAADF} but the maximum intensity is not yet reached at 100 nm sample thickness for ZnO. The thickness of the large ZnO NP was measured to be ~ 70 nm by EFTEM which is indicated by the grey line in Fig. 4.11. The local ZnO thickness in regions with voids is reduced compared to regions without voids. I_{DF1} (solid curve in Fig. 4.11) suggests that I_{DF1} increases if the sample thickness decreases from 70 nm, which explains higher I_{DF1} of small voids compared to the surrounding region. In contrast, I_{HAADF} decreases with decreasing ZnO thickness (dotted line in Fig. 4.11) in accordance with a lower I_{HAADF} in pores [65].

The TED pattern in Fig. 4.10 (d) was acquired with the on-axis CCD-camera while the electron beam was positioned on a single NP. Although a projection lens system is missing, a well-focused TED pattern is observed. In this particular case, only two Bragg reflections (zero-order beam and the (002)-reflection) are strongly excited which corresponds to a two-beam diffraction condition. Further evaluation of the TED pattern reveals that the two-beam condition is close to the [410] zone axis of the hexagonal wurtzite structure of ZnO [65].

The analysis of ZnO NPs in Fig. 4.10 illustrates further benefits of correlative SEM/STEM. It allows straight-forward distinction of voids and surface corrugation. Selecting specific scattering angle ranges on the STEM-detector with four DF- and one HAADF-segments allows to highlight nanoscaled composition changes. TED reveals the diffraction condition of nanoscaled regions and facilitates crystal structure analysis.
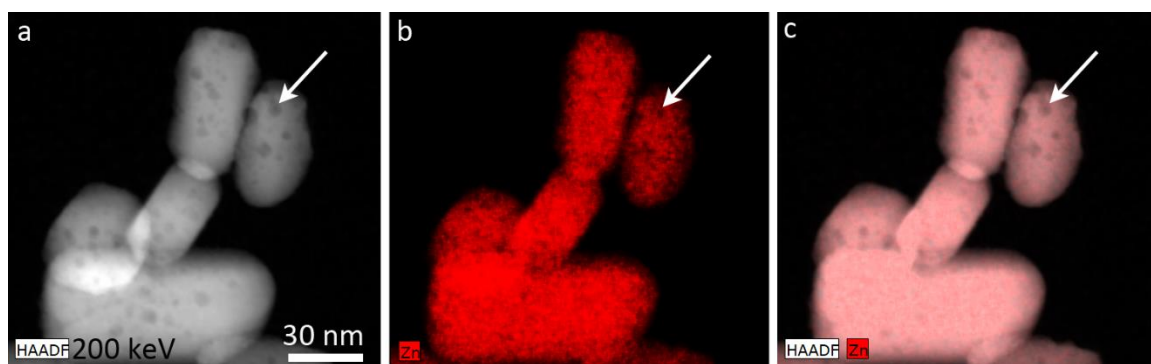
Figure 4.12. STEM (TEM) imaging and EDXS mapping of ZnO NPs. (a) 200 keV HAADF-STEM image, (b) 200 keV EDXS Zn-map, (c) superposition of (a) and (b). Scale bar in (a) applies to (b,c).

HAADF-STEM and EDXS images in Fig. 4.12 taken with Osiris TEM at 200 keV further confirm the presence of voids in Fig. 4.10. The EDXS intensity mapping of the Zn-K line in Fig. 4.12 (b) shows inhomogeneous signal and therefore, an uneven Zn distribution. Fig. 4.12 (c) is the superposition of Fig. 4.12 (a) and Fig. 4.12 (b). The dark voids in Fig. 4.12 (a) match the regions with reduced Zn signal in Fig. 4.12 (b) (e.g., the white arrows marked area).

Fig. 4.13 and Fig. 4.14 further illustrate the importance of simulations for the understanding of low-keV STEM images. The images in Fig. 4.13 were taken only with STEM. Without SE, one cannot distinguish the relative positions of different NPs. The collection angle range increases from Fig. 4.13 (a) to Fig. 4.13 (d) leading to a substantial contrast change of the ZnO NPs and the supporting carbon film.

Fig. 4.14 shows simulations for the ZnO NPs in Fig. 4.13 with CeTE1.4 software. The BF intensity decreases with increasing sample thickness with the collection angle range of 0-7 mrad for both ZnO and aC. This explains well why the thin carbon film in Fig. 4.13 (a) is brighter than the ZnO NPs. The BF intensity (red dashed line) for carbon (smaller atomic number) in Fig. 4.14 is always higher than the BF intensity for ZnO at the same thickness. Since in reality the carbon film is much thinner than the size of ZnO NPs, aC has an even higher intensity. The thicker ZnO NPs are darker, in particular in regions where more than one ZnO NP is arranged in electron-beam direction (e.g. the region marked by a white arrow in Fig. 4.13 (a)). The collection angles for DF_1 and DF_2-STEM imaging are 16-24 mrad and 24-32 mrad (Figs. 4.13 (b,c)), respectively. The

simulated DF_1 (solid orange line) curve has lower intensity than DF_2 (solid blue line) curve for ZnO material with same thickness (Fig. 4.14). This is in accordance with Figs. 4.13 (b,c). However, the DF_1 (gray value, 25300) and DF_2 (gray value, 25800) difference for aC is rather small (Figs. 4.13 (b,c)) because the dashed orange and blue curves in Fig. 4.14 almost overlap. Therefore, the collection angle change from 16-24 mrad to 24-32 mrad leads to small aC contrast changes. With the further enlargement of collection angle (68-272 mrad) for HAADF, the dashed black line for aC in Fig. 4.14 has a significantly lower intensity than ZnO at the same thickness (solid black line). As a matter of fact, aC is much thinner than ZnO, the aC intensity is even lower which explains its dark contrast in Fig. 4.13 (d) in comparison with the bright ZnO NPs.
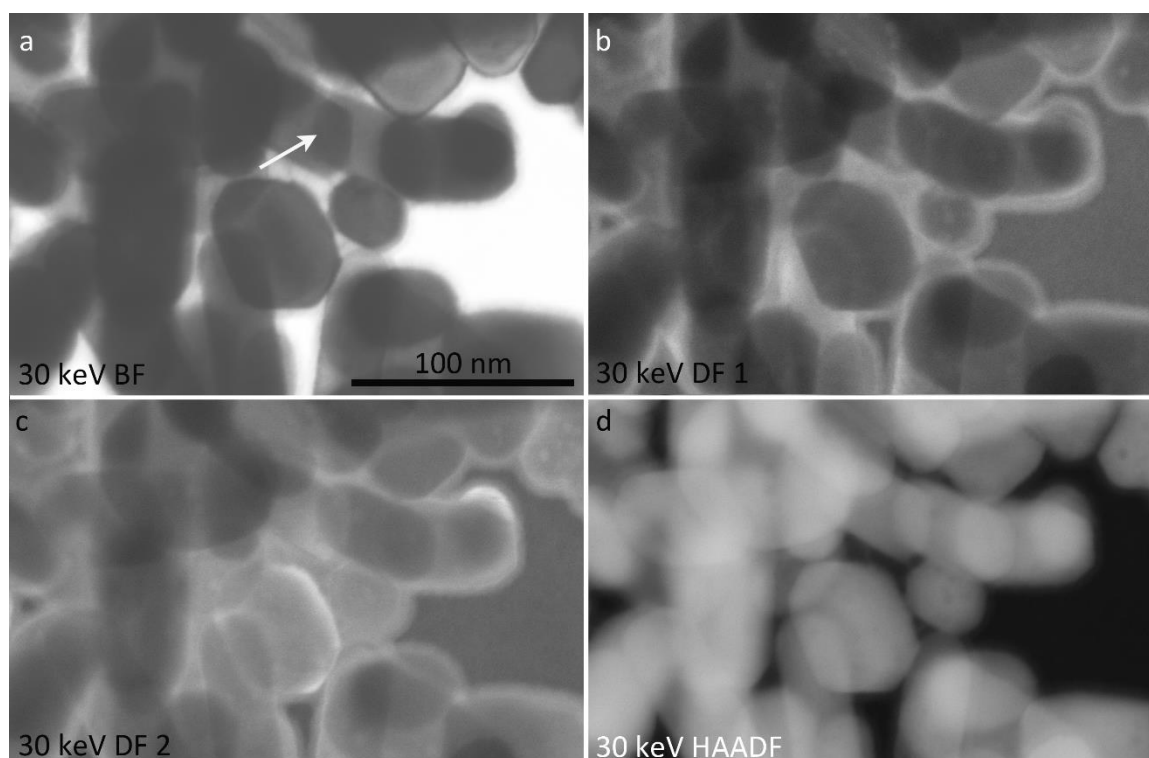
Figure 4.13. Low-keV STEM imaging of the ZnO NPs. (a) 30 keV BF-STEM image, (b) 30 keV DF_1-STEM image, (c) 30 keV DF_2-STEM image, (d) 30 keV HAADF-STEM image. Scale bar in (a) applies to (b-d).
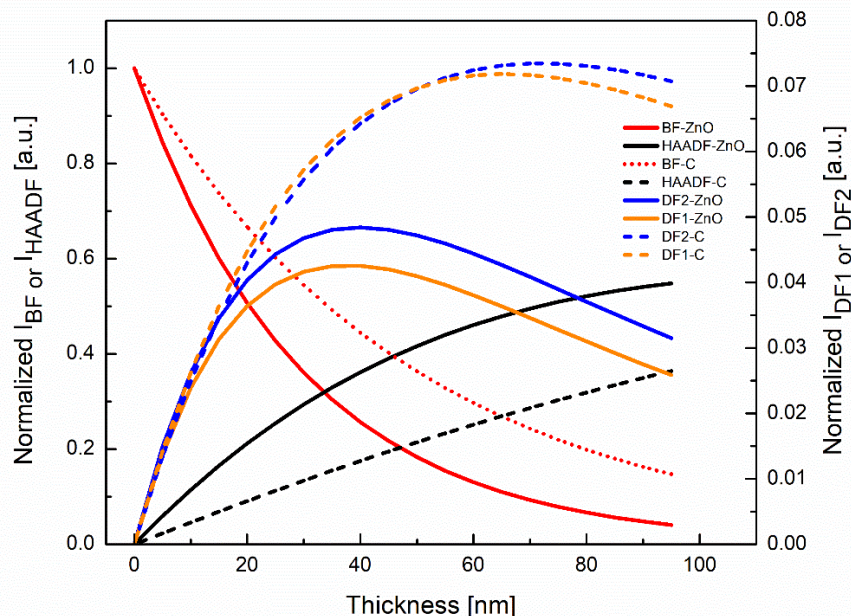
Figure 4.14. Simulated BF-STEM, DF-STEM (DF_1, DF_2) and HAADF-STEM intensities for both ZnO and amorphous carbon (aC) as a function of the specimen thickness for an electron energy of 30 keV. I_{BF}, I_{DF1}, I_{DF2} and I_{HAADF} are normalized with respect to the intensity of the incident electrons.

4.3.2 Pt/γ-Al₂O₃ catalysts

The second presented nanomaterial is a Pt/γ-Al$_2$O$_3$ catalyst material which can be applied for CO and NO oxidation reactions. It is rather costly because it contains noble metal in the form of Pt NPs. The study of the distribution of the noble metal NPs is important for the sake of improving the efficiency of oxidation reactions by the Pt/γ-Al$_2$O$_3$ catalyst [86]. Even though high-energy STEM is commonly used for the characterization of the distribution of Pt NPs in Al$_2$O$_3$ [87], low-keV STEM in a SEM provides a viable alternative especially in modern instruments with significantly improved STEM resolution. Moreover, it will be shown that information on topography by SEM imaging is important for STEM contrast interpretation.
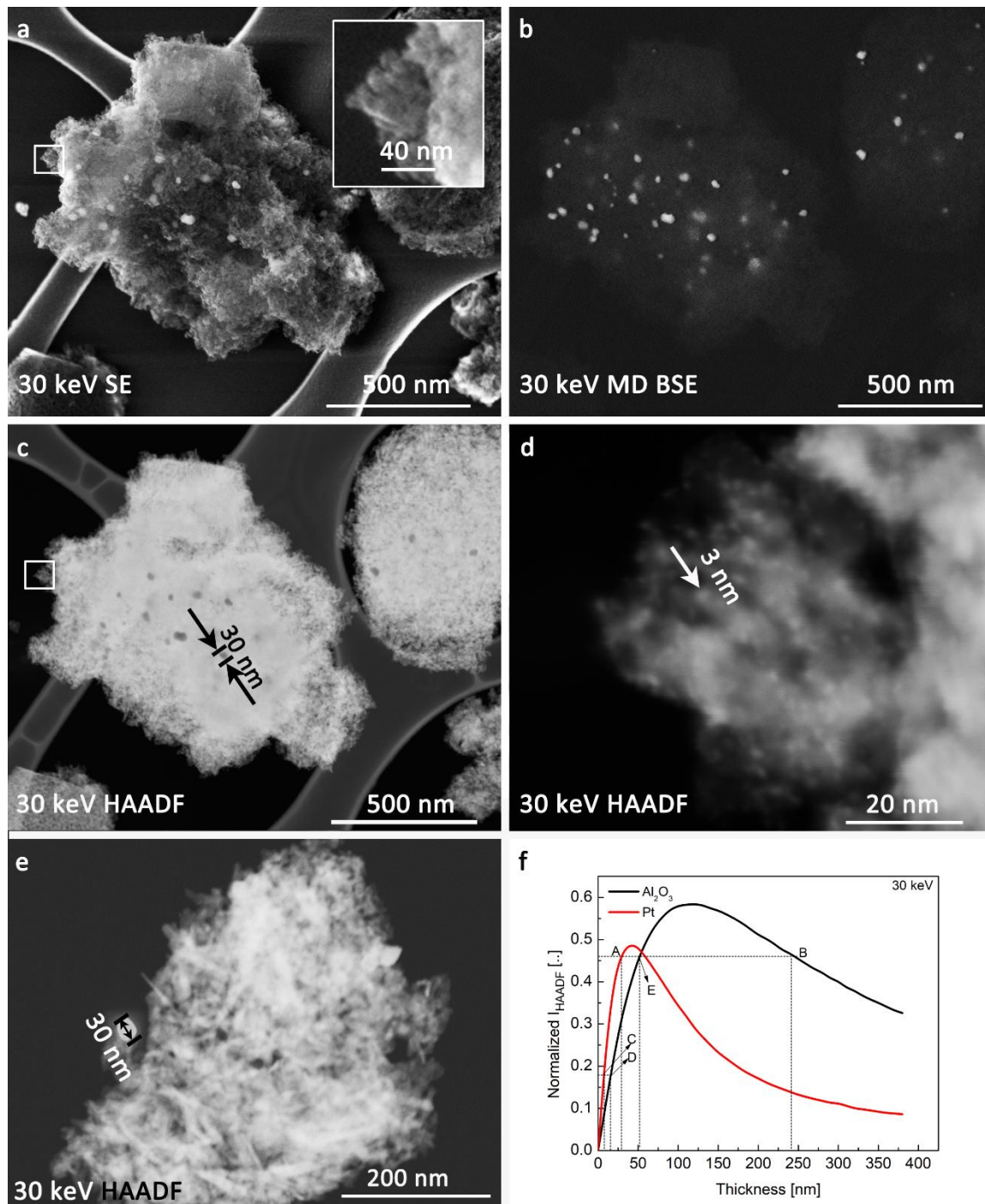
Figure 4.15. Correlative SEM/STEM imaging of Pt NPs on a porous Al_2O_3 carrier. (a) 30 keV SE-TLD image, (b) 30 keV BSE-MD image, (c) 30 keV HAADF-STEM image, (d) 30 keV HAADF-STEM image, (e) 30 keV HAADF-STEM image, (f) simulated HAADF-STEM intensities of both Pt and Al_2O_3 as a function of the specimen thickness for an electron energy of 30 keV. I_{HAADF} is normalized with respect to the intensity of the incident electrons.

The SE SEM image Fig. 4.15 (a) displays the topography of a cluster of porous Al_2O_3 with Pt NPs (~ 30 nm) on the surface. As already explained for Fig. 4.8 (b), the larger SE yield for higher atomic number Pt NPs compared with Al_2O_3 leads to higher SE yield resulting in white NPs on dark Al_2O_3 substrate. By using BSE imaging, as seen in Fig. 4.15 (b), the contrast of Pt NPs can be increased significantly as BSE yield strongly depends on the average atomic number (cf. Eq. (12), chapter 2). Due to the high primary electron energy (here 30 keV) and therefore, large interaction volume and escape depth, even NPs located below the surface are clearly visible. By comparing BSE and SE images, it is possible to distinguish Pt NPs which are located on the surface and within the Al_2O_3 carrier. The area marked by the small white frame in Fig. 4.15 (a) is enlarged in the inset. It is difficult to identify small Pt NPs based on the regular topography contrast at such a high magnification. It is interesting to note that for the same region, the HAADF image in Fig. 4.15 (d) could resolve very small Pt NPs (~ 3 nm) in Al_2O_3. This indicates that either the SE imaging condition needs to be improved to resolve such small NPs on Al_2O_3 or the small NPs are preferentially located within the Al_2O_3. Comparing the BSE image Fig. 4.15 (b) with the HAADF-STEM image Figs. 4.15 (c,d), not all NPs visible in the BSE image are visible in the HAADF image and vice versa. Especially small NPs are missing in the BSE image which can be rationalized by the small material volume and therefore, extremely low BSE yield.

Interestingly, there is a contrast inversion of Pt NPs in the HAADF-STEM images (Figs. 4.15 (c-e)) which can be understood by simulations of the HAADF-intensity. MC simulations (Fig. 4.15 (f)) of the normalized HAADF-STEM intensity of Pt and Al_2O_3 as a function of thickness were preformed using the NistMonte software [63]. The thickness of the Pt NPs marked in Figs. 4.15 (c-e) are assumed to be around 3-30 nm according to their lateral sizes. When comparing the simulated intensity for Pt NPs and Al_2O_3 in Fig. 4.15 (f), the intensity of Pt NPs with diameter around 30 nm and 3 nm is marked with A and C on the red curve. The Al_2O_3 shows a similar intensity as the Pt NPs in Figs. 4.15 (d,e) which allows a rough estimate of the Al_2O_3 thickness. The Al_2O_3 in Fig. 4.15 (d) has a similar HAADF-STEM intensity as the 3 nm Pt NPs, meaning its thickness is around 13 nm shown by the D point in Fig. 4.15 (f). In the same way, Fig. 4.15 (f) indicates a 238 nm thick Al_2O_3 (B point) for Fig. 4.15 (e). Comparison of Figs. 4.15 (c,e) reveals a contrast reversal within the HAADF-STEM images between Pt NPs and Al_2O_3 which is

counterintuitive. Since the 30 nm Pt NPs in Fig. 4.15 (c) is darker than Al_2O_3, it indicates that the Al_2O_3 intensity lies between E and B points in Fig. 4.15 (f). In other words, the thickness of the Al_2O_3 in Fig. 4.15 (c) is between 50 ~ 238 nm.

Additional SE images taken from the Pt NPs/Al_2O_3 sample (cf. Fig. 4.16) demonstrate how contamination affects the topography of samples. The high porosity of the Al_2O_3 surface can be clearly observed in Fig. 4.16 (a). The area displayed in Fig. 4.16 (b) was imaged first by STEM and then by SE SEM. Therefore, more contamination is built up on the surface of the sample owing to prolonged electron illumination. That explains why fine topography features cannot be recognized on the Al_2O_3 surface in Fig. 4.16 (b) due to carbon contamination. The growth of carbon contamination is especially pronounced within the area used for focusing (marked by white arrow) in Fig. 4.16 (b). Therefore high-resolution SE SEM images should be acquired before STEM imaging and methods for the reduction of contamination should be applied as discussed in chapter 2.

Another factor affecting SE imaging is charge accumulation on the surface of samples which is especially pronounced for electron insulators like Al_2O_3. The irregularly shaped black regions (e.g., marked by white arrow) in Fig. 4.17 (a) taken at 3 keV are caused by charging. Since SEs have low energies, they are easily affected by local charges. One method to reduce charging effects is to find the electron energy at which the total electron yield σ (the sum of the SE and BSE yield) equals to 1. For instance, the SE images of Fig. 4.16 which were taken at 2 keV show no charging due to the balanced total electron yield. In contrast to SE, BSEs are less affected by charging due to their significant higher energies. Therefore, charging artifacts disappear completely in BSE images as presented in Fig. 4.17 (b).
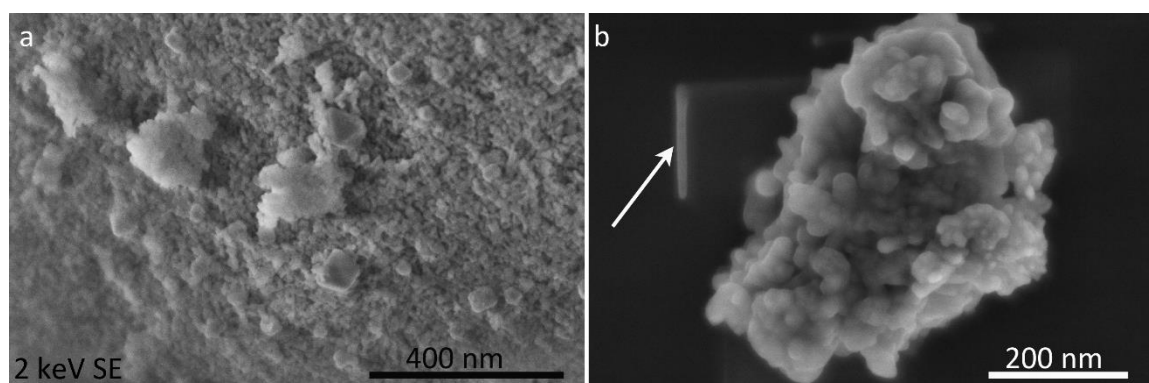
Figure 4.16. (a,b) 2 keV SE-TLD SEM images of Pt NPs on a porous Al_2O_3 carrier.
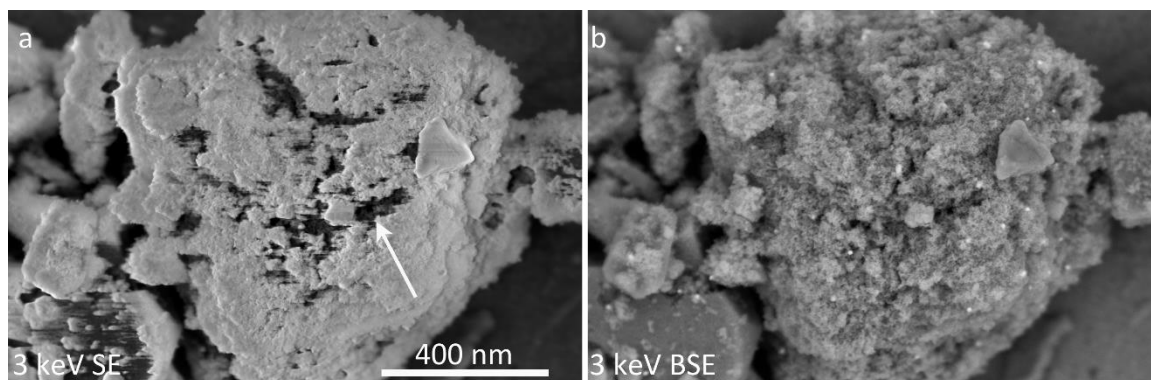
Figure 4.17. SEM imaging of Pt NPs on a porous Al_2O_3 carrier. (a) 3 keV SE-TLD image, (b) 3 keV BSE-TLD image. Scale bar in (a) applies to (b).

4.3.3 CNTs

Multi-walled carbon nanotubes (CNTs) were also investigated by correlative SEM/STEM imaging because they have stimulated the developments in many research fields due to their specific atomic structure and properties. Although TEM is frequently used to characterize CNT materials for understanding their physical and chemical properties [88], correlative SEM/STEM is feasible to get additional information on topography. It will be shown that it is possible to obtain nano-beam diffraction patterns and lattice fringe BF-STEM images of CNTs in a modern SEM instrument.

An overview SE image of multi-walled CNTs deposited on a holey carbon film is shown in Fig. 4.18 (a). Increasing the magnification in the region marked with the white frame gives an impression of the surface topography and three-dimensional arrangement of the CNTs (Fig. 4.18 (b)). Due to their small thickness, multi-walled CNTs are semi-transparent in the 30 keV SE-SEM image. The BF-STEM image (Fig. 4.18 (c)) from the same sample region clearly reveals the inner CNT structure. It shows the presence of nanoparticles (black arrows in Figs. 4.18 (c,d)) which were used as catalysts for CNT fabrication. The particles consist of Ni as revealed by energy-dispersive X-ray spectroscopy. The position of the catalyst particles is indicated by arrows in Fig. 4.18 (b) to point out the absence of SE contrast, which clearly demonstrates that the particles are not located at the upper CNT surface. Diffraction-contrast features are visible in the BF-STEM image Fig. 4.18 (c). Bragg diffraction and overlapping Bragg diffraction disks on the BF-detector segment are mandatory prerequisites for obtaining lattice fringe BF-STEM images. This corresponds to phase-contrast imaging in STEM. Lattice fringes with

a distance of 3.7 Å are indeed resolved for the inner-shell distance in the multi-walled CNTs (cf. inset in Fig. 4.18 (c)) in agreement with TEM results [88]. HAADF-STEM images are sensitive towards the average atomic number and the local thickness of the specimen. The high image intensity of the particles in Fig. 4.18 (d) suggests that they consist of a material with substantially higher atomic number than carbon. Locally enhanced intensity is also observed in regions where CNTs are stacked on top of each other [65].
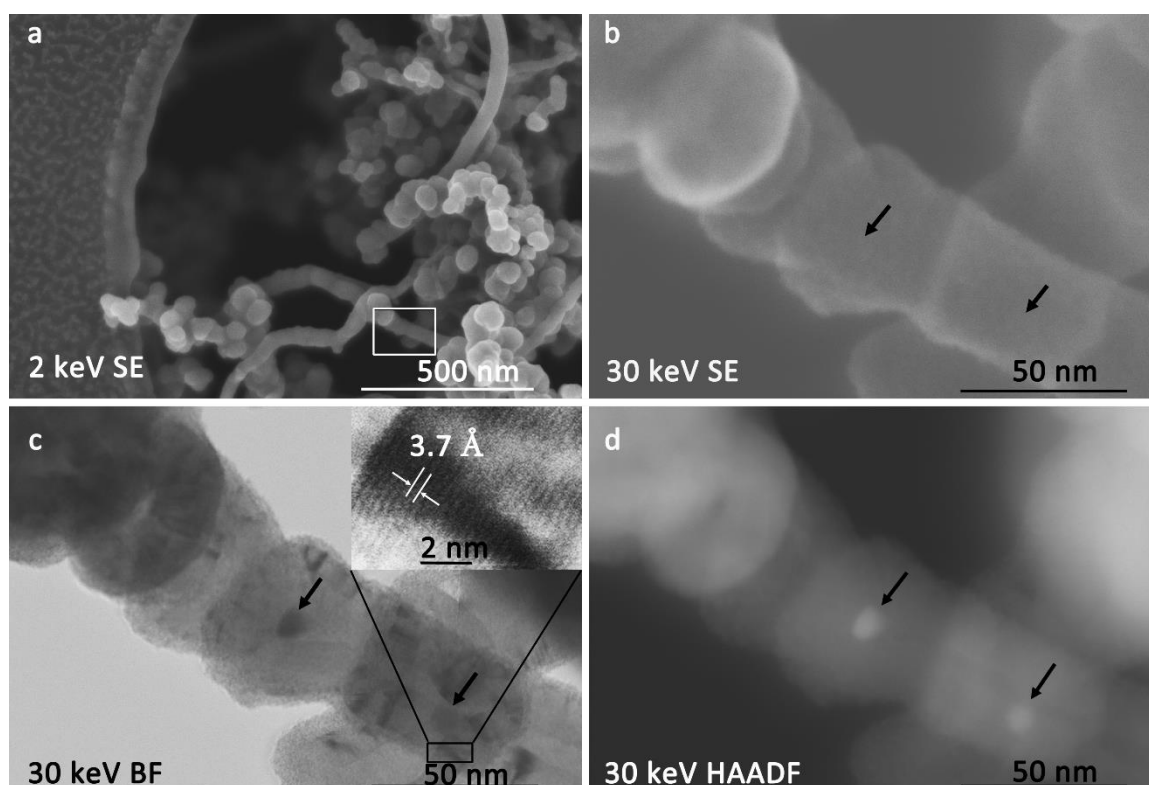
Figure 4.18. Correlative SEM/STEM imaging of a multi-walled CNT specimen. (a) 2 keV SE-TLD overview image, (b) high-magnification 30 keV SE-TLD image from the region marked with a white frame in (a), (c) 30 keV BF-STEM image and (d) 30 keV HAADF-STEM image [65].

Fig. 4.19 demonstrates two CNTs SE-TLD SEM images from the same area but with different electron-beam focus positions. The rectangular marked area is in focus in Fig. 4.19 (a). Most of the CNTs in Fig. 4.19 (a) have clear contrast which illustrates that these CNTs are at a similar distance to the objective pole piece as the marked area. The focused area (ellipse area) in Fig. 4.19 (b) shows a lower intensity for the CNTs compared with the blurred CNTs. The SEs generated from CNTs further away from the pole piece will

have lower possibility to reach TLD leading to a lower intensity. It indicates that the CNTs which are in focus in Fig. 4.19 (b) have lower position than the other blurred CNTs. This also matches Fig. 4.19 (a) that CNTs located closer to the electron pole piece show a higher intensity compared to CNTs further away.
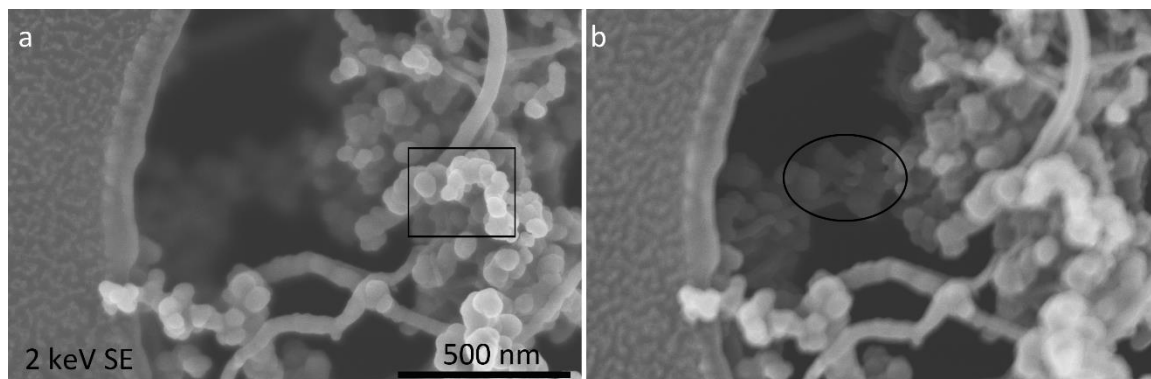
Figure 4.19. (a,b) 2 keV SE-TLD SEM images of a multi-walled CNT specimen with different focus positions. Scale bar in (a) applies to (b).

Another example for correlative SEM/STEM imaging of the same sample region within the CNTs is presented in Fig. 4.20. The arrangement of different CNTs is shown clearly in the SE image (Fig. 4.20 (a)). Combined with STEM images in Figs. 4.20 (b-d), the inner and outer structures of the CNTs can be imaged completely. The diffraction contrast in BF (Fig. 4.20 (b)) is the inverse of that in DF (Fig. 4.20 (c)). Because the unscattered transmitted beam used for BF imaging is in a first approximation complementary to the intensity of the diffracted beam(s) used for DF-STEM imaging, especially for the two-beam condition. In contrast, the HAADF image in Fig. 4.20 (d) shows exclusively mass-thickness contrast. The typical diameter of CNTs is in the range of 50 nm. According to the HAADF intensity simulation for carbon (black dashed line) in Fig 4.14, there is no inversion of contrast up to a thickness of 100 nm. Therefore, the HAADF intensity for CNTs should increase with increasing carbon thickness. Thus, the dark elongated features in Fig. 4.20 (d) can be assigned to the hollow interior of the tubes while the brighter regions depict thicker CNT regions.

As described in Fig. 4.18 (c), recent advances in resolution for BF-STEM in SEM instruments allow imaging of lattice fringes. An example for imaging of lattice fringes of CNTs is shown in Fig. 4.21. The lattice fringes clearly show the distance between individual CNT walls. In Fig. 4.21 (a), for example, some of the walls (marked by arrow)

are detached from the rest of the CNT. Interestingly, the lattice fringes can also be distinguished for multiple CNTs superimposed on each other as seen in Fig. 4.21 (b) with two CNTs perpendicular to each other. High-resolution BF-STEM imaging is extremely sensitive regarding changes of the environment (electromagnetic or mechanical vibrations) of the microscope. This manifests itself in scanning errors during image acquisition as seen in image Fig. 4.21 (c). High-resolution BF-STEM images also allow the identification of hollow regions within the CNTs which are identified as regions encapsulated by lattice fringes. In Fig. 4.21 (d), the hollow region of a CNT is highlighted by a white arrow.
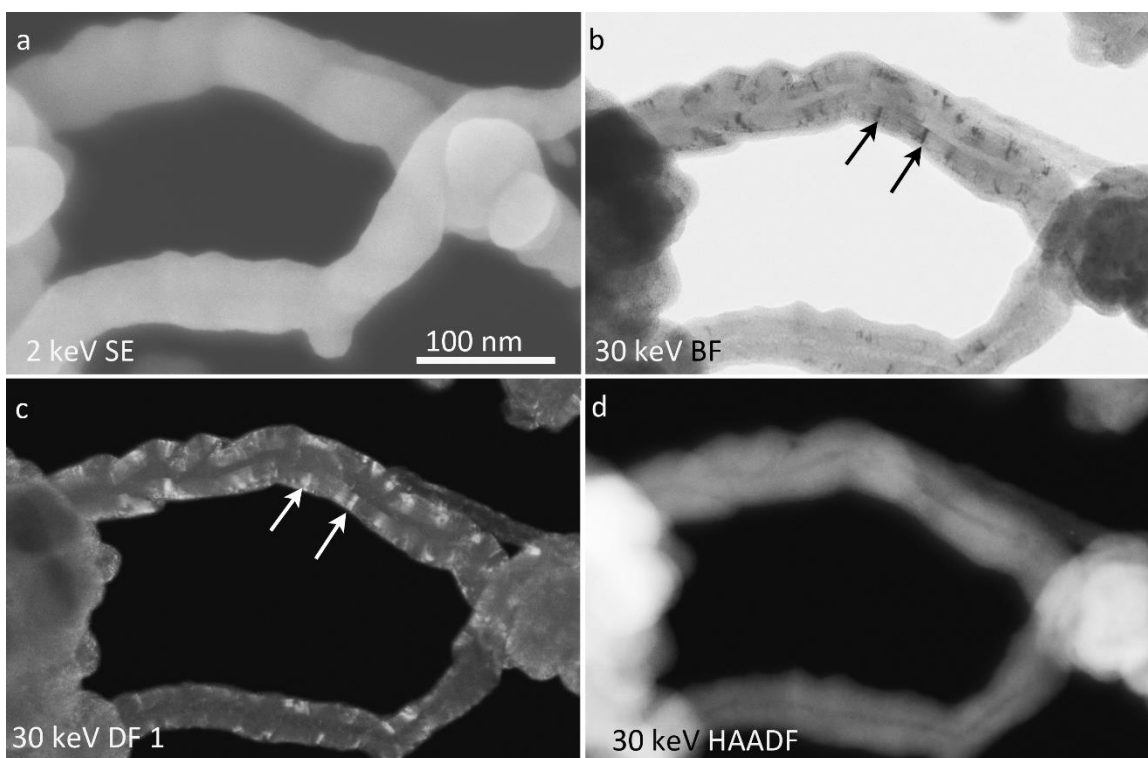
Figure 4.20. Correlative SEM/STEM imaging of a multi-walled CNT specimen. (a) 2 keV SE-TLD image, (b) 30 keV BF-STEM image, (c) 30 keV DF$_1$-STEM image, (d) 30 keV HAADF-STEM image. Scale bar in (a) applies to (b-d).
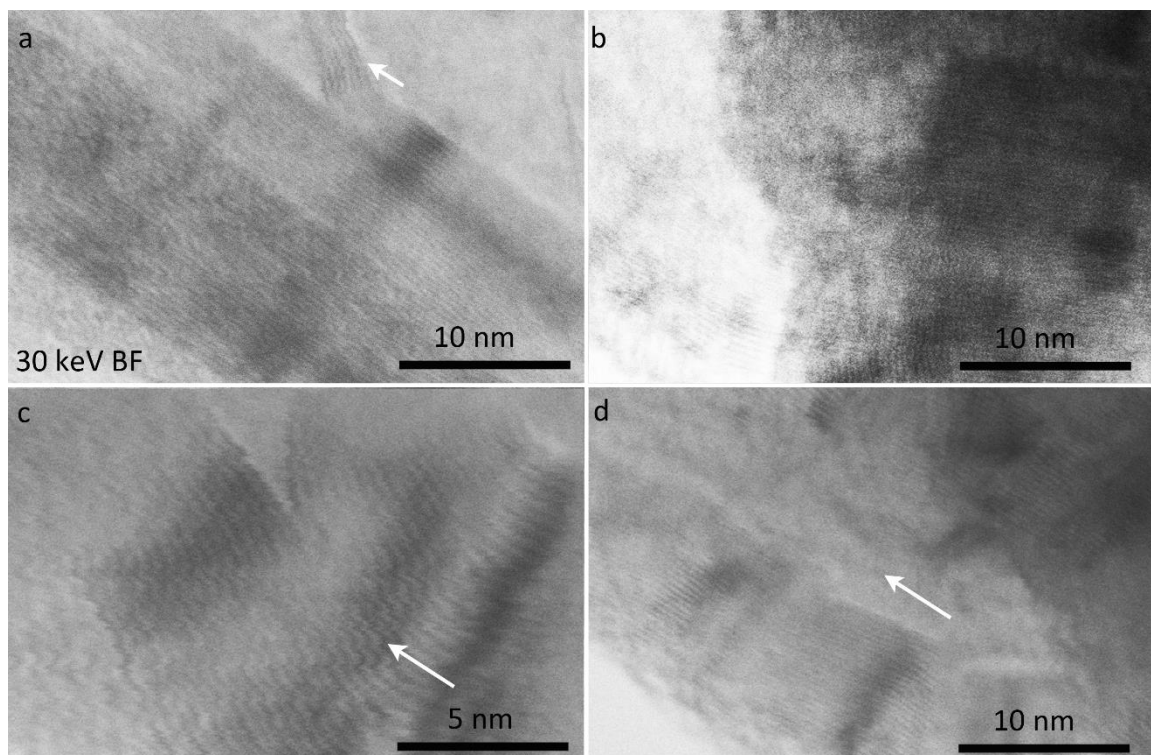
Figure 4.21. (a-d) 30 keV BF-STEM lattice fringes imaging of a multi-walled CNT specimen.

Stacked graphene layers can also form large tube structures as depicted in Fig. 4.22 (a) for SE and Fig. 4.22 (b) for BF-STEM. A magnified SE image in Fig. 4.22 (c) demonstrates the hollow tube with a wrinkled surface. The BF-STEM image in Fig. 4.22 (d) complements image information by showing the pronounced diffraction contrast of the stacked graphene layers. Not to mention, lattice fringe images were obtained from the area marked with a black arrow in Fig. 4.22 (d).

The introduction of the double-tilt TEM sample holder also makes topography contrast SEM imaging more powerful. The large β´ tilt range (10° ~ -190°) of the sample holder of the Helios Nanolab G4 FX allows to flip samples. The SE images Figs. 4.23 (a,b) were taken from the top and bottom sides of CNTs with Ni catalyst showing the topography of both sides. By imaging top and bottom sample topography, STEM contrast in Figs. 4.23 (c,d) can be understood easily. Apparently the region marked by arrows in Figs. 4.23 (a,b) is thicker than the region marked by rectangles which explains its dark BF (Fig. 4.23 (c)) and bright HAADF contrast (Fig. 4.23 (d)). The Ni catalyst in the rectangles (Figs. 4.23 (c,d)) is clearly visible because of its diffraction contrast in BF-STEM and mass-thickness

contrast in HAADF-STEM images. The topography of the same area is shown in Figs. 4.23 (a,b) which do not show any prominent features on the top and bottom CNT surfaces. Therefore, it is safe to assume that the catalyst is located inside the CNTs. Similar results are shown in Figs. 4.24 (a,b) where top and bottom SE images are displayed. Considering the mass-thickness contrast of the Ni catalyst in Fig. 4.24 (c) and topography contrast in Figs. 4.24 (a,b), the position of the Ni catalyst (marked by white arrows) relative to CNTs can be concluded. The black arrow in Fig. 4.24 (a) shows the CNTs which are located above the carbon film. Interestingly, if the CNTs are located below the carbon film, there is still a weak SE signal from the CNTs as shown in Fig. 4.24 (b). Hence, some of the SE generated on the back side can reach the TLD.
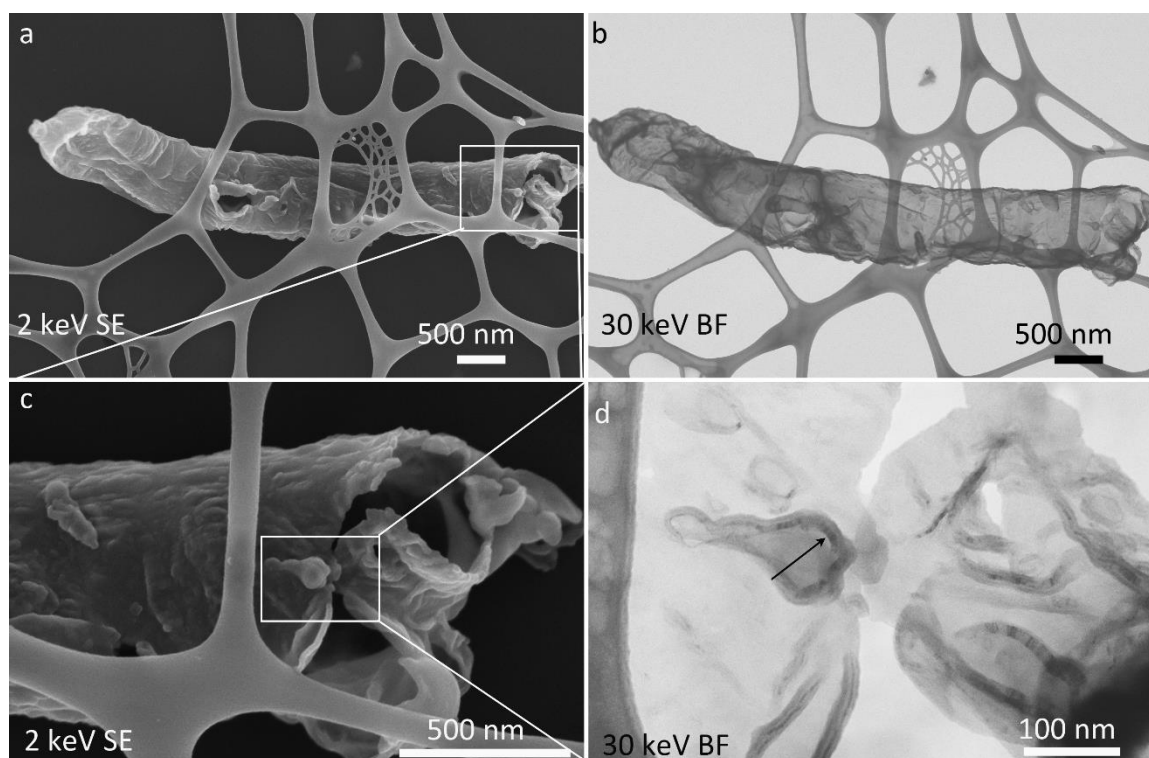
Figure 4.22. Correlative SEM/STEM imaging of a specimen with stacked graphene layers. (a) 2 keV SE-TLD image, (b) 30 keV BF-STEM image, (c) 2 keV SE-TLD image, (d) 30 keV BF-STEM image.
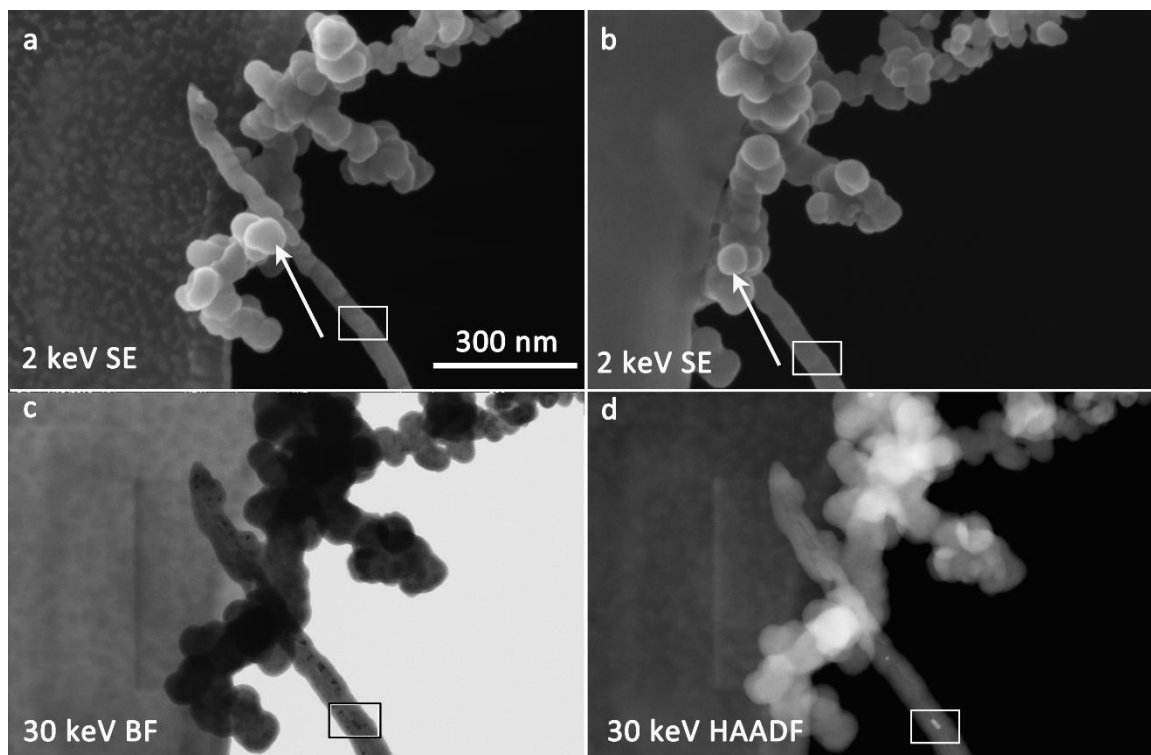
Figure 4.23. Correlative SEM/STEM imaging of a multi-walled CNT specimen. (a) 2 keV SE-TLD image, (b) 2 keV SE-TLD image, (c) 30 keV BF-STEM image, (d) 30 keV HAADF-STEM image. Scale bar in (a) applies to (b-d).

In addition to SEM/STEM imaging, TED patterns of CNTs were recorded using the on-axis CCD-camera. After Iijima first reported graphitic carbon tubes [89], TEM diffraction patterns were frequently taken for structure analysis of CNTs. CNTs consist of concentrically stacked graphene sheets leading to a rather complex reciprocal lattice. Based on the analysis of diffraction patterns, non-helical and helical CNTs can be distinguished [90] and the chirality can be explained [91]. Since the graphitic arrangement of the graphene planes is conserved in parts of the CNTs, the distance of the graphene planes can be obtained by the (000l) diffraction spots (l being an even number) [92] with $\vec{g}_{(000l)}$ perpendicular to the CNT tube axis. Additionally different sizes of hexagons are regularly shown in the diffraction patterns for single-walled CNTs. The smallest angle between the tube axis and the row of hexagons can be used for the description of the helicity of the tubes [90]. The inset in Fig. 4.24 (c) shows the (000l) Bragg reflection with a reciprocal lattice vector aligned perpendicular to the CNT tube axis. Although, it is difficult to deduce more information about the stacking of graphene layers for our multi-walled CNTs based on the TED pattern from Fig. 4.24 (c), there is great potential of

applying TED analyses on single-walled CNTs. One of the insets in Fig. 4.24 (d) shows a TED pattern of the catalyst particle (cf. marked by a circle) which is consistent with Ni. The second TED in Fig. 4.24 (d) shows the TED of the amorphous carbon film which shows diffused rings as expected for amorphous materials.

The CNT study illustrates the improvement of BF-STEM resolution in SEM and the benefits of correlative SEM/STEM imaging. Using either SEM or STEM would not have given the complete information on surface topography, three-dimensional CNT arrangement, inner structure and information on composition leaded material contrast changes. The TED patterns of CNTs illustrate that local information on the crystal structure can be obtained and distinction of crystalline and amorphous materials is straightforward.
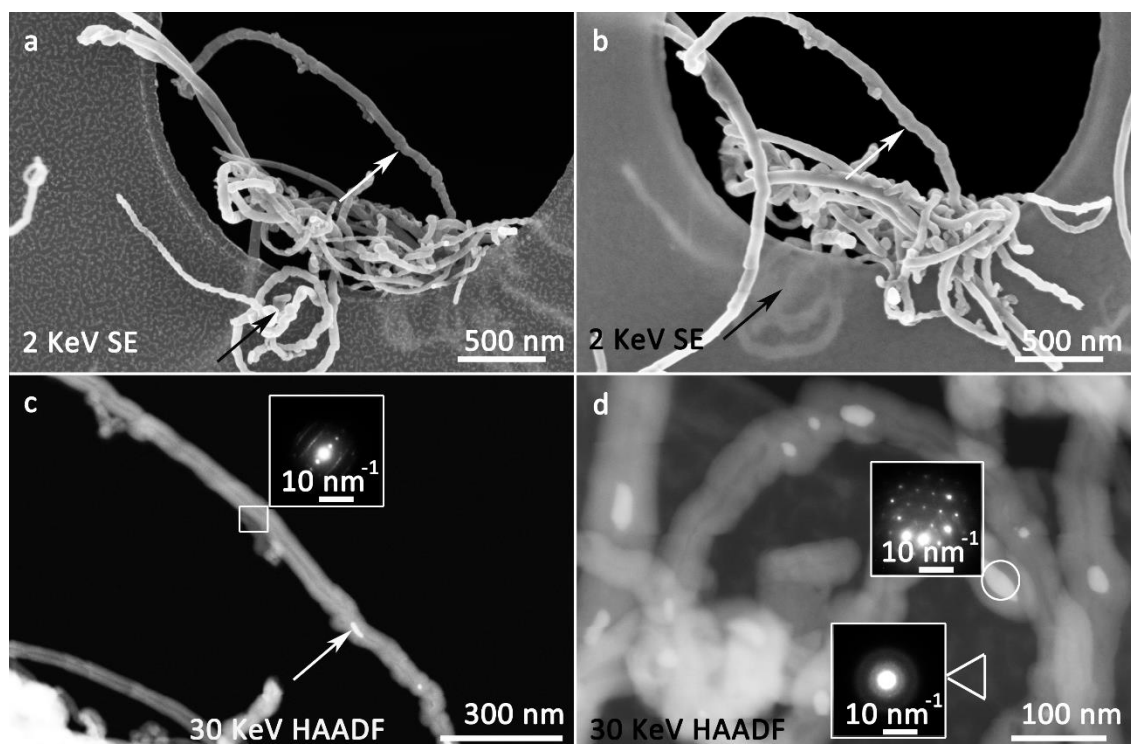
Figure 4.24. Correlative SEM/STEM imaging of a multi-walled CNT specimen. (a,b) 2 keV SE-TLD images and (c,d) 30 keV HAADF-STEM images. Superimposed pictures in (c,d) show TED patterns of the marked regions.

4.3.4 α-Fe$_2$O$_3$/ZnO

Correlative SEM/STEM was applied to investigate α-Fe$_2$O$_3$ NPs grown on ZnO. The sample was previously analyzed by TEM/EDXS. Hence, it was known that the area in Figs. 4.25 (a,b) are α-Fe$_2$O$_3$ particles which were successfully grown on the shell of ZnO, while Figs. 4.25 (c,d) show the raw materials (ZnO rod with few α-Fe$_2$O$_3$ particles). In the SE images Figs. 4.25 (a,c), the topography of the small α-Fe$_2$O$_3$ particles is displayed clearly (e.g. the regions marked by rectangles). The ZnO surface in Fig. 4.25 (a) is covered by the agglomeration of α-Fe$_2$O$_3$ particles while the original ZnO particle in Fig. 4.25 (c) shows smooth surface. Besides, the ZnO in Figs. 4.25 (a,b) shows a hollow structure as marked by white arrows. However, the ZnO rod marked by the arrow in Fig. 4.25 (c) is not hollow according to the constant BF-STEM intensity for ZnO in Fig. 4.25 (d). This indicates that when α-Fe$_2$O$_3$ and ZnO grew together, the structure of the ZnO was changed. This example emphasizes the convenience of using correlative SEM/STEM to detect hollow structures of nanotubes.
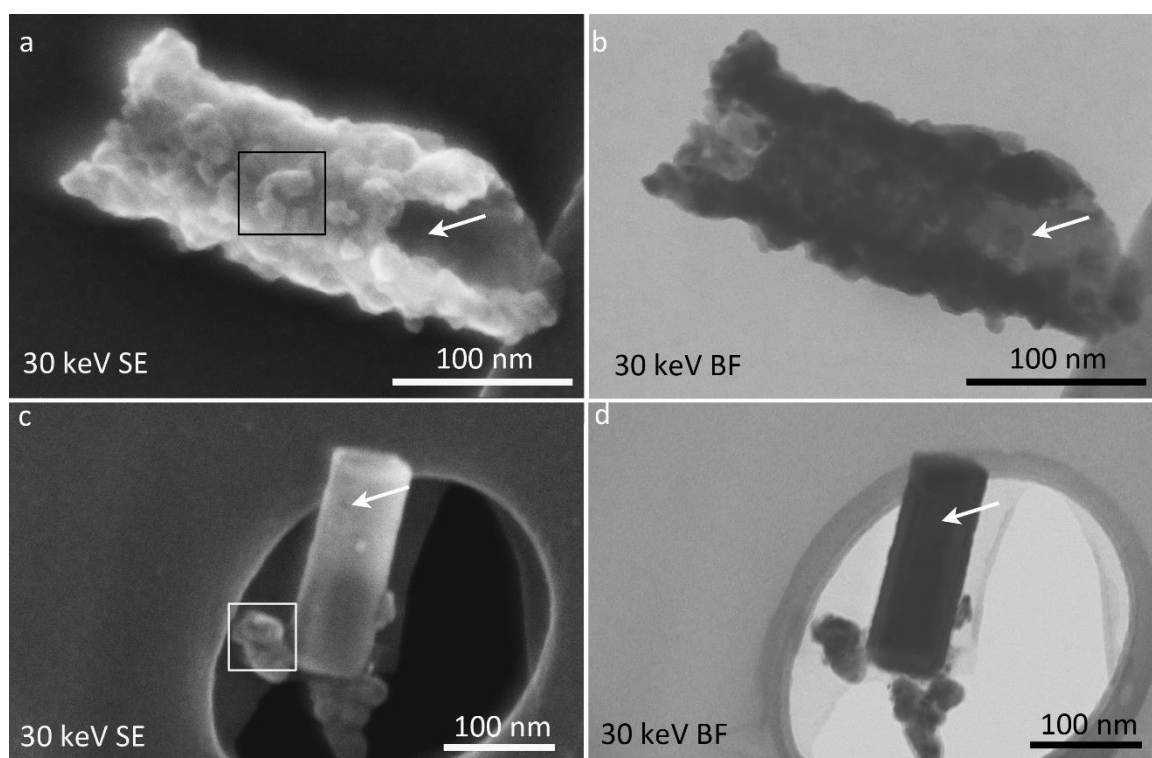
Figure 4.25. (a) 30 keV SE-TLD image of α-Fe$_2$O$_3$/ZnO tubes, (b) 30 keV BF-STEM image of α-Fe$_2$O$_3$/ZnO tubes, (c) 30 keV SE-TLD image of α-Fe$_2$O$_3$ and ZnO tubes, (d) 30 keV BF-STEM image of α-Fe$_2$O$_3$ and ZnO tubes.

4.3.5 Lattice fringe imaging of NPs

Cerium dioxide NPs (CeO_2) are interesting for application in fuel cells and microelectronics or as catalysts for heterogeneous catalytic reactions [93, 94] and were also investigated by correlative SEM/STEM (cf. Fig. 4.26).

The SE image Fig. 4.26 (a) shows an agglomerate of small CeO_2 NPs. Here, surface details of the NPs are obscured due to contamination. However, the application of STEM allows to distinguish contamination from NPs and reveals the real (projected) shape of the CeO_2 NPs as shown in Figs. 4.26 (b,c). The size of the NPs is measured to be approximately 13 nm in the HAADF image whereas it is impossible to obtain this information by SE SEM considering contamination. This indicates that even though SE topography contrast is beneficial in many cases, caution should be paid because the properties of object in SE images are prone to be modified by contamination. Lattice fringes of CeO_2 NP were resolved by low-keV BF-STEM imaging as presented in Fig. 4.26 (d). The obtained lattice parameter of 3.3 Å agrees well with the $(11\bar{1})$ lattice plane distance in CeO_2 [95, 96].
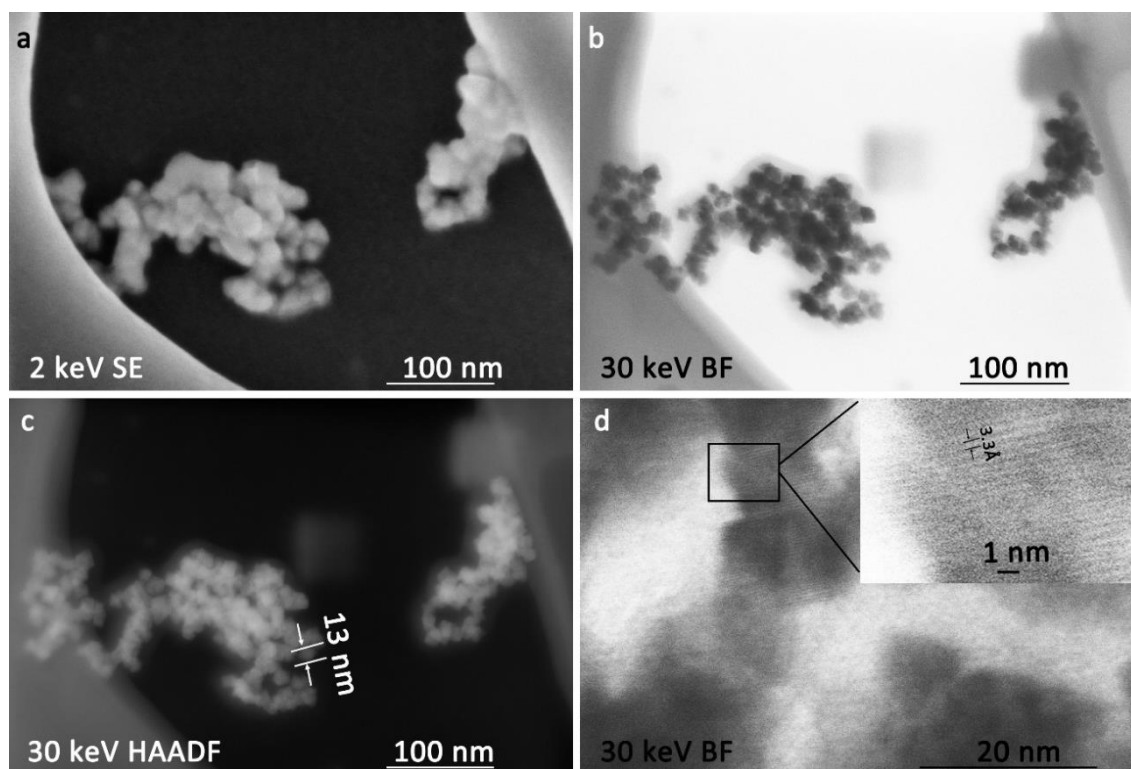
Figure 4.26. Correlative SEM/STEM imaging of CeO_2 NPs. (a) 2 keV SE-TLD image,

(b) 30 keV BF-STEM image, (c) 30 keV HAADF-STEM image, (d) 30 keV BF-STEM image.

Titanium dioxide (TiO_2) NPs are considered as one of the most interesting materials for photocatalysis [97]. Correlative SEM/STEM images in Fig. 4.27 show that the TiO_2 NPs are also covered with carbon contamination. STEM images in Figs. 4.27 (b,c) reveal the real shape and size of the small NPs while the SE image Fig. 4.27 (a) mainly shows the carbon contamination layer on the sample. Lattice fringes with a distance of 3.5 Å from TiO_2 NPs could also be imaged clearly (c.f. inset in Fig. 4.27 (d)) which agrees with the (Ti-Ti) lattice distance of $(10\bar{1})$ planes in anatase discussed by Horn [98]. Since SE topography of the sample is affected largely by contamination, sample/chamber cleaning methods such as plasma cleaning of the sample and SEM chamber are favorable [43]. Images of plasma-cleaned TiO_2 NPs are shown in Fig. 4.28. Without the contamination layer, the shape of TiO_2 NPs can now be clearly recognized as opposed to the carbon-contaminated sample surface in Fig. 4.27 (a).
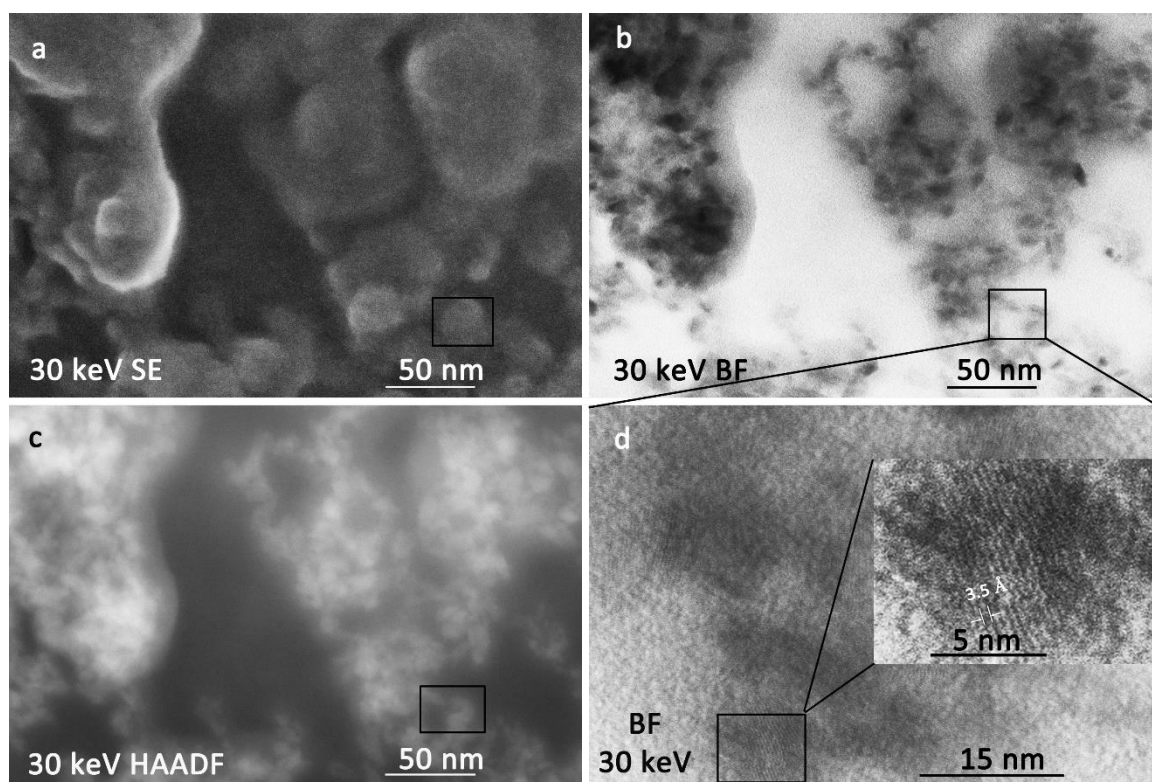
Figure 4.27. Correlative SEM/STEM imaging of TiO_2 NPs. (a) 30 keV SE-TLD image, (b) 30 keV BF-STEM image, (c) 30 keV HAADF-STEM image, (d) 30 keV BF-STEM image.
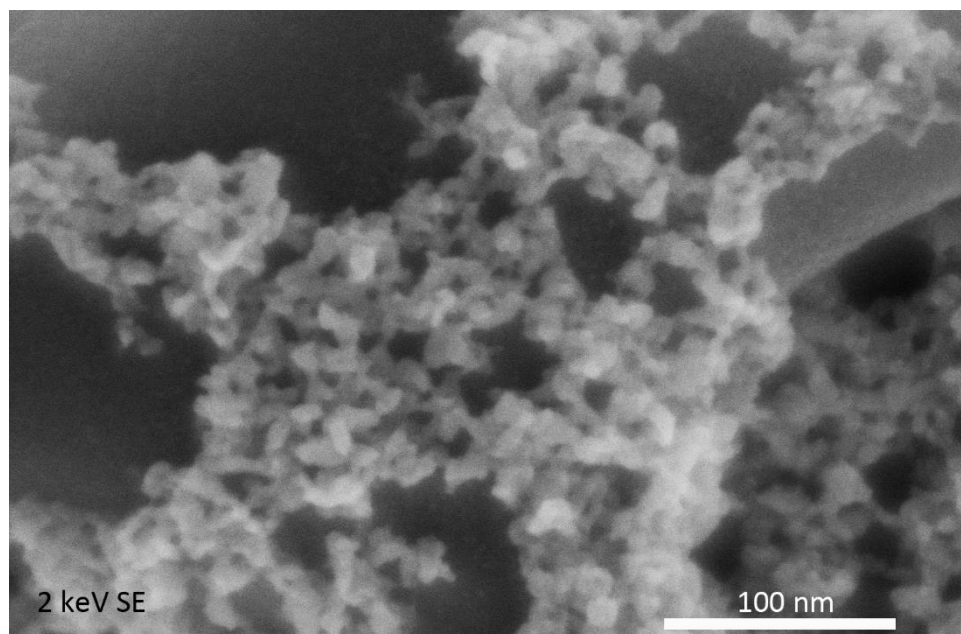
Figure 4.28. SE-TLD imaging of TiO_2 NPs at 2 keV. This time, no contamination layer on the top of the TiO_2 NPs was formed.

4.3.6 NiIr$_4$ NPs

Another type of NPs is nickel iridium (NiIr$_4$) bimetallic NPs which possesses a high catalytic activity for hydrogenation reactions [99]. The advantage of combining different signals for the analysis of NiIr$_4$ NPs in a SEM will be demonstrated. NiIr$_4$ NPs were analyzed with a particular focus on comparing SE images taken with different electron energies and the advantages of in-lens BSE detectors for analyzing their shapes.

Fig. 4.29 displays SEM/STEM overview images of the same sample region taken with 2 keV and 30 keV, respectively. Obviously, the SE image taken with 2 keV Fig. 4.29 (a) shows better resolution and higher contrast of the NPs compared with 30 keV SE image Fig. 4.29 (b). This is a result of decreasing SE yield with increasing electron energy. The SE1s, which are generated close to the incident electron beam, dominate in Fig. 4.29 (a) with respect to other SE-types (SE2-SE5) leading to the bright contrast for the NiIr$_4$ NPs and high resolution of small topography features. In contrast, the fraction of SE2 increases considerably at 30 keV due to the larger interaction volume for high electron beam energy and hence, results in a loss of resolution as can be seen in Fig. 4.29 (b). STEM images in Figs. 4.29 (c,d) clearly display all NiIr$_4$ NPs including those located below the carbon film which could not be observed by the SE images in Figs. 4.29 (a,b).

Fig. 4.30 represents magnified images from the area marked by white rectangle in Fig. 4.29 (c). As shown by the arrow in Fig. 4.29 (c), the area is covered by a contamination layer. Using 2 keV SE imaging as depicted in Fig. 4.30 (a), the surface details (white contamination dots marked by white arrow) are recognized on the $NiIr_4$ NPs because the SE1 signal dominates and only a comparably small number of SE2s are generated due to the small interaction volume at 2 keV. BSE images (Figs. 4.30 (b,c)) taken with MD and ICD detectors do not show the small surface features but reveal more clearly the NP shapes which are characterized by the sharp edges and corners. The sharp edge marked by the black arrow in the BSE image taken with ICD (Fig. 4.30 (c)) is slightly clearer than that in the BSE image acquired by the MD (Fig. 4.30 (b)). Considering that ICD is located above the MD in the electron column, firstly the backscattered electrons obtained by ICD can be assumed to have less energy loss than those acquired by MD. The second reason could be that BSEs reaching ICD come from a smaller sample region (sharp edge) compared with those reaching MD.
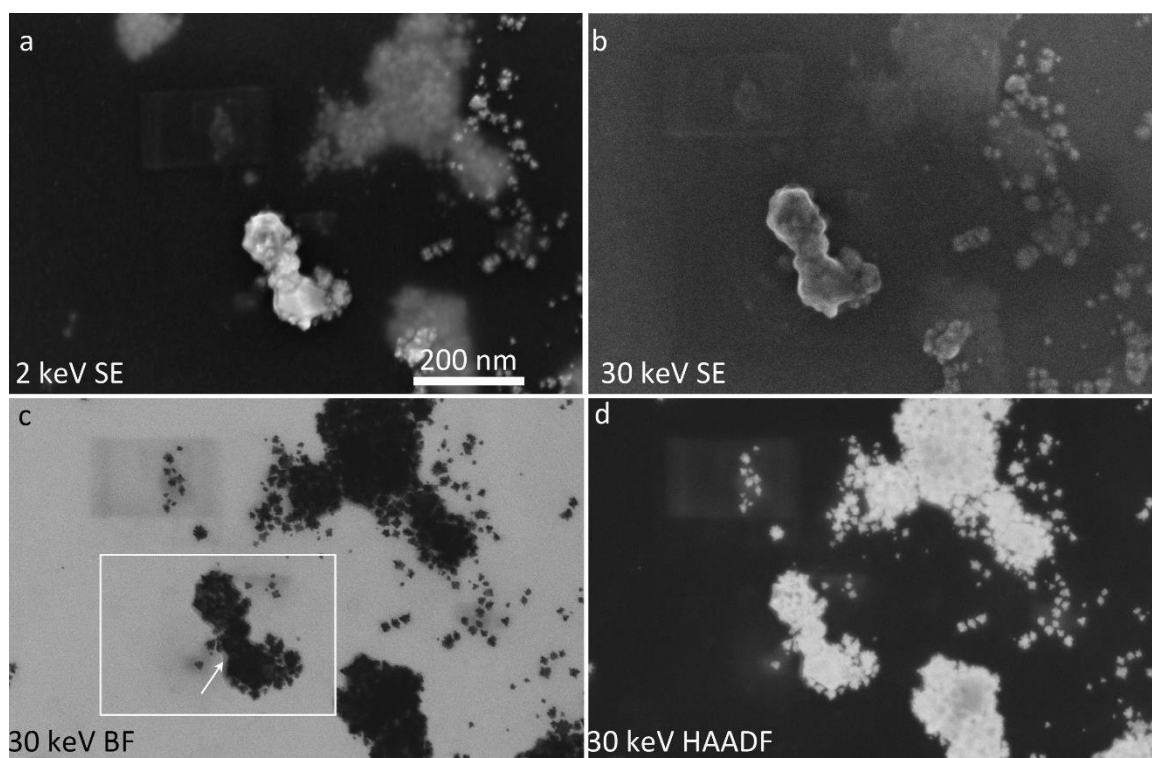
Figure 4.29. Correlative SEM/STEM imaging of $NiIr_4$ NPs. (a) 2 keV SE-TLD image, (b) 30 keV SE-TLD image, (c) 30 keV BF-STEM image, (d) 30 keV HAADF-STEM image. Scale bar in (a) applies to (c-d).
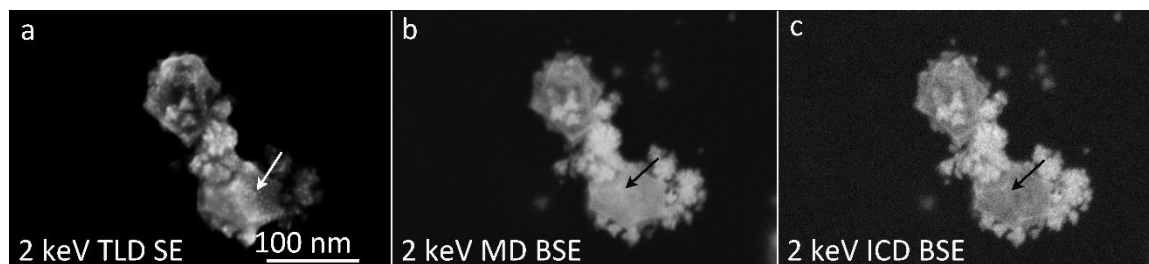
Figure 4.30. SE/BSE imaging of NiIr$_4$ NPs. (a) 2 keV SE-TLD image, (b) 2 keV BSE-MD image, (c) 2 keV BSE-ICD image. Scale bar in (a) applies to (b,c).

4.3.7 Core-shell NPs
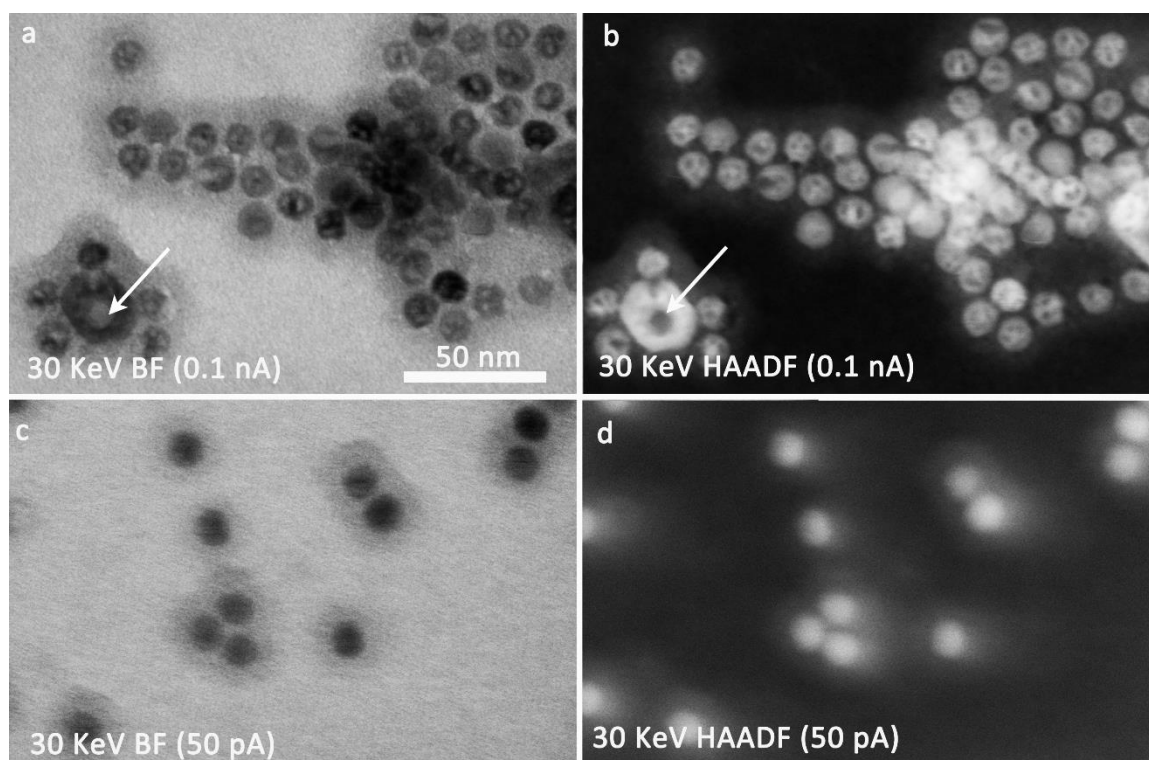
Figure 4.31. Low-keV STEM imaging of NaGdYbErF@NaYGdYbErF core-shell NPs. (a) 30 keV BF-STEM image, (b) 30 keV HAADF-STEM, (c) 30 keV BF-STEM image, (d) 30 keV HAADF-STEM image. Scale bar in (a) applies to (b-d).

Another nanomaterial NaGdYbErF@NaYGdYbErF core-shell NPs were characterized with low-keV STEM. This material has the capability to upconvert low-energy photons into high-energy photons and can be applied in the fields of energy harvesting, medical imaging or solid-state lighting [100]. These core-shell NPs consist of beam-sensitive

materials and low-keV STEM was applied for studying their sensitivity to different electron-beam energies and beam currents.
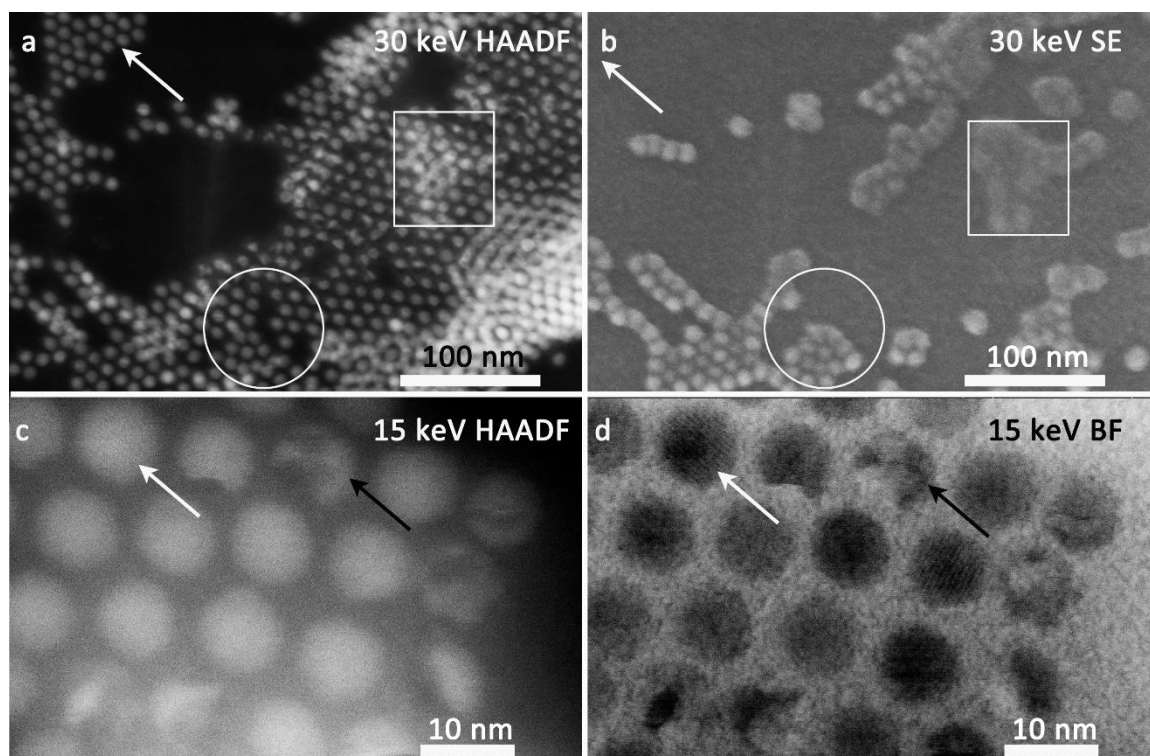
Figure 4.32. Low-keV STEM/SEM imaging of NaGdYbErF@ NaYGdYbErF core-shell NPs. (a) 30 keV HAADF-STEM image, (b) 30 keV SE-TLD image, (c) 15 keV HAADF-STEM image, (d) 15 keV BF-STEM image.

Fig. 4.31 and Fig. 4.32 show the beam-sensitivity of the core-shell NPs at low energies. The asymmetrical pores (marked by arrows) in the NPs in Figs. 4.31 (a,b) show that imaging with 0.1 nA and 30 keV largely destroys the core-shell structure of the NPs. As the NPs show significant charging, the damage mechanism is assumed to be mainly radiolysis, which is regarded as being proportional to the time and the energy dose [101]. By reducing the beam current to 50 pA, the NPs can be imaged at 30 keV without obvious damage (Figs. 4.31 (c,d)). In addition, the rectangle in the 30 keV HAADF image Fig. 4.32 (a) displays increased brightness as a result of stacking of NPs in comparison to an area where NPs are less stacked (cf. circle in Fig. 4.32 (a)). The SE image in Fig. 4.32 (b) indicates that the increase in brightness is also caused by accumulation of a contamination layer at the surface. As discussed in chapter 2, radiolysis damage can be increased by secondary processes. With a decreased beam energy (15 keV), the number of scattering

processes increases. Therefore, beam damage to the core-shell samples is shown to be more severe in Figs. 4.32 (c,d) (e.g., NPs marked by black arrows) compared with Figs. 4.31 (c,d). Even though contamination and beam damage were observed, 0.6 nm lattice fringes for this core-shell material [100] were still resolved as marked by the white arrow in Fig. 4.32 (d) even at 15 keV. However, the core and shell parts of the sample were not able to be distinguished with 30/15 keV STEM imaging. In order to differentiate the core and shell (average atomic number 44 and 33), HAADF intensity simulations can be carried out in order to find an optimized electron energy for a maximum HAADF-STEM contrast difference between the core and shell materials.

4.3.8 Mesoporous silica
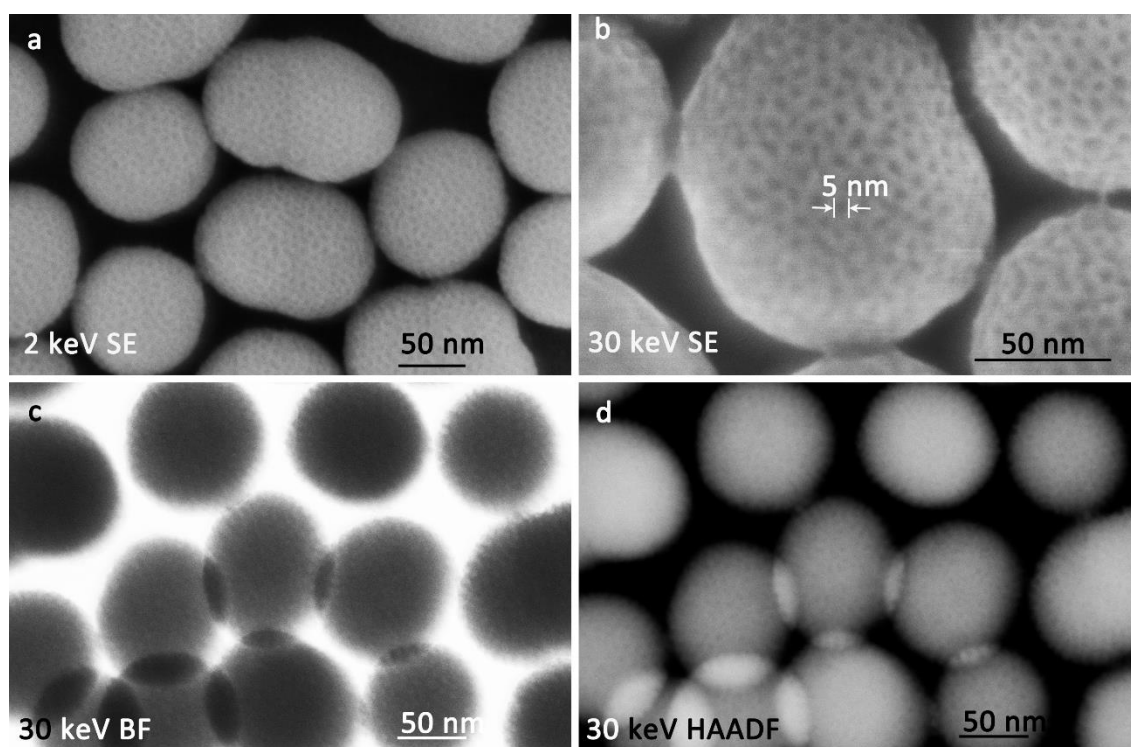
Figure 4.33. Correlative SEM/STEM imaging of mesoporous silica nanospheres. (a) 2 keV SE-TLD image, (b) 30 keV SE-TLD image, (c) 30 keV BF-STEM image, (d) 30 keV HAAD-STEM image.

Similarly, the effects of electron energy on SE imaging for mesoporous silica nanospheres were studied. Owing to the high surface area and large pore volume, mesoporous silica-based materials have great potential for nanodrug delivery applications [102].

Surprisingly, the small pores on the surface of silica can be characterized clearly with SEs taken at both 2 keV and 30 keV, respectively (Figs. 4.33 (a,b)). Usually the SE yield is lower at high energy, one might predict that the small pores on silica could not be visualized with 30 keV SE. However, the number of SE2 is reduced more than the number of SE1 at 30 keV, mostly due to the low average atomic number of silica. Furthermore, the small sizes of the particles supported on a thin carbon film lead to a small interaction volume at 30 keV. The contrast of pores with 5 nm diameter in BF- and HAADF-STEM images Figs. 4.33 (c,d) is faint, which indicates the small size of the pores in electron-beam direction leading to a small effective thickness change.
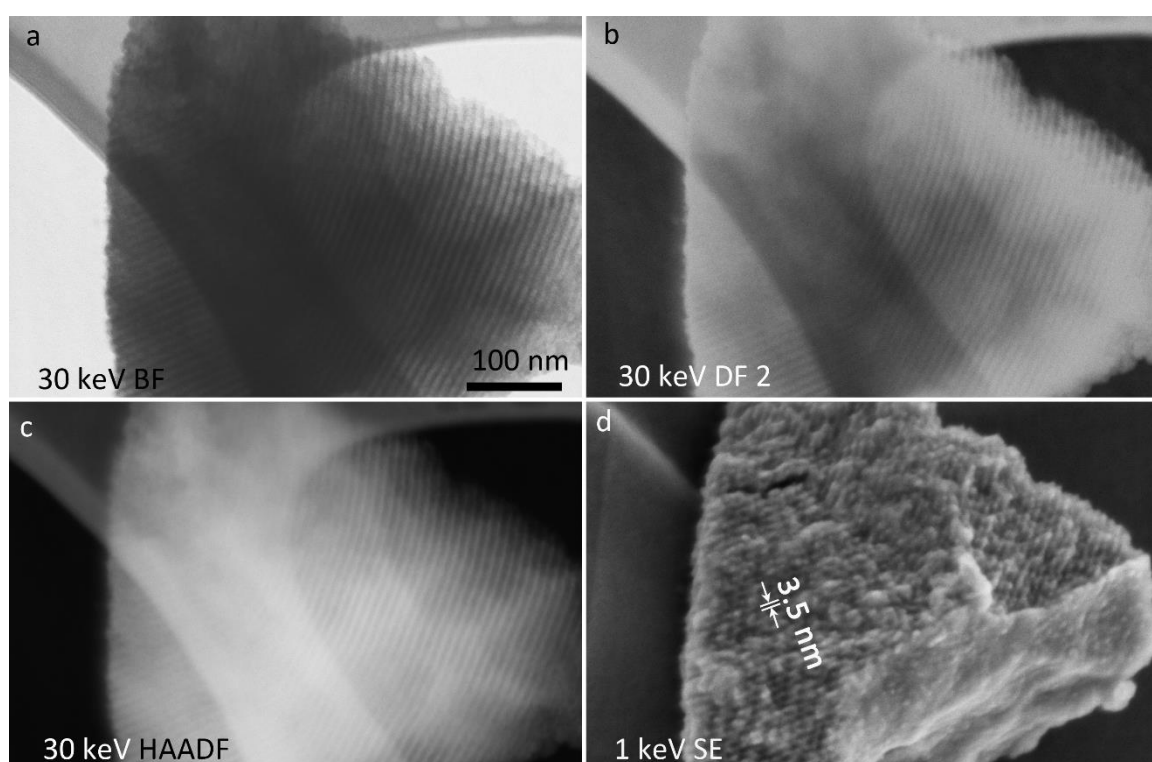
Figure 4.34. Correlative SEM/STEM imaging of KIT-6 material. (a) 30 keV BF-STEM image, (b) 30 keV DF_2-STEM image, (c) 30 keV HAADF-STEM image, (d) 1 keV SE-TLD image. Scale bar in (a) applies to (b-d).

KIT-6 is the second type of silica material examined by correlative SEM/STEM. KIT-6 is usually applied as support for catalyst NPs used in liquid fuels [103]. The well-ordered pore structure of KIT-6 is shown clearly by the STEM images in Figs. 4.34 (a-c) and the SE SEM topography image (Fig. 4.34 (d)). The contrast of the highly organized tunnels in the STEM images Figs. 4.34 (a-c) indicates the large depth of these structures. The

topography contrast in Fig. 4.34 (d) exhibits the wall thickness between the tunnels (3.5 nm) in KIT-6.

4.3.9 Au NPs
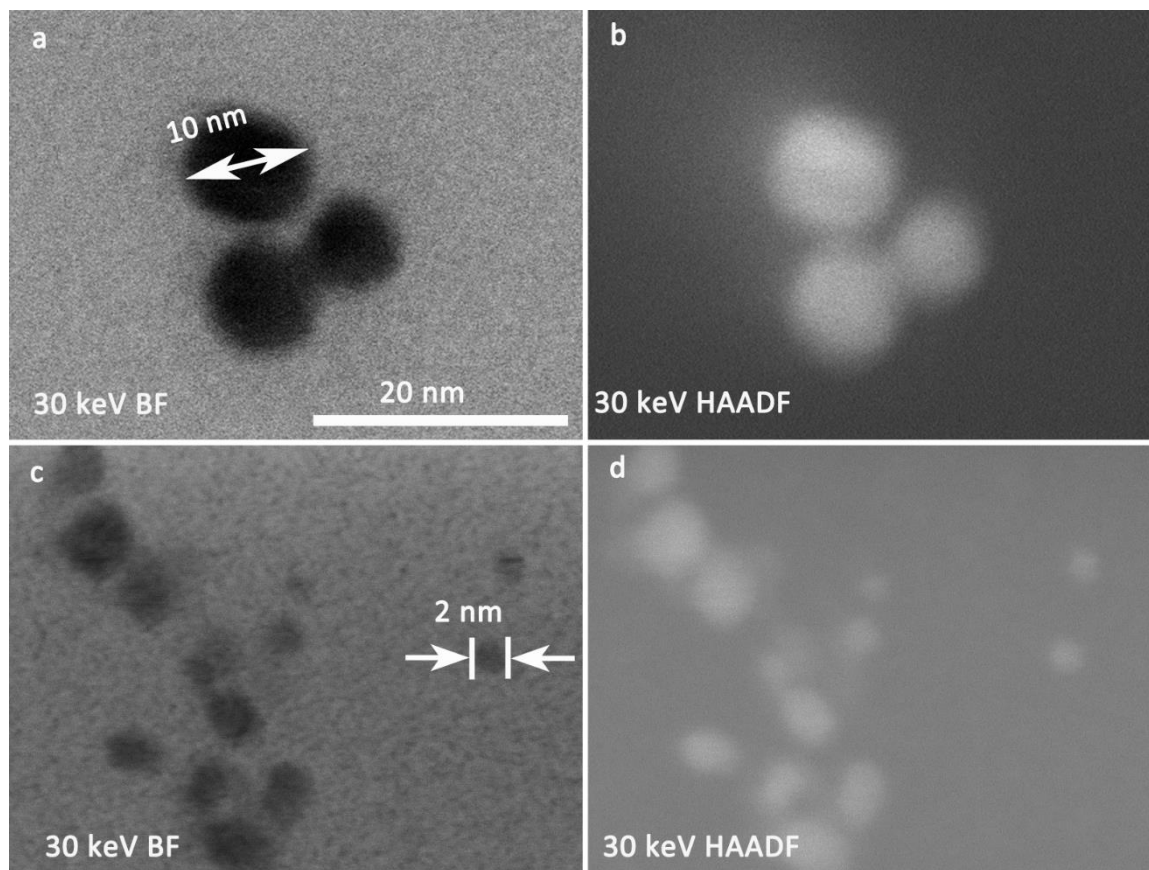
Figure 4.35. Low-keV imaging of Au NPs. (a) 30 keV BF-STEM image, (b) 30 keV HAADF-STEM image, (c) 30 keV BF-STEM image, (d) 30 keV HAADF-STEM image. Scale bar in (a) applies to (b-d).

Finally, results from the investigation of commercial gold nanoparticles (Au NPs) are presented which are frequently used in biological and medical applications due to their biocompatibility [104]. In this work, Au NPs were investigated to test the STEM resolution of the Helios Nanolab G4 FX with respect to resolving small NPs. Au NPs with different diameters are shown in Fig. 4.35. Figs. 4.35 (a,b) show an agglomeration of 10 nm Au NPs while Figs. 4.35 (c,d) show Au NPs with diverse sizes. Even an Au NP with 2 nm diameter can be resolved clearly by 30 keV BF and HAADF-STEM imaging demonstrating that STEM in SEM is suitable for size quantification of small NPs.

4.3.10 Xonotlite and tobermorite
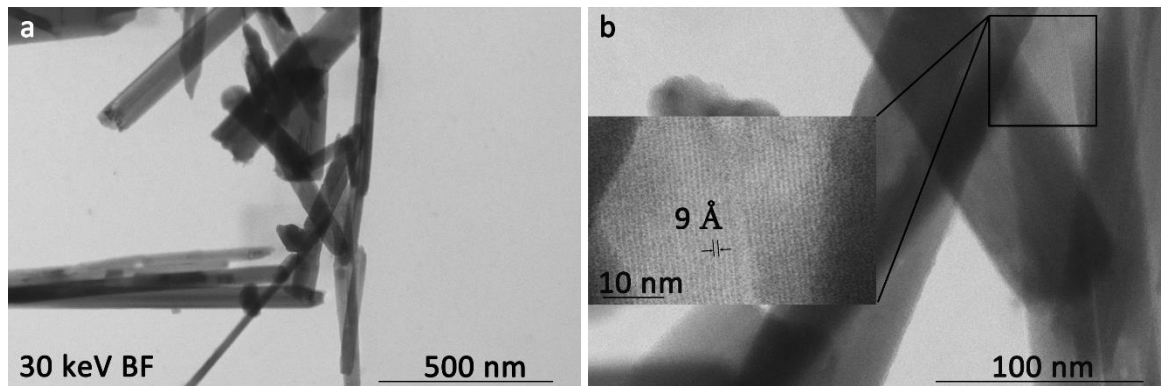
Figure 4.36. Low-keV STEM imaging of xonotlite. (a) 30 keV BF-STEM image, (b) 30 keV BF-STEM image [65].
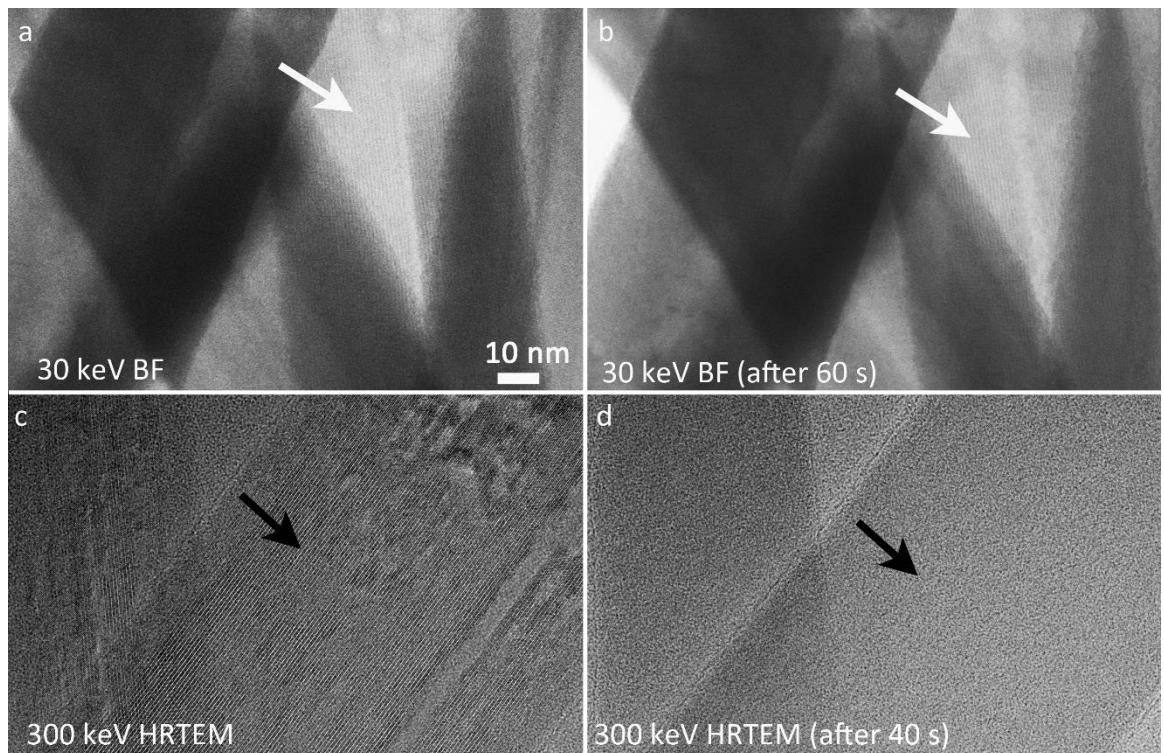
Figure 4.37. Low-keV STEM/HRTEM imaging of xonotlite. (a) 30 keV BF-STEM image, (b) 30 keV BF-STEM image, (c) 300 keV HRTEM image, (d) 300 keV HRTEM image. Scale bar in (a) applies to (b-d).

Xonotlite ($Ca_6Si_6O_{17}(OH)_2$) and tobermorite ($Ca_5Si_6O_{22}H_{10}$) belong to the class of calcium silicate hydrate (C-S-H) compounds which are extremely sensitive to knock-on damage. They often show poor crystallinity and can be found in cement materials [105]. Due to their low thermal conductivity, low density and environmental friendliness, they

are widely used as ultralight heat-insulating material [106]. C-S-H compounds were reported to be highly susceptible towards beam damage in high-energy TEM [107]. Therefore, low-keV STEM is especially suitable for the investigation of C-S-H materials.

Fig. 4.36 (a) presents xonotlite needles dispersed on a thin carbon film. The magnified region (Fig. 4.36 (b)) reveals lattice fringes with a distance of 0.9 nm which is in good agreement with the maximum lattice-plane distance of 0.83 nm in this material [65].

The same xonotlite sample was also investigated at 300 keV (Figs. 4.37 (c,d)) in a transmission electron microscope (FEI Titan) to assess the beam sensitivity of (C-S-H) compounds. Figs. 4.37 (c,d) are HRTEM images taken at 300 keV while Figs. 4.37 (a,b) were taken by low-keV STEM (Helios) for comparison. The lattice fringes marked by the white arrow can be imaged clearly in Fig. 4.37 (a). After 60 seconds of continuously scanning of the electron beam on the sample, another BF image was recorded (Fig. 4.37 (b)) which still shows lattice fringes. In comparison, the HRTEM in Fig. 4.37 (c) also shows lattice fringe contrast of xonotlite. However, the lattice fringes disappear (Fig. 4.37 (d)) within only 40 seconds due to electron-beam-induced amorphization. This demonstrates the advantage of low-keV STEM for investigation of materials which are extremely sensitive to knock-on damage.

Figure 4.38. Low-keV STEM imaging of the same tobermorite region. (a) 30 keV SE-TLD image, (b) 30 keV BF-STEM image, (c) 30 keV HAADF-STEM image. Scale bar in (a) applies to (b,c).

Correlative SEM/STEM images of tobermorite, another (C-S-H) compound, are displayed in Fig. 4.38. The SE image in Fig. 4.38 (a) reveals the lamella-type nature of tobermorite. Based on the BF and HAADF images in Figs. 4.38 (b,c), the number of lamellae can be determined due to the pronounced thickness-sensitivity of the low-keV STEM intensity. The correlative SE image (Fig. 4.38 (a)) shows in addition the topographical arragement of the different lamellae which is not obvious from STEM

images. Even though the largest lattice-plane distance is 1.4 nm [108], it was not possbile to resolve these lattice planes because they are oriented perpendicular to the electron beam. Nevertheless, tobermorite shows a reasonable stability under the illumination of the electron beam in the SEM.

4.4 Other solid-state materials

Within this subchapter, further analytical capabilities of modern SEMs will be presented by the investigation of different perovskite-type materials. This includes EDXS for chemical analysis and on-axis t-EBSD for crystal structure/orientation analysis.

Recently, all-solid-state lithium ion batteries have attracted considerable attention as next-generation energy storage systems [109]. In the following, a study of the solid electrolyte $Li_{3x}La_{2/3-x}TiO_3$ (LLTO) is presented. In general SEM is widely used for the investigation of solid electrolytes to gain new insights into the electrolyte's microstructure like grain size, porosity and secondary phases. The studied LLTO solid electrolyte was sintered at 1400 °C and fabricated by conventional TEM sample-preparation techniques. It was investigated with the Strata 400S using BSE imaging and STEM-EDXS for composition analysis.

Fig. 4.39 (a) shows a BSE image of the LLTO solid electrolyte TEM specimen. In the image dark gray and black features are visible. Black regions correspond to pores (white arrow) in the material and dark regions represent secondary phases (black arrow). Due to the darker BSE intensity of the secondary phase, one can deduce that the average atomic number $\bar{Z}$ is lower compared to the LLTO matrix as the BSE yield increases with $\bar{Z}$ (Eq. (12), chapter 2). By increasing the image contrast, individual grains of the material become visible as depicted in Fig. 4.39 (b). As previously discussed for BSE imaging, the contrast arises due to the grain-orientation dependence of electron channeling. In addition to pore size, grain-size data and the position of secondary phases with respect to the individual grains can be extracted. According to Figs. 4.39 (a,b), it is obvious that secondary phases are preferentially located at grain-boundary triple points. By employing EDXS in the Strata, the elemental composition of one of the precipitates was investigated. A 30 keV BF-STEM image displaying one precipitate is shown in Fig. 4.40 (a). EDXS data in Figs. 4.40 (b-d) suggests that the secondary phase in LLTO is rich in both Ti and O but poor in La compared to the matrix. This is in agreement with the lower BSE yield

of the secondary phase as the atomic number of Ti (Z=22) and O (Z=8) is much lower compared to La (Z=57).
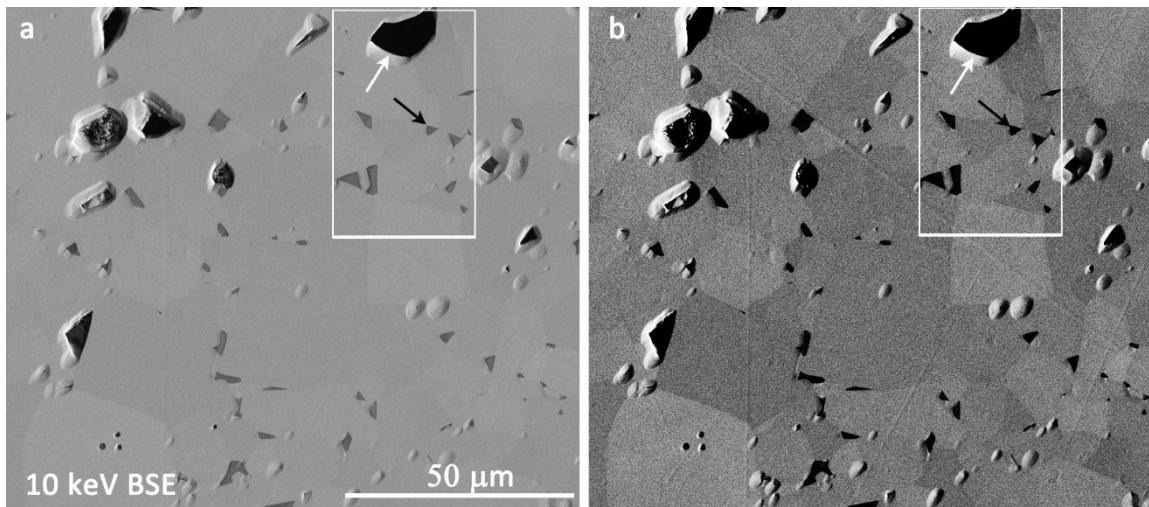
Figure 4.39. (a,b) 10 keV BSE-TLD images of the same region of a LLTO specimen at different contrast settings. Scale bar in (a) applies to (b).
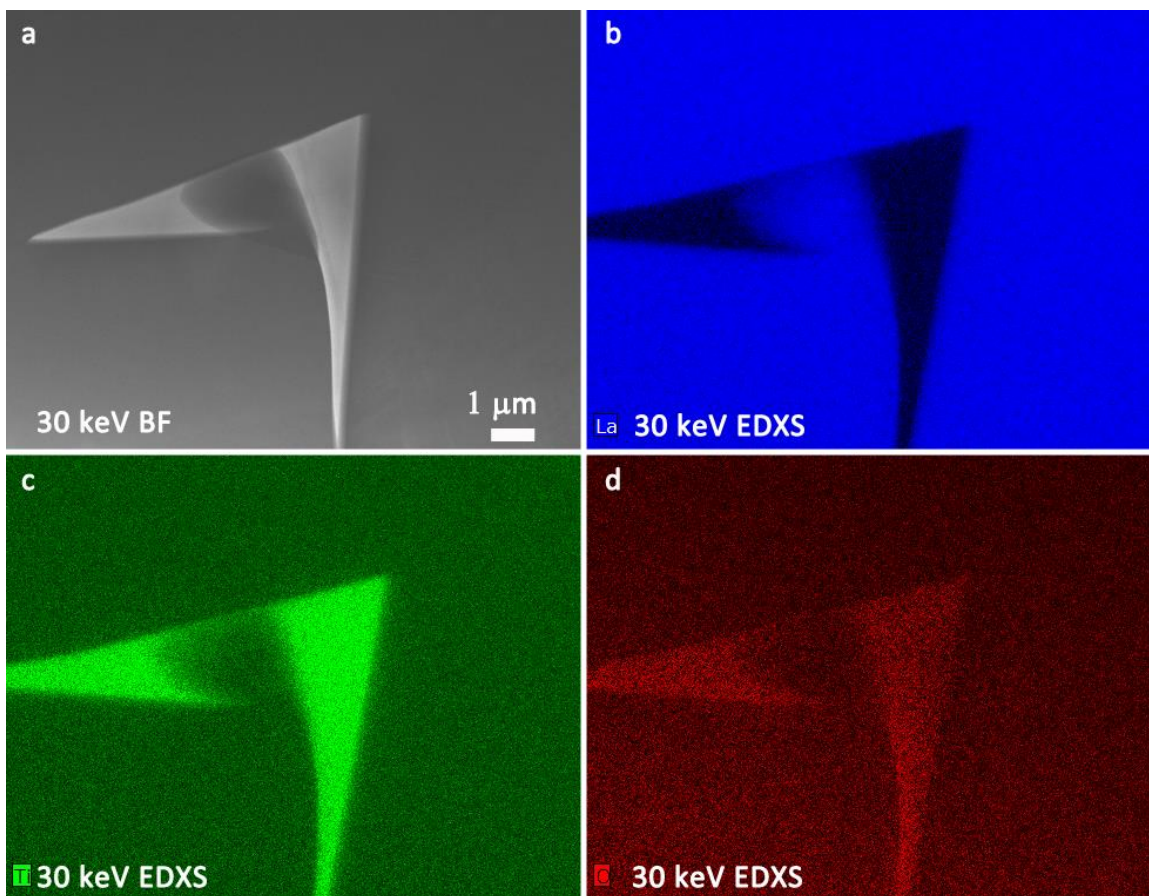
Figure 4.40. Low-keV STEM/EDXS mapping of LLTO. (a) 30 keV BF-STEM image and EDXS maps of (b) La, (c) Ti and (d) O. Scale bar in (a) applies to (b-d).
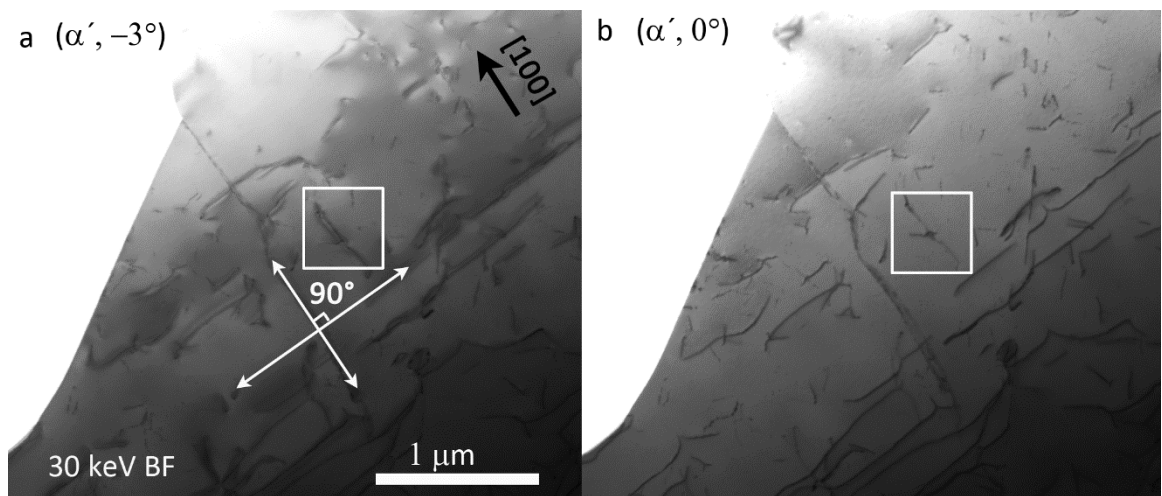
Figure 4.41. (a-b) 30 keV BF-STEM images of a $SrTiO_3$ specimen under different tilt angles (cf. insets in (a,b)). Scale bar in (a) applies to (b).

The next example concerns strontium titanate ($SrTiO_3$), an important ceramic material, which is also often used as a substrate for epitaxial oxide growth. The investigated $SrTiO_3$ wafer was used as a substrate for a $SrTiO_3/Al_2O_3$ heterostructure which forms a two-dimensional electron gas at the interface. It also shows anisotropic electronic transport properties which are suggested to result partly from the lattice dislocations [110]. The study was performed in the Strata 400S. This instrument is not equipped with a CCD-camera for the acquisition of TED patterns and only one tilt axis is available to change the specimen orientation. Nevertheless, dislocation imaging is demonstrated to be possible.

Fig. 4.41 displays BF-STEM images showing numerous dislocations in $SrTiO_3$ prepared by the conventional TEM sample-preparation procedure (c.f. chapter 3, 3.2.2). Interestingly, the dislocation lines are mainly along two directions (marked by white arrows in Fig. 4.41 (a)). One direction is parallel to the [100] $SrTiO_3$ wafer growth direction and the other is oriented perpendicular to the substrate normal. The high concentration of dislocations will cause charge carrier scattering, leading to an increase of resistance in the perpendicular current direction [110]. Although it is impossible to obtain the orientation of the dislocation Burgers vectors with Strata, the change of diffraction contrast of the dislocations at different tilting angles can be observed (Figs.

4.41 (a,b)). By changing the α' tilt angles from -3° to 0° (cf. Figs. 4.41 (a,b)), the contrast of the dislocation marked by the rectangle changes. The change in diffraction contrast can be utilized for defect characterization. However, this requires an on-axis CCD-camera and double-tilt specimen holder to set up well-defined two-beam conditions. Dislocation analysis performed in the Helios Nanolab G4 FX is presented in chapter 5.

$SrTiO_3$ is also widely applied as functional ceramic material [111]. The properties of $SrTiO_3$ are strongly determined by its microstructure, especially the grain-size, space-charge regions at grain boundaries and grain orientations. By doping $SrTiO_3$ with Fe ($SrTi_{1-x}Fe_xO_{3-\delta}$), the resulting microstructure can be tuned according to desired properties [111].

The Helios Nanolab G4 FX was used for studying the $SrTi_{1-x}Fe_xO_{3-\delta}$ sample. BF-STEM (Fig. 4.42 (a)) displays the grain structure in this sample. With the exception of the sharp grain boundaries, there are dark contrast features that do not coincide with grain-boundaries (cf. Fig. 4.42 (a), white arrow). This is associated with a pronounced surface topography that can be clearly observed in the SE SEM image Fig. 4.42 (b). Surface topography can be traced back to the TEM sample preparation because argon ion milling can cause the formation of pits at the sample surface. The white line features in the SE image can be attributed to charging because $SrTiO_3$ is an insulating material.

Due to the small grain sizes in $SrTi_{1-x}Fe_xO_{3-\delta}$, EBSD cannot be performed to extract grain-orientation and grain-size data. However, by recording transmission Kikuchi patterns acquired from TEM specimens using a conventional EBSD camera as off-axis detector (t-EBSD), the lateral resolution can be increased significantly [27]. Due to the off-axis detection and the unfavorable position of the EBSD camera, the intensity of the transmitted Kikuchi pattern is low and also appears strongly distorted on the detector [70]. Recently, the first on-axis t-EBSD detector became available allowing to record on-axis transmission Kikuchi patterns without distortion and support high signal-to-noise ratio at high lateral resolution. Fig. 4.42 (c) shows a t-EBSD map acquired by an on-axis CCD-camera (on-axis t-EBSD). The on-axis t-EBSD map displays the color-coded orientations (Euler angles) of grains. The $SrTi_{1-x}Fe_xO_{3-\delta}$ sample contains agglomerated small grains (around 70 nm size) such as those marked by the circle and large grains (e.g. marked by the white arrow) in Fig. 4.42 (c). On-axis t-EBSD maps are helpful for quantification of

grain sizes (cf. histogram of grain sizes in Fig. 4.42 (d)). A large percentage of grains is shown to have a diameter below 200 nm for the $SrTi_{1-x}Fe_xO_{3-\delta}$ sample.
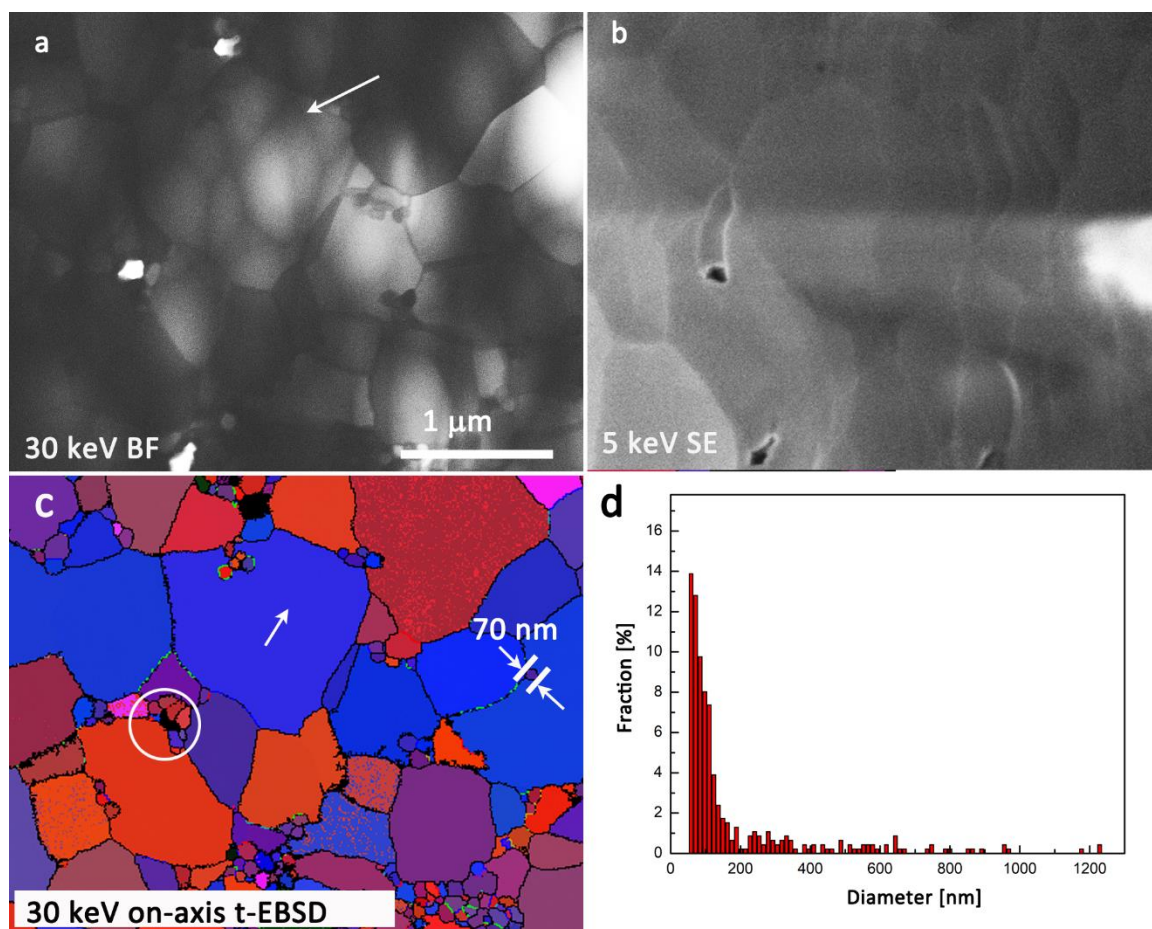
Figure 4.42. Correlative SEM/STEM/t-EBSD imaging of $SrTi_{1-x}Fe_xO_{3-\delta}$. (a) 30 keV BF-STEM image, (b) 5 keV SE-TLD image, (c) 30 keV on-axis t-EBSD image, (d) grain-size distribution in (c). Scale bar in (a) applies to (b,c).

In summary, channeling contrast from SE and BSE imaging in a SEM can be utilized to distinguish grains in crystalline materials and extract statistically relevant data even far away from the electron transparent region of a TEM specimen. On-axis t-EBSD is useful for the quantification of grains sizes and grain orientations (grain boundary types), especially for samples with small grain-sizes. Besides, the on-axis CCD-camera is also able to capture diffraction patterns that provide additional information on the sample. EDXS yields compositional information. Moreover, combined SE topography and STEM imaging supported by simulations, enables the understanding of diffraction and mass-thickness contrast. In short, correlative SEM/STEM facilitates the combination of all the

detectors in a modern SEM to gather information from the same specimen area for a comprehensive study of materials.

5 DEFECTS ANALYSIS BY STEM IN A SCANNING ELECTRON MICROSCOPE

Dislocations and stacking faults are crystal defects which determine the mechanical properties of materials [104]. The characterization of dislocations with respect to dislocation type, dislocation density and distribution is therefore of significant interest to understand material properties. TEM has been used for decades to analyze the properties of dislocations and stacking faults. Scanning transmission electron microscopy has been less frequently considered for defect characterization although the reciprocity theorem suggests equivalent diffraction contrast for STEM and TEM imaging [59]. STEM can also be carried out in a SEM if the instrument is equipped with a STEM detector with low voltages ≤30 kV (low-keV STEM). However, defect analyses with low-keV STEM in SEMs were hampered up to now because the knowledge of specimen orientation, which is essential for defects analysis, could not be obtained. Especially for dislocation and stacking fault analysis, there is the necessity for setting up specific diffraction conditions with precise knowledge of specimen orientation. Therefore, the motivation for this chapter was to apply STEM on analysis of defects in SEMs. In the first part of this chapter, the fundamentals of dislocations, stacking faults and their analysis using TEM and STEM are presented. The materials used for defect studies are presented within the second part. In the last part of this chapter three different approaches are presented to determine the specimen orientation in a scanning electron microscope in order to characterize defects with low-keV STEM. The most promising approach demonstrates the ability of a state-of-the-art SEM to detect sample orientation with an on-axis CCD-camera. Based on that, comprehensive defect analyses were performed with low-keV STEM such as obtaining Burgers vectors of dislocations.

5.1 Fundamentals of defects and their characterization

This subsection gives an overview of the basics of defects according to the book written by Hirsch [61]. A general way to classify defects is based on their dimensions. Structural (e.g. vacancies, interstitials) and chemical defects (e.g. dopants, impurities) are considered as point defects or zero-dimensional defects. Dislocations (e.g. edge dislocations, screw dislocations) are regarded as line defects due to their one-dimensional nature. Two-dimensional defects are grain boundaries, phase boundaries and stacking

faults (SF). Precipitates and voids are considered as three-dimensional defects [112]. This thesis comprises analyses of dislocations and stacking faults. Hence, a detailed introduction on these specific types of defects is given in the following.

5.1.1 Dislocations and stacking faults

Dislocations in crystals disturb the local arrangement of atoms. They can be described by the Burgers vector $\vec{b}$ representing the relative movement of the sample atoms on the glide plane from their perfect positions. The glide plane is often the plane with the highest density of atoms. The slip direction which is the direction of $\vec{b}$ is usually the most closely spaced direction in the slip plane [112]. The boundary between slipped and not slipped parts of the crystal is considered as a dislocation. The dislocation type is determined by the angle between the Burgers vector $\vec{b}$ and line direction $\vec{u}$. Figs. 5.1 (a,b) display a simplified representation of the distorted crystal lattice caused by different types of dislocations [112]. If $\vec{b}$ (blue arrow) is perpendicular to $\vec{u}$ (black line) $(\vec{b} \cdot \vec{u} = 0)$, the dislocation is called an edge dislocation (Fig. 5.1 (a)). If $\vec{b}$ is parallel to $\vec{u}$, it is a screw dislocation (Fig. 5.1 (b)). Edge dislocations are generated by an extra half-plane of atoms (marked by grey color in Fig. 5.1 (a)) inserted or removed from the perfect crystal structure. A screw dislocation will result in a different distorted crystal structure such as Fig. 5.1 (b). In addition to edge and screw dislocations, there are also mixed-type dislocation containing a mixture of screw and edge dislocation components. The length of $\vec{b}$ for a perfect dislocation is related to a lattice translation vector in the unit cell of crystals. Perfect dislocations can split into partial dislocations whose Burgers vectors are not lattice translation vectors. Hence, a stacking fault plane is generated between the two partial dislocations such as SFs in Fig. 5.1 (c). Alternatively, SFs can be generated during material fabrication if a plane is displaced from its position with respect to the undisturbed lattice.
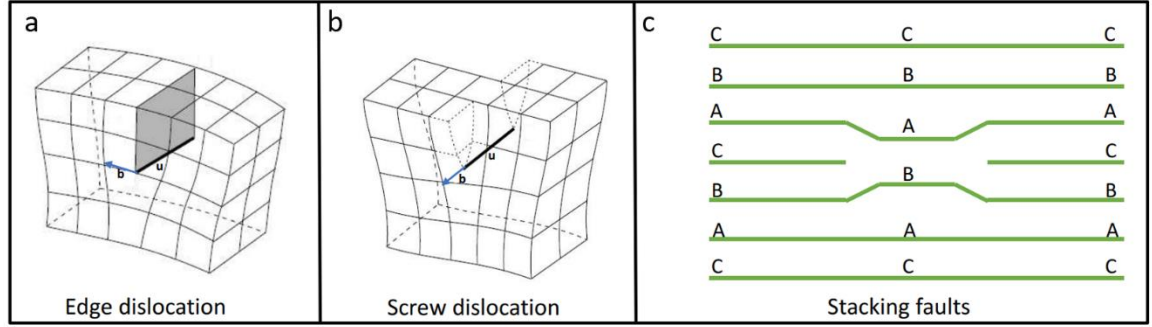
Figure 5.1. Simplified models of (a) an edge dislocation, (b) a screw dislocation and (c) stacking faults with partial dislocations [112].

5.1.2 Fundamentals of dislocation and stacking fault image contrast

As described in chapter 2, the scattering amplitude of an electron wave elastically scattered by a group of atoms which represents diffraction contrast for the diffracted beam can be described by Eqs. (19-23) with the kinematical diffraction theory. To characterize defect diffraction contrast, $\vec{r}_{pi}$ in Eq. (21) (chapter 2) can be replaced by $(\vec{r}_{pi} + \vec{R})$ with $\vec{R}$ being the displacement vector related to defects (Eq. (30)) [61, 113]. As shown in Eq. (30), the amplitude of a diffracted beam $\vec{g}$ can be calculated for a column in the sample by integration over the whole sample thickness t.

$$F = F_S \int_0^t exp(2\pi i[\vec{g} + \vec{s}_g][\vec{r}_{pi} + \vec{R}])dz \qquad (30)$$

Since $\vec{g} \cdot \vec{r}_{pi}$ is an integer number and $\vec{s}_g \cdot \vec{R}$ is much smaller compared with $\vec{g} \cdot \vec{R}$, Eq. (30) can be further simplified to Eq. (31) considering only the z-component s_z of the excitation error $\vec{s}_g$. z indicates the coordinate parallel to the electron beam direction. Therefore, for a two-beam condition with small s_z, the scattering amplitude of the defect is essentially determined by $\vec{g} \cdot \vec{R}$ (Eq. (31)).

$$F = F_S \int_0^t exp(2\pi i[zs_z + \vec{g} \cdot \vec{R}])dz \qquad (31)$$

One can see that if $\vec{g} \cdot \vec{R} = 0$, there is no contribution of $\vec{R}$ to the scattering amplitude which indicates that a dislocation with $\vec{g} \cdot \vec{R} = 0$ does not show any contrast. To setup the $\vec{g}$ diffraction condition for applying Eq. (31), the sample must be tilted into a two-beam condition where only a single Bragg spot (diffraction vector $\vec{g}$) and the undiffracted zero-

order beam (ZB) are excited. By either using the single diffracted beam **g** or undiffracted beam ZB for imaging, the defect is invisible if $\vec{g} \cdot \vec{R} = 0$ is fulfilled.

The displacement vector field $\vec{R}$ introduced by a dislocation in the specific column of the sample can be explained by Fig. 5.2 [61] which displays a model for a thin sample with an edge dislocation oriented parallel to the sample surface. The effect of the dislocation on the area located at a distance z from the sample surface with a thickness of dz within the green column (cf. Fig. 5.2) can be shown by the displacement vector $\vec{R}$ (Eq. (32)) [61]. The atoms in dz have an x distance to the dislocation at O with an angle ø. The angle between the dislocation glide plane and the flat sample surface is γ with y being the distance from O to the specimen surface.

$$\vec{R} = \frac{1}{2\pi}\left[\vec{b}\Phi + \frac{\vec{b}_e sin2\Phi}{4(1-v)} + (\vec{b} \times \vec{u})\left\{\frac{1-2v}{2(1-v)} \cdot ln\frac{r}{r_0} + \frac{cos2\Phi}{4(1-v)}\right\}\right] \quad ; \quad \Phi = ø - \gamma \qquad (32)$$

$\vec{u}$ is the unit vector parallel to the dislocation line and v is the Poisson's ratio. The inner cutoff radius of the displacement field is r_0. $\vec{b}_e$ indicates the edge component of the Burgers vector $\vec{b}$. For the edge dislocation in Fig. 5.2, $\vec{u}$ points into the paper plane. Eq. (32) illustrates that dislocation contrast completely vanishes only if $\vec{g} \cdot \vec{b} = 0$, $\vec{g} \cdot \vec{b}_e = 0$ and $\vec{g} \cdot (\vec{b} \times \vec{u}) = 0$. However, edge dislocations might also be invisible if $\vec{g} \cdot \vec{b} = 0$ and $\vec{g} \cdot (\vec{b} \times \vec{u})$ is reasonably small. According to literature, residual dislocation contrast is possible if $\vec{g} \cdot \vec{b} = 0$ and $\vec{g} \cdot (\vec{b} \times \vec{u})$ is larger than 0.64 [51].

In case of a screw dislocation ($\vec{b} \times \vec{u} = 0$) oriented parallel to the foil surface, its displacement vector field can be described according to Eq. (33) which is simplified from Eq. (32) [61]:

$$\vec{R} = \vec{b}\left(\frac{1}{2\pi} \cdot ø\right) \qquad (33)$$

At $\vec{g} \cdot \vec{b} = 0$ imaging condition, $\vec{g} \cdot \vec{R}$ is 0 and screw dislocations vanish.

Diffraction contrast for a mixed dislocation under two-beam condition depends on both, the edge components ($\vec{b}_e$) and screw components ($\vec{b}_s$) of the total Burgers vector $\vec{b}$ with the displacement vector given also by Eq. (32). For the case of $\vec{g} \cdot \vec{b} = 0$, $\vec{g} \cdot \vec{b}_e$ is also 0.

Similar to the explanation for edge dislocation, only if $\vec{g} \cdot (\vec{b} \times \vec{u})$ is smaller than 0.36, the contrast of mixed dislocations can disappear completely [51].

Qualitative considerations and simulations show that double-line dislocation contrast is frequently observed in bright field TEM images for dislocations under $|\vec{g} \cdot \vec{b}| = 2$ conditions and single-line contrast for $|\vec{g} \cdot \vec{b}| = 1$ conditions [42, 61]. Besides, dislocation contrast is also affected by the excitation error from the Bragg reflecting condition $\vec{g}$ and depends on the dislocation type, TEM sample thickness, dislocation depth in the sample and degree of crystal anisotropy which may lead to deviations from the contrast behavior described above [61, 114].
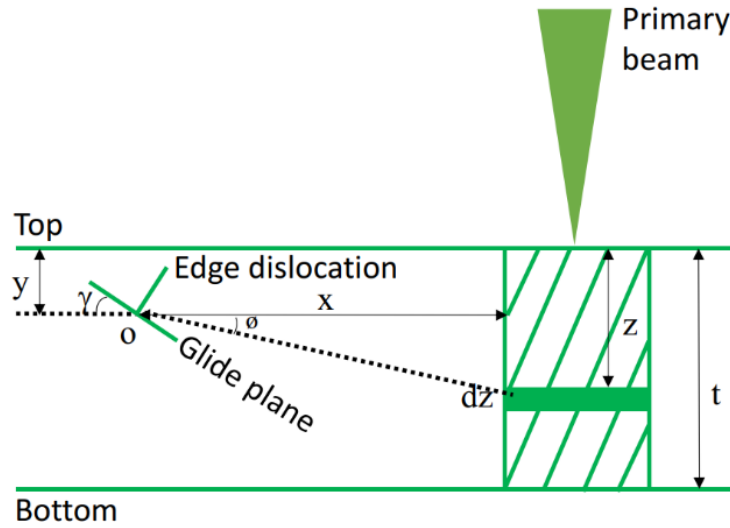
Figure 5.2. Column approximation for defect displacement vector. Typical lateral column dimensions are in the order of 1 nm [61].

Imaging parameters can have a strong impact on dislocation contrast. Studies show that the width of dislocations correlates with the extinction distance ξ_g (Eq. (34)) [51] for a given two-beam condition.

$$\xi_g = \frac{\pi V_e \cos \theta_B}{\lambda F_g} \qquad (34)$$

V_e, F_g are the volume and structure factor of the unit cell. With the effect of excitation error s_z for $\vec{g}$ two-beam condition, the effective extinction distance $\xi_{g,eff}$ is given by Eq. (35),

$$\xi_{g,eff} = \frac{\xi_g}{\sqrt{(1+w^2)}} \qquad (35)$$

with the deviation parameter w=$s_z\xi_g$.

Therefore, the sharpness enhancement of dislocation contrast can be enhanced by the reduction of $\xi_{g,eff}$ since in reality one can hardly reach perfect two-beam conditions ($s_z = 0$) and most of the measurement conditions have $s_z \neq 0$.

One way of reducing $\xi_{g,eff}$ in order to record dislocations with narrower widths is increasing s_z by tilting sample away from the exact two-beam condition leading to the decrease of $\xi_{g,eff}$. Dynamical diffraction theory shows that a positive deviation parameter w can lead to more direct transmitted electrons for two-beam conditions while a negative w can enhance the absorption [42]. However, for dark-field imaging, deviations will always reduce the penetration of the diffracted electrons [42]. Accordingly, it is recommended to use positive w for bright-field defect analysis [42]. One way to achieve high w for dark-field imaging is to utilize a weak diffracted beam with longer exposure time. For example, the two-beam condition can be set to $3\vec{g}$ (third order) or other higher order beams instead of $\vec{g}$. When imaging is performed with $\vec{g}$, a large excitation error results in a small $\xi_{g,eff}$ and therefore, sharp dislocation contrast. Some researchers also suggest using high-order reflections (e.g. $3\vec{g}$) for imaging dislocations. Generally, for high-order two-beam (n**g**) conditions, the extinction distance ξ_{ng} is larger than ξ_g for low-index two-beam (**g**) conditions. However, many high-order two-beam conditions are intrinsically many-beam conditions which results in a small $\xi_{g,eff}$ [42].

The image contrast of planar defects like SFs can also be described by their displacement vector $\vec{R}$. Here, $\vec{R}$ describes the shift of the stacking fault plane with respect to its position in the undisturbed lattice. There is the so-called phase factor $\alpha_1=2\pi\vec{g}\cdot\vec{R}$. A phase shift of multiples of 2π ($\vec{g}\cdot\vec{R}$=n, n is integer number) will cause the extinction of SFs [61]. The dark or bright intensity of fringes in different types of SFs in bright-field and dark-field TEM images changes depending on the sign of α_1 [115, 116]. Therefore, the type of SFs can be investigated based on the contrast extinction of SFs and their fringe intensity variations at different two-beam conditions [117].

5.1.3 Dislocation and stacking fault analysis in low-keV STEM

The invisibility of dislocations for imaging conditions satisfying $\vec{g} \cdot \vec{b} = 0$ can be applied for obtaining the Burgers vector direction of perfect dislocations [51, 61]. Contrast extinction for at least two two-beam conditions has to be found. For two linearly independent imaging vectors $\vec{g}_1$ and $\vec{g}_2$ satisfying $\vec{g} \cdot \vec{b} = 0$, the Burgers vector can be straightforwardly determined by $m\,\vec{b} = \vec{g}_1 \times \vec{g}_2$, with m being a scalar quantity. Besides, double-line and single-line dislocation contrast [42] can also be utilized to support Burgers vector determination. Previous work showed the difficulties of determination of Burgers vector for partial dislocations based on the contrast extinction theory [42]. Therefore, for partial dislocations analysis it is necessary to compare experiments with simulated results [118]. This is the foundation of defect analysis in BF/DF-TEM, which can also be used for defect investigation with STEM since the reciprocity theorem suggests equivalent diffraction contrast for STEM and TEM imaging [59]. However, STEM has been less frequently applied for defect characterization. After some early work on defect imaging by BF-STEM [6-8], more researchers such as Philipps et al. [119], Su et al. [120] and Zhu et al. [121] recently investigated dislocations and stacking faults by STEM and demonstrated dislocation analyses by experiments and simulations. They also pointed out that the application of STEM provides advantages compared to TEM because STEM can be performed on thicker TEM samples. Moreover, bend contours and thickness fringes are less pronounced due to the convergent probe while defect contrast is maintained if BF-STEM collection angles are moderately increased [140]. In one study, the defect contrast and bend contour artifacts dependence of STEM parameters were investigated [121]. Applying similar beam convergence angles and BF-STEM collection angles (a few mrad) on defect analysis can potentially alleviate strong bend contours in the background of BF-STEM images [121].

Many SEM instruments are capable of STEM imaging at typically 30 keV and lower (low-keV STEM), allowing diffraction contrast imaging which is one of the prerequisites for dislocation and stacking fault analysis. Callahan et al. showed that defect images obtained from low-keV STEM have less thickness fringes and bending contours compared with those acquired by TEM [122]. Schweizer et al. discussed a method to in-situ manipulate dislocations in bilayer graphene on a nanometer scale in SEMs [123]. Low-keV STEM stimulates the process of using scanning electron microscopy as a

platform for examining defects [124, 125]. However, samples must be tilted to suitable two-beam conditions which is not possible for many SEMs due to the lack of a camera to acquire diffraction patterns. The last requirement is the avoidance of interference of the diffracted and undiffracted beam on the BF-STEM detector in order to determine $\vec{b}$ based on the $\vec{g} \cdot \vec{b} = 0$ condition. This does not happen realistically in a standard SEM. But for the field free mode in Helios Nanolab G4 FX SEM, it can fulfill the two requirements above allowing the feasibility of $\vec{b}$ determination.

5.2 InN/GaN materials

Group III-nitride semiconductor materials are widely used in modern electronic and optoelectronic components. Crystal defects like dislocations and stacking faults are well known within this material class as they introduce states within the band gap leading to unintended recombination sites for electron-hole pairs. In the past, InN and GaN have been broadly investigated and are therefore excellent materials to evaluate methods for dislocation analysis since their defects are well known. Within this subchapter, InN and GaN including their crystal defects are introduced.

5.2.1 InN

InN is a small-band-gap semiconductor which occurs in the wurzite crystal structure. It is important for light-emitting and other optoelectronic devices [126]. Defects, specifically dislocations, are undesirable in light-emitting devices and lead to non-radiative recombination of charge carriers, which motivates detailed dislocation analyses.

5.2.2 GaN

GaN has a direct wide band gap of 3.39 eV and high photoluminescence efficiency (pronounced chemical inertness, thermal stability, radiation hardness) [127]. Therefore, GaN is an interesting semiconducting material for light-emitting devices in the blue to ultraviolet spectral range [127]. In the past years, researchers focus on the growing of high quality GaN layers in order to apply GaN on light emitting diodes (LEDs), semiconductor lasers and high-power electronic amplifiers [128]. Sapphire is extensively used as substrate for growing group-III nitride epitaxial layers. The large mismatch in the lattice constants and thermal coefficients between the two materials leads to strain at the GaN/Al_2O_3 interface, resulting in misfit dislocations at the interface and threading

dislocations in the GaN epilayer [129]. Threading dislocations extend through the GaN layer and can cause leakage currents that deteriorate the performance of devices. Similarly, SFs in GaN can destabilize the performance of power devices made from GaN [130]. Since structural defects are one of the reasons for the low efficiency of optoelectronic materials [131] and affect the lifetime and efficiency of LEDs [132], many GaN growth strategies were developed to reduce defect densities and thereby, improve the efficiency of GaN-based devices [133, 134]. The formation of SFs can result from those growth strategies such as the strategy for using growth of non- and semi-polar GaN layers to reduce dislocations [135]. Defects in wurzite GaN were already investigated in detail by TEM [127]. In this thesis, low-keV STEM was applied successfully to obtain Burgers vectors of dislocations in FIB-prepared GaN samples. It demonstrates that STEM in a scanning electron microscope facilitates analogous defect characterizations as STEM in a transmission electron microscope.

5.2.3 Dislocations in InN/GaN

Both InN and GaN crystallize in hexagonal wurzite structure. The close-packed plane is the (0001) basal plane and the $\langle 11\bar{2}0\rangle$ directions are the close-packed directions in this plane. Since the shortest lattice translation vector for the close-packed direction is $1/3\langle 11\bar{2}0\rangle$ (translation vector $\vec{a}$ for the unit cell), dislocation glide on the basal plane with a Burgers vector $1/3\langle 11\bar{2}0\rangle$ is frequently observed. As listed in Table 5.1, another common Burgers vector is oriented along the $[0001]$ direction corresponding to the $\vec{c}$ translation vector of the unit cell which is perpendicular to the basal plane. Finally dislocations with a mixed Burgers vector $(\vec{a}+\vec{c})$ [112, 127] are also frequently observed. The dislocations discussed above are the perfect dislocations in the wurzite structure while partial dislocations usually have Burgers vectors which are not complete lattice translation vectors. The appearance of partial dislocations is therefore accompanied by stacking fault formation.

Table 5.1. Burgers vectors of perfect dislocations in wurzite materials.

Burgers vector	$1/3\langle 11\bar{2}0\rangle$	$[0001]$	$1/3\langle 11\bar{2}3\rangle$
lattice translation vector	$\vec{a}$	$\vec{c}$	$\vec{a}+\vec{c}$

5.2.4 Stacking faults in GaN

The fundamentals of basal stacking faults in wurzite GaN are presented in this part because only the basal stacking faults in GaN were investigated in this thesis. Two intrinsic (I_1 and I_2) and one extrinsic (E) SFs are commonly observed in GaN. The stacking order of (0001) basal planes is shown in Fig. 5.3 for the different SF types with images rendered by the VESTA software package. The green atoms in Fig. 5.3 denote gallium (Ga) atoms while nitrogen (N) atoms are light blue. The stacking order for perfect wurzite GaN in [0001] direction (Fig. 5.3 (a)) is …aAbBaAbB… where a/b represent N atom planes and A/B Ga atom planes. Two intrinsic stacking faults with stacking orders …aAbBaAbB|cCbBcC… (I_1) and …aAbBaAbB|cCaAcCaAcC… (I_2) are shown in Figs. 5.3 (b,c). Furthermore, the extrinsic stacking fault is characterized by a …aAbBaAbB|cC|aAbBaAbB…(E) stacking order (Fig. 5.3 (d)). The displacement vectors $\vec{R}$ for wurtzite GaN SFs on the basal plane are $1/6\langle 20\bar{2}3\rangle$ (I_1), $1/3\langle 10\bar{1}0\rangle$ (I_2) and $1/2[0001]$ (E), respectively [140].
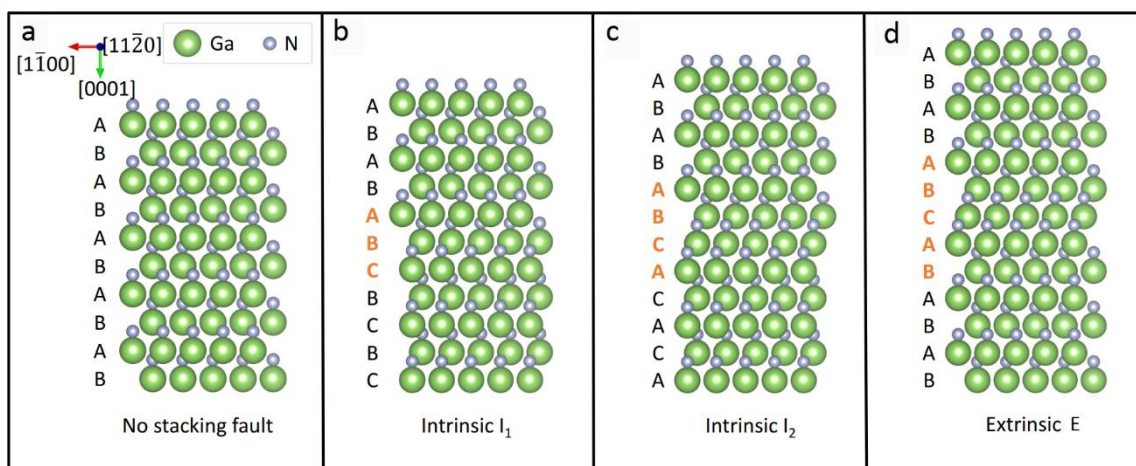
Figure 5.3. Stacking sequences for the wurzite GaN (a) without SFs and (b) for intrinsic I_1, (c) intrinsic I_2, and (d) extrinsic E SFs.

5.3 Methods for sample orientation in SEM

In order to apply low-keV STEM in SEM for defects analysis, one first needs to determine the sample orientation and tilt the sample to specific two-beam diffraction conditions. There are a number of methods available in SEM instruments to obtain information about the crystal orientation of the sample. Three approaches were investigated and discussed within this subchapter including their advantages and disadvantages.

5.3.1 ECP and ECCI

Electron channeling pattern (ECP, cf. chapter 2) images can be obtained for single crystal bulk specimens using the annular BSE detector (CBS). This produces Kikuchi bands according to the crystalline orientation in the vicinity of the sample surface. One example of an ECP is shown in Fig. 5.4 for a monocrystalline silicon wafer. Kikuchi bands are clearly seen in Fig. 5.4 with the image center marked by a black cross. From Fig. 5.4 (a) to Fig. 5.4 (b), the α' tilt changes from -2.7° to 0.1° leading to displacements of the Kikuchi bands. If the Kikuchi bands are not symmetrically arranged with respect to the center of the image (cf. Fig. 5.4 (a)), the incidence direction of the electron beam does not correspond to a zone-axis orientation. If the Kikuchi bands cross is at the center of the image (cf. Fig. 5.4 (b)), the sample is at an exact zone-axis orientation. Each Kikuchi band represents one set of lattice planes. As shown in Fig. 5.4 (a), $2\tan\theta_B$ (Bragg angle θ_B) can be calculated based on the ratio between the width of the Kikuchi band (d_1) and the working distance (WD). Accordingly, the Kikuchi bands can be indexed and the corresponding zone axis can be determined. It is also convenient to tilt the sample to a two-beam condition based on ECP images by setting the $\vec{g}$ Kikuchi bands to the center of the image. Since the ECP images can only be obtained at low magnification, this requires large monocrystalline flat bulk samples typically in the range of a few millimeters which makes this type of orientation determination unsuitable for most dislocation studies.
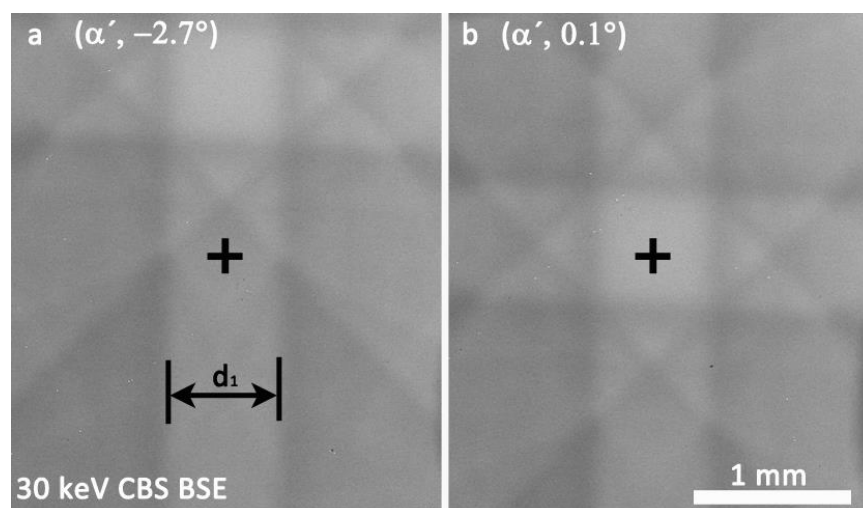
Figure 5.4. ECP images for a silicon wafer taken by a solid-state BSE-CBS detector with (a) -2.7° and (b) 0.1° α' tilt angles.

Instead of using bulk samples it is also possible to obtain BSE channeling contrast for thin specimens. For that purpose an InN sample was prepared by conventional mechanical thinning procedures (cf. chapter 3). As shown in Figs. 5.4 (a,b), tilting the sample changes the relative position of Kikuchi bands with respect to the image center. Therefore, the intensity of electron channeling contrast image (ECCI) (cf. chapter 2) which is available for high magnification BSE images should also change during sample tilting even for thin specimens. Hence, ECCI images were obtained in order to find a way to acquire sample orientation at high magnifications in a SEM. As displayed in Fig. 5.5, with the tilting of a thin InN sample from 2.2° to 2.4°, the local intensity change of the ECCI images is hardly distinguishable by eye. A tilt series was conducted and the average ECCI intensity of the InN sample at different tilt angles was measured (Fig. 5.6). Even though the ECCI intensity in Fig. 5.6 changes very much for different tilting angles, it was not possible to obtain obvious ECCI intensity regulations for different tilting angles. Therefore, no orientation information was obtained for the InN sample with the ECCI measurement. The main reason could be that the sample is near a zone-axis orientation. During tilting, all Kikuchi bands from the zone axis contribute to the ECCI intensity change. Secondly, only one tilt axis is available in the Quanta 650 SEM that was used for this investigation. Thirdly, taking several images from the same region leads to enhanced sample contamination which strongly influences the contrast. One also has to consider that the local sample thickness changes when tilting the sample. However, this might be only relevant for large tilt angles.
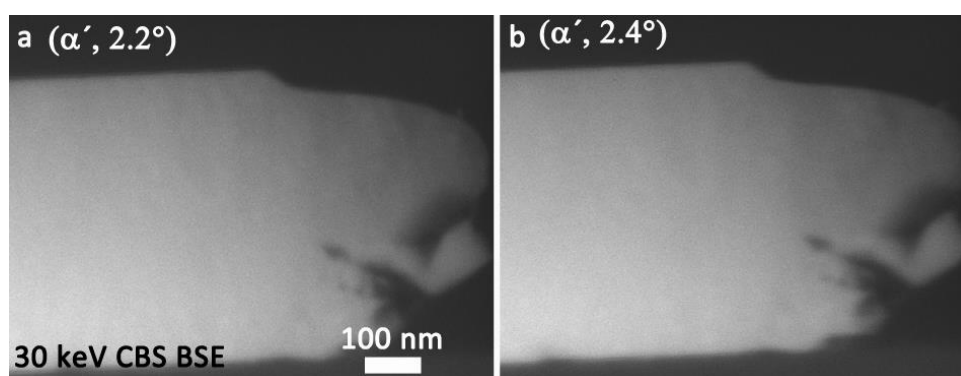
Figure 5.5. ECCI images taken by CBS detector for InN sample with (a) 2.2° and (b) 2.4° α´ tilting angles.
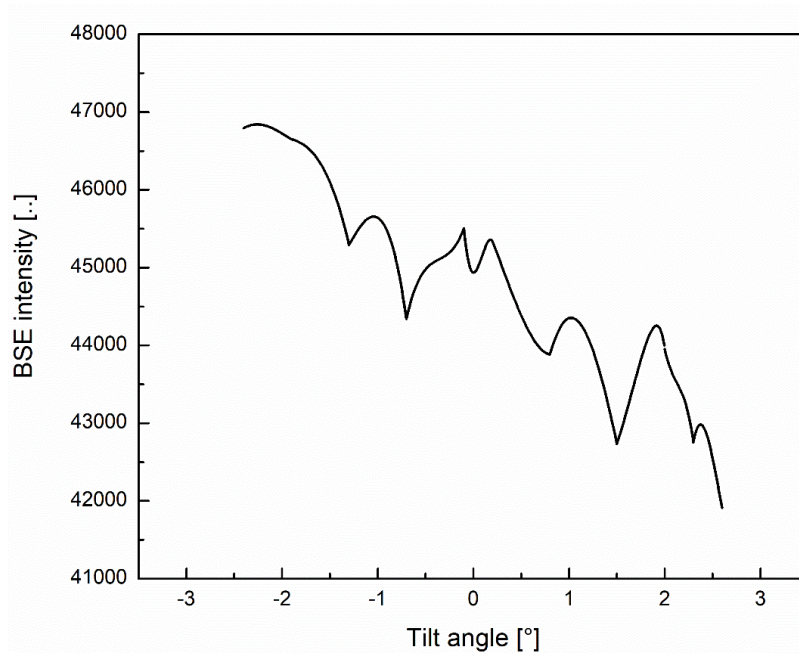
Figure 5.6. The ECCI image intensity changes for InN sample under different tilting angles.

5.3.2 Segmented STEM detector

The second approach for extracting sample orientation information is by utilizing the segmented STEM detector.

Fig. 5.7 shows two BF-STEM images for an InN sample containing numerous dislocations. With -1° tilt for α′ direction, the dislocations marked by arrows in Fig. 5.7 (a) are displayed clearly with dark contrast while these dislocations disappear in Fig. 5.7 (b) (α′, 1°). The dislocation contrast in BF images mainly results from diffraction contrast. The tilting of the sample will affect the angle between the lattice planes in the sample and the incident electron beam and hence, the dislocation contrast disappears if the extinction criterion $\vec{g} \cdot \vec{b} = 0$ is fulfilled.
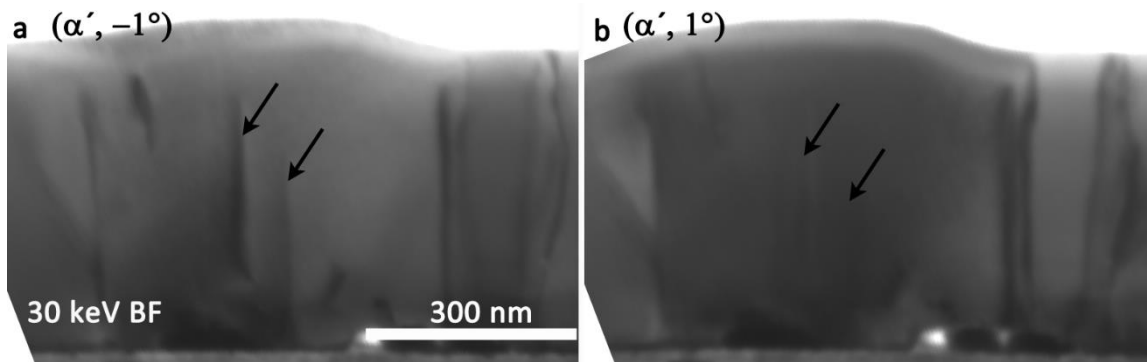
Figure 5.7. BF-STEM images for an InN sample taken at α′ tilt angles of (a) -1° and (b) 1°.
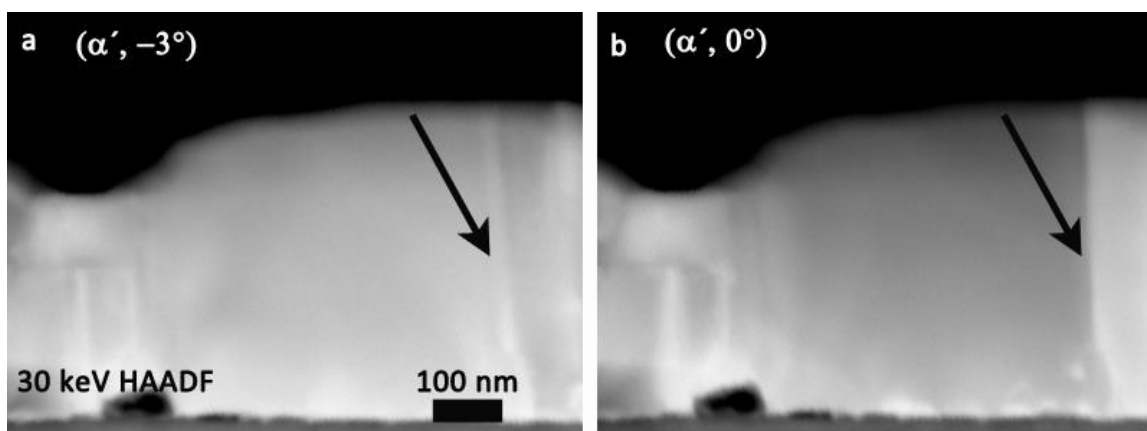
Figure 5.8. HAADF-STEM images for an InN sample taken at different tilt angles of (a) -3° and (b) 0°.

The HAADF images for the InN sample also taken under different tilting conditions are shown in Fig. 5.8. Even though mass-thickness contrast is the dominant contrast in HAADF images, diffraction still contributes to HAADF-STEM contrast as shown Fig. 5.8. The arrows in Fig. 5.8 indicate an interface between two subgrains in the InN sample. At -3° α′ tilt, the two subgrains near the black arrow in Fig. 5.8 (a) show similar contrast, whereas Fig. 5.8 (b) shows clearly different intensities for these two grains. Since the sample has a rather homogeneous composition and thickness, mass-thickness contrast cannot lead to the contrast change in Fig. 5.8 (b). Hence, it can only be explained by diffraction contrast. This indicates that coherent elastic scattering takes place even into rather large angles (HAADF detector collection angle: 187-683 mrad). Tilting of the sample leads to a change of diffraction conditions for the subgrains in Fig. 5.8. This demonstrates that diffraction contrast can be acquired by both the BF and HAADF detector segments in a SEM (FEI Strata 400S). Therefore, diffraction contrast in BF and

HAADF imaging can in principle be utilized to obtain sample orientation information to analyze defects such as dislocations. Based on this, methods were developed to obtain the orientation of TEM samples with the STEM detector. One method is to use the BF detector to monitor the changes in diffraction contrast when tilting the sample. Since diffraction information can be also obtained at high scattering angles, the six-segmented design of the HAADF-STEM detector provides another way to obtain sample orientation information. By tilting the sample, the Kikuchi pattern of the inspected sample region moves across the HAADF detector leading to relative image intensity changes between different segments.

An InN sample was prepared roughly along the $[10\bar{1}0]$ zone-axis which was verified by selected area electron diffraction in a CM 200 TEM beforehand. As shown in the BF-TEM image Fig. 5.9 (a), the epitaxial InN layer is grown along the $[0001]$ direction. Without any tilting of the sample, the diffraction pattern Fig. 5.9 (b) obtained in the TEM shows that the sample is oriented close to the $[10\bar{1}0]$ zone-axis. Since TEM samples in the Strata 400S can only be tilted in one direction, the InN sample is inserted in the SEM with a way to support tilting of the sample along the $\vec{g}_{(1\bar{2}10)}$ (Fig. 5.9 (b)) direction.
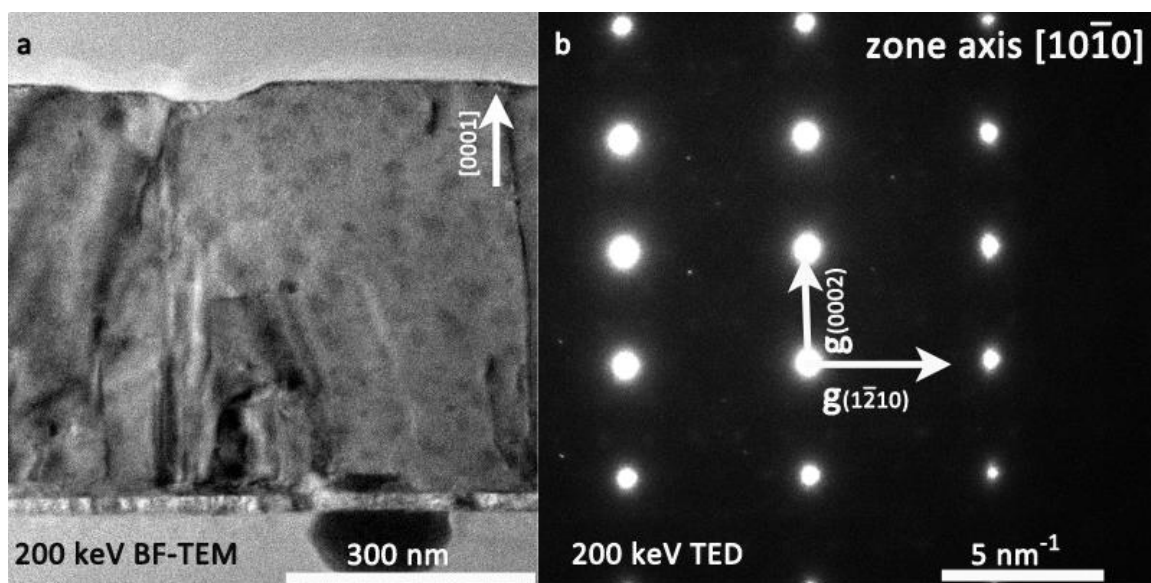
Figure 5.9. (a) BF-TEM image of an InN sample and (b) its diffraction pattern obtained with CM 200 TEM.

30 keV BF-STEM images were normalized as mentioned previously by scanning over the detector. Fig. 5.10 (a) shows the BF-STEM image which was used as a reference for the normalization of the BF-STEM detector. The inset in Fig. 5.10 (a) indicates the

relative position of the $[10\bar{1}0]$ zone-axis Kikuchi bands and the BF-STEM detector in the Strata 400S according to the TEM results. A series of BF images for the InN sample was taken at different sample tilt angles (-1° to 5°) as exemplified in Fig. 5.10 (b) with 0° tilt angle. The normalization of the BF intensity was performed based on Eq. (36). The normalized BF intensity (I_{NOR-BF}) equals to the difference between the experimental BF intensity from the marked area in Fig. 5.10 (b) (I_{EXP-BF}) and the black intensity of the BF detector ($I_{Black-BF}$) from Fig. 5.10 (a) (I_{EXP-BF}- $I_{Black-BF}$) divided by the difference between the white intensity of the BF detector ($I_{White-BF}$) and $I_{Black-BF}$ from Fig. 5.10 (a) ($I_{White-BF}$-$I_{Black-BF}$).

$$I_{NOR-BF} = \frac{I_{EXP-BF} - I_{Black-BF}}{I_{White-BF} - I_{Black-BF}} \qquad (36)$$

It is obvious that the I_{NOR-BF} in Fig. 5.11 reaches its minimum at tilt angles between 2° and 3°. This indicates that one Bragg condition is fulfilled around those tilt angles. By measuring the angular width of this intensity dropping area, the corresponding Bragg angle displayed by the curve in Fig. 5.11 was calculated to be approximately 1.2° which is close to the theoretical Bragg angle 1.14° for $\vec{g}_{(1\bar{2}10)}$ at 30 keV which also matches the orientation information obtained from TEM.

Since the sample was tilted along $\vec{g}_{(1\bar{2}10)}$ direction, the Kikuchi bands in the inset in Fig. 5.10 (a) will move while tilting the sample. When the $\vec{g}_{(1\bar{2}10)}$ Kikuchi band passes by both the zero-order beam ZB and the diffraction spot $(1\bar{2}10)$, the exact Bragg diffraction for $(1\bar{2}10)$ (two-beam condition) is fulfilled. Therefore, the $(1\bar{2}10)$ reflection will reach its maximum intensity which leads to the decrease of intensity in the ZB. The ZB is used for BF-STEM imaging, thus I_{NOR-BF} in Fig. 5.11 reaches its minimum. This explains the strong reduction of I_{NOR-BF} between the two dashed lines in Fig. 5.11. The variation of other parts of the curve in Fig. 5.11 can be explained that except the Kikuchi bands for $(1\bar{2}10)$, other Kikuchi bands also pass by the BF detector hence having an effect on I_{NOR-BF} since the sample is near to one zone-axis. Unfortunately, it is not possible to reduce the effect of other Kikuchi bands since the Strata 400S does not have a double-tilt sample holder. In principle, the BF-STEM method for gathering orientation information is similar with the ECCI method discussed in the last subsection. Even though it is possible to obtain orientation information with the BF detector, the procedure is time consuming and lacks accuracy due to limited tilt accuracy of the stage in the SEM instrument. Furthermore, a

priori information on the approximate sample orientation is necessary. However, since many SEMs are equipped with a STEM detector, no additional hardware is required.
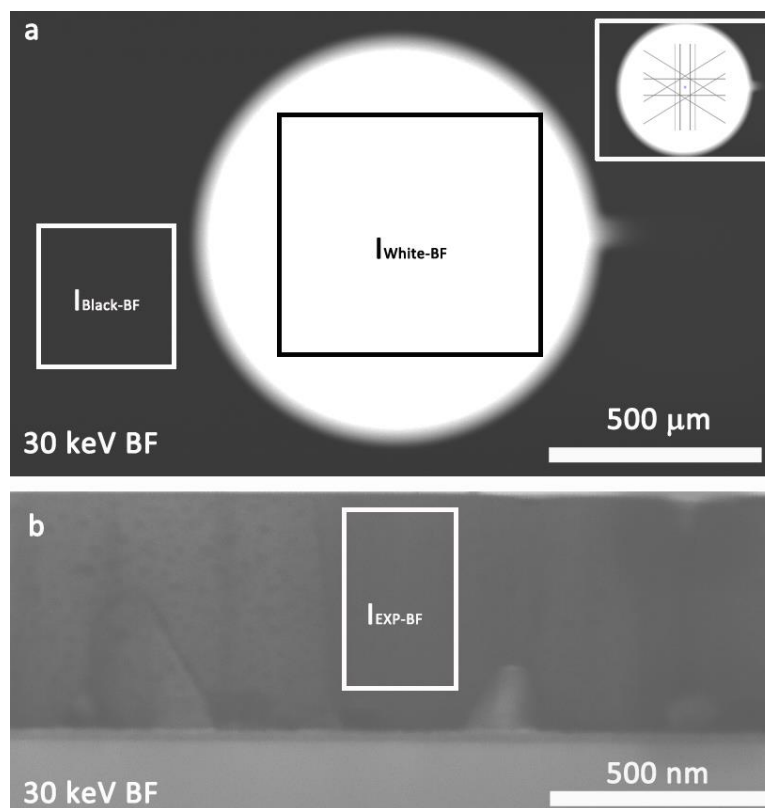
Figure 5.10. (a) BF-STEM image of the BF-STEM detector. (b) BF-STEM image of the InN sample.
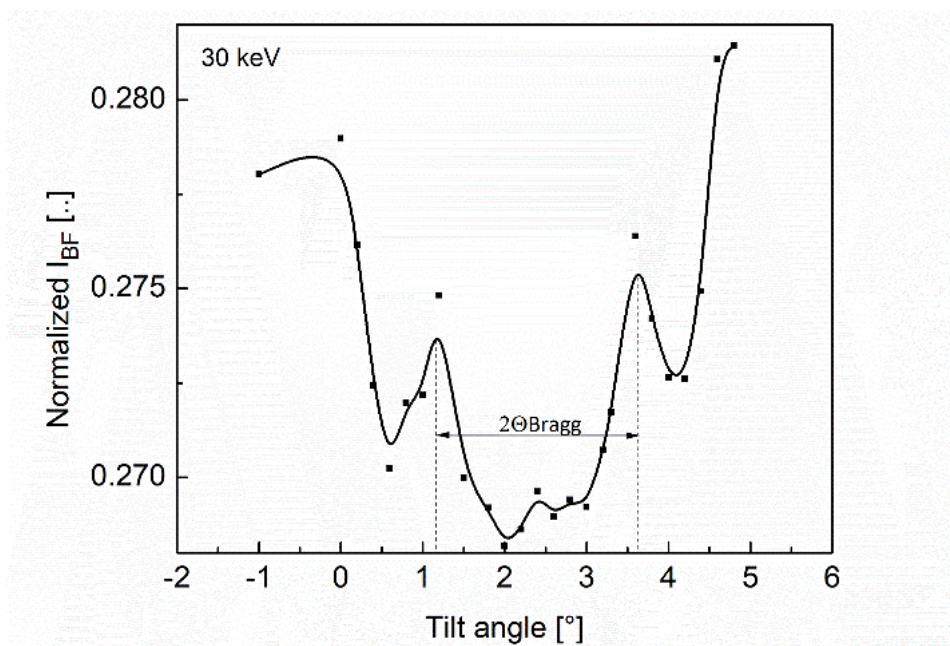
Figure 5.11. Normalized BF-STEM intensity of InN at different tilt angles.

The experiment was repeated with the HAADF detector in the Strata 400S for the same InN sample. As outlined in chapter 3 Fig. 3.1 (b), the HAADF detector in the Strata 400S has a symmetrical design with six segments. Hence, if the sample is at exact zone-axis orientation, the intensity of HAADF-STEM images obtained with half of HAADF detector (segments A, B, F in Fig. 3.1 (b)) should be equal to that from the images obtained with the other half of the HAADF detector (segments C, D, E). Equivalently, the same intensity should be found for images taken with segments A, B, C and segments D, E, F. The normalization of the HAADF image intensity obtained from HAADF segment C in Fig. 5.12 is based on Eq. (37) which is similar with Eq. (29) in chapter 2. Fig. 5.12 (a) displays the HAADF reference image for the inner part of the HAADF segment C, while Fig. 5.12 (b) represents the HAADF-STEM image for InN obtained with the HAADF segment C.

$$I_{NOR-HAADF(C)} = \frac{I_{EXP-HAADF(C)} - I_{Black-HAADF(C)}}{I_{White-HAADF(C)} \cdot \zeta - I_{Black-HAADF(C)}} \qquad (37)$$

The normalization of STEM images for other HAADF segments is similar. The example in Fig. 5.13 shows the normalized difference between the intensity of images acquired by two half sides of the HAADF detector at different sample tilt angles. At a tilt angle of 3°, the difference between the top and bottom half sides of the HAADF ($I_{NOR-HAADF(A+B+F)} - I_{NOR-HADF(C+D+E)}$) is 0. This means the Kikuchi bands are symmetrical with respect to the x-axis passing by the HAADF detector center. If the images obtained by the left and right half of the HAADF detectors also have same intensity, then the sample must be oriented in an exact zone-axis orientation. As for the BF-STEM method discussed above, the HAADF-STEM method can only provide orientation information if there is a priori knowledge of sample orientation available.

Nevertheless, the BF-STEM and HAADF-STEM methods developed in this thesis facilitate to orient a specimen along zone-axis and two-beam conditions and allow Bragg angle determination in a SEM. However, in case of defect analysis, a double-tilt sample holder is essential which is not available in the Strata scanning electron microscope.
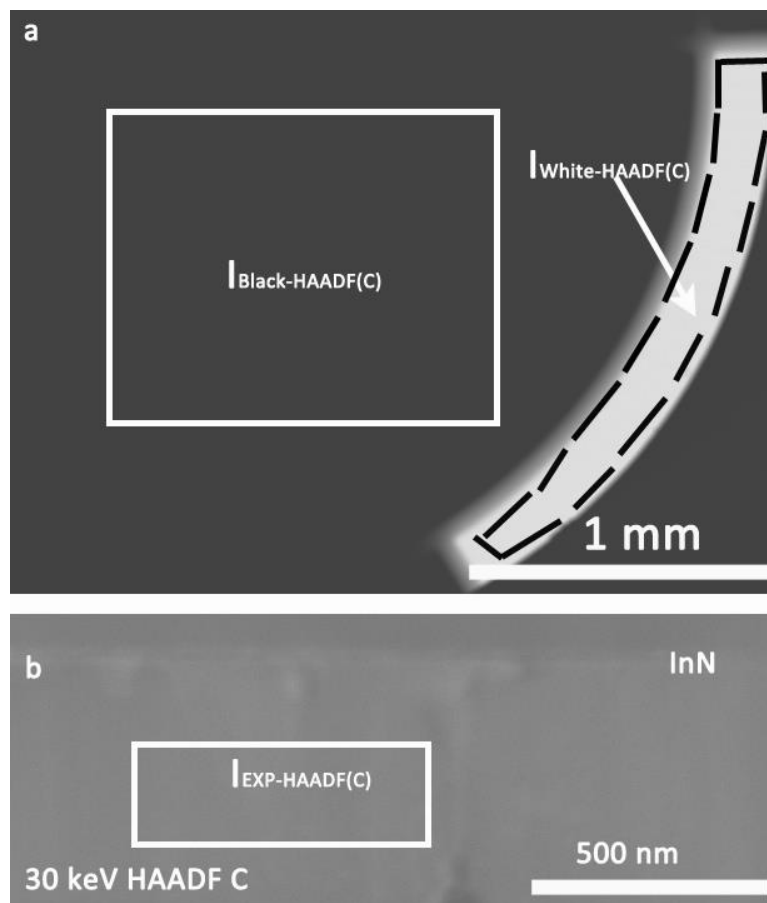
Figure 5.12. (a) HAADF-STEM image of the C segment of the HAADF detector. (b) HAADF-STEM image of an InN sample obtained with the HAADF$_C$ segment.
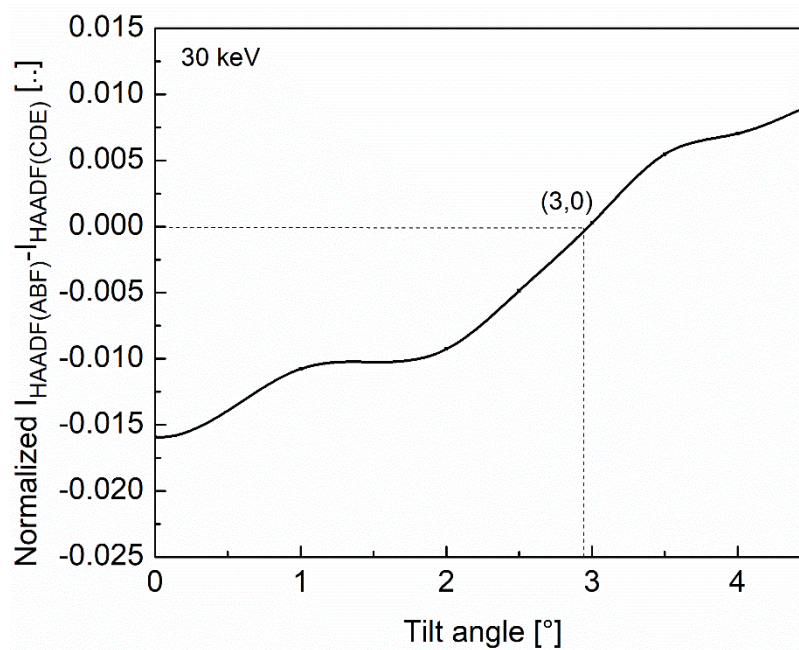
Figure 5.13. Normalized HAADF-STEM intensity difference between the images obtained by the $HAADF_{A,B,F}$ segments and images obtained by $HAADF_{C,D,E}$ segments for an InN sample as a function of the tilt angle.

5.3.3 Acquisition of transmission electron diffraction (TED) patterns

In most recent SEM instruments, on-axis TKD detectors became available. These detectors are designed to image Kikuchi-patterns in diffraction space. Since TKD detectors are basically on-axis CCD-cameras, they can also be used to image TED patterns containing Bragg diffraction spots. This allows setting up two-beam conditions more precisely. In addition, imaging diffraction spots enables measuring the convergence angle of the electron beam and understanding the contrast obtained by the individual segments of the STEM detector.

The TKD camera turned out to be suitable to acquire diffraction patterns of TEM samples. In this case, it is crucial to prepare thin samples ($\leq$ 100 nm) as with increasing thickness Kikuchi patterns become increasingly pronounced until Bragg spots disappear completely. With the double-tilt sample holder of the Helios SEM, the GaN sample could be tilted into two zone axes $[10\bar{1}0]$ and $[11\bar{2}0]$ to demonstrate the capability of the TKD detector to image TED patterns. As shown in Fig. 5.14, the TED patterns (marked by black dots) for the $[10\bar{1}0]$ and $[11\bar{2}0]$ zone axes obtained from the on-axis CCD-camera are superimposed on the STEM detector which were drawn to scale (except the HAADF ring). The arrow in Fig. 5.14 (a) displays the symmetrical design of the cover marked by hatched lines which leads to the small BF collection angle (0-7 mrad with 4 mm WD) in Helios SEM. The 1.7 mrad convergence semi-angle for 30 keV is measured from the diameter of the diffraction spots on the camera which was also verified by the technique suggested by Lyman et al [136] (cf. appendix). The convergence angle is significantly smaller than the 7 mrad collection (half) angle of the BF-STEM detector segment. All relevant Bragg angles of GaN reflections are larger than 12 mrad at 30 keV. The only exception is the (0001) reflection with 6 mrad Bragg angle which can be dynamically excited in the $[11\bar{2}0]$ zone axis. Large Bragg angles compared to small convergence and collection angles are advantageous because overlap of diffraction disks does not occur and distinct separation of ZB and Bragg reflections on the BF-STEM detector is achieved as displayed in Fig. 5.14. For the zone axis in Fig. 5.14 (a), two different two-beam conditions were

utilized in this thesis with Bragg reflections (± 0002) and ($\pm 1\bar{2}10$). In addition, one other two-beam condition with ($\pm 1\bar{1}00$) was applied in the thesis from the [$11\bar{2}0$] zone-axis in Fig. 5.14 (b). With a double-tilt holder, the α' and β' angles for tilting samples to a suitable two-beam condition can be obtained by acquiring TED patterns with the CCD-camera inserted.

Figure 5.14. Scheme of the Helios STEM-detector superimposed on TED patterns for two zone axes (a) [$10\bar{1}0$] and (b) [$11\bar{2}0$].

Since TED patterns are essential for setting up two-beam conditions to conduct defect analyses, the visibility of TED patterns under two-beam conditions for a GaN wedge sample was investigated with different electron energies as shown in Fig. 5.15. The GaN wedge sample was prepared by FIB with the top and side views shown in Figs. 5.15 (a,b) respectively. Fig. 5.15 (c) displays a cross-section BF-STEM image taken under ($1\bar{2}10$) two-beam conditions (c.f. inset) of the wedge indicated by the arrow in Fig. 5.15 (a). The arrow-marked area in Fig. 5.15 (b) demonstrates topography contrast of the GaN sample area shown in Fig. 5.15 (c) for better understanding of the BF image contrast. According to Figs. 5.15 (a,b), the GaN sample thickness decreases linearly from the left to the right side of BF-STEM image (Fig. 5.15 (c)). Dislocations appear on the right side of the dashed line in Fig. 5.15 (c). However, the left side of the dashed line (thickness $\geq$ 200 nm) shows no dislocation contrast because scattering of electrons in higher angles is pronounced for the thicker area.

Figure 5.15. SE-TLD image of a GaN wedge sample, (a) top-view, (b) side-view. (c) BF-STEM cross-section image of the same sample in (a,b) imaged with a $(1\bar{2}10)$ two-beam condition.

Setting the primary electron energy to 30 keV, 20 keV, 10 keV and 5 keV, the corresponding TED patterns are displayed in Fig. 5.16. Images were taken at five different positions on the GaN wedge with the sample thickness ranging between 8 and 44 nm. The thickness was measured experimentally with an accuracy of ±5 nm. Details on the thickness measurement can be found in the appendix. Exposure settings for all TED patterns were kept constant. The increase of the electron energy leads to the reduction of electron wavelength. Therefore, the distance between diffraction spots for GaN with a constant thickness decreases with increasing electron energy (cf. red rectangles in Fig.

5.16). The TED patterns are shown clearly at 30 keV for all the sample thicknesses, while at 20 keV the intensity of ZB decreases for GaN sample thickness changing from 8 nm (ZB$_1$) to 17 nm (ZB$_2$). The intensity of the Bragg reflection increases from $\mathbf{g}_1$ to $\mathbf{g}_2$ due to elastic scattering. However, with further increase of the specimen thickness (44 nm), both the ZB$_3$ and $\mathbf{g}_3$ lose intensity since more electrons are scattered to high angles. The outer diffraction spots disappear obviously with larger sample thickness as inelastic scattering becomes more pronounced. At 10 keV, diffraction spots disappear at a thickness larger than 17 nm which might set a limit for diffraction contrast. At 5 keV, only the zero-order beam is visible for the thinnest sample area (8 nm). The disappearance of the diffraction spots is due to the extensive multiple inelastic scattering at very low energies. Hence, in order to set up two-beam conditions based on TED patterns and obtain information based on elastically scattered electrons (diffraction contrast) in low-keV STEM, one should either choose a suitable electron energy based on the sample thickness or find an appropriate sample thickness range according to the chosen electron energy.
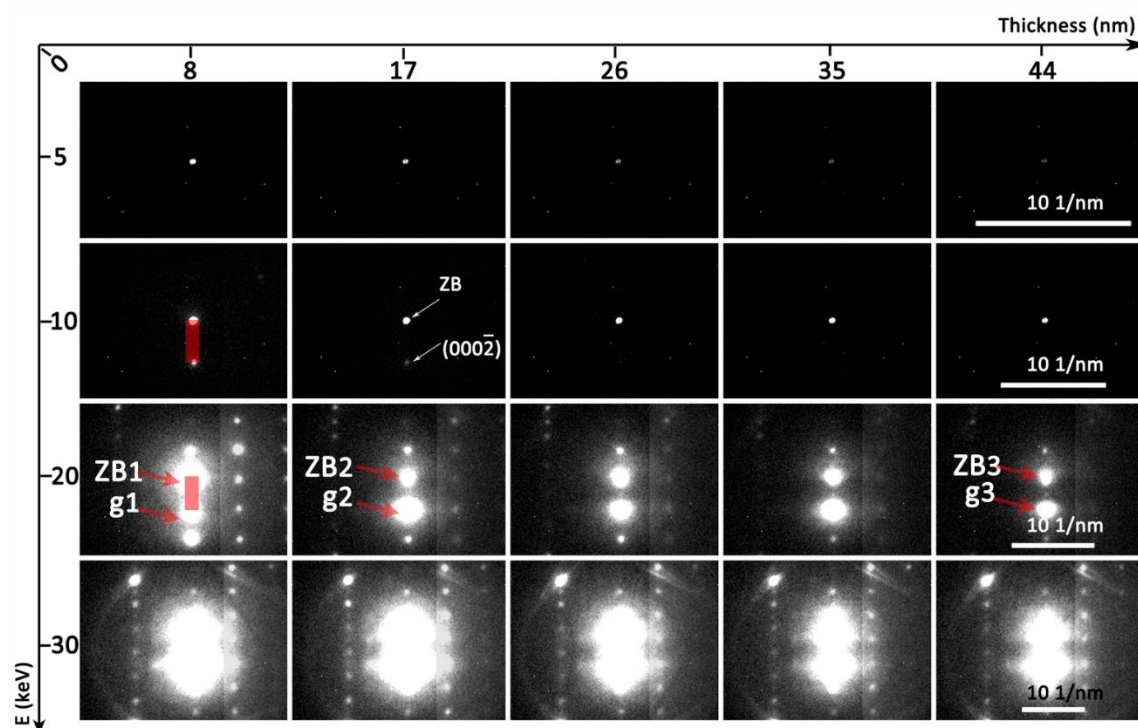
Figure 5.16. TED patterns obtained at different electron energies under $(000\bar{2})$ two-beam conditions for different GaN thicknesses.

5.4 Defect investigation with low-keV STEM

The on-axis CCD-camera was considered most suitable to tilt the sample into two-beam conditions as demonstrated in the previous section. With the STEM detector in place, the sample holder is inserted with α' and β' tilt-angle previously determined with the on-axis CCD-camera which may lead to small deviations from the selected two-beam condition (estimated error $\pm$ 0.1º). As sample orientation in SEM is feasible, a full study of defects in GaN was performed using low-keV STEM in a SEM instrument which will be discussed in the following.

5.4.1 Burgers vector determination for dislocations

An advantage of performing STEM in a scanning electron microscope is the option to access the surface topography of the TEM specimen with SE imaging and support STEM contrast interpretation. A high density of threading dislocations is typically observed in epitaxial GaN layers grown on (0001) Al_2O_3 [137], as displayed in the BF-STEM image in Fig. 5.17 (a). There are dislocations with sharp dark lines such as the one marked by the white arrow in Fig. 5.17 (a). However, trenches resulting from FIB-milling (e.g. the one marked by a dashed line in Fig. 5.17 (a) are very common in BF-STEM images which may disturb the dislocation type determination. Therefore, SE images were obtained for all GaN samples to obtain the topography of the top and bottom surface of the FIB-prepared samples such as Figs. 5.17 (b,c) for the sample given in Fig. 5.17 (a). With the combination of Fig. 5.17 (a) and Figs. 5.17 (b,c), one can easily recognize that the contrast marked by a dashed line results from the topography of the TEM lamella. The other sharp black line contrast such as the white arrow marked one in Fig. 5.17 (a) is a dislocation because no obvious topography contrast exists for the same area in Figs. 5.17 (b,c). With comparison of SE-SEM and BF-STEM images, surface topography related contrast features can be recognized and distinguished from dislocations. In addition, the black arrow marked dark contrast in Fig. 5.17 (a) can be attributed to contamination of the sample surface based on Fig. 5.17 (b). The area marked by the black rectangle in Fig. 5.17 was selected for Burgers vector determination of dislocations.
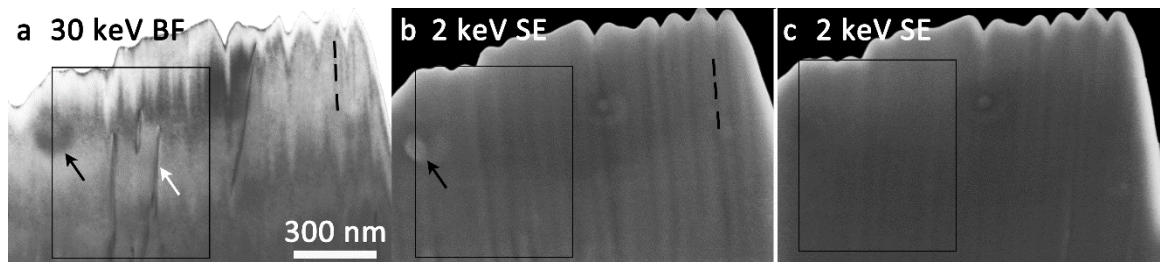
Figure 5.17. (a) 30 keV BF-STEM image of a GaN sample and 2 keV SE-TLD images of (b) top and (c) bottom side of the same region. Scale bar in (a) applies to (b,c).

In chapter 5.1 it was elaborated that one of the prerequisites for the $\vec{g} \cdot \vec{b} = 0$ invisibility criterion is that dislocations are parallel to the sample surface (cf. Eqs. (32,33)). To justify this assumption, TEM tomography in a FEI Titan microscope was performed on one of the GaN samples to check the orientation of dislocations regarding the sample surface. A BF-STEM tilt-series from -70° to 70° with a step size of 2° was recorded with the FEI Titan TEM operated at 300 keV. However, reconstruction of individual dislocations using conventional reconstruction algorithms was unsuccessful due to the strong diffraction contrast in BF-STEM images as can be seen in the image (sample tilt, 0°) Fig. 5.18 (a). Since dislocations can be approximated by lines, the orientation in 3D space can be calculated by manually measuring the length change between different sample tilts. The result is shown in Fig. 5.18 by a (b) top- and (c) side-view of the reconstruction. The dislocations were rendered with different colors using the VESTA software package. In Fig. 5.18 (b), the top-view BF-STEM image (Fig. 5.18 (a)) of the sample is also included. According to the side-view in Fig. 5.18 (c), one can see that long dislocations are reasonably parallel to the surface whereas some of the short dislocations show moderate inclination angles. Therefore, the $\vec{g} \cdot \vec{b} = 0$ theory can be used for the GaN samples. Nevertheless, changes in the distance between dislocation and sample surface along the dislocations line can give rise to inhomogeneous BF-STEM contrast along the dislocation line.

Based on the discussion above, dislocation Burgers vector determination with low-keV STEM is demonstrated with the images in Fig. 5.19 obtained from the rectangular area shown in Fig. 5.17 (a). There are more dark spot-like regions in the BF-STEM images in Fig. 5.19 compared to Fig. 5.17 (a) because more contamination occurred during sample tilting to set up two-beam conditions. The same specimen region is imaged with BF-STEM under three different two-beam conditions (Figs. 5.19 (a-c)) using different $\vec{g}$

vectors (diffraction spot $\mathbf{g} = (000\bar{2})$, $(1\bar{2}10)$ and $(1\bar{1}00)$) as demonstrated by the TED patterns (Figs. 5.19 (d-f)). Threading dislocations appear as dark lines, which are oriented along or close to the [0001] GaN layer growth direction. Seven dislocations are marked in the images which show different contrast in Figs. 5.19 (a-c). Dislocations 1-6 show strong contrast in Fig. 5.19 (a) using $\mathbf{g} = (000\bar{2})$ predominantly with double-lines. Dislocation 7 appears with weak residual contrast and is considered to be out of contrast $(\vec{g} \cdot \vec{b} = 0)$ in Fig. 5.19 (a). The latter dislocation shows strong contrast in Fig. 5.19 (b) taken with $\vec{g} = (1\bar{2}10)$ while dislocation 1 is out of contrast here. Double-line contrast is observed for most other dislocations. Dislocations 1 and 7 are invisible using $\mathbf{g} = (1\bar{1}00)$ (Fig. 5.19 (c)) and all other dislocations show single-line contrast. The result of the contrast analyses for dislocations 1-7 are summarized in Table. 5.2 where '+/-' symbols indicate visibility or extinction of dislocation contrast.
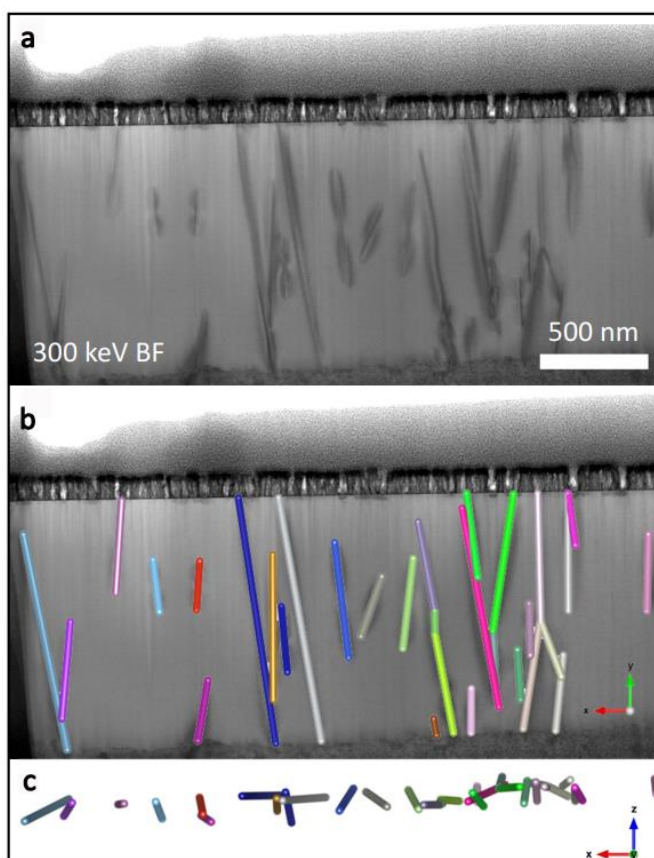
Figure 5.18. (a) 300 keV BF-STEM image of a GaN sample obtained with the Titan microscope, (b) top-view of 3D reconstructed dislocations including the top-view BF-STEM image, (c) side-view of 3D reconstructed dislocations. Scale bar in (a) applies to (b,c).
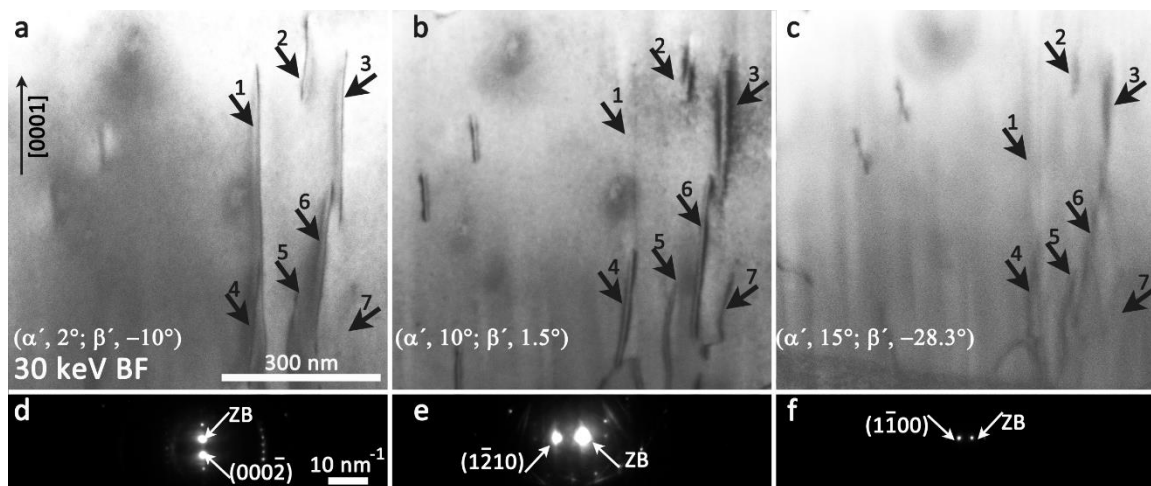
Figure 5.19. 30 keV BF-STEM images of a GaN sample and corresponding TED patterns for different two-beam conditions (a,d) $(000\bar{2})$, (b,e) $(1\bar{2}10)$, and (c,f) $(1\bar{1}00)$. ZB and strongly excited Bragg reflections are marked in (d,e,f). The settings of the α' and β' tilt angle are given in the BF-STEM images. Scale bars in (a) and (d) apply to all BF-STEM images and diffraction patterns, respectively [140].

Only dislocations 1 and 7 show contrast extinction for two different imaging vectors which allows straightforward Burgers vector determination. According to the (in)visibility of these dislocations, the Burgers vectors must be parallel to [0001] (dislocation 1) and parallel to $[11\bar{2}0]$ (dislocation 7). With dislocation line directions along or close to [0001], dislocation 1 is a screw and dislocation 7 an edge dislocation. The other dislocations in Fig. 5.19 do not show any contrast extinctions. However, even without contrast extinctions we can assign Burgers vectors based on previous work on dislocations in hexagonal lattices in general and specifically in GaN [112, 127, 138]. Burgers vectors of the type [0001] (corresponding to the direction and length of the $\vec{c}$-lattice parameter), $1/3\langle11\bar{2}0\rangle$ (corresponding to the direction and length of the $\vec{a}$-lattice parameter) and $1/3\langle11\bar{2}3\rangle$ (corresponding to the direction and length of $(\vec{c}+\vec{a})$) were previously observed. The acute brackets indicate that several crystallographic equivalent directions of this type exist, e.g., there are six independent Burgers vectors for $1/3\langle11\bar{2}3\rangle$ dislocations. Due to the pre-knowledge of possible Burgers vectors, further assignments can be made. From the visibility of dislocations 2-6 for $(000\bar{2})$, $(1\bar{2}10)$ and $(1\bar{1}00)$ we can conclude that they must be mixed dislocations. Therefore, six possible Burgers vectors $(1/3\,[\bar{2}113],\ 1/3\,[\bar{2}11\bar{3}],\ 1/3\,[1\bar{2}13],\ 1/3\,[1\bar{2}1\bar{3}],\ 1/3\,[11\bar{2}3]$ and $1/3\,[11\bar{2}\bar{3}]$) for mixed dislocations are expected [140].

Although caution is necessary to interpret details of dislocation line contrast, different dislocation line contrast in Figs. 5.19 (a-c) can be exploited for further Burgers vector specification. The observation of double-line contrast for most dislocations in Figs. 5.19 (a,b) suggests $|\vec{g} \cdot \vec{b}| = 2$ (for $|\vec{s_g}| = 0$) because double-line contrast is frequently obtained under these conditions [42, 51, 61]. The mixed dislocations with pronounced double-line contrast in Fig. 5.19 (b) are therefore, only compatible with $1/3\,[1\bar{2}13]$ and $1/3\,[1\bar{2}1\bar{3}]$ Burgers vectors to fulfill $|\vec{g} \cdot \vec{b}| = 2$ using $(1\bar{2}10)$. This assignment is consistent with Fig. 5.19 (c) where these dislocations show single-line contrast as expected for $\vec{g} \cdot \vec{b} = 1$ with $\vec{g} = (1\bar{1}00)$. Double-line contrast of dislocations in GaN under $\vec{g} \cdot \vec{b} = 2$ conditions is also seen in a TEM image published by Ponce et al. [138], although the authors did not exploit this contrast feature in their Burgers vector analyses.

We exclude that double-line contrast results from dislocation dissociation into partial dislocations although high-resolution annular dark-field STEM performed by Hirsch et al. [139] indicates dissociation of threading dislocation cores with $1/3\,\langle11\bar{2}3\rangle$ Burgers vector in an epitaxial GaN layer. However, dissociation widths are only in the order of nanometers, which is far too small to be resolved by BF-STEM imaging with $|\vec{s}_g| = 0$ in a SEM [140].

Table 5.2. Visibility (+)/extinction (-) of dislocation contrast and $\vec{g} \cdot \vec{b}$ of dislocations 1-7 in Fig. 5.19 for different two-beam conditions [140].

Two-beam condition	1	2	3	4	5	6	7
$(000\bar{2})$	+	+	+	+	+	+	-
$|\vec{g} \cdot \vec{b}|$	2	2	2	2	2	2	0
$(1\bar{2}10)$	-	+	+	+	+	+	+
$|\vec{g} \cdot \vec{b}|$	0	2	2	2	2	2	1
$(1\bar{1}00)$	-	+	+	+	+	+	-
$|\vec{g} \cdot \vec{b}|$	0	1	1	1	1	1	0
Burgers vector	[0001]	$1/3\,[1\bar{2}13]$	$1/3\,[1\bar{2}13]$	$1/3\,[1\bar{2}13]$	$1/3\,[1\bar{2}13]$	$1/3\,[1\bar{2}13]$	$1/3\,[11\bar{2}0]$
		$1/3\,[1\bar{2}1\bar{3}]$	$1/3\,[1\bar{2}1\bar{3}]$	$1/3\,[1\bar{2}1\bar{3}]$	$1/3\,[1\bar{2}1\bar{3}]$	$1/3\,[1\bar{2}1\bar{3}]$	
Dislocation type	screw	mixed	mixed	mixed	mixed	mixed	edge

5.4.2 Other parameters affecting STEM dislocation contrast

Not only $\vec{g} \cdot \vec{b}$ affects dislocation contrast but also other factors such as excitation error with the corresponding effective extinction distance, electron energy, electron current and beam convergence angle have great influence on dislocation contrast. These effects will be discussed in this subsection.

Impact of the excitation error on dislocation contrast

As discussed before, reducing $\xi_{g,eff}$ can in principle lead to narrower line contrast for dislocations. This can be achieved by using a weak-beam condition. Figs. 5.20 (a-d) display 30 keV BF-STEM images of a GaN sample obtained under 3**g**, **g**, -**g** and -3**g** two-beam conditions using **g** = (0002) while Figs. 5.20 (e-h) are DF-STEM images recorded under **g**/3**g** weak-beam, **g** two-beam, -**g** two-beam and -**g**/-3**g** weak-beam conditions, respectively. The insets in Fig. 5.20 display the diffraction conditions for acquisition of corresponding images. The rectangles in the insets mark the beams which were applied for obtaining the STEM images in Fig. 5.20. In Helios Nanolab G4 FX, the two-beam or weak-beam conditions can only be reached with uncontrollable excitation errors because changing from diffraction to STEM mode needs to retract and then reinsert the sample holder. However, the tilting accuracy of the sample holder is $\pm 1°$. Because of excitation error, extra diffracted beams marked by circles in the insets (Fig. 5.20) exist in the two-beam and weak-beam conditions.

On first sight, Figs. 5.20 (e,h) taken under $(\pm(\mathbf{g}/3\mathbf{g}))$ weak-beam conditions show sharper dislocation lines compared with the other images in Fig. 5.20 because of the larger excitation error. The lower dislocation contrast shown in Figs. 5.20 (e,h) is due to the low intensity of the diffracted beam. Hence, it is necessary to use longer exposure time or higher beam current to obtain weak-beam DF images. All other images in Fig. 5.20 taken under either two-beam or high order two-beam conditions can display sharp dislocation contrast. However, the background intensity of those images is less homogeneous with more obvious trenches compared with Figs. 5.20 (e,h) because two-beam (Figs. 5.20 (b,c,f,g)) or high order two-beam conditions (Figs. 5.20 (a,d)) are stronger diffraction conditions compared with weak-beam conditions.

Intensity line profiles (Fig. 5.21) were acquired along the white arrows in Fig. 5.20. The motivation for this is to understand how different low-keV imaging conditions will affect

the width of dislocation line contrast. As shown in Fig. 5.21, the dislocation intensity line profiles change dramatically for different imaging conditions. However, it is hard to measure the width of the dislocation lines since trenches and Ga islands on the GaN surface lead to a complex background contrast for images in Fig. 5.20. Further research is needed in order to establish a reliable method to analyze the width of dislocation lines for different imaging conditions.

Figs. 5.22 (a-h) display low-keV STEM images for the same area in Fig. 5.20 taken with a different imaging vector $\vec{g}_{(1\bar{1}00)}$ and much larger α', β' tilting angles which increase the specimen thickness. Comparing BF images (Figs. 5.22 (a-d)) with DF images (Figs. 5.22 (e-h)), the dislocations in the DF images are blurred because of the low signal-to-noise ratio. This illustrates that low-keV BF-STEM imaging is more suitable for dislocation imaging with large specimen thickness compared to low-keV DF-STEM imaging.

Compared with STEM/TEM at high electron energies, extinction lengths ξ_g in low-keV STEM/SEM are generally smaller (e.g. $\xi_{g(0002)-30keV}=25$ nm and $\xi_{g(0002)-200keV}=50$ nm) which is favorable for achieving smaller dislocation widths [42]. This is especially beneficial for investigation of samples with high dislocation densities. With examples in Figs. (5.20-5.22), one can see that two-beam and high-order two-beam conditions can be achieved conveniently at low energies for dislocation analysis. Besides, $\pm(\mathbf{g}/3\mathbf{g})$ weak-beam DF conditions can also be realized in low-keV STEM for imaging dislocations with comparably small dislocation line widths. Even though at high tilting angle low-keV DF-STEM images have poor signal-to-noise ratio, it still indicates the potential for applying low-keV STEM in SEM for dislocation characterization.
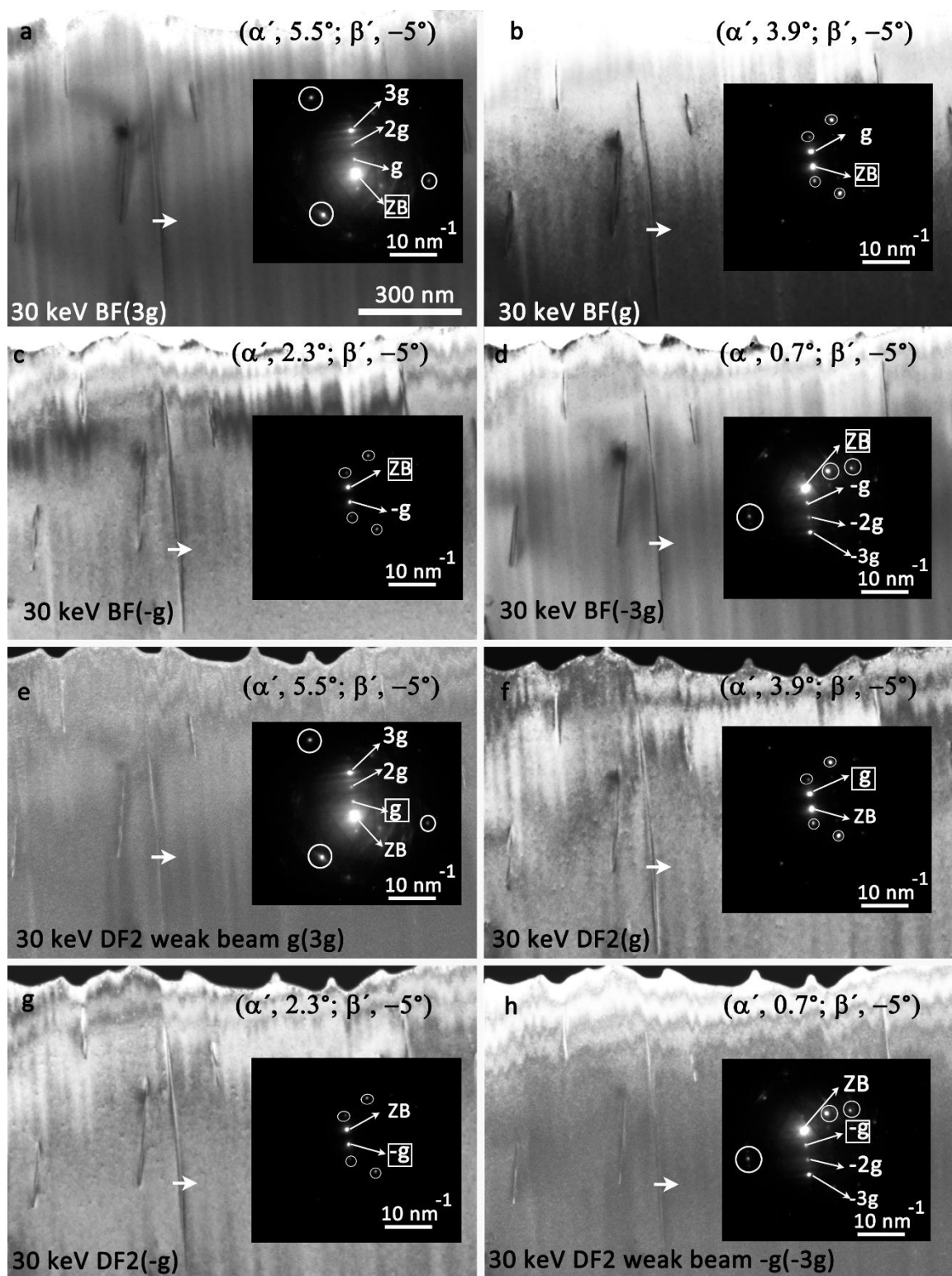
Figure 5.20. 30 keV BF-STEM images of a GaN sample taken with **g**=(0002) under (a) 3**g**, (b) **g**, (c) -**g** and (d) -3**g** two-beam conditions. DF-STEM images recorded under (e) **g**/3**g** weak-beam, (f) **g** two-beam, (g) -**g** two-beam and (h) -**g**/-3**g** weak-beam conditions. Scale bar in (a) applies to (b-h).

a BF two-beam (3g)

b BF two-beam (g)

c BF two-beam (-g)

d BF two-beam (-3g)

e DF two-beam g(3g)

f DF two-beam (g)

g DF two-beam (-g)
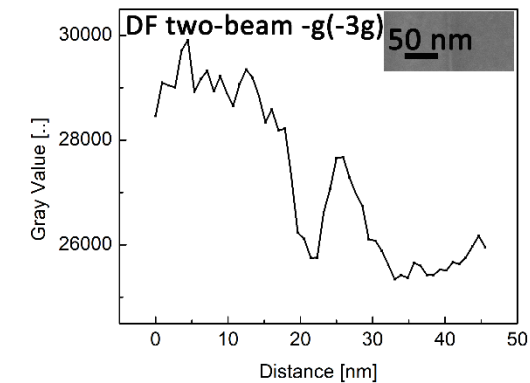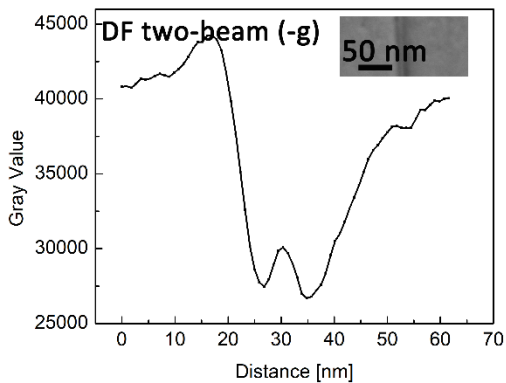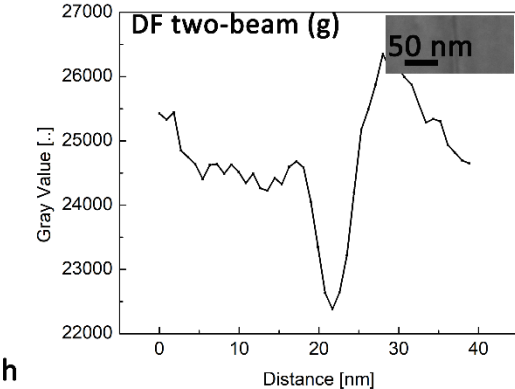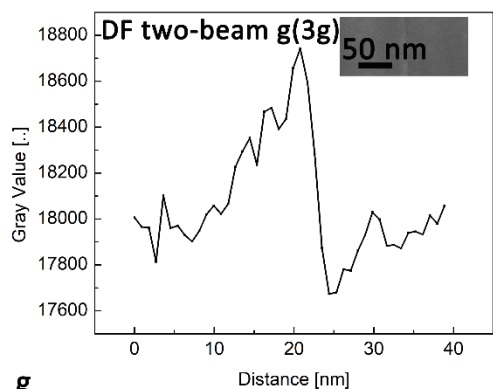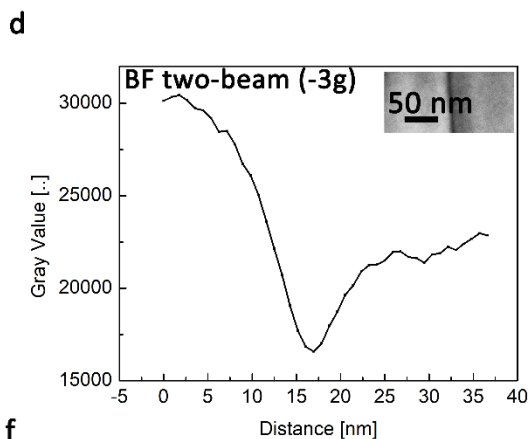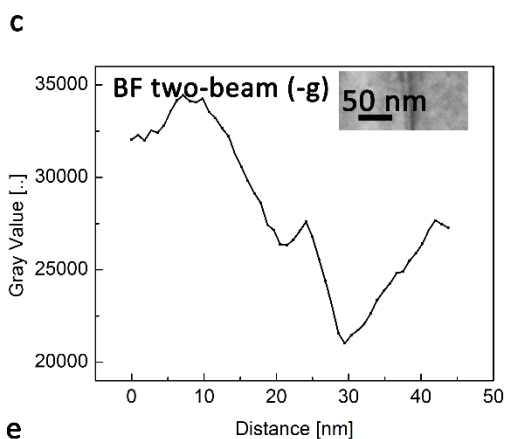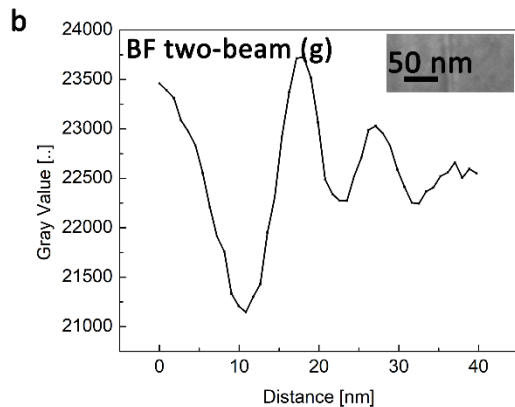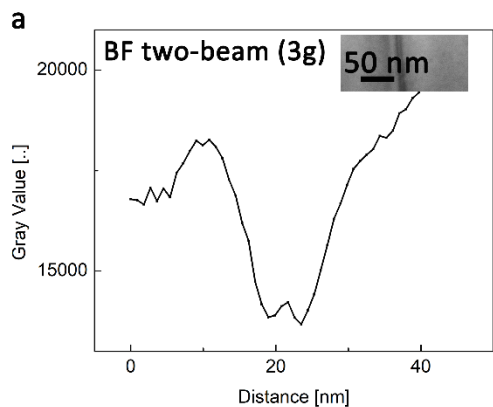
h DF two-beam -g(-3g)

Figure 5.21. Intensity line profiles across STEM images of a mixed dislocation in GaN imaged under BF two-beam conditions of the type (a) 3**g**, (b) **g**, (c) -**g** and (d) -3**g** and DF conditions of the type (e) **g**/3**g** weak-beam, (f) **g** two-beam, (g) -**g** two-beam and (h) -**g**/-3**g** weak-beam conditions with **g** = (0002).
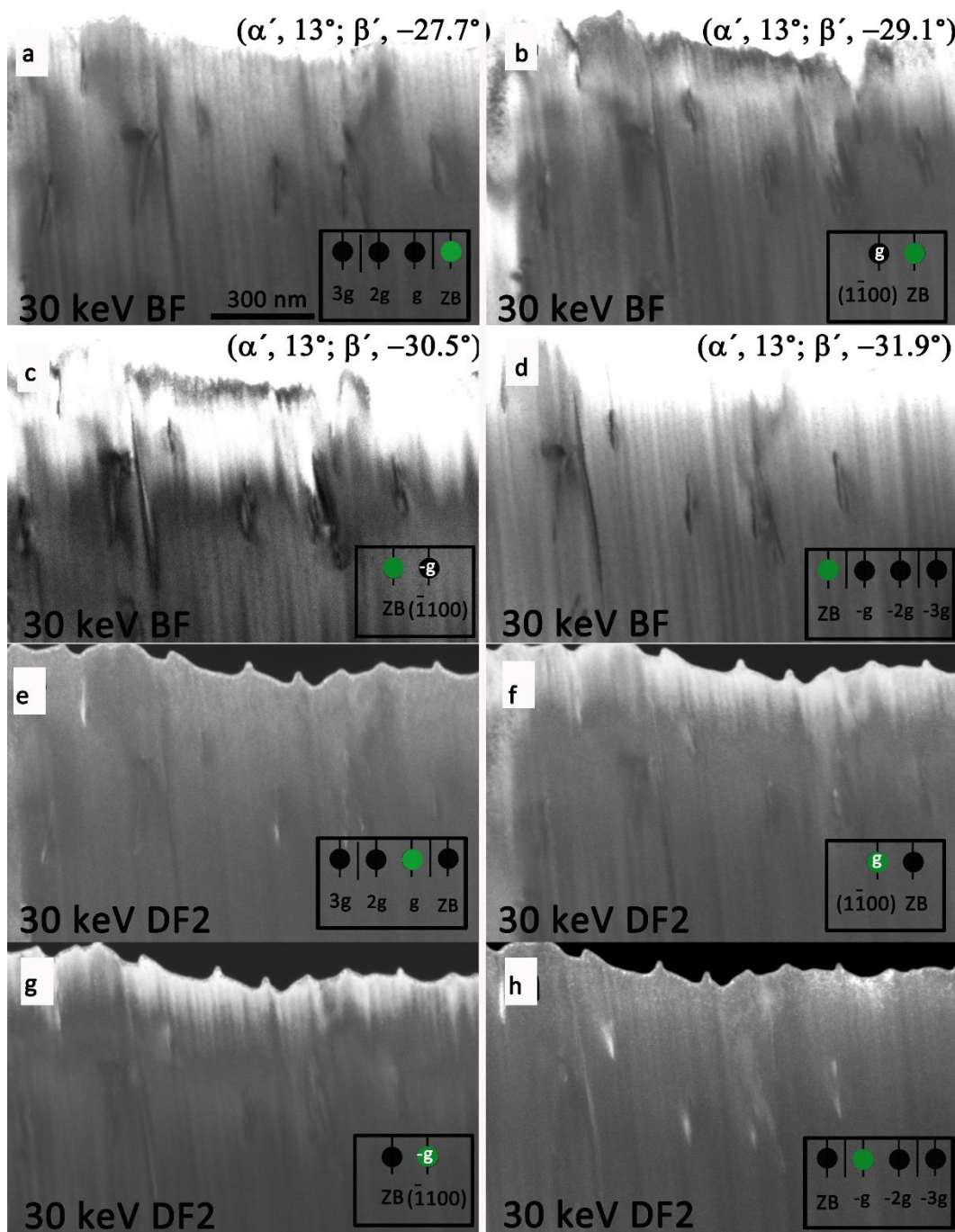
Figure 5.22. 30 keV BF-STEM images of a GaN sample using $\mathbf{g} = (1\bar{1}00)$ obtained under (a) 3**g**, (b) **g**, (c) -**g** and (d) -3**g** two-beam conditions. DF-STEM images recorded

with (e) **g**/3**g** weak-beam, (f) **g** two-beam, (g) -**g** two-beam and (h) -**g**/-3**g** weak-beam conditions. Scale bar in (a) applies to (b-h).

Impact of electron energy on dislocation contrast
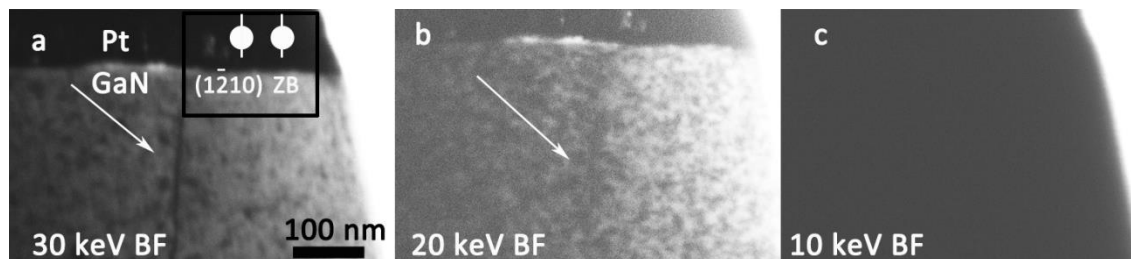
Figure 5.23. BF-STEM images of a GaN sample obtained under ($1\bar{2}10$) two-beam conditions with (a) 30 keV, (b) 20 keV and (c) 10 keV. Scale bar in (a) applies to (b,c) [140].

Fig. 5.23 is an example to demonstrate the effect of electron energy (30 keV, 20 keV, 10 keV) on dislocation contrast using BF-STEM ($1\bar{2}10$) two-beam conditions. At 30 keV, a dislocation (marked by a white arrow) is displayed clearly in Fig. 5.23 (a). With the energy decreasing to 20 keV, Fig. 5.23 (b) still shows a blurred dislocation image. However, for an electron energy of 10 keV (Fig. 5.23 (c)), the dislocation cannot be recognized anymore in a specimen region with a thickness of ∼150 nm.

Impact of electron-beam current on dislocation contrast

With the same sample from Fig. 5.23, the effect of electron-beam current on dislocation contrast in low-keV BF-STEM images taken at 20 keV with the same exposure time is investigated (Fig. 5.24). Under ($1\bar{2}10$) two-beam condition, the dislocation marked with a white arrow shows strong contrast in Fig. 5.24 (a) taken with a beam current of 0.2 nA. With decreasing beam current (25 pA), the dislocation contrast becomes weaker in Fig. 5.24 (b). With a 13 pA beam current, the dislocation cannot be recognized anymore in Fig. 5.24 (c) due to the low signal-to-noise ratio. This illustrates that increasing electron current can improve the contrast of defects to a certain degree. Theoretically, increasing exposure times are expected to have the same effect as increasing beam current. However, sample drift may affect the sharpness of dislocation contrast with increasing exposure time.
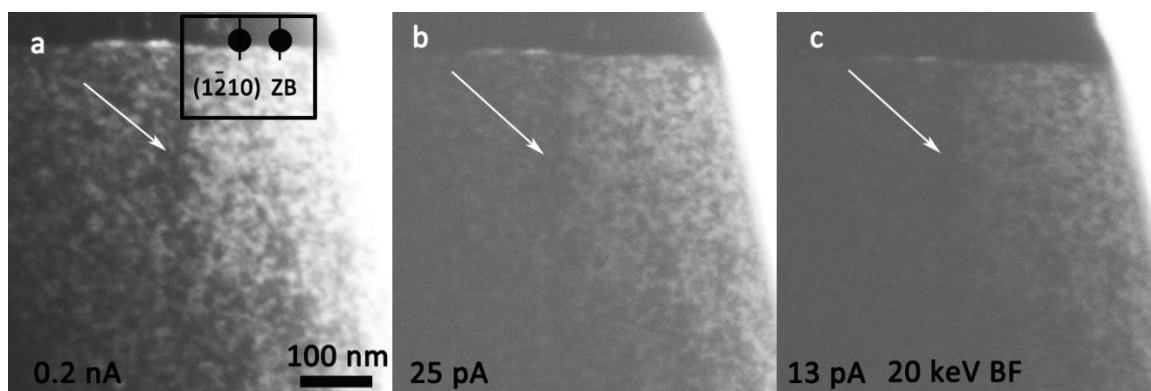
Figure 5.24. 20 keV BF-STEM images of a GaN sample obtained under (1$\bar{2}$10) two-beam condition with electron current (a) 0.2 nA, (b) 25 pA and (c) 13 pA. Scale bar in (a) applies to (b,c).

Impact of beam convergence angle on dislocation contrast

The influence of the beam convergence angle on diffraction contrast in BF-STEM images is illustrated in Fig. 5.25. The same specimen region is imaged with a small convergence angle (1.7 mrad) in the field-free mode (Fig. 5.25 (a)) and with a large convergence angle (around 10 mrad) in the immersion mode (Fig. 5.25 (b)). It is obvious that bend contours indicated by black arrows are more severe for a smaller beam convergence angle compared Fig. 5.25 (a) with Fig. 5.25 (b). However, diffraction contrast of dislocations is not strongly impaired by the bend contours in Fig. 5.25 (a). The immersion mode is in general not well suited for diffraction contrast analyses using two-beam conditions because diffraction patterns are distorted and overlap of Bragg discs may occur [140]. Therefore, except for Fig. 5.25 (b), all other defect imaging utilizing the low-keV STEM method presented in this thesis were obtained under field-free mode in SEMs.

Study showed an optimal large beam convergence angle and BF-STEM collection angle (a few mrad) can alleviate bend contours [121] and produce a uniform background for STEM imaging of dislocations. However, when beam convergence angle is enlarged too much, the generated short depth of field will reduce the intensity of dislocations in BF-STEM images [121]. Furthermore, the overlapping of diffraction discs due to a big beam convergence angle can lead to obvious degradation of DF-STEM images. Therefore, the optimized condition for dislocation characterization with STEM detector is a large beam convergence angle precluding diffraction disc overlap combined with a similar large BF-STEM collection angle.
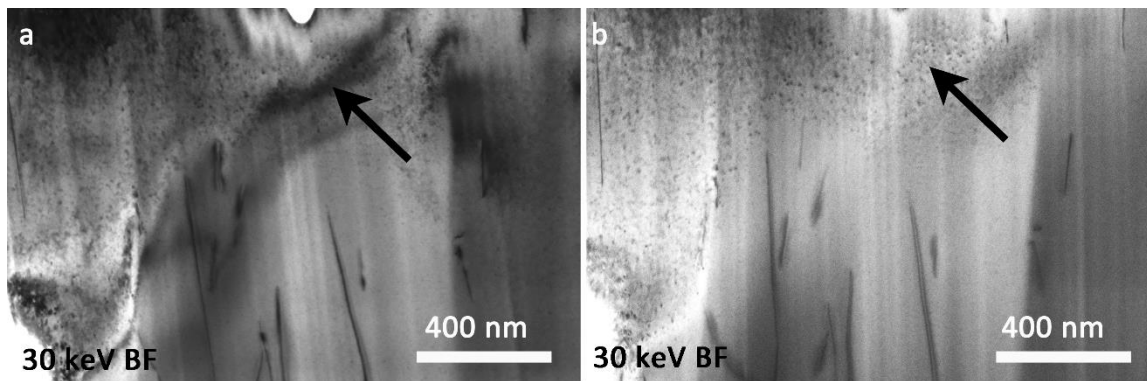
Figure 5.25. 30 keV BF-STEM images of the same specimen region taken (a) in the field free mode (convergence angle 1.7 mrad) and (b) in the immersion mode (convergence angle 10 mrad). The images were taken with a collection angle of 7 mrad in both cases [140].

5.4.3 Displacement vector analysis of stacking faults
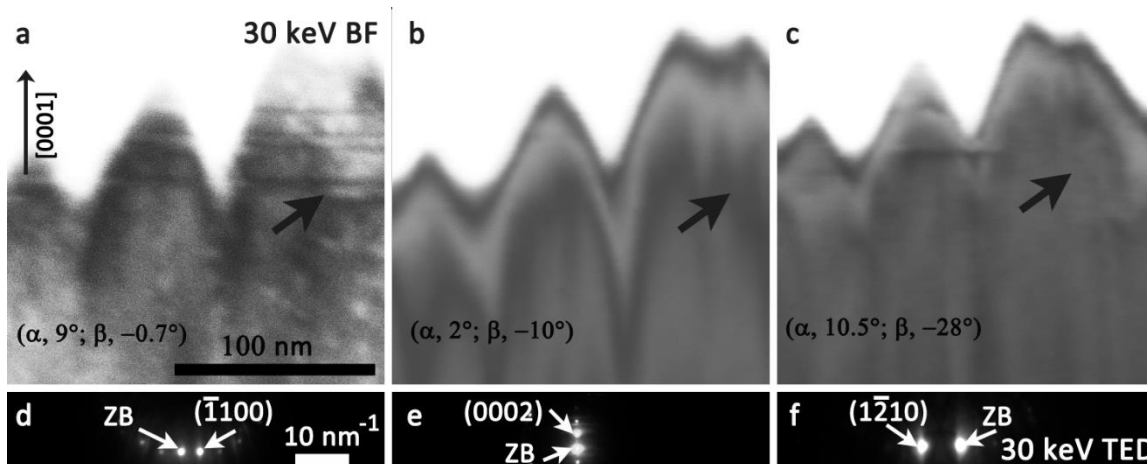
Figure 5.26. 30 keV BF-STEM cross-section images of a GaN sample and corresponding TED patterns for different two-beam conditions using (a,d) ($\bar{1}100$), (b,e) (0002), (c,f) ($1\bar{2}10$). Scale bars in (a) and (d) apply to all BF-STEM images and diffraction patterns, respectively [140].

The 30 keV cross-section BF-STEM image of the GaN layer in Fig. 5.26 (a) shows several stacking faults on the (0001) basal plane in the region marked by the back arrow. These stacking faults are out of contrast for $\mathbf{g} = (0002)$ and ($1\bar{2}10$) (Figs. 5.26 (b,c)). The invisibility of the stacking faults is compatible with I_1- or I_2-type stacking faults while extrinsic stacking faults ($\vec{R} = 1/2[0001]$) can be ruled out on the basis of the $\vec{g} \cdot \vec{R} = n$ criterion. Distinction between I_1- and I_2-type intrinsic stacking faults is not possible with

the three diffraction conditions applied and would require to image fringe contrast changes of SFs with additional diffraction conditions. In addition, thickness fringes are observed in Figs. 5.26 (b,c) which yield an estimate of the specimen thickness at the location of the stacking faults. Fig. 5.26 (b) shows a dark fringe at the specimen edge, indicating that the local thickness must be at least $0.5\,\xi_g$. The majority of the stacking faults are located in a region with a thickness of at least $1.5\,\xi_g$ which corresponds to a thickness of 37.5 nm with $\xi_{g(0002)}$=25 nm. This consideration demonstrates that Bragg diffraction contrast is not impaired at 30 keV with moderate specimen thickness [140].

At the beginning of the defect studies presented in this work, imaging with backscattered electrons in a Quanta 650 SEM was applied to obtain sample orientation information since BSE channeling contrast is related to crystal orientation. However the ECP image displaying Kikuchi bands directly is only available for single crystals at low magnification. At high(er) magnification, the intensity change by ECCI imaging during tilting could theoretically yield orientation information. However, the experimental ECCI results did not show a clear relation to the sample orientation. For the second approach, the transmitted electrons in a Strata 400S SEM were utilized in order to obtain sample orientation information with a segmented STEM detector. Even though the procedure was time-consuming, the intensity change for low-keV BF-STEM and HAADF-STEM images during tilting yields sample orientation information. However, the single-tilt holder limit adds a degree of difficulty to this approach, not to mention the need of a priori orientation information of the specimen. The third approach for defects analysis was made possible by the recently introduced on-axis CCD-camera and double-tilt holder for SEMs. The compustage in the Helios with the double-tilt holder allows to control the specimen orientation and set up defined two-beam conditions by taking TED patterns with the on-axis CCD-camera. The small electron beam convergence angle and BF-STEM collection angle prevent the overlap of diffracted and undiffracted beam in two-beam conditions. Therefore, systematic analyses of dislocation Burgers vectors $\vec{b}$ and distinction of stacking faults types were performed with low-keV STEM in the Helios SEM by exploiting the $\vec{g} \cdot \vec{b} = n$ and $\vec{g} \cdot \vec{R} = n$ criteria, respectively. Using FIB-prepared TEM specimens, which were not specifically optimized for a particularly small sample thickness, diffraction contrast of dislocations and stacking faults is not impaired at 30 keV and even lower electron energies like 20 keV and 10 keV. In addition to the invisibility

of defect contrast, specific dislocation contrast features such as single-line and double-line contrast appear and can be exploited in Burgers vector analyses. This demonstrates that diffraction contrast analyses of defects which are traditionally performed in a TEM can be well carried out by low-keV STEM in a modern SEM equipped with STEM-detector, on-axis CCD-camera and a double-tilt specimen holder. Moreover, the surface topography of the prepared TEM sample can be imaged by secondary electron detectors which supports STEM contrast interpretation by revealing specimen thickness changes and other topography effects that influence STEM contrast. It also demonstrates how to improve dislocation contrast with low-keV STEM according to factors like sample thickness, excitation error, electron energy, electron current and electron beam convergence angle.

6 SUMMARY

With the ongoing development of electron microscopy technology, state-of-the-art scanning electron microscopes (SEMs) are far beyond their initial ability of imaging bulk specimens. For example, the installation of a scanning transmission electron microscopy (STEM) detector extends the capabilities of SEMs to investigate electron-transparent specimens in transmission mode. Since the electron energy in a SEM is low compared to conventional STEM, it is referred to as low-keV STEM in the following. Low electron energies ($\leq 30\,keV$) provide advantages compared to STEM at high electron energies ($\geq 80\,keV$) like reduced knock-on damage for the analysis of beam-sensitive materials and improved contrast of weakly scattering materials due to increased scattering cross-sections. The addition of an on-axis charge-coupled device (CCD)-camera in most recent instruments provides direct access to diffraction patterns. Contrary to transmission electron microscopes, SEMs are equipped with several secondary electron (SE) and backscattered electron (BSE) detectors providing complementary information that is not accessible in a transmission electron microscope. Projected structure information on the interior of a sample observed in STEM images is in this way complemented by three-dimensional topography information of features. Although spatial resolution is not yet competitive with high-energy STEM, it is shown in this thesis that low-keV STEM and, in particular, correlative SEM and low-keV STEM imaging of the same specimen region is interesting for comprehensive material characterization. Hence, a wide range of material classes (soft-matter materials, micro- and nano-structured materials and a selection of solid-state materials including magnetic steel) was investigated in this thesis to illustrate the benefits of correlative SEM/low-keV STEM. The second part of this thesis focuses on methods to characterize dislocations and stacking faults in a SEM.

Correlative SEM and low-keV STEM is particularly well suited for the study of nanostructured materials with pronounced topography and small sample thickness. For example, combining high-angle annular dark-field (HAADF-) and bright-field (BF-) STEM with SE- and BSE-SEM yielded comprehensive information on a catalytically active material consisting of porous Al_2O_3 with dispersed Pt nanoparticles. For mesoporous silica and ZnO nanoparticles, the combination of SEM topography contrast and mass-thickness STEM contrast allowed to straightforwardly distinguish between voids and surface features. Other investigated nanostructured materials were carbon

nanotubes and other various nanoparticles. For these materials topography SEM imaging is essential to obtain complete microstructure information. For very thin samples like multiwalled carbon nanotubes, 0.37 nm lattice distances were resolved by BF-STEM lattice fringe imaging demonstrating the improvement of resolution in modern SEMs. Soft-matter materials with small material density and average atomic number are also particularly well suited for low-keV STEM because contrast is improved by enhanced scattering at low electron energy. Preliminary studies of thin sections of biological cells and microparticles consisting of two different polymers indicate the potential of the technique because staining can be reduced to a minimum.

Correlative SEM/low-keV STEM imaging is not confined to imaging nanostructured materials. Samples from several different bulk materials prepared by conventional techniques were shown to be well suited for correlative SEM/low-keV STEM imaging. For example, magnetic steel can be conveniently investigated in the field-free operation mode in SEMs avoiding microscope realignment, which is frequently necessary in a transmission electron microscope due to the interaction with the magnetic field of the objective lens. Bragg diffraction contrast revealed dislocations by low-keV BF-STEM imaging. Information on grain sizes over macroscopic regions of the prepared TEM specimen far away from the electron transparent area was obtained by SE channeling contrast. Further investigations of samples prepared from bulk materials like $SrTiO_3$ illustrate that correlative SEM/low-keV STEM in combination with on-axis transmission (t-) EBSD mapping yields additional information on grain orientations and grain sizes. The spatial resolution of on-axis t-EBSD is improved compared to the more conventional off-axis t-EBSD because the sample is not tilted which leads to a smaller specimen thickness and interaction volume. It was shown in several cases that topography contrast supports the interpretation of STEM contrast and vice versa.

Thin flakes of xonotlite and tobermorite were investigated as examples for radiation sensitive materials. Comparative TEM investigation on xonotlite at 300 keV illustrates strong knock-on damage in these materials where lattices fringes quickly disappeared within less than one minute after exposure by electron beam. In contrast, amorphization can be prevented for longer time and lattice fringes remain visible for at least 60 s if high-resolution low-keV BF-STEM is performed.

The second part of this thesis was devoted to the characterization of dislocations and stacking faults in SEMs which up to now was only possible in a deterministic manner in a transmission electron microscope. The main obstacle to this goal was the necessity to tilt specimens in well-defined two-beam diffraction conditions, which requires a double-tilt specimen holder and methods to determine the crystal orientation. Using the on-axis CCD-camera, two-beam diffraction conditions could be set up to determine dislocation Burgers vectors and displacement vectors of stacking faults in GaN on the basis of the $\vec{g} \cdot \vec{b}$ or $\vec{g} \cdot \vec{R}$ criterion in analogy to defect analysis by TEM. For diffraction contrast analyses it is advantageous that the curvature of the Ewald sphere increases with decreasing electron energy and allows to set up two-beam conditions with weaker excitation of other Bragg reflections. Another advantage consists in smaller extinction distances at low electron energies, yielding narrower dislocation line contrast compared to high-energy (S)TEM imaging. If a CCD-camera is not available, a new method of utilizing a segmented STEM detector was introduced in this work for tilting TEM samples into well-defined diffraction conditions.

Monte-Carlo (MC) simulations were frequently used in this work and were shown to be essential to achieve a general understanding of HAADF-STEM contrast. For example, MC simulations revealed the origin of contrast inversion between strongly and weakly scattering materials in low-energy HAADF-STEM which is at first sight counterintuitive. MC simulations also showed the strong thickness dependence of low-keV STEM which can be exploited for sample thickness determination.

Correlative SEM/low-keV STEM was demonstrated in this work to be a promising technique in materials research. Further developments in this direction are certainly motivated by the wide availability of scanning electron microscopes. Although all mandatory accessories for the control of the specimen orientation are commercially available meanwhile, the choice of collection angles is limited in SEMs because a projection lens system is missing. In addition, the convergence angle of Helios Nanolab G4 FX cannot be adjusted freely as there is no user access to the condenser system. This limitation prevents diffraction-contrast optimization by adequate selection of convergence and collection angles to reduce bend and thickness contours in diffraction-contrast STEM images. Future technical developments in scanning electron microscopy are therefore desirable to allow for the variation of the camera length. A huge potential

lies in the extension of correlative SEM/low-keV STEM to include other techniques which are routinely available in scanning electron microscopes. This comprises, e.g., cathodoluminescence (CL), electron-beam-induced current (EBIC) and in-situ studies (mechanical and electrical testing), which are restricted in transmission electron microscopes due to limited space.

7 REFERENCES

1. Knoll, M., et al., *Beitrag zur geometrischen elektronenoptik. I.* Annalen der Physik, 1932. **12**(5): p. 607-640.

2. Von Ardenne, M., *On the history of scanning electron microscopy, of the electron microprobe, and of early contributions to transmission electron microscopy* in *the beginnings of electron microscopy*. 1985, Academic Press Orlando. p. 1-21.

3. Krivanek, O.L., et al., *Atom-by-atom structural and chemical analysis by annular dark-field electron microscopy.* Nature, 2010. **464**(7288): p. 571-574.

4. Kaiser, U., et al., *Transmission electron microscopy at 20kV for imaging and spectroscopy.* Ultramicroscopy, 2011. **111**(8): p. 1239-1246.

5. Bell, D.C., et al., *40keV atomic resolution TEM.* Ultramicroscopy, 2012. **114**: p. 31-37.

6. Bell, D.C., et al., *Low voltage electron microscopy: principles and applications*. 2013, West Sussex: John Wiley & Sons. p. 3-28.

7. Bell, D.C., et al., *Successful application of low voltage electron microscopy to practical materials problems.* Ultramicroscopy, 2014. **145**: p. 56-65.

8. Egerton, R., *Choice of operating voltage for a transmission electron microscope.* Ultramicroscopy, 2014. **145**: p. 85-93.

9. Linck, M., et al., *Chromatic aberration correction for atomic resolution TEM imaging from 20 to 80 kv.* Phys. Rev. Lett., 2016. **117**(7): p. 076101.

10. Suenaga, K., et al., *Visualizing and identifying single atoms using electron energy-loss spectroscopy with low accelerating voltage.* Nat. Chemi., 2009. **1**(5): p. 415-418.

11. Dellby, N., et al., *Dedicated STEM for 200 to 40 keV operation.* Eur. Physi. J-Appl. Phys., 2011. **54**(3).

12. Sasaki, T., et al., *Evaluation of probe size in STEM imaging at 30 and 60kV.* Micron, 2012. **43**(4): p. 551-556.

13. Sasaki, T., et al., *Aberration-corrected STEM/TEM imaging at 15kV.* Ultramicroscopy, 2014. **145**: p. 50-55.

14. Merli, P., et al., *Low-energy STEM of multilayers and dopant profiles.* Microsc. Microanal., 2005. **11**(1): p. 97-104.

15. Morandi, V., et al., *Scanning electron microscopy of thinned specimens: from multilayers to biological samples.* Appl. phys. lett., 2007. **90**(16): p. 163113.

16. Morandi, V., et al., *Contrast and resolution versus specimen thickness in low energy scanning transmission electron microscopy.* J. Appl. Phys., 2007. **101**(11): p. 114917.

17. Volkenandt, T., et al., *Quantification of sample thickness and In-concentration of InGaAs quantum wells by transmission measurements in a scanning electron microscope.* Microsc. Microanal., 2010. **16**(5): p. 604-613.

18. Pfaff, M., et al., *Low-energy electron scattering in carbon-based materials analyzed by scanning transmission electron microscopy and its application to sample thickness determination.* J. Microsc., 2011. **243**(1): p. 31-39.

19. Klein, T., et al., Chapter *6-TSEM: a review of scanning electron microscopy in transmission mode and its applications.* Adv. Imag. Elect. Phys., 2012. **171**: p. 297.

20. Volkenandt, T., et al., *Sample thickness determination by scanning transmission electron microscopy at low electron energies.* Microsc. Microanal., 2014. **20**(1): p. 111-123.

21. Hondow, N., et al., *STEM mode in the SEM: a practical tool for nanotoxicology.* Nanotoxicology, 2011. **5**(2): p. 215-227.

22. Blank, H., et al., *Application of low-energy scanning transmission electron microscopy for the study of Pt-nanoparticle uptake in human colon carcinoma cells.* Nanotoxicology, 2014. **8**(4): p. 433-446.

23. Pfaff, M., et al., *Nanomorphology of P3HT:PCBM-based absorber layers of organic solar cells after different processing conditions analyzed by low-energy scanning transmission electron microscopy.* Microsc. Microanal., 2012. **18**(6): p. 1380-1388.

24. Van Ngo, V., et al., *STEM imaging of lattice fringes and beyond in a UHR in-lens field-emission SEM.* Microsc. Today, 2007. **15**(2): p. 12-16.

25. Konno, M., et al., *Lattice imaging at an accelerating voltage of 30kV using an in-lens type cold field-emission scanning electron microscope.* Ultramicroscopy, 2014. **145**: p. 28-35.

26. Michael, J., et al., *Challenges in achieving high resolution at low voltages in the SEM.* Microsc. Microanal, 2009. **15**(S2): p. 660.

27. Keller, R.R., et al., *Transmission EBSD from 10 nm domains in a scanning electron microscope.* J. Microsc., 2012. **245**(3): p. 245-251.

28. Demers, H., et al., *Low accelerating voltage scanning transmitted electron microscope: imaging, diffraction, X-ray microanalysis, and electron energy-Loss spectroscopy at the nanoscale.* Microsc. Microanal., 2017. **23**(S1): p. 528-529.

29. Brodu, E., et al., *On-axis TKD for orientation mapping of nanocrystalline materials in SEM.* Mater. Character., 2017. **130**: p. 92-96.

30. Reimer, L., *Scanning electron microscopy: physics of image formation and microanalysis*. 2000, IOP Publishing. p. 1-444.

31. Egerton, R.F., *Physical principles of electron microscopy*. 2005, Springer. p. 1-52.

7 REFERENCES

32. Schönbrodt, L., *Purchase order for Helios Nanolab G4 FX.* 2016. p. 1-30.

33. Kawasaki, T., et al., *Beam brightness and its reduction in a 1.2-MV cold field-emission transmission electron microscope.* Ultramicroscopy, 2019. **202**: p. 107-113.

34. Kovács, A., et al., *FEI Titan G2 80-200 CREWLEY.* Journal of large-scale research facilities JLSRF, 2016. **2**: p. 43.

35. Hosokawa, F., et al., *Development of Cs and Cc correctors for transmission electron microscopy.* Microsc., 2013. **62**(1): p. 23-41.

36. Haider, M., et al., *Current and future aberration correctors for the improvement of resolution in electron microscopy.* Phil. Trans. R. Soc., 2009. **367**(1903): p. 3665-3682.

37. Zach, J., et al., *Correction of spherical and chromatic aberration in a low voltage SEM.* Optik, 1995. **98**(3): p. 112-118.

38. Joy, D.C., *Scanning electron microscopy: second best no more.* Nat. Mater., 2009. **8**(10): p. 776-777.

39. Zhu, Y., et al., *Imaging single atoms using secondary electrons with an aberration-corrected electron microscope.* Nat. Mater., 2009. **8**(10): p. 808-812.

40. Konno, M., et al., *Lattice imaging at an accelerating voltage of 30 kV using an in-lens type cold field-emission scanning electron microscope.* Ultramicroscopy, 2014. **145**: p. 28-35.

41. Liao, Y., *Practical electron microscopy and database.* 2018, www.globalsino.com/EM/.

42. Thomas, G., et al., *Transmission electron microscopy of materials.* 1979, John Wiley & Sons. p. 20-310.

43. Hettler, S., et al., *Carbon contamination in scanning transmission electron microscopy and its impact on phase-plate applications.* Micron, 2017. **96**: p. 38-47.

44. Roediger, P., et al., *Focused electron beam induced etching of silicon by chlorine gas: negative effects of residual gas contamination on the etching process.* J. Appl. Phys., 2010. **108**(12): p. 124316.

45. Wanzenboeck, H.D., et al., *Novel method for cleaning a vacuum chamber from hydrocarbon contamination.* J. Vac. Sci. Technol. A, 2010. **28**(6): p. 1413-1420.

46. Egerton, R., et al., *Radiation damage in the TEM and SEM.* Micron, 2004. **35**(6): p. 399-409.

47. Schmidt, P.F., et al., *Praxis der Rasterelektronenmikroskopie und Mikrobereichsanalyse*. 1994, Expert Verlag Renningen-Malsheim. p. 10-200.

48. Krohn, V.E., et al., *Ion source of high brightness using liquid metal.* Appl. Phys. Lett., 1975. **27**(9): p. 479-481.

49. Yao, N., *Focused ion beam systems: basics and applications*. 2007, Cambridge University Press. p. 5-16.

50. Iakoubovskii, K., et al., *Thickness measurements with electron energy loss spectroscopy.* Microsc. Res. Techniq., 2008. **71**(8): p. 626-631.

51. Williams, D.B., et al., *Transmission electron microscopy: a textbook for materials science*. 2009, Springer. p. 23-479.

52. Koch, C.C., *Nanostructured materials: processing, properties and applications*. 2006, William Andrew. p. 293-356.

53. Kanaya, K., et al., *Penetration and energy-loss theory of electrons in solid targets.* J. Phys. D-Appl. Phys., 1972. **5**: p. 43-58.

54. Kurniawan, O., et al., *Investigation of range-energy relationships for low-energy electron beams in silicon and gallium nitride.* Scanning, 2007. **29**(6): p. 280-286.

55. Wilson, G., et al., *Approximation of range in materials as a function of incident electron energy.* IEEE T. Plasma Sci., 2012. **40**(2): p. 291-297.

56. Angker, L., et al., *Quantitative analysis of the mineral content of sound and carious primary dentine using BSE imaging.* Arch. Oral Biol., 2004. **49**(2): p. 99-107.

57. Hong, Z., et al., *Quantitative backscattered electron analysis of cement paste.* Cement Concrete Res., 1992. **22**: p. 695-706.

58. Goodhew, P.J., et al., *Electron microscopy and analysis*. 2014, CRC Press. p. 170-180.

59. Cowley, J.M., *Image contrast in a transmission scanning electron microscope.* Appl. Phys. Lett., 1969. **15**(2): p. 58-59.

60. Reimer, L., *Transmission electron microscopy: physics of image formation.* 2013, Springer. p. 45-329.

61. Hirsch, P., et al., *Electron microscopy of thin crystals.* 1977, Robert E. Krieger. p. 1-548.

62. Bragg, W.H., et al., *The reflection of X-rays by crystals.* P. Roy. Soc. Lond. A MAT., 1913. **88**(605): p. 428-438.

63. Ritchie, N.W., *A new Monte Carlo application for complex sample geometries.* Surf. Interface. Anal., 2005. **37**(11): p. 1006-1011.

64. Joy, D., et al., *An empirical stopping power relationship for low-energy electrons.* Scanning, 1989. **11**(4): p. 176-180.

65. Sun, C., et al., *On the progress of scanning transmission electron microscopy (STEM) imaging in a scanning electron microscope.* Microsc. Microanal., 2018. **24**(2): p. 99-106.

66. Goudsmit, S., et al., *Multiple scattering of electrons.* Phys. Rev., 1940. **57**(1): p. 24-29.

7 REFERENCES

67.   Negreanu, C., et al., *Calculation of multiple-scattering angular distributions of electrons and positrons.* Radiat. Phys. Chem., 2005. **74**(5): p. 264-281.

68.   Rose, M., *Electron path lengths in multiple scattering.* Phys. Rev., 1940. **58**(1): p. 90.

69.   Wilkinson, A.J., et al., *Electron diffraction based techniques in scanning electron microscopy of bulk materials.* Micron, 1997. **28**(4): p. 279-308.

70.   Yuan, H., et al., *On-axis versus off-axis transmission Kikuchi diffraction technique: application to the characterisation of severe plastic deformation-induced ultrafine-grained microstructures.* J. Microsc., 2017. **267**(1): p. 70-80.

71.   Niessen, F., et al., *A systematic comparison of on-axis and off-axis transmission Kikuchi diffraction.* Ultramicroscopy, 2018. **186**: p. 158-170.

72.   Lubomir, T., *Configurable charged-particle apparatus*. 2014, Google Patents.

73.   S, L., *Formation of porous layers with different morphologies during anodic etching of n-InP.* Electrochem. Solid St. Lett., 2000. **3**: p. 514-516.

74.   Klaar, H.-J., et al., *A new preparation method for cross-sectional TEM specimens.* Mater. Charact. 1996. **36**: p. 365-369.

75.   Langford, R., et al., *In situ lift-out: steps to improve yield and a comparison with other FIB TEM sample preparation techniques.* Micron, 2008. **39**(8): p. 1325-1330.

76.   Schaffer, M., et al., *Sample preparation for atomic-resolution STEM at low voltages by FIB.* Ultramicroscopy, 2012. **114**: p. 62-71.

77.   Joy, D.C., et al., *Electron channeling patterns in the scanning electron microscope.* J. Appl. Phys., 1982. **53**(8): p. 81-122.

78.   Teeguarden, J.G., et al., *Particokinetics in vitro: dosimetry considerations for in vitro nanoparticle toxicity assessments.* Toxicol. Sci., 2007. **95**(2): p. 300-12.

79.   Kowoll, T., et al., *Contrast of backscattered electron SEM images of nanoparticles on substrates with complex structure.* Scanning, 2017. **2017**.

80.   Kowoll, T., et al., *Quantification of SiO_2 nanoparticle sedimentation on A549 cells.* European Microscopy Conference, 2016: p. 11-12.

81.   Gehrke, H., et al., *In vitro toxicity of amorphous silica nanoparticles in human colon carcinoma cells.* Nanotoxicology, 2012. **7**(3): p. 274-293.

82.   Varadharajan, D., et al., *Surface-reactive patchy nanoparticles and nanodiscs prepared by tandem nanoprecipitation and internal phase separation.* Adv. Funct. Mater., 2018. **28**(39): p. 1800846.

83.   Jin, Z., et al., *Self-assembly of nanostructured block copolymer nanoparticles.* Soft Matter, 2014. **10**(46): p. 9212-9.

84.   Gyu-Chul, Y., et al., *ZnO nanorods: synthesis, characterization and applications.* S. Semi. Sci, 2005. **20**(4): p. S22.

85.   Cazaux, J., *From the physics of secondary electron emission to image contrasts in scanning electron microscopy.* J. Electron Microsc. (Tokyo), 2012. **61**(5): p. 261-84.

86.   Ogel, E., et al., *Impact of preparation method and hydrothermal aging on particle size distribution of Pt/γ-Al2O3 and its performance in CO- and NO-oxidation.* J. Phys. Chem. C, 2019. **123**: p. 5433-5446.

87.   Casapu, M., et al., *Origin of the normal and inverse hysteresis behavior during CO oxidation over Pt/Al_2O_3.* ACS Catalysis, 2016. **7**(1): p. 343-355.

88.   Belin, T., et al., *Characterization methods of carbon nanotubes: a review.* Mater. Sci. Eng. B-Adv., 2005. **119**(2): p. 105-118.

89.   Iiiima, S., *Helical microtubules of graphitic carbon.* Nature, 1991. **354**(6348): p. 56-58.

90.   Zhang, X.F., *Carbon nano-tubes; their formation process and observation by electron microscopy.* J. Cryst. Growth, 1993. **130**: p. 368-382.

91.   Amelinckx, S., *A structure model and growth mechanism for multishell carbon nanotubes.* Science, 1995. **267**: p. 1334-1338.

92.   Zhang, X.B., *The reciprocal space of carbon tubes: a detailed interpretation of the electron diffraction effects.* Ultramicroscopy, 1994. **54**: p. 237-249.

93.   Wang, Z.L., et al., *Polyhedral shapes of CeO_2 nanoparticles.* J. Phys. Chem. B, 2003. **107**: p. 13563-13566.

94.   Trovarelli, A., *Catalytic properties of ceria and CeO_2-containing materials.* Cataly. Rev., 1996. **38**(4): p. 439-520.

95.   Yang, Z., et al., *Atomic and electronic structure of unreduced and reduced CeO_2 surfaces: a first-principles study.* J. Chem. Phys., 2004. **120**(16): p. 7741-9.

96.   Wang, Z.L., et al., *Polyhedral shapes of CeO_2 nanoparticles.* J. Phys. Chem. B, 2003. **107**(49): p. 13563-13566.

97.   Gupta, S.M., *A review of TiO_2 nanoparticles.* Chinese Sci. Bull., 2011. **56**(16): p. 1639-1657.

98.   Horn, M., et al., *Refinement of the structure of anatase at several temperatures.* Z. Kristallogr. Cryst. Mater., 1972. **136**(1-6): p. 273-281.

99.   Egeberg, A., et al., *Bimetallic nickel-iridium and nickel-osmium alloy nanoparticles and their catalytic performance in hydrogenation reactions.* Chem. Cat. Chem., 2017. **9**(18): p. 3534-3543.

7 REFERENCES

100.   Hudry, D., et al., *Direct evidence of significant cation intermixing in upconverting Core@Shell nanocrystals: toward a new crystallochemical model.* Chem. Mater., 2017. **29**(21): p. 9238-9246.

101.   Egerton, R.F., *Mechanisms of radiation damage in beam-sensitive specimens, for TEM accelerating voltages between 10 and 300 kV.* Microsc. Res. Tech., 2012. **75**(11): p. 1550-6.

102.   Shen, D., et al., *Biphase stratification approach to three-dimensional dendritic biodegradable mesoporous silica nanospheres.* Nano. Lett., 2014. **14**(2): p. 923-32.

103.   Soni, K., et al., *3-D ordered mesoporous KIT-6 support for effective hydrodesulfurization catalysts.* Appl. Catal. B-Environ., 2009. **90**(1-2): p. 55-63.

104.   Tomar, A., *Short review on application of gold nanoparticles.* Global J. Pharmacol., 2013. **7**(1): p. 34-38.

105.   Hejny, C., et al., *Polytypism in xonotlite $Ca_6Si_6O_{17}(OH)_2$.* Z. Krist. Cryst. Mater., 2001. **216**(7): p. 396-408.

106.   Cao, J., et al., *Hydrothermal synthesis of xonotlite from carbide slag.* Prog. Nat. Sci., 2008. **18**(9): p. 1147-1153.

107.   Kim, Y.J., et al., *TEM study of synthetic hillebrandite ($Ca_2SiO_4 \cdot H_2O$).* J. Mater. Res., 1993. **8**(11): p. 2948-2953.

108.   Bonaccorsi, E., et al., *The crystal structure of tobermorite 14 angstrom (Plombierite), a C-S-H Phase.* J. Am. Ceram. Soc., 2005. **88**(3): p. 505-512.

109.   Braun, P., et al., *Separation of the bulk and grain boundary contributions to the total conductivity of solid lithium-ion conducting electrolytes.* J. Electroceram., 2017. **38**(2-4): p. 157-167.

110.   Wolff, K., et al., *Anisotropic electronic transport of the two-dimensional electron system in $Al_2O_3/SrTiO_3$ heterostructures.* Phys. Rev. B, 2017. **95**(245132): p. 1-8.

111.   Kraschewsk, S.M., *Investigation of Fe-doped $SrTiO_3$ by electron microscopy.* European Microscopy Congress. 2012.

112.   Hull, D., et al., *Introduction to dislocations*. 2001, Butterworth-Heinemann. p. 9-139.

113.   Hornbogen, E., et al., *Werkstoff-Mikroskopie: direkte durchstrahlung mit elektronen zur analyse der mikrostruktur*. 2013, Springer-Verlag. p. 10-80.

114.   Nikolaichick, V., et al., *A review of the determination of dislocation parameters using strong- and weak-beam electron microscopy.* J. Microsc., 1989. **155**(2): p. 123-167.

115.   Hitzenberger, C., et al., *Contrast analysis of intrinsic and extrinsic stacking faults in HCP cobalt.* Phys. Stat. Sol. (a), 1985. **89**(1): p. 133-146.

7 REFERENCES

116. Blank, H., et al., *Fault structures in wurtzite.* Phys. Stat. Sol. (b), 1964. **7**(3): p. 747-764.

117. Feng, J., et al., *A general procedure for analysing stacking faults and antiphase boundaries in crystals by using diffraction contrast imaging and/or defocus convergent-beam electron diffraction.* Philos. Mag. A, 1995. **72**(4): p. 1121-1130.

118. Edington, J.W., *Interpretation of transmission electron micrographs*, in *Interpretation of transmission electron micrographs*. 1975, Springer. p. 1-112.

119. Phillips, P.J.,et al., *Systematic row and zone axis STEM defect image simulations.* Philos. Mag., 2011. **91**(16): p. 2081-2101.

120. Su, X., et al., *Identifying dislocations and stacking faults in GaN films by scanning transmission electron microscopy.* Mater. Res. Express, 2016. **3**(8): p. 086401.

121. Zhu, Y., et al., *Towards bend-contour-free dislocation imaging via diffraction contrast STEM.* Ultramicroscopy, 2018. **193**: p. 12-23.

122. Callahan, P.G., et al., *Transmission scanning electron microscopy: Defect observations and image simulations.* Ultramicroscopy, 2018. **186**: p. 49-61.

123. Schweizer, P., et al., *In situ manipulation and switching of dislocations in bilayer graphene.* Sci. Adv., 2018. **4**(8): p. eaat4712.

124. Stinville, J., et al., *Dislocation dynamics in a nickel-based superalloy via in-situ transmission scanning electron microscopy.* Acta Mater., 2019. **168**: p. 152-166.

125. Gianola, D.S., et al., *New techniques for imaging and identifying defects in electron microscopy.* MRS Bulletin, 2019. **44**(6): p. 450-458.

126. Ambacher, O., *Growth and applications of group III-nitrides.* J. Phys. D: Appl. Phys, 1998. **31**(20): p. 2653.

127. Wu, X.H., et al., *Defect structure of metal-organic chemical vapor deposition-grown epitaxial (0001) GaN/Al$_2$O$_3$.* J. Appl. Phys., 1996. **80**(6): p. 3228.

128. Müller, E., et al., *Electrical activity of dislocations in epitaxial ZnO- and GaN-layers analyzed by holography in a transmission electron microscope.* Mater. Sci. Semicond. Processing, 2006. **9**(1-3): p. 127-131.

129. Kaiser, S., *Quantitative transmission electron microscopy investigation of the relaxation by misfit dislocations confined at the interface of GaN Al$_2$O$_3$ (0001).* 1998.

130. Fujita, S., *Wide-bandgap semiconductor materials: for their full bloom.* Jpn. J. Appl. Phys., 2015. **54**(3): p. 030101.

131. Rosner, S.J., et al., *Correlation of cathodoluminescence inhomogeneity with microstructural defects in epitaxial GaN grown by metalorganic chemical-vapor deposition.* Appl. Phys. Lett., 1997. **70**(4): p. 420-422.

132. Kim, H.-J., et al., *Effects of reactive ion beam treatment of a sapphire surface to optimite the deposition of GaN films.* J. Appl. Phys., 2000. **87**(11): p. 7940-7945.

133. Zheleva, T.S., et al., *Dislocation density reduction via lateral epitaxy in selectively grown GaN structures.* Appl. Phys. Lett., 1997. **71**(17): p. 2472-2474.

134. Nam, O.-H., et al., *Lateral epitaxy of low defect density GaN layers via organometallic vapor phase epitaxy.* Appl. Phys. Lett., 1997. **71**(18): p. 2638-2640.

135. Lähnemann, J., et al., *Luminescence associated with stacking faults in GaN.* J. Phys. D: Appl. Phys., 2014. **47**(42): p. 423001.

136. Lyman, C.E., et al., *Scanning electron microscopy, X-ray microanalysis, and analytical electron microscopy: a laboratory workbook*. 2012, Springer Science & Business Media. p. 3-42.

137. Jain, S.C., et al., *III–nitrides: growth, characterization, and properties.* J. Appl. Phys., 2000. **87**(3): p. 965-1006.

138. Ponce, F.A., et al., *Characterization of dislocations in GaN by transmission electron diffraction and microscopy techniques.* Appl. Phys. Lett., 1996. **69**(6): p. 770-772.

139. Hirsch, P.B., et al., *The dissociation of the [a + c] dislocation in GaN.* Philos. Mag., 2013. **93**(28-30): p. 3925-3938.

140. Sun, C., et al., *Analysis of crystal defects by scanning transmission electron microscopy (STEM) in a modern scanning electron microscope.* Adv. Struct. Chem. Imaging, 2019. **5**(1): p. 1.

8 LIST OF FIGURES AND TABLES

Figure 2.1. Simplified scheme of the components of a scanning electron microscope.

Figure 2.2. Scheme of spherical aberration of an electron lens.

Figure 2.3. Scheme of chromatic aberration of an electron lens.

Figure 2.4. Scheme of astigmatism of an electron lens.

Figure 2.5. Scheme of diffraction error of an electron lens.

Figure 2.6. Simulated effect of working distance on the beam diameter (E = 30 keV, I_p = 13 pA, ΔE = 0.5 eV, objective aperture diameter 32 μm). The red line indicates the overall beam diameter d_p. d_0, d_d, d_c and d_s show contributions of different aberrations and effects (see legend).

Figure 2.7. Simulated effect of working distance on the beam diameter (E = 2 keV, I_p = 13 pA, ΔE = 0.5 eV, objective aperture diameter 32 μm). The red line indicates the overall beam diameter d_p. d_0, d_d, d_c and d_s show contributions of different aberrations and effects (see legend).

Figure 2.8. Simulated effect of the primary electron energy on the beam diameter (WD = 2 mm, I_p = 13 pA, ΔE = 0.5 eV, α = 8 mrad). The red line indicates the overall beam diameter.

Figure 2.9. Simulated effect of the beam current on the overall beam diameter d_p (WD = 2 mm, ΔE = 0.5 eV, α = 8 mrad).

Figure 2.10. Different SE and BSE signals from the interaction volume of a (a) bulk sample and (b) thin TEM sample.

Figure 2.11. FIB milling and deposition procedure.

Figure 2.12. Simple model of elastic electron scattering at a nucleus.

Figure 2.13. Simple model of electron-electron scattering.

Figure 2.14. Scheme of energy spectrum for electrons emitted from a bulk specimen.

Figure 2.15. Sample-electron interaction volume model with exit volume for BSEs (dark green) and SEs (bright green).

Figure 4.23. Correlative SEM/STEM imaging of a multi-walled CNT specimen. (a) 2 keV SE-TLD image, (b) 2 keV SE-TLD image, (c) 30 keV BF-STEM image, (d) 30 keV HAADF-STEM image. Scale bar in (a) applies to (b-d).

Figure 4.24. Correlative SEM/STEM imaging of a multi-walled CNT specimen. (a,b) 2 keV SE-TLD images and (c,d) 30 keV HAADF-STEM images. Superimposed pictures in (c,d) show TED patterns of the marked regions.

Figure 4.25. (a) 30 keV SE-TLD image of α-Fe$_2$O$_3$/ZnO tubes, (b) 30 keV BF-STEM image of α-Fe$_2$O$_3$/ZnO tubes, (c) 30 keV SE-TLD image of α-Fe$_2$O$_3$ and ZnO tubes, (d) 30 keV BF-STEM image of α-Fe$_2$O$_3$ and ZnO tubes.

Figure 4.26. Correlative SEM/STEM imaging of CeO$_2$ NPs. (a) 2 keV SE-TLD image, (b) 30 keV BF-STEM image, (c) 30 keV HAADF-STEM image, (d) 30 keV BF-STEM image.

Figure 4.27. Correlative SEM/STEM imaging of TiO$_2$ NPs. (a) 30 keV SE-TLD image, (b) 30 keV BF-STEM image, (c) 30 keV HAADF-STEM image, (d) 30 keV BF-STEM image.

Figure 4.28. SE-TLD imaging of TiO$_2$ NPs at 2 keV. This time, no contamination layer on the top of the TiO$_2$ NPs was formed.

Figure 4.29. Correlative SEM/STEM imaging of NiIr$_4$ NPs. (a) 2 keV SE-TLD image, (b) 30 keV SE-TLD image, (c) 30 keV BF-STEM image, (d) 30 keV HAADF-STEM image. Scale bar in (a) applies to (c-d).

Figure 4.30. SE/BSE imaging of NiIr$_4$ NPs. (a) 2 keV SE-TLD image, (b) 2 keV BSE-MD image, (c) 2 keV BSE-ICD image. Scale bar in (a) applies to (b,c).

Figure 4.31. Low-keV STEM imaging of NaGdYbErF@NaYGdYbErF core-shell NPs. (a) 30 keV BF-STEM image, (b) 30 keV HAADF-STEM, (c) 30 keV BF-STEM image, (d) 30 keV HAADF-STEM image. Scale bar in (a) applies to (b-d).

Figure 4.32. Low-keV STEM/SEM imaging of NaGdYbErF@NaYGdYbErF core-shell NPs. (a) 30 keV HAADF-STEM image, (b) 30 keV SE-TLD image, (c) 15 keV HAADF-STEM image, (d) 15 keV BF-STEM image.

9 APPENDIX

Convergence angle measurement

Figure 9.1. (a) 30 keV GaN zone axis $[10\bar{1}0]$ transmission electron diffraction pattern. (b) Line scan of the diffraction spots in (a).

For the defects analyses in this work, the beam half convergence angle α is essential for setting a suitable two-beam condition to determine the Burgers vector. Therefore, two methods were applied to measure α experimentally.

The first method is displayed in Fig. 9.1. Using the on-axis CCD-camera, transmission electron diffraction patterns (TEDs) were obtained (e.g. Fig. 9.1 (a)). The diameter of the diffraction spots is related to 2α. The recorded diffraction pattern was calibrated by the known Bragg-angle (θ_B) for the given diffraction spots in GaN. Note, the scattering angle for a specific diffraction spot **g** is given by $2\theta_B$. Fig. 9.1 (b) shows a line profile along the blue arrow in Fig. 9.1 (a). The width of the diffraction spots was measured using the full width half maximum (FWHM) method (Fig. 9.1 (b)). α was calculated to be 1.7 mrad for Helios Nanolab G4 FX operated at an electron beam energy of 30 keV, a beam current 50 pA and a working distance of 4.18 mm.

Another method relies on measuring the defocused beam diameter using a specimen with a sharp sample-vacuum edge. As demonstrated in Fig. 9.2 (a), the specimen is situated at the desired working distance WD. If the beam is condensed on the sample surface, the convergence angle of the beam is α_1. By defocusing the beam (defocus value, Δf; convergence angle, α_2) without changing the working distance of the sample, the image

of the sample becomes blurred (e.g. Fig. 9.2 (b)) due to the increased electron probe radius at the sample position. Since the defocus value is negligible compared to the working distance, the change of half convergence angle due to defocus is neglected ($\alpha_1 \approx \alpha_2$, cf. Fig. 9.2 (a)). In addition, the radius of the focused electron probe is quite small compared to the radius for defocused electron probe (R´). Therefore, only the defocused electron probe is considered in the calculation. Hence, the half convergence angle can be determined by $\alpha_1 \approx \alpha_2 = tan^{-1}\left(\frac{R^{'}}{\Delta f}\right)$. In SEMs, the obtained image is a convolution of the specimen with the electron probe. Given a known sample geometry (sharp edge), the size of the gaussian electron probe can be extracted. With a line scan of the sample-vacuum edge in the SE image (Fig. 9.2 (b)) taken with the defocused electron beam, the defocused electron probe radius can be measured (cf. inset in Fig. 9.2 (b)). Based on the method explained above, 1.79 mrad half convergence angle for the same imaging condition as in Fig. 9.1 was obtained. Therefore, the α value obtained from Fig. 9.1 was confirmed.
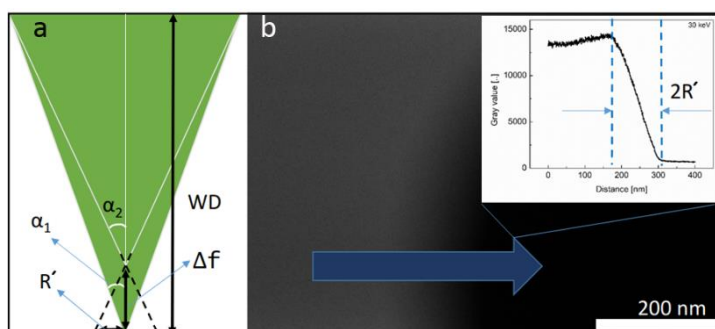
Figure 9.2. (a) Scheme of beam convergence angle measurement, (b) the overfocused 30 keV SE image of a specimen with a sharp sample-vacuum edge.

Sample-thickness measurement

Fig. 9.3 displays a method used in this thesis for sample-thickness determination. Fig. 9.3 (a) displays a low-keV BF-STEM image of a GaN wedge sample. The GaN thickness increases from the right to the left of Fig. 9.3 (a). When the sample is tilted to a two-beam condition (e.g. $\vec{g}_{(000\bar{2})}$), thickness contours are observed as indicated by the white arrow in Fig. 9.3 (a). In the intensity line profile (along the white arrow in Fig. 9.3 (a)) of the thickness contours, several BF-STEM intensity maxima can be observed (e.g. Fig. 9.3 (b)) with increasing distance from the right edge side of the wedge sample. Since the intensity oscillations in the BF-STEM image under two-beam conditions are related

to the corresponding extinction distance ξ_g, the thickness of the wedge sample can be determined. For instance, based on Fig. 9.3 (b), at 25 nm distance from the right edge side of the wedge, the third maximum occurs. Therefore, the thickness of this position is approximately $2 \cdot \xi_{g(000\text{-}2)}$.
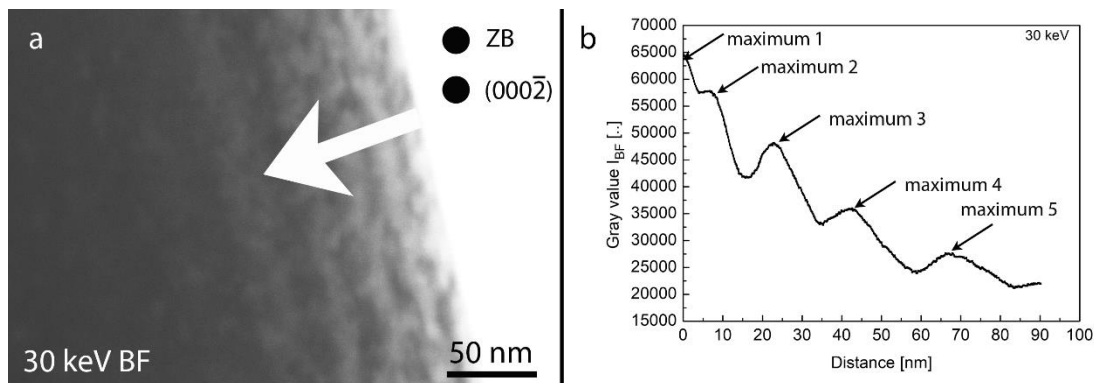
Figure 9.3. (a) Low-keV BF-STEM image for a GaN wedge sample under $\mathbf{g} = (000\bar{2})$ two-beam condition. (b) Line scan of the BF-STEM wedge sample image.

PUBLICATIONS

Reviewed publications

Sun, C. et al. (2019). Analysis of crystal defects by scanning transmission electron microscopy (STEM) in a modern scanning electron microscope. Advanced Structural and Chemical Imaging, 5(1), 1-9.

Sun, C. et al. (2018). On the progress of scanning transmission electron microscopy (STEM) imaging in a scanning electron microscope. Microscopy and Microanalysis, 24, 99-106.

Contributions to scientific conferences

Sun, C. et al. (2019). Investigation of dislocations by STEM in a scanning electron microscope. Microscopy Conference (Berlin): Proceedings, page 592-593.

Sun, C. et al. (2019). Opportunities of correlative SEM and STEM imaging in a

scanning electron microscope. Germany-Japan Joint Seminar on Advanced Electron Microscopy and Its Application (Nagoya).

Sun, C. et al. (2019). On the benefits of obtaining surface topography and volume structure information by correlative S(T)EM in a scanning electron microscope. Microscopy and Microanalysis, 25(S1), 73-74.

Sun, C. et al. (2018). Investigation of dislocations by STEM in a scanning electron microscope. 19 th International Microscopy Congress (Sydney): Proceedings.

Sun, C. et al. (2018). Sample thickness determination by HAADF-STEM in a scanning electron microscope. 19 th International Microscopy Congress (Sydney): Proceedings.

Sun, C. et al. (2018). Correlative STEM and SEM for imaging nanoscaled materials in a scanning electron microscope. 19 th International Microscopy Congress (Sydney): Proceedings.

Sun, C. et al. (2018). Progress of STEM imaging in a scanning electron microscope. IAMNano2018 Conference (Hamburg): Proceedings, 25.

Gerthsen, D. Meffert, M. Sun, C. et al. (2017). Chances and challenges of high-resolution imaging in a scanning electron microscope. Third Salve Symposium (Ulm): Proceedings, page 58-59.

Sun, C. et al. (2017). Low-energy scanning transmission electron microscopy for high-resolution characterization of solid-state and soft-matter samples. Microscopy Conference (Lausanne): Proceedings, page 456-457.

Sun, C. et al. (2016). A new method to orient samples by STEM in a scanning electron microscope. European Microscopy Congress (Lyon): Proceedings, page 639-640.

ACKNOWLEDGEMENTS